FCT Fundação para a Ciência e a Tecnologia
MINISTÉRIO DA EDUCAÇÃO E CIÊNCIA

Sebastian Calderon Velasco
Universidade do Minho
Escola de Engenharia

PRODUCTION AND CHARACTERIZATION OF ZrCN-Ag COATINGS DEPOSITED BY MGANETRON SPUTTERING

outubro de 2015

PRODUCTION AND CHARACTERIZATION OF ZrCN-Ag COATINGS DEPOSITED BY MGANETRON SPUTTERINGulo
Sebastian Calderon Velasco
UMinho | 2015

Universidade do Minho
Escola de Engenharia

Sebastian Calderon Velasco

PRODUCTION AND CHARACTERIZATION OF ZrCN-Ag COATINGS DEPOSITED BY MGANETRON SPUTTERING

Tese de Doutoramento
Programa doutoral em Engenharia de Materiais

Trabalho efectuado sob a orientação de
Professora Doutora Sandra Carvalho
Professor Doutor Albano Cavaleiro

outubro de 2015

STATEMENT OF INTEGRITY

I hereby declare having conducted my thesis with integrity. I confirm that I have not used plagiarism or any form of falsification of results in the process of the thesis elaboration.

I further declare that I have fully acknowledged the Code of Ethical Conduct of the University of Minho.

University of Minho, _____

Full name: Sebastian Calderon Velasco

Signature: _____

ACKNOWLEDGEMENTS

I would like to express my more truthful and special appreciation to every person and institution that made possible the development of this work. My supervisors, Professor Dr. Sandra Carvalho and Professor Dr. Albano Cavaleiro to their tremendous contribution to this work, all the hours sharing and discussing the results, providing their knowledge, without limiting my contribution, enriching my learning process. I would like to thank them for letting me be part of their research groups, encouraging my research work and supporting every step in my growth as a research scientist.

I would like also to thank my co-workers throughout all these years of research, some of which are, to the date, still part of the research group. Isabel Carvalho, Mariana Marques, Edgar Carneiro, Cristiana Alves, Noora Manninen, Isabel Ferreri, Rita Rebelo thank for making this journey an enjoyable period, and for the brilliant comments and suggestions in the process.

Special thanks to Dr. Ramon Escobar from the Autonoma National University of Madrid, Dr. Juan Carlos Sanchez Lopez from the CSIC Sevilla, Dr. Joao Carlos Oliveira from University of Coimbra and Professor Dr. Jeff de Hosson from University of Groningen, for giving me the opportunity to learn about new experimental techniques, sharing their knowledge and for their invaluable pieces of advice that are embodied in this thesis.

I would like also to thank all the technicians and professors that support these research at the Center of Physics from the University of Minho and the Mechanical department from the University of Coimbra.

A special thanks to my beloved wife Lina Fernanda for her support and all the priceless talks and discussion around our Ph.D theses and all the sleepless nights that we spent, during the difficult moment and stressful periods in this journey, it would not have been possible without her support.

To all my family, I cannot express how grateful I am to my mother, father, grandmother and siblings for all of the sacrifices that they have made on my behalf. I would also like to thank all of my friends who, at the distance, support and encourage me to pursuit my goal.

This thesis was financially supported by a PhD scholarship from Fundação para a Ciência e Tecnologia (Ref.: SFRH/BD/80947/2011), inserted in the Programa Potencial Humano Quadro de Referência Estratégico Nacional (POPH - QREN) Tipologia 4.1 – Formação Avançada. The POPH-QREN is co-financed by Fundo Social Europeu (FSE) and by Ministério da Ciência, Tecnologia e Ensino Superior (MCTES).

ABSTRACT

Zr-C-N coatings, incorporating silver as antibacterial agent, are deposited onto stainless steel 316L (SS316L) and Si (100) substrates by unbalanced magnetron sputtering; their corrosion and tribological properties were evaluated to understand their potential to be used in joint orthopedic devices. Zirconium carbonitride was selected owing to both its excellent biocompatibility and non-toxic behavior. Despite ZrCN has been widely studied, no other report on the deposition and characterization of Zr-C-N-Ag coatings exist in the literature, to the author knowledge. Therefore, the contribution of this project for the state of the art on Zr-C-N system alloyed novel metallic elements is:

(i) A structural characterization, including the phase composition, based on the identification of crystalline (X-ray diffraction and transmission electron microscopy) and amorphous phases (Raman spectroscopy), and the chemical composition of the material both in bulk (electron probe microanalysis) and at the surface (X-ray photonelectron spectroscopy). The morphology of the coatings was also studied (scanning electron microscopy), in order to evidence the influence of the deposition parameters on the coatings cross-section and surface morphology, and correlate them with the functional properties.

(ii) In order to optimize the adhesion, mechanical and electrochemical properties of the coatings; an optimization method was applied to the deposition process to decrease the final number of coating runs.

(iii) The in-depth electrochemical and tribological characterization of the coatings was performed in a Hank's balanced salt solution with 10 gr/L of bovine serum albumin, in order to mimic as much as possible the condition of the biological fluid of human body.

In Zr-C-N-Ag system a diversity of phases can occur, such as zirconium carbonitride (ZrCN), amorphous carbon (a-C or a-(C, N)) and metallic silver (Ag). By controlling the deposition conditions, it is possible to adjust the amount of each phase, and then, to tune the properties of the system.

The optimization of the deposition process shows that the ideal composition of the Zr-C-N-Ag coatings is attained when the Zr_2CN phase is deposited, with less than 8 at. % of silver nanoparticles, allowing achieving the best compromise between mechanical, electrochemical

and tribological properties. The electrochemical evaluation reveals that both silver and amorphous carbon phases are detrimental to the corrosion resistance. The increase of silver triggers a more active electrochemical reactions in the system that increases the corrosion process. In addition, the combination of silver and amorphous phases produces a more electrochemical porous materials, which promotes the penetration of the electrolyte.

Although marginally, silver also negatively affects the wear resistance of the system, when tested against an ultra-high molecular weight polyethylene, due to a delay it causes in the formation of a protective albumin layer. The coefficient of friction (COF) of the coatings, did not show any correlation with the amount of silver, while the amorphous carbon phases seems to reduce the COF.

Finally, the phase distribution showed a relevant role in the silver ion release to the electrolyte, as a function of the silver nanoparticles surrounding. This distribution of phases creates nano-galvanic couples in the system that controls the silver ion release, depending on a:C or ZrCN phases, the oxidation of silver can be enhanced or retarded, respectively. The antibacterial effect of the system does not have a direct relation with the silver ion release. Even coatings with low silver ion release may possess antibacterial capabilities, if silver is highly agglomerated on the surface.

RESUMO

Neste trabalho foram depositados revestimentos do sistema Zr-C-N-Ag, incorporando a prata como um agente antibactericida, em substratos de aço inoxidável 316L e silício (100), utlizando a técnica de pulverização catódica por magnetrão. Os revestimentos foram caraterizados no que concerne o seu comportamento tribológico e à corrosão, no sentido de compreender o seu potencial para serem utilizados em próteses ortopédicas. O zircónio foi selecionado por causa da sua biocompatibilidade e comportamento não tóxico. Ao conhecimento do autor, apesar do sistema ZrCN ter sido amplamente estudado, não existe na literatura qualquer referência à investigação deste sistema incorporando prata. Assim, a contribuição deste trabalho para o estado da arte dos revestimentos Zr-C-N com adições de outros elementos é:

(i) Caraterização estrutural, incluindo a análise da composição fásica, baseada quer na identificação das fases cristalinas (difração de raios X e microscopia eletrónica de transmissão) e amorfas (espectroscopia Raman) quer na avaliação da composição química dos revestimentos, no maciço (microssonda eletrónica) e na superfície (espectroscopia de fotoeletrões de raios X). A morfologia dos revestimentos em superfície e secção transversal foi analisada por microscopia eletrónica de varrimento, pondo em evidência a influência dos parâmteros de deposição na rugosidade e compacidade dos revestimentos.

(ii) De modo a otimizar a adesão e as propriedades mecânicas e eletroquímicas dos revestimentos, um método de otimização foi aplicado ao processo de deposição para diminuir o número total de experiências.

(iii) A caraterização eletroquímica e tribológica dos revestimentos foi realizada numa solução salina balanceada com 10 gr/L de albumina sérica bovina de modo a mimetizar as condições dos fluidos biológicos caraterísticos do corpo humano.

Podem occorrer no Sistema Zr-C-N-Ag diversas fases, tais como os carbonitretos de zircónio (ZrCN), carbono amorfo (a-C or a-(C, N)) e prata metálica (Ag). Controlando as condições de deposição, é possível ajustar a quantidade de cada uma das fases e, então, alcançar as propriedades desejadas.

A otimização do processo de deposição mostra que a composição ideal para os revestimentos de Zr-C-N-Ag é atingida quando é depositada a fase Zr_2CN, com menos de 8 % at. de nanopartículas de prata, permitindo encontrar o melhor compromisso entre propriedades

mecânicas, eletroquímicas e tribológicas. A caraterização eletroquímica permitiu concluir que ambas as fases de prata e de carbono amorfo são prejudiciais para a resistência à corrosão. Adicionalmente, a prata tem uma ação negativa na resistência ao desgaste do sistema, quando os testes são realizados contra um contracorpo de polietileno de alta densidade de elevado peso molecular, devido ao atraso que ela provoca na formação no contato da camada protetora de albumina.

Finalmente, a distribuição de fases tem um papel relevante na libertação de iões de prata para o eletrólito, dependente da vizinhança que têm as nanopartículas de prata. Dependendo de haver a fase de carbono amorfo ou de ZrCN, a oxidação da prata pode ser, respetivamente, realçada ou retardada. O efeito antibactericida do sistema não tem uma relação direta com a libertação dos iões de prata. Mesmo revestimentos com libertação de iões de Ag reduzida podem possuir capacidades antimicrobianas, se houver suficiente teor de prata aglomerada na superfície.

TABLE OF CONTENTS

LIST OF FIGURES

LIST OF TABLES

STRUCTURE OF THE THESIS

This document is divided in 9 chapters in order to provide a logical sequence to understand the production of ZrCN-Ag coatings by magnetron sputtering and their characterization. Each chapter is based on papers published in international journals, or in the submission process. In the beginning of each chapter, reference to the correspondent papers is done. The first chapter corresponds to an introduction to the topic of the thesis, focused on the main problems that need to be addressed for the development of materials or surface treatments in the field of orthopedic prostheses, specifically hip joint prosthesis. Finalizing the introduction, the main and specific objectives of the thesis are presented, describing the methodology followed to solve the established problem.

The second chapter consists of a detailed review of the literature regarding ceramic coatings with embedded silver nanoparticles, for different types of application. The review is focused on the effects of silver nanoparticles incorporation on the physical and chemical properties of the coatings and their functional properties, providing a broad understanding and newest advances on these types of films, in the last decade.

Chapter III includes a brief description of the experimental methods used to produce and characterize the coatings. A short explanation of the techniques and the experimental parameters used during the development of the work will be provided.

Chapter IV reports the optimization of the coatings deposition parameters to achieve the best compromise between three functional properties, the electrochemical response, the hardness and the adhesion.

Based on the results achieved in the fourth chapter, a set of samples is selected to evaluate in-detail the chemical, structural and functional properties of the coatings. Therefore, chapter V consists on the chemical and structural characterization of ZrCN-Ag coating, emphasizing the determination of the chemical composition of the bulk and the surface as well as the phase composition (crystalline and amorphous) of the coatings.

The detailed characterization carried out in Chapter V provides also a base to analysis and correlate the functional properties studied in Chapter VI, VII and VIII. Thus, Chapter VI includes a more developed electrochemical characterization, in which additional evaluation of the surface

composition is carried out after the electrochemical tests, as well as immersion tests in a simulated synovial body fluid as a function of time.

Chapter VII presents the tribological characterization of the coatings, against a counter body, which is a widely used material in hip and knee joint prostheses (ultrahigh molecular weight polyethylene), and the simulated synovial fluid, as lubricant.

Chapter VIII summarizes the silver evolution in the Zr-C-N matrix, by evaluating the silver segregation and the silver ion release in simple simulated body fluid.

Finally, chapter IX presents an overall conclusion of the thesis and discusses possible future perspectives of the research.

PRODUCTION AND CHARACTERIZATION OF ZrCN-Ag COATINGS DEPOSITED BY MAGNETRON SPUTTERING

CHAPTER I- Introduction

1 INTRODUCTION

This document is focused on the production and characterization of a novel coating material composed of Zr-C-N-Ag. This surface modification approach is proposed for enhancing functionalities in terms of corrosion, wear resistance and antibacterial properties of medical devices. This chapter presents a discussion on the importance of developing such a new surface modification to improve materials used in orthopedic implants; focusing on the necessities from the state of the art in the beginning of this project (2010) that motivated the development of the research project. The main functionalities, the principal type of failures and the materials used in the market for hip joint prosthesis will be highlighted. Finally, the project proposal for this thesis is explained.

This report is focused on the development of coating for implantable orthopedic joint prosthesis in contact with synovial fluid. The two most effective and studied orthopedic joint prosthesis to the date are those for hip and knee. The organization for Economic Cooperation and Development (OECD) reported that, the hip and knee replacement showed a monotonic increase from 2000 to 2009, as shown in Figure 1-1. The same entity summarizes the hip and knee replacement in 2009 organized per country, where in the majority of the cases the hip joint prosthesis is a predominant need (Figure 1-2) [1].

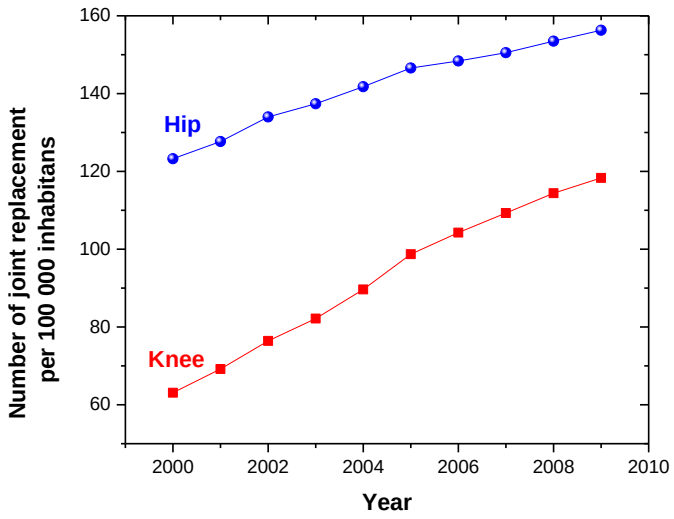

Figure 1-1 Hip and knee prostheses used between 2000 and 2009 [1] (adapted from the corresponding reference).

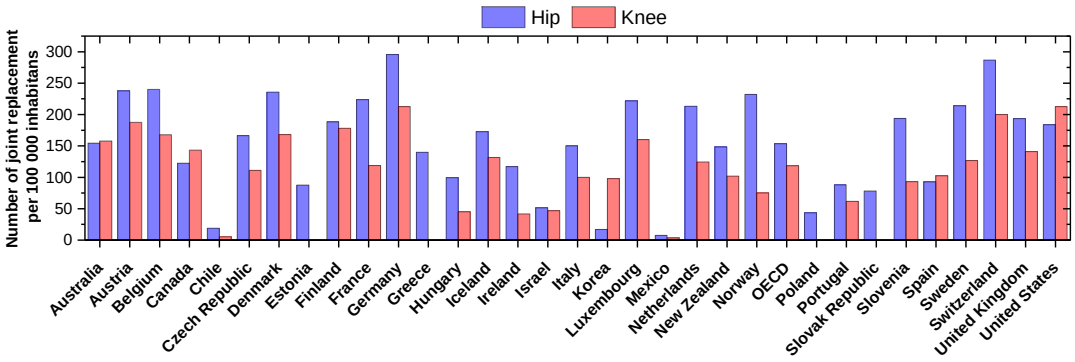

Figure 1-2 Hip and knee prostheses used in 2009 for different countries [1] (adapted from the corresponding reference).

1.1Hip joint prosthesis

The human hip joint is a classic ball and socket joint and is roughly composed by the femoral head and the acetabulum of the pelvis [2] (Figure 1-3). The configuration of this joint provides, a wide range of movements and it is subjected to substantial forces during simple activities, reaching up to six times the human body weight [2-6].

The hip joint prosthesis could be divided into two major components, the femoral and the acetabular parts. The femoral component mainly includes the femoral head and femoral stem. The acetabular part is primarily composed of an element to restore the articulating surface of the acetabular socket and an element to anchor to the pelvis, as shown in Figure 1-3.

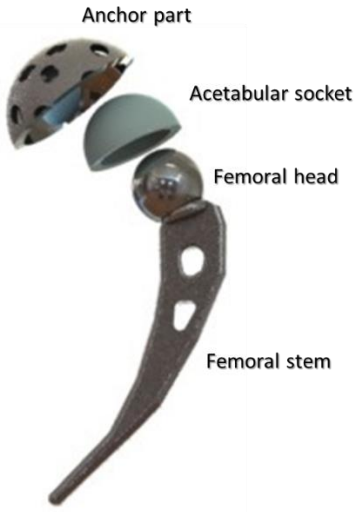

Figure 1-3 Hip joint prosthesis example.

1.1.1 Requirements for a hip joint prosthesis

In general terms, requirements for implants can be divided into three main categories: biocompatibility, mechanical/tribological properties and manufacturing, being ascetic and mechanical loosening the most common causes of failure [6]. The requirements within each of these categories highly depend on the function of the implant part. The femoral stem, for instance, has the main role to connect the femoral head and the femoral bone, and hence, it requires to provide high rates of osseointegration and to possess similar mechanical properties to the femoral bond such as Young modulus and mechanical strength, among other. The femoral head, on the contrary, do not require osseointegration and has less demanding structural requirements due to the spherical shape. A summary of the requirements for the materials and the designs of the hip joint prosthesis is presented below, focused on the femoral head part of the implants, due to its importance for this project.

1.1.1.1Biocompatibility requirements

The biocompatibility deals with the ability of the implant to guarantee that the surface causes no tissue reaction, since it may cause the failure of the implant or toxicity to the cells, or in general to the patients. In fact, the chemical properties of the body can cause corrosive attack, which may degrade the implant and cause release of ions that adversely affect the body [7]. Although the temperature conditions in the human body are not extreme for the materials (37 °C), the chemical and biomechanical environments can be extreme. In particular, the acetabular cup and the head of the femur of the hip joint are in contact with the synovial joint, which acts as a biological lubricant and shock absorber [8]. Therefore, it is compulsory that both the correct materials and design are selected to ensure a successful prosthetic device to support the aggressive environment.

The corrosion of metals in biologic fluids is an electrochemical reaction that results in the release of metal ions into the surrounding aqueous electrolyte or the formation of corrosion products on the surface of the implant. Depending on the nature of the corrosion products, they can cause different reactions such as wear, inflammation, infection or even toxicity issues. Normally, the materials used in orthopaedic biomaterials possess a passivating oxide layer [6], which protects the implant from corrosion; however, this passive layer is not always optimal for wear or mechanical resistance and can be deteriorated.

Many types of corrosion must be avoided after implantation, such as pitting, crevice, and intergranular types, among others. General corrosion, on the other hand, despite of being

tolerable, must remain below 0.00025 mm/yr to consider a material corrosion resistance [7]. This value is highly dependent on the composition of the material, the total area and the finish of the joint surfaces.

The conditions to simulate human body fluids are usually achieved by Hanks's and Ringer's solutions with pH of 7.4 and isotonic with the human body [7]. Of all the ionic components of this fluids, the chlorine ions are typically the most aggressive to metal implants. Several types of chloride-induced corrosion attacks have been reported to affect implants; pitting, intergranular and crevice corrosion have been observed [7].

1.1.1.2Mechanical and tribological requirements

Orthopedic devices must maintain mechanical strength. In the case of hip joint prostheses, they support several times the body human weight, depending on the activity performed by the patients. For the articulation element, the structural requirements are less demanding compared to the anchor parts, because the domed shape of the acetabular part provides intrinsic stiffening. Moreover, the loads are more compressive type and hooplike than in the femoral stem where bending dominates [9].

One of the most critical problems of the hip joint implants is the resistance to cyclic loading, since it should sustain more than $3x10^6$ cycles per year [7]. Considering that a patient under 60 year of age has a life expectancy exceeding 20 years, the service life of the devices is a limiting factor, reaching values of only around 15 years [8].

Wear is recognized as the main cause of hip implant failure, and therefore, it has been widely investigated both experimentally and clinically, demonstrating the coexistence of abrasive, adhesive, fatigue and corrosive wear [8]. As previously mentioned, the hip implants are lubricated by the synovial fluid, which depending on the patient and his/her health statue, can vary in volume from 1 to 5 ml [8].

Depending on the materials couple used for the articulating part, the wear of the implant may be, among other types, abrasive or adhesive. One of the most commonly material used in implants is ultrahigh molecular weight polyethylene (UHMWPE). Due to its low mechanical strength, UHMWPE suffers adhesive and abrasive wear, which promotes the formation of wear debris [9]. Such debris has been found to cause a series of events that lead to the destruction of healthy bond, destabilizing the implant, etc. [6].

1.1.1.3 Antibacterial

Additionally to the corrosion resistance and mechanical requirements, the development of antimicrobial materials has become an intensive field of study during the last decade, due to

the necessity for controlling bacterial colonization on materials surfaces used on manufacturing prosthetic devices. Many antibacterial agents have been considered, being silver extensively studied. Silver is known as the most ancient antimicrobial agent and it was used for hundreds of years as disinfectant and bactericidal material until the development of antibiotics [10]. Recently, due to the successfully development of nanotechnology and drug delivery systems, silver became very popular and it has been studied in nano-forms as a potential antimicrobial agent for biomedical materials. Silver nanoparticles, nanorods and thin films, among others, have been investigated in order to elucidate the potential of these approaches in terms of antimicrobial effectiveness and durability [11-13], as well as toxicity effects for human beings. The efficacy has been substantially proven and very good results have been published [12-22]. Nevertheless, the effect of the silver on functional properties, such as wear and corrosion resistance of implants, has not been addressed properly and must be carefully studied in order to ensure that the functionalities of the system are not degenerated.

1.1.2 Biomaterials for hip joint prosthesis

The materials for the hip joint prosthesis are generally stainless steel, cobalt-based alloy, titanium-based alloy, zirconia and UHMWPE [7-8, 23]. The combination of all these materials has been studied since the 1930's, starting with metal on metal prosthesis of stainless steel, followed by cobalt-chromium alloys in the 1940's [9], ceramic on ceramic prosthesis developed in 1970s and, finally in the last decades, the polymer on metal/ceramic [9]. However, each combination present its drawbacks, including the presence of potentially cancerous metal ions in metal on metal devices, the brittleness in prosthesis involving ceramics, and the wear debris in polymers [8]. Some remarks regarding the most used material in hip joint prosthesis devices are shown in Table 1-1.

.

Table 1-1 Characteristics of the most common materials used for prosthesis devices [7].

Stainless steel	***Cobalt alloys***	***Titanium-alloys***	**UHMWPE**
It possesses an invisible and adherent chromium-rich oxide surface film that offers general corrosion resistance.	The alloys are noted for high strength, good corrosion and wear resistance, but they release high doses of	Low-density element. Strengthened by alloying and deformation. Corrosion resistance	Performs poorly in direct contact with bone. UHMWPE is still the gold standard for the articulation element.

Stainless steel	*Cobalt alloys*	*Titanium-alloys*	UHMWPE
However, it has low pitting corrosion resistance. **Advantages** Some advantages of the stainless are cost, availability, easy processing. **Disadvantages** Long-term behavior, high modulus.	metals ions after implanted. **Advantages** Wear resistance, corrosion resistance, fatigue strength. **Disadvantages** High modulus, biocompatibility	from the stable oxide film on its surface. **Advantages** High biocompatibility, corrosion resistance, low Young´s modulus, fatigue strength. **Disadvantages** Low wear resistance, low shear strength.	**Advantages** Low wear rates, biocompatibility. **Disadvantages** Wear debris, oxidative degeneration.

Additionally to the previous materials, zirconium oxide has demonstrated good biocompatibility that offers potential advantages with respect to fracture toughness properties compared to other ceramic materials [9].

1.2 Surface modification and project proposal

Surface engineering is considered an efficient approach for orthopedic devices, since the material surface is the first part in contact with the environment, being responsible for failures due to wear, corrosion and bacterial colonization [24]. Such modifications can be used to reduce implants ion release, enhance corrosion and wear resistance and even to provide additional properties as antibacterial effect. Thus, taking into consideration that the hip joint implants mainly fail due to wear, corrosion or bacterial colonization, a surface modification approach is suggested in this work to provide multifunctional characteristics.

A countless number of techniques and materials can be considered as candidates to design and produce surface modification; however, physical vapor deposition techniques allow a large variety of material production without the necessity of high temperatures, or hazardous chemical, being very attractive as eco-friendly technology for the industry. Using these techniques, the topography and surface chemistry modification of stainless steel using ceramics and bactericidal agents has shown promising outcomes for improving the mechanical properties [16, 24-25] and reducing the risk of infection on the implants [26]. TiN and ZrN coatings, for instance, have been used for increasing both the corrosion resistance and the mechanical properties,

with the consequent improvement of the tribo-chemical behavior and the biocompatibility [27-28]. Moreover, by adding carbon (TiCN and ZrCN) a further enhancement of these properties can be achieved, with the coatings fulfilling the requirements to be implanted in the human body, as later explained [28-29].

Silver and copper ions are the most effective metals known for bactericidal effect, with considerable good biocompatibility [18, 30-32], being silver the most used since it does not strongly affect the corrosion resistance of the coating [17]. Numerous reports have been published during the last few years regarding silver NPs; they allow attaining antimicrobial properties in countless kinds of materials and for a considerably good number of microorganisms; some examples can be found in [19, 33-38]. Hsieh et al [19], for instance, have shown an antibacterial effect against *E. Coli* for TaN with 1.6 to 10 at. % of silver in tests carried out for 24 hours; in their study, they concluded that the dissolution of the silver prompts the antibacterial effect, with 80% of antibacterial efficiency for a sample with 10 at. % of silver. Akhavan et al [13] have evaluated the influence of the silver form embedded in TiO_2 on the antibacterial effect and the silver ion release to the media, finding that the latter can be increased or reduced depending on how silver was, as thin films, nanorods or nanoparticles. Jamuna et al [39], have demonstrate that very low concentrations of silver ions can show antibacterial behavior in Ag-TiO_2 coatings. In their study, the Ag^+ released is largely reduced after 4 days of immersion, reaching values no larger than 140 ppb (~28 ppb cm^{-2}) of Ag^+ after 1 day of immersion into 30 ml of phosphate buffered saline.

This project foresees a combination of these two families of materials combining the resistance of the ZrCN with the antibacterial effect of silver to develop a biomaterial suitable to be used in implant devices. Thus, the deposition of Zr-C-N-Ag coatings onto stainless steel is proposed, focused on the understanding of the structural, mechanical, tribological and electrochemical properties of the system, aiming materialist potential application in hip joint prosthesis. Due to the large variety of requirement of the biomaterials, depending on the local of implantation, this study is focused on the necessities of a material for the femoral head part in hip joint prosthesis, as schematized in Figure 1-4.

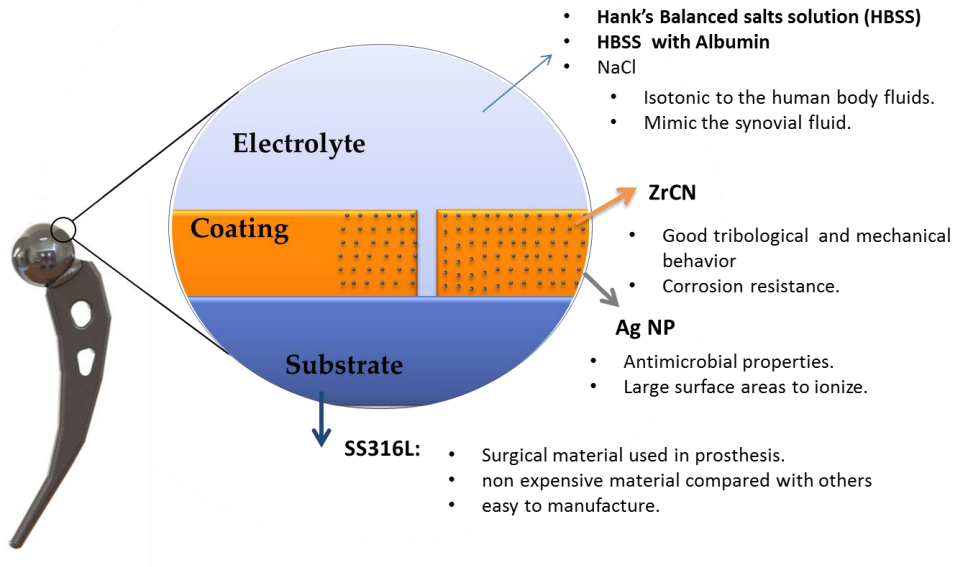

Figure 1-4. Scheme of the thesis proposal.

Stainless steel 316 L (SS316L) is a well-known, non-expensive, biocompatible material used in this kind of devices, but exhibits lower mechanical and corrosion resistance, being justified the use of to the more resistant $ZrC_{1-x}N_x$ films [40-41]. Cotrut et al. [42], for instance, have demonstrated that $ZrC_{1-x}N_x$ deposited by magnetron sputtering can improve the corrosion resistance and reduce the friction coefficient of Ti6Al4V. In addition, in $ZrC_{1-x}N_x$ system, for instance, by tuning the amount of C in the films, amorphous carbon phase can be formed, altering the structural [43-45] and mechanical characteristics [46] and interfering in the functional properties, such as the tribological [47], corrosion resistance [48] and biocompatibility [28-29]. Furthermore, the addition of silver to the already complex ternary Zr-C-N coatings entails the coexistence of a large variety of phases in the films, altering their chemical bonding states [42], but providing the system with additional properties.

The silver nanoparticles (Ag) will be embedded into the $ZrC_{1-x}N_x$ matrix to provide the antibacterial properties to the system, which has been previously demonstrated by other groups, and mentioned in preceding sections. Thus, the mechanical, tribological and electrochemical properties of the system must be monitored in a simulated synovial fluid, to determine the influence of the Ag on the mentioned properties.

The general objective of this project is to deposit Zr-C-N-Ag coatings onto SS316L, for the protection of biomedical implants. Zr-C-N-Ag is expected to accomplish multifunctional properties, simultaneously confering enhanced tribological and electrochemical resistance, as well as antibacterial properties to the system. Therefore, this document will be mainly focused on:

- **Identifying** proper deposition parameters to produce zirconium carbonitrides coatings onto stainless steel 316L with different silver nanoparticles contents.
- **Correlating** the deposition parameters with the coatings chemical, structural and morphological characteristics.
- **Optimizing** the composition of the coatings to obtain the best response in their functional properties (mechanical, electrochemical and adhesion).
- **Understanding** the relationship between the deposition parameters, structure, mechanical properties and morphology with the tribological behavior and electrochemical response of the system.
- **To obtain** a detailed description of the silver behavior in the matrix and its correlation with the antibacterial activity.

1.3 References

1. Indicators, O., Hip and Knee Replacement. In *Health Care Activities*, Oct-2011 ed.; online library of the Organisation for Economic Cooperation and Development: **2011**.

2. Maciel, A. *Biomechanics of Hip Joint Capsule*; The National Center of Comp etence in Research Computer Aided and Image Guided Medical Interventions: swiss, **2002**; pp 1-32.

3. Nordin, M.; Frankel, V. H., *Basic Biomechanics of the Musculoskeletal System*. Lippincott Williams & Wilkins: **2001**; p 872.

4. Andriacchi, T. P.; Hurwitz, D. E., Gait Biomechanics and the Evolution of Total Joint Replacement. *Gait & Posture* **1997,** *5* (3), 256-264.

5. Hurwitz, D. E.; Sumner, D. R.; Andriacchi, T. P.; Sugar, D. A., Dynamic Knee Loads During Gait Predict Proximal Tibial Bone Distribution. *Journal of Biomechanics* **1998,** *31* (5), 423-430.

6. Alvarado, J.; Maldonado, R.; Marxuach, J.; Otero, R., Biomechanics of Hip and Knee Prostheses. *Applications of Engineering Mechanics in Medicine* **2003**, 1-17.

7. Davis, J. R., *Handbook of Materials for Medical Devices*. ASM International: United States of America, **2003**; Vol. 1, p 341.

8. Mattei, L.; Di Puccio, F.; Piccigallo, B.; Ciulli, E., Lubrication and Wear Modelling of Artificial Hip Joints: A Review. *Tribology International* **2011,** *44* (5), 532-549.

9. Callaghan, J. J.; Rosenberg, A. G.; Rubash, H. E., *The Adult Hip*. Lippincott Williams & Wilkins: **1998**; p 1792.

10. Chopra, I., The Increasing Use of Silver-Based Products as Antimicrobial Agents: A Useful Development or a Cause for Concern? *Journal of Antimicrobial Chemotherapy* **2007,** *59* (4), 587-90.

11. J. Zhao, X. C., H. Tang, T. Liu, H. Gu, and R. Cui,, Bactericidal and Biocompatible Properties of Tin/Ag Multilayered Films by Ion Beam Assisted Deposition. *Journal of Materials Science: Materials in Medicine* **2009,** *20* (101), S101–S105.

12. Krasimir Vasilev, V. S., Karine Anselme, Chi Ndi, Mihaela Mateescu, Bjorn Dollmann, Petr Martinek, Hardi Ys, Lydie Ploux, and Hans J. Griesser, Tunable Antibacterial Coatings That Support Mammalian Cell Growth. *Nano Letters* **2010,** *10* (1), 202-207.

13. Akhavan, O.; Ghaderi, E., Capping Antibacterial Ag Nanorods Aligned on Ti Interlayer by Mesoporous Tio2 Layer. *Surface and Coatings Technology* **2009,** *203* (20-21), 3123-3128.

14. Niall Stobie, B. D., Steven J. Hinder, Patrick McHale, Declan E. McCormack, Silver Doped Perfluoropolyether-Urethane Coatings: Antibacterial Activity and Surfece Analisys. *Colloids and Surfaces B: Biointerfaces* **2009,** *72* (1), 62–67.

15. C.Y. Flores, C. D., A. Rubert, G.A. Benítez, M.S. Moreno, M.A. Fernández, Lorenzo de Mele, R.C. Salvarezza, P.L. Schilardi, C. Vericat, Spontaneous Adsorption of Silver Nanoparticles on Ti/Tio2 Surfaces. Antibacterial Effect on Pseudomonas Aeruginosa. *Journal of Colloid and Interface Science* **2010,** *350* (2), 402-8.

16. Llinos G Harris, R. G. R., Staphylococci and Implant Surfaces: A Review. *Injury, Int. J. Care Injured* **2006,** *37*, S3–S14.

17. Wei Shao, Q. Z., Effect of Corrosion Rate and Surface Energy of Silver Coatings on Bacterial Adhesion. *Colloids and Surfaces B: Biointerfaces* **2010,** *76* (1), 98–103.

18. Y.Z. Wan, S. R., F. Hea, Y. Huang, Surface Modification of Medical Metals by Ion Implantation of Silver and Copper. *Vacuum* **2007,** *81* (9), 1114–1118.

19. Hsieh, J. H.; Tseng, C. C.; Chang, Y. K.; Chang, S. Y.; Wu, W., Antibacterial Behavior of Tan–Ag Nanocomposite Thin Films with and without Annealing. *Surface and Coatings Technology* **2008,** *202* (22–23), 5586-5589.

20. T. Bechert, M. B. s., S. Lugauer, A. Regenfus, J. Greil, J.-P. Guggenbichler, Antimicrobial Activity of the Erlanger Silver Catheter. *Infection* **1999,** *27*, S24-S29.

21. Piersandro Pallavicini, A. T., Giacomo Dacarro, Yuri Antonio Diaz-Fernandez, Matteo Galli, Pietro Grisoli, Maddalena Patrini, Giorgio Santucci De Magistris, Robertino Zanoni, Self-Assembled Monolayers of Silver Nanoparticles Firmly Grafted on Glass Surfaces: Low Ag+ Release for an Efficient Antibacterial Activity. *Journal of Colloid and Interface Science* **2010,** *350* (1), 110-6.

22. Qilin Cheng, C. L., Vladimir Pavlinek, Petr Saha, Huanbing Wang, Surface-Modified Antibacterial Tio2/Ag+ Nanoparticles: Preparation and Properties. *Applied Surface Science* **2006,** *252* (12), 4154–4160.

23. Narayan, R., *Biomedical Materials*. Springer Verlag: India, **2009**; p 566.

24. U Kamachi Mudali, T. M. S. a. B. R., Corrosion of Bio Implants. *Sadhana* **2003,** *28*, 601–637.

25. Y.M. Chena, G. P. Y., J.H. Huang, Comparison of Electrochemical Porosity Test Methods for Tin-Coated Stainless Steel. *Surface and Coatings Technology* **2002,** *150* (2-3), 309–318.

26. Rabih O. Darouiche, G. G., Mohammad D. Mansouri, Antimicrobial Activity of Antiseptic-Coated Orthopaedic Devices. *International Journal of Antimicrobial Agents* **1998,** *10* (1), 83–86.

27. Marina Brama, N. R., John Hunt, Andrea Ricci, Roberto Teghil, Silvia Migliaccio, Carlo Della Rocca, Silvia Leccisotti, Attilio Lioi, Marta Scandurra, Giovanni De Maria, Daniela Ferro, Fanrong Pu, Gianluca Panzini, Laura Politi, Roberto Scandurra, Effect of Titanium Carbide

Coating on the Osseointegration Response in Vitro and in Vivo. *Biomaterials* **2007,** *28* (4), 595–608.

28. Hollstein, F.; Kitta, D.; Louda, P.; Pacal, F.; Meinhardt, J., Investigation of Low-Reflective Zrcn–Pvd-Arc Coatings for Application on Medical Tools for Minimally Invasive Surgery. *Surface and Coatings Technology* **2001,** *142–144* (0), 1063-1068.

29. Balaceanu, M.; Petreus, T.; Braic, V.; Zoita, C. N.; Vladescu, A.; Cotrutz, C. E.; Braic, M., Characterization of Zr-Based Hard Coatings for Medical Implant Applications. *Surface & Coatings Technology* **2010,** *204* (12–13), 2046-2050.

30. Anchun Moa, J. L., Wei Xu, Suqin Xian, Yubao Li, Shi Bai, Preparation and Antibacterial Effect of Silver–Hydroxyapatite/Titania Nanocomposite Thin Film on Titanum. *Applied Surface Science* **2008,** *255* (2), 435–438.

31. Kumar, R.; Munstedt, H., Silver Ion Release from Antimicrobial Polyamide/Silver Composites. *Biomaterials* **2005,** *26* (14), 2081–2088.

32. Damm, C.; Munstedt, H., Kinetic Aspects of the Silver Ion Release from Antimicrobial Polyamide/Silver Nanocomposites. *Applied Physics A* **2008,** *91* (3), 479–486.

33. Betts, A.; Dowling, D.; McConnell, M.; Pope, C., The Influence of Platinum on the Performance of Silver-Platinum Anti-Bacterial Coatings. *Materials & design* **2005,** *26* (3), 217-222.

34. El-Kady, A. M.; Ali, A. F.; Rizk, R. A.; Ahmed, M. M., Synthesis, Characterization and Microbiological Response of Silver Doped Bioactive Glass Nanoparticles. *Ceramics International* **2011,** *38* (1), 177-188.

35. Lok, C. N.; Ho, C. M.; Chen, R.; He, Q. Y.; Yu, W. Y.; Sun, H.; Tam, P. K. H.; Chiu, J. F.; Che, C. M., Silver Nanoparticles: Partial Oxidation and Antibacterial Activities. *Journal of Biological Inorganic Chemistry* **2007,** *12* (4), 527-534.

36. Cao, H.; Liu, X.; Meng, F.; Chu, P. K., Biological Actions of Silver Nanoparticles Embedded in Titanium Controlled by Micro-Galvanic Effects. *Biomaterials* **2011,** *32* (3), 693-705.

37. Dowling, D.; Betts, A.; Pope, C.; McConnell, M.; Eloy, R.; Arnaud, M., Anti-Bacterial Silver Coatings Exhibiting Enhanced Activity through the Addition of Platinum. *Surface and Coatings Technology* **2003,** *163*, 637-640.

38. Kelly, P. J.; Li, H.; Benson, P. S.; Whitehead, K. A.; Verran, J.; Arnell, R. D.; Iordanova, I., Comparison of the Tribological and Antimicrobial Properties of Crn/Ag, Zrn/Ag, Tin/Ag, and Tin/Cu Nanocomposite Coatings. *Surface and Coatings Technology* **2010,** *205* (5), 1606-1610.

39. Jamuna-Thevi, K.; Bakar, S. A.; Ibrahim, S.; Shahab, N.; Toff, M. R. M., Quantification of Silver Ion Release, In vitro Cytotoxicity and Antibacterial Properties of Nanostuctured Ag

Doped Tio2 Coatings on Stainless Steel Deposited by Rf Magnetron Sputtering. *Vacuum* **2011,** *86* (3), 235-241.

40. Calderon V, S.; Galindo, R. E.; Benito, N.; Palacio, C.; Cavaleiro, A.; Carvalho, S., Ag+ Release Inhibition from Zrcn–Ag Coatings by Surface Agglomeration Mechanism: Structural Characterization. *Journal of Physics D: Applied Physics* **2013,** *46* (32), 325303.

41. Calderon Velasco, S.; Lopez, V.; Almeida Alves, C. F.; Cavaleiro, A.; Carvalho, S., Structural and Electrochemical Characterization of Zr–C–N–Ag Coatings Deposited by Dc Dual Magnetron Sputtering. *Corrosion Science* **2014,** *80* (0), 229-236.

42. Cotrut, C.-M.; Braic, V.; Balaceanu, M.; Titorencu, I.; Braic, M.; Parau, A. C., Corrosion Resistance, Mechanical Properties and Biocompatibility of Hf-Containing Zrcn Coatings. *Thin Solid Films* **2013,** *538* (0), 48-55.

43. Braic, M.; Braic, V.; Balaceanu, M.; Zoita, C. N.; Kiss, A.; Vladescu, A.; Popescu, A.; Ripeanu, R., Structure and Properties of Zr/Zrcn Coatings Deposited by Cathodic Arc Method. *Materials Chemistry and Physics* **2011,** *126* (3), 818-825.

44. Grigore, E.; Ruset, C.; Li, X.; Dong, H., Zirconium Carbonitride Films Deposited by Combined Magnetron Sputtering and Ion Implantation (Cmsii). *Surface and Coatings Technology* **2010,** *204* (12–13), 1889-1892.

45. Chen, C.-S.; Liu, C.-P., Diffusion Barrier Properties of Amorphous Zrcn Films for Copper Metallization. *Journal of Non-Crystalline Solids* **2005,** *351* (49-51), 3725-3729.

46. Larijani, M. M.; Zanjanbar, M. B.; Majdabadi, A., The Effect of Carbon Fraction in Zr(C, N) Films on the Nano-Structural Properties and Hardness. *Journal of alloys and compounds* **2010,** *492* (1–2), 735-738.

47. Silva, E.; Rebelo de Figueiredo, M.; Franz, R.; Escobar Galindo, R.; Palacio, C.; Espinosa, A.; Calderon V, S.; Mitterer, C.; Carvalho, S., Structure-Property Relations in Zrcn Coatings for Tribological Applications. *Surface and Coatings Technology* **2010,** *205* (7), 2134-2141.

48. Gu, J.-D.; Chen, P.-L., Investigation of the Corrosion Resistance of Zrcn Hard Coatings Fabricated by Advanced Controlled Arc Plasma Deposition. *Surface and Coatings Technology* **2006,** *200* (10), 3341-3346.

PRODUCTION AND CHARACTERIZATION OF ZrCN-Ag COATINGS DEPOSITED BY MAGNETRON SPUTTERING

CHAPTER II – State of the Art

2 Introduction

In order to be able to better understand the solution proposed for the problems mentioned in the previous chapter, it is indispensable to understand the chemical, structural and morphological properties and their influence on the functional performance of ceramic-Ag coatings. Therefore, this chapter will provide a critical interpretation of the state of the art of those ceramic-Ag coatings deposited using similar experimental technique as the one covered in this thesis, magnetron sputtering.

Ceramic-Ag coatings have attracted a lot of attention due to their large range of applications. Their multi-phase character confer independent properties of each immiscible phase to the system, providing functional properties such as antibacterial effect, self-lubrication, wear resistance, corrosion resistance, light absorption enhancement, among other. One of the most interesting characteristics of these materials is that the functional properties may be tailored by selecting the appropriate phases, distribution and sizes.

A large number of techniques has been commonly used to produce ceramic-Ag coatings onto a large range of substrates. Among these techniques, electrochemical methods, physical vapor deposition (PVD), chemical vapor depositions (CVD) and sol-gel techniques, among others, are highlighted. However, in the present document, the literature review is focused on coatings consisting on silver nanoparticles in ceramic matrices deposited by one of the most used physical vapor deposition techniques, magnetron sputtering. This procedure will allow the readers to link the current development in the area with the results presented in the following chapters. As the rainbow of properties exhibited by this family of materials are mainly dominated by the silver nanoparticles diffusion and growth in the matrix, the structural and morphological characteristics of the coatings are fundamental parts for the puzzle of understanding of coatings behavior. These characteristics are strongly affected by the production conditions and process resulting in a myriad of situations, reason why the state of the art is limited to magnetron sputtering technique.

2.1 Magnetron sputtering

Magnetron sputtering (MS) has several advantages over other coating methods, its versatility and wide range of variants allow to deposit a large spectrum of materials, with different composition, eliminating the need of hazardous chemicals and sometimes large temperatures to achieve the desired composition. A detailed description of the technique will be provided in

Chapter III. For now, it is important to take into consideration the variables that can affect the properties of the films, as follows:

- Magnetic field, to control the ionization rate of the inert gas used (e.g. Ar) and pulverization rate of the target.
- The type of power supply (RF, DC, Pulsed, HIPIMS, etc), which depends on the composition of the target.
- The distance between the target and the substrate, which partly controls the energy and number of particles that arrive to the substrate.
- The pressure in the chamber (known as discharge pressure), also controls the energy of the particles by changing their mean free path.
- The temperature of the chamber / substrate that provides kinetic energy to the depositing species on the substrate surface to modify their mobility.
- The substrate bias potential, which also contributes to the kinetic energy of the deposited species, and responsible for their back-sputtering.
- Finally, the addition of reactive gases to form compounds between the reactive species and the target material.

Most of these variables were taken into consideration when analyzing the different techniques used to produce ceramic-Ag coatings in this chapter.

2.2 Deposition of ceramic-Ag coating

The production of ceramic films with embedded silver nanoparticles could be divided into five classes, considering the nature of the matrix: nitrides, carbides, carbonitrides, carbon-based films (diamond-like carbon or DLC) and oxides.

Nitrides, carbides and carbonitrides with different stoichiometry are easily deposited by reactive magnetron sputtering due to the possibility of varying either the amount of reactive gases or the power applied to the targets. In these types of coatings, N_2 and hydrocarbons (C_2H_2 and CH_4) gases are used to react with the transition metal (Me) element (Al, Cr, Ti, Nb, Zr, Mo, V, Ta) and form MeN_x MeC_x or $MeC_{1-x}N_x$ phases. By increasing the content of the reactive gas(es) and varying the target power density, it is possible to change from what is known as metallic mode (films rich in metal component) up to a reactive mode (films rich in reactive gas elements). For very high reactive gases contents, poisoning of the target is reached, being formed a stable phase

on its surface (nitride, carbide or carbonitride). In these conditions, the films usually maintain the stable phase stoichiometry.

For the case of C-containing reactive gases, carbon-based amorphous phases can be formed, in a process very similar to plasma enhanced CVD. Hydrogen is, in these cases, incorporated into the coating, which often is not quantify, but which alters largely the properties of these amorphous phases, as exemplify in [1-2]. C-based matrixes can also be achieved by sputtering a graphite target allowing, then, to deposit single C coatings, usually known as DLCs [3-4]. As before, if C-target is sputtered in a reactive C-H atmosphere, H is present in the deposited film.

Oxides-matrixes, on the other hand, have been mainly produced by non-reactive magnetron sputtering combining silver and oxide targets. A summary of the conditions and the different types of matrixes found in the literature is presented in Table 2-1.

In general, the incorporation of silver in the films is achieved by using an additional target in the system or placing silver pellets on the target (multi-target sputtering and/or co-sputtering). In the first case, the silver content may be increased by increasing the power density applied to the silver target [3, 5-12]; due to the very high sputtering rate of Ag, in this configuration small changes in the silver target power lead to large variation of the silver content in the films [3, 11]. When pellets are used, the amount of silver is also controlled by the number of Ag pellets (ratio between Ag and ceramic target areas) [13-17]. Both approaches demonstrate different behaviors in the deposition rates and poisoning of the targets. For a pure silver target, as expected, the deposition rate increases when more power density is applied to the silver target [8, 12]; even though the same total power is applied to the discharge, an increase in the deposition rate is observed, in agreement with the higher sputtering yield of silver when compared with most of the ceramic and metallic targets reported in this document. However, for Ag-pellets on ceramic/metallic target configuration, controversial results are observed in the literature. In some cases, the expected increase in the deposition rate is registered when Ag-pellets number increases [18]; whereas, in others, an unexpected reduction of the deposition rates is shown for large Ag/ceramic areas ratio [13, 17]. This behavior may be explained due to the poisoning of the ceramic/metallic part of the target, near to the pellets location, modifying the deposition rate and target impedance, depending on the power applied in the discharge.

Table 2-1 Deposition conditions of different types of Ceramic-Ag films by MS

Matrix	Method	Temperature [1] [ºC]	Target element	Gas type and flux[2] [sccm]	Other Target Power[3] [W cm^{-2}]	Ag Target Power[3] [W cm^{-2}]	Working pressure[1] [Pa]	Bias[1] [V]	REF
AlN	MS-Mu-DC	NM	Al and Ag	Ar = 12 N_2 = 8	0.74* or 4.93*	0.148, 0.74 and 1.23 *		NM	19
CrN	MS, MS-DC, MS-U-DC, MS-U-P-DC, MS-U-RF, MS-P	190 to 700 and NM	Ag and Cr	Ar and N_2	3.3, 10.2, ~23 or 3 A or 5.3 kW or NM	0 to 8.15 or 0.2 to 2 A or 0.1 and 0.2 kW	$2x10^{-5}$ to 15	-150 to -30 or ground	5, 20-27
MoN	MS-Mu and MS-U	350	Mo and Ag	Ar and N_2	9.2 to 10.2	0 to 7.4	0.34 to 1	-30 or -60	28-30
NbN	MS-U	350	Nb and Ag	Ar = 0.533 Pa N_2 = 0.08 Pa	200 W	30 W	NM	-60	31
TaN	MS-U and MS-Mu	100 and NM	Ta and Ag	Ar and N_2	7.6 to 12.7	0 to 1.10	0.65 to 1.1	40 W, -40	32-37
TiN	MS-U-P-DC	100 to 325	Ti, Ti + Ag pellets or Ag	Ar and N_2	3 to 6.2 1.5 kW 10 mA cm^{-2}	0 to 7.1 or 120 W combined target	0.24 to 0.6	-200 to ground	6, 13, 23, 38-42
VN	MS-U	350	V and Ag	Ar = 0.3Pa N_2 = 0.04Pa	10.2*	0 to 3.8 *	0.34	-60	43
ZrN	MS-U-DC, MS-P-DC and MS-DC	Room Temperature (RT)	Zr and Ag	Ar and N_2	5 or 70 W	0 to 0.77 or 0 to 18W	0.21 to 0.5	-30 to -170	23, 44-49
HfC	MS-RF-Mu	200	HfC and Ag	Ar	250 W	0 to 42 W	1.33	NM	50
SiC	MS-Mu	200	SiC and Ag	Ar	200 W	0 to 25 W	1.33	NM	50
TiC	MS-RF and MS-U	180 to 275	TiC, Ti + Ag bars or Ag	Ar and CH_4	2 A	Combined target or NM	1 to 1.33	NM or -500	51-52
Ti(Si, Ge or Sn)C	MS-DC	300	TiC and Ag, Si, Ge or Sn	Ar	NM	NM	0.53	-50	53
TiSiC	MS and MS-DC	230 and 300	Ti_3SiC_2 and Ag	Ar	NM	NM	NM	NM	53-54

Matrix	Method	Temperature [1] [ºC]	Target element	Gas type and flux[2] [sccm]	Other Target Power[3] [W cm^{-2}]	Ag Target Power[3] [W cm^{-2}]	Working pressure[1] [Pa]	Bias[1] [V]	REF
WC	MS-RF	275	WC and Ag	Ar	NM	NM	1.33	NM	55
MoCN	MS	300	Mo, C and Ag	Ar and N_2	4.4 mA cm^{-2} for Mo and C	NM	0.2	-50	56
TiCN	MS-U-DC, MS-DC	100 to 300	Ti and (Ti + Ag pellets)	Ar, N_2 and C_2H_2	3.5 to 10 mA cm^{-2}	0 to 7. mA cm^{-2}	0.2 to 0.47	-50 to -70	15, 17, 57-60
ZrCN	MS-U-DC	100	Zr, (Zr + Ag pellets) or Ag	Ar, C_2H_2 and N_2	1.83 to 3.75 *	0 to 1.78	0.2 to 0.71	-50	61-63
DLC	MS-DC, MS-U-DC, Microwave sputtering MS-P-AC-Mu MS-FIB MS-U-DC, MS-PECVD, MS-U-AC, MS-RF and MS-RF-DC	RT to 200	(C + Ag pellets) or Ag	Ar, CH_4 and C_2H_2	3.5 to 7.5 or 400 W 3 to 14 A	5 to 10 or 0 to 14 A or 2.2 to 6.6 mA cm^{-2} or 16 to 400W	0.08 to 20	-600 to ground	3-4, 7-10, 18, 64-74
ZrON	MS-P-U, MS-U	RT to 110	Zr and Ag	Ar, N_2 and O_2	4.6 to 10.2	1.02 to 13.75	0.1 to 1.2	-40	75-76
TaON	MS-DC	RT and 300	Ta and Ag	Ar, N_2 and O_2	9.7	0.92	0.65	40 W (RF)	77-78
TiON	MS-DC	NM	Ti and Ag	Ar, N_2 and O_2	6.5 *	7.1 *	NM	NM	76
Al2O3	MS-U-Mu and MS-Mu	RT	Al_2O_3, Ag and Al	Ar = 30	2.15 and 115W	0.039 to 0.083 or 9 W	0.22 and 3.2	NM	79-80
ZnO	MS-RF and MS-Mu	RT to 750	ZnO, Ag (Zn+ Ag pellets) and (ZnO doped with $AgNO_3$)	Ar and O_2	100 to 1000W	3 to 13W or combined target	0.5 to 4	NM	14, 81-85
YSZ	MS and MS combined with vaccum arc and	150	Ag	Ar	Produced by PLD	1 to 5	1.6	-150	12, 86-87

Matrix	Method	Temperature [1] [ºC]	Target element	Gas type and flux[2] [sccm]	Other Target Power[3] [W cm^{-2}]	Ag Target Power[3] [W cm^{-2}]	Working pressure[1] [Pa]	Bias[1] [V]	REF
	pulsed laser deposition								
ZrO2	MS-U-P	110	Zr and Ag	Ar = 75 O_2 = 0 to 0.6 Pa	10.18*	1.53 *	0.6	-40	88
Bi2O3	MS-Mu	150	Bi_2O_3 and Ag	Ar	NM	NM	0.4	NM	89
NiO2	MS-DC	200	(Ni + Ag pellets)	O_2= 0.01 to 0.09 Pa	1.3 *	Combined target	0.2	NM	90
SiO2	MS-RF, MS-RF-Mu, MS-Mu	100 and NM	(SiO_2 + Ag pellets), SiO_2 and Ag	Ar and NM	1.1 or 100 to 200W	0.2 or combined with SiO2	0.5 and 1.33	NM	16, 91-96
TiO2	MS-Mu, MS-P-DC, MS-DC, MS-DC-RF-Mu, MS and MS-RF	100 to 150	Ti, (Ti + Ag pellets), (Ag doped Ti) and Ag	Ar and O_2	10 or 25 to 90 W or 2.5 kW or 100 mA cm^{-2}	1 to 2.5 or 6 to 330W or Combined target	0.7 to 1.7	-100 to ground	97-103
ZnS	MS-RF and MS-DC-RF-Mu	RT and 300	ZrS-Ag, Zn and In-Ag	Ar and H_2S	1.97 to 2.96	2.5 to 2.8	0.7 to 0.8	NM	104-105
WS2	MS-RF and MS-Mu	RT	WS_2, (WS_2-Ag composite) and Ag	Ar	1.2 to 6.4 or 150 W	3 or 0 to 40 W or Combined target	0.4 and 2	-50 and 120	106-108
TiCaPCON	MS + ion source	NM	$TiC_{0.5}Ca_3(PO_4)_2$ and Ag	Ar and N_2	900 W	50 mA	NM	NM	109

[1] "NM" is used when the variable is not mentioned
[2] When provided.
[3] Power, current or current density are given when the information for power density is not provided.
***Calculated from the data**
MS = Magnetron Sputtering; P=Pulsed; DC= Direct current; RF=Radio frequency; U=Unbalanced; Multi-target= Mu

The proper control of the silver content with these two approaches can only be possible if other parameters, such as the reactive gases flow rates and substrate bias voltage remain constant. In fact, Ag atomic percentage can be decreased either by reducing the mean free path of the species and reinforcing the poisoning of the Ag target (increasing the reactive gas) [17, 65, 69-70, 74, 90, 102], or by increasing the negative bias potential applied to the substrate, responsible for a preferential re-sputtering of the silver from the coatings [45, 69].

An unexpected increase of oxygen content was reported in a few studies in the literature when high power is applied to the silver target, but no satisfactory explanation to this phenomena has been found, yet [70, 73]. In these studies, the only common observation is the use of C_2H_2 as reactive gas and a silver target. It should be stressed that even when oxygen is used as reactive gas, to produce Ni, Zn and Ti oxides, among other, no silver oxide has been reported [14, 90, 101, 103], probably due to its lower enthalpy of formation when compared to the matrix oxides.

2.3 Chemical, structural, morphological and topographical properties

The incorporation of a metallic phase such silver into ceramic films, is expected to produce structural, morphological and chemical changes on the ceramic matrix. Taking into consideration that silver is a noble metal, and thus the metallic state is thermodynamically more stable than most of the silver compounds that can be produced in solid state by magnetron sputtering, the formation of silver nitrides, carbides, carbonitrides or, even, some types of oxides is very unlikely. Therefore, the modifications caused by silver addition largely depend on its amount, size and distribution within the ceramic matrix, with the consequent influence on the crystallinity, texture and chemical phase distribution.

2.3.1 Ceramic-Ag coating chemistry.

In order to evaluate the coatings chemical bonds, X-ray photoelectron spectroscopy analysis is usually carried out. The bonding states of the elements, on the coatings surface, such as the (transition) metal used for the ceramic phase, nitrogen, carbon, oxygen and silver are determined. Silver is consider to be a very poor nitride and carbide forming element [110], and therefore, it is expected to be in the metallic state or forming oxides or sulfides, depending on the matrix. However, alloys can also be expected, since silver is found to form stable alloys. The majority of the reports have described the formation of metallic phases of silver, with the Ag 3d core level peak located around 368.2 to 368.6 eV binding energies [8, 17, 19, 28, 34, 46, 52, 57, 111].

Silver oxidized state is not always observed when reactive oxygen is introduced, being silver found in metallic state for some cases, such as TiO_2, ZnO, NiO and SiO_2, as previously commented. However, when oxidized as Ag_2O and AgO, Ag 3d peak is located close to 367.7 eV and 367.2 eV, respectively [75]. Very often a combination of metallic and oxidized states is detected [88]. In spite of the low affinity of silver to oxygen, silver oxide is usually avoided by increasing the power density to the Ag target [46, 85], avoiding any poisoning of the target. Films with other elements highly reactive with silver, such as sulfur, have been demonstrated to possess silver oxidized states; however, the lack of a detailed spectrum at S 2p peak limits the analysis of the results and prevents to conclude the possible formation of Ag-S phases, such as Ag_2S [107].

The above results clearly showed that silver does not establish chemical bonding or formation of alloys with the matrix elements, with the exception of silver oxides. Additionally to the metallic state, some authors [19, 57, 111], have found that the deconvolution of the silver peak results in an additional peak, corresponding to a much broader peak shifted to higher binding energies assigned to silver clusters (<4 nm), explained by the size-dependent shift of the Fermi level. These cluster phase has been reported to be constant to a 4 at.% for different content of silver in AlN-Ag [19].

The main changes in the matrices chemical bonding, due to the silver incorporation, are reported for carbon containing films. DLC coatings, for instance, showed alteration on the sp^2/sp^3 ratio of C-C bonds as silver is incorporated [3, 64, 66, 74]. The explanation is based on the reduction of the residual stress induced by the silver addition that prevents the densification of carbon network. Carbides and carbonitrides, showed an increment in the amorphous-carbon phases content as silver increases, due to the relative reduction of the amount of metal forming the ceramic matrix (Ti or Zr). Therefore, the metal reaction with the hydrocarbons in the chamber is lower, remaining more reactive gas available to form amorphous carbon-based phases [15, 17, 52, 57, 111].

In order to better characterize the amorphous carbon phases in the MeC-Ag, MeCN-Ag and a-C-Ag, Raman spectroscopy is usually utilized. The a-C state are determine, in terms of graphitic (G) and disordered (D) carbon bands, observed around 1350 and 1560 cm^{-1}, respectively. For pure DLC or a-C phases, the reduction of the sp^3/sp^2 ratio due to the inclusion of silver has been repeatedly reported [3, 65-66, 70, 74]. Such reduction helps to understand the decrease of the

hardness directly related to the reduction of the stress of the films. As referred above, the reduction of the films stress decreases the densification of the amorphous carbon phases and produce more sp^2 clusters. This effect may be interpreted as a more graphitic-like behavior of the amorphous carbon phases [18, 112].

In MeCN-Ag systems, Raman spectroscopy also confirms the segregation of carbon that do not react with the transition metal element. In the case of these carbonitride systems, when Me is completely consumed by other elements, such as N, O with higher affinity for Me than C, the excess of C forms additional a-C phases. During the deposition process, in which the increase of silver induces a reduction of the Me relative content, more hydrocarbon reactive gas is available to decompose and form amorphous carbon phases similarly to a plasma enhanced-CVD process [17, 56, 62]. On the other hand, nitrides have not shown significant changes in the matrix with silver incorporation [34], when analized by XPS.

Agglomeration of silver on the surface has been also observed by depth profiling of the coatings using sputtering etching before XPS analysis; with this procedure, higher amount of silver on the surface was detected compared to the bulk composition [50]. Other techniques such as glow discharge optical emission spectroscopy (GD-OES) and Rutherford backscattering spectroscopy (RBS) have also confirmed the surface silver enrichment on the topmost layer of the coatings (<20 nm) [17], which will be addressed in the morphological section.

2.3.2 Ceramic-Ag coatings structure

Transmision electron microscopy (TEM) diffraction patterns of the films usually show a characteristics nanocrystalline randomly oriented grains for the crystalline phases present in the material, with silver face-centered cubic phase (FCC) crystallites, showing diffuse rings [4, 17]. In terms of X-ray diffraction (XRD) analysis, silver in the majority of the studies is reported as a face-centered cubic phase (FCC), otherwise not mentioned due to the lack of signal in XRD, when possessing very low grain sizes (approx. <2 nm). The grains sizes are between 2 and 80 nm (more usually lower than 25 nm), depending on the phase in which it is embedded.

Due to the fact that the structure nature (i.e. crystalline or amorphous) differs among the already mentioned ceramic matrixes, the following discussion is divided in nitrides, carbides, carbonitrides, C-based and oxides. The main structural information is summarized in Table 2-2.

Table 2-2 Structural data for ceramic matrix/Ag nanocomposite films.

		Ag grain size [nm]	Ceramic phase	Grain size [nm]
Nitrides (MeN)	AlN[19]	1.5 to 4.5	FCC AlN	0 to 32
	CrN[20, 24, 26-27]	9 to 23	FCC CrN	12 to 25
	MoN[28-30]	–	Tetragonal and cubic Mo_2N	7 to 20
	NbN[31]	–	Cubic NbN	–
	TaN[33-37]	–	Orthorhombic Ta_3N_5 and FCC TaN	5.4 to 7.3
	TiN[6, 13, 39-40, 113]	6 tp 78	FCC TiN	12 to 80
	VN[43]	–	Tetragonal VN.	36
	ZrN[45-46]	–	FCC ZrN	3 to 25
Carbides and carbonitrides (MeC and MeCN)	HfC[50]	–	FCC HfC	–
	SiC[50]	–	Amorphous SiC	–
	TiSiC[53-54]	5 to 9	FCC TiC + amorphous SiC	5 to 15
	TiC[51-52]	–	FCC TiC	–
	WC[55]	–	WC	–
	MoCN[56]	–	Mixture of carbides and nitrides	–
	TiCN[15, 17, 57, 60]	5 to 20	FCC TiCN + amorphous C	5 to 45
	ZrCN[61-62, 111]	3.4 to 4.2	FCC ZrCN + amorphous C	3 to 14
DLC	DLC[9, 18, 65, 67, 69-70, 112]	2 to 26	Amorphous DLC	–
Oxides	NiO_2[90]	–	FCC NiO	7.6 to 9.0
	SIO_2[92-93, 96]	8.5 to 17.5	Amorphous Si-O	–
	Al_2O_3[79-80]	3 to 8	Amorphous Al-O	–
	TiO_2[97, 99-100, 103]	12.5 to 20	Amorphous Ti-O or tetragonal TiO_2 (anatase)	–
	ZnO[81, 85]	–	Hexagonal ZnO	–
	YSZ[12, 86]	–	Tetragonal ZrO_2	–
	ZrO_2[88]	–	Tetragonal	–
Sulfides	WS_2[107]	–	HCP WS_2	–
	ZnS[104-105]	–	BCC and hexagonal ZnS	8 to 15

2.3.2.1 Transition metal nitrides matrices (MeN-Ag)

For transition metal nitride, no XRD peaks could be attributed to silver when its content is below a threshold value, probably due to grain sizes lower than 2 nm [19, 34, 36, 39, 81, 113]. As silver increases in the matrix, the FCC silver phase is detected in the XRD pattern. The intensity of the nitride phase is reduced and the peak width increases, indicating a reduction of its grain size [13, 19, 26, 28, 31, 34-36, 43, 45-46, 81] down to a level characteristic of a material with a XRD amorphous structure [19, 46]. This reduction is believed to be caused by either hindering the nitride grain growing due to the silver segregation to the grain boundaries or by the increasing number of new nucleation sites provided by silver particles/atoms.

Besides the influence in the crystallinity, silver has other influences on the structure of the nanocomposite films. In the case of CrAlN [20] and VN [43] a strong (111) preferential orientation of

the ceramic matrix is achieved whereas, as shown by Aouadi et. al [29] for Mo-N-Ag system, a transformation of Mo_2N phase from tetragonal to cubic occurs.

After annealing of the coatings, further structural transformations may take place. Complex phases of $AgNbO_3$ [31] and AgMoO [30] are observed when the coatings are thermal treated at 750 ^{o}C and 400 ^{o}C respectively. The occurrence of these phases on Mo and Nb-based systems will be analysed in the tribological behavior of the films, since they can play a very important role as self-lubricant features for sliding at high temperatures.

2.3.2.2 Transition metal carbides and carbonitrides matrices (MeC-Ag and MeCN-Ag)

Although transition-metal carbides and carbonitrides phases revealed similar tendencies to the nitrides, whenever an excess of carbon exists in the coatings, amorphous carbon phases can be formed. When silver is increased an augment in the amorphous carbon phases is observed, which indicates that hydrocarbons can be incorporated into the film via a PECVD process, as previously mentioned. In fact, a consequent higher discharge power due to an additional Ag target, increases the decomposition of the hydrocarbon gas, producing films with larger amounts of amorphous carbon phases. The formation of the C-amorphous phase has a synergetic effect with the silver nanoparticles, promoting changes of the crystalline structure, as above explained, such as the reduction of the grain size of the ceramic matrix. Therefore, the C-phase contributes for increasing the nucleation rate of the ceramic phase (MeC(N)) and preventing the grain growth [11, 15, 17, 52-54, 57, 61-62, 114].

The combination of the loss of crystallinity of the ceramic phase, promoted by the formation of the amorphous C-phase, with the low grain size of Ag nanoparticles, for low Ag-content films, makes difficult very often the undoubtful detection of crystalline silver, due to the overlapping of the broad peaks of both phases. Moreover, an additional effect has been reported, with the main peak of MeCN phases being shifted to higher angles enhancing the difficulty in XRD peaks indexation [57, 111]. This behavior may be due either to a reduction of the compressive residual stress after the addition of silver; (being a soft phase, silver can help to release this stress) or to a less incorporation of carbon in the MeC phase or to the loss of carbon from the MeCN phase, due to the formation of the a:C phase.

2.3.2.3 C-based matrices (a-C-Ag)

For DLC or amorphous carbon matrices (a-C) XRD does not offer any information about the ceramic phase. Only and FCC silver phase is identified with grain sizes varying from 2 to 26

nm, calculated by Scherer formula [7, 9, 18, 66, 70, 74]. Similarly to MeN, MeC and MeCN, a-C matrices showed no sign of silver diffraction peaks for low silver content, attributed to the low grain sizes (<2 nm), which are undetectable in XRD [18]. The XRD spectra showed an evolution of the silver peaks as a function of the silver content, increasing in intensity and reducing their width, indicating larger grains.

The amount of the a:C phase can also determine the preferential growth of silver. In fact, Meškinis et al.[69] show that depositing with different fluxes of reactive gas in the magnetron sputtering process (C_2H_2), for high gas flow the XRD pattern only shows the (111) Ag diffraction peak, while for low acetylene flows all the Ag diffraction peaks are observed, which may indicate changes on the silver energy due to the mean free path alteration, as previously mentioned in the deposition section.

2.3.2.4 Oxides matrices (MeO-Ag)

The oxide matrices can be crystalline [12, 75, 83-85] or amorphous [79], depending on the element and the deposition temperature. The silver in these matrices is also evidenced as a face-centered cubic lattice, which increases in crystallinity with the augment in silver content [12, 14, 80, 86, 100] or annealing temperature [78, 90, 93]. Similarly to the other matrices, the silver phase is not detected for low silver content [99] and the oxide crystallinity decreases with the increase of the silver content [84-85]. However, an opposite behavior was observed for tantalum oxynitride for which an increase of the crystallinity occurs with the silver content increase, despite the other deposition conditions were kept constant, the Ta target density power, as well as the O and N_2 ratios [78].

Some authors have reported that the oxide peak can shift to lower angles when silver is incorporated in the lattice [81-84], contrary to what was observed for other matrices (see above). Structural transformation can also be observed in Ag-oxides systems. The incorporation of silver makes ZrO_2 transforms from the monoclinic to the tetragonal phase [88], probably due to the relaxation of the lattice.

2.3.3 Ceramic-Ag coatings morphology and topography

2.3.3.1 Surface and cross-section morphology

The morphology of the coatings, in both surface and cross section analysis, is usually evaluated by scanning electron microscopy. The architecture, type of films growth, phase segregations, among other features, have been reported.

Figure 2-1 shows the most common five architectures when depositing ceramic-Ag films by MS. Depending on the design, properties such as density, porosity and phase segregation can be altered with the consequent influence on the functional properties.

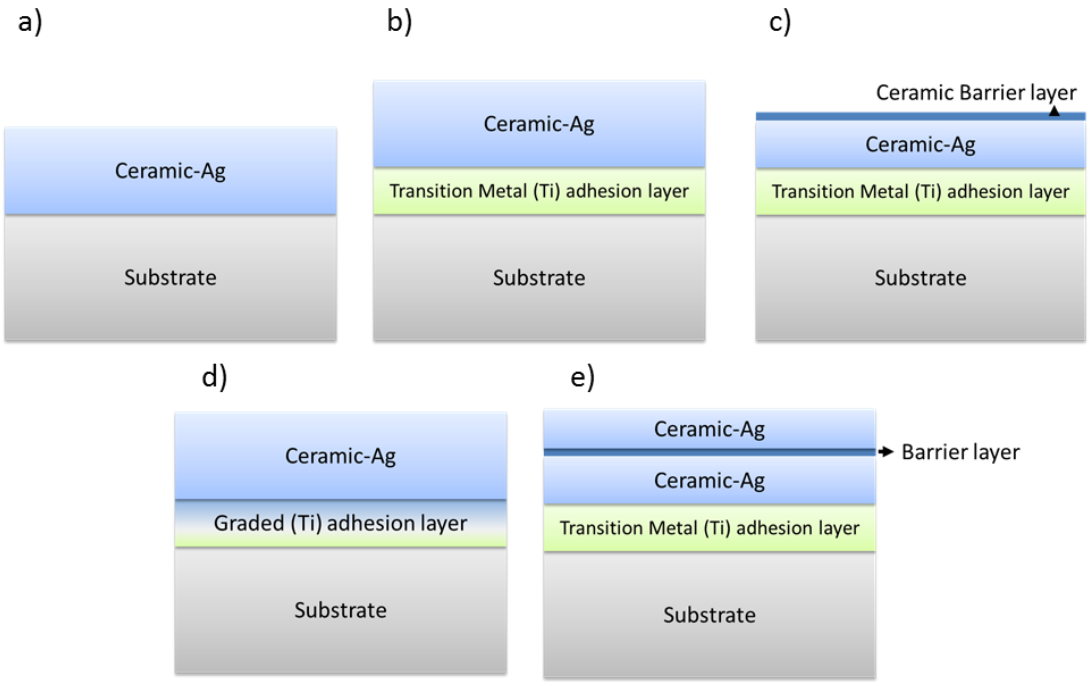

Figure 2-1 common architectures of ceramic-Ag films. a) Pure ceramic-Ag, b) transition metal interlayer between the ceramic-Ag coatings, c) architecture b with ceramic barrier layer, d) graded interlayer between the substrate and ceramic-Ag and e) architecture c with an additional ceramic-Ag.

Transmission electron microscopy (TEM) has revealed the existence of nanoparticles with sizes varying from two up to hundreds of nanometers [6, 20, 34, 52, 65, 74]; however, the dependency of their sizes on the silver composition is not well defined. Köstenbauer et al. [6], for example, did not find any correlation between the size of the silver domains and its content, for TiN-Ag films. On the other hand, Choi et al. [65] state that the size of the particles increases for higher Ag contents, in agreement with other researchers [10, 72, 74]. Such differences may be due to the nature of the matrix since crystalline matrices may offer more lateral barrier diffusion when compared to the amorphous phases, in which the silver may growth by coalescence as silver content increases.

The shape of the silver particles has been mainly identified as spherical; however, cylindrical particles can also be observed [45]. The distribution of the silver largely depends on the matrix composition, since when amorphous phases, such as oxides or carbon-based, are present, the silver nanoparticles are surrounded and well distributed in the matrix [34, 85, 97]. Some authors have demonstrated an increase of the particle sizes in the film growing direction [10, 16], as shown in

Figure 2-2. For nitrides, where no amorphous phases are detected, the silver is located in the grain boundaries of such phase [6].

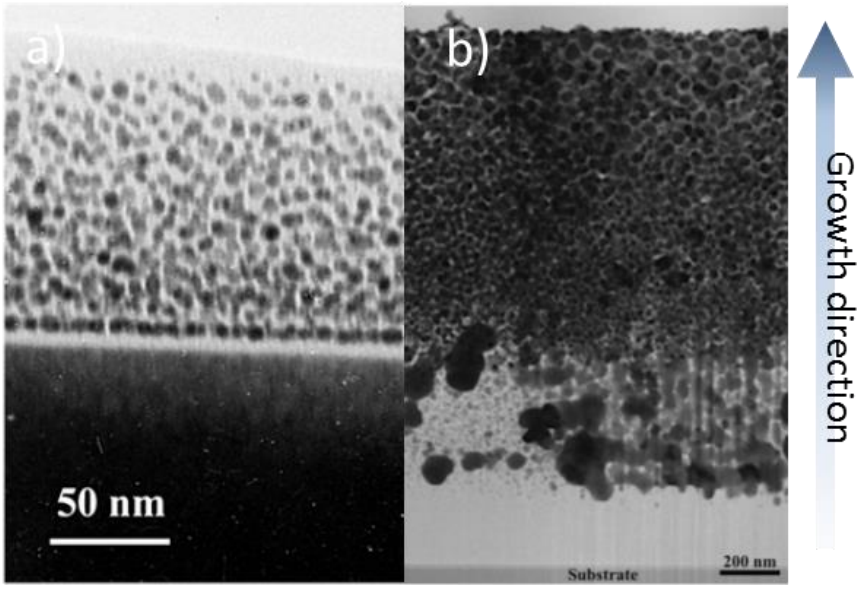

Figure 2-2 Silver nanoparticles sizes in cross-sectional TEM images for a) SiO_2 [16] and b) DLC [10] (adapted from the corresponding reference).

In scanning electron microscopy (SEM) the morphology of the coatings showed a dependency not only on the composition of the films (type of matrix and silver content), but also on the deposition conditions, such as substrate bias potential, substrate temperature and working pressure, since altering these settings the depositing species mobility can change. However, the morphological characteristics demonstrate major dependency on the type of ceramic matrix, commonly showing columnar-like growth for nitrides and carbonitride, granular-like features in carbontrides and carbon-based coating, featureless cross-sections for C-based and oxides and very particular acicular-like morphology for sulfides (cf. Figure 2-3) [107]. When Ag is added to these matrixes specific modifications to the surface and cross-sectional morphologies are observed.

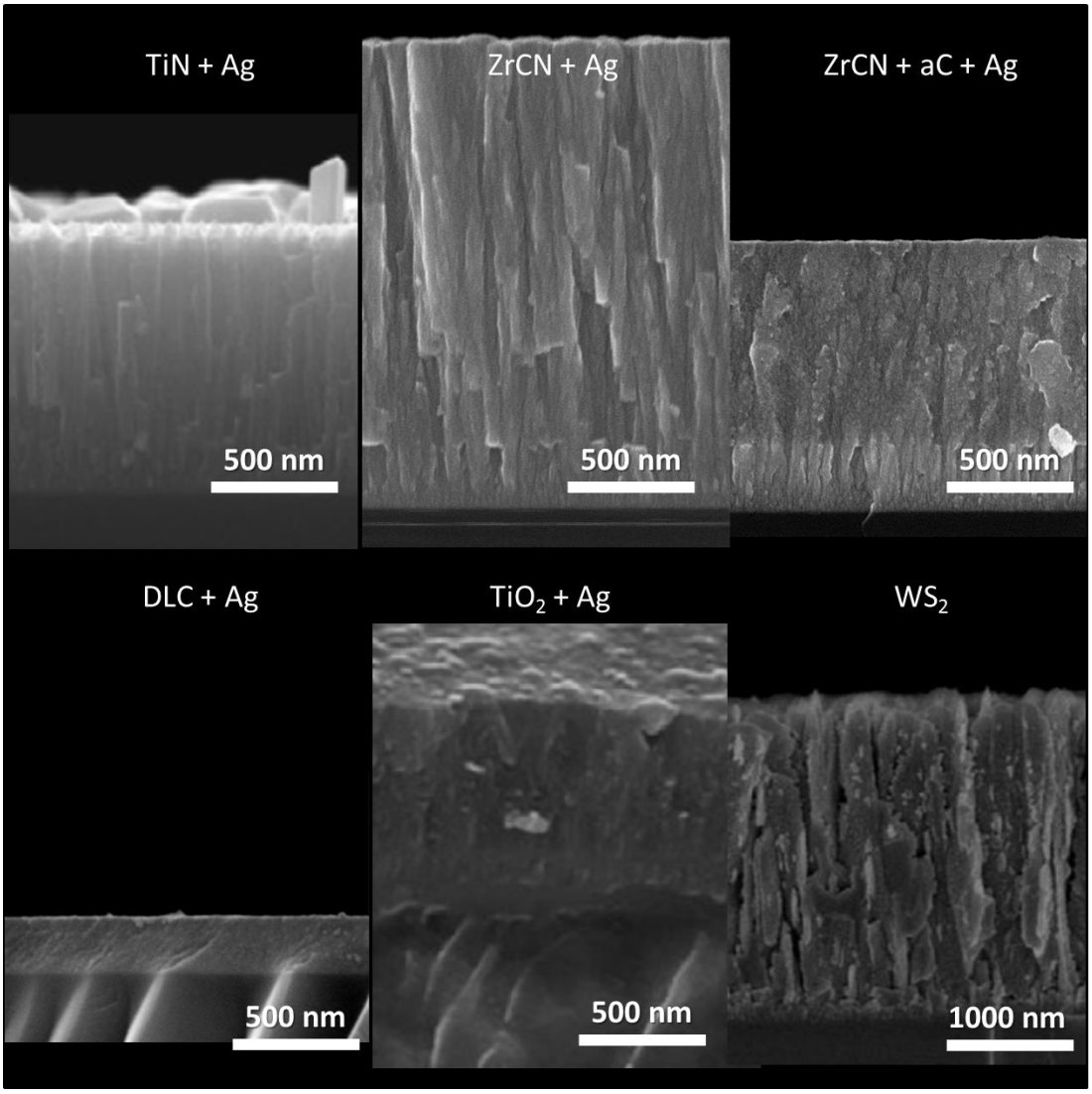

Figure 2-3 Cross-section morphology for representative ceramic matrices with similar content of silver a) TiN-Ag with ~4.5 at. % [13], b) ZrCN-Ag with 6 at% [114], c) ZrCN+aC-Ag with 7 at% [114], d) DLC-Ag with 20 at% [67], e) TiO_2-Ag with 6 at % [101] and f) WS_2-Ag with 5.5 at% [107] (adapted from the corresponding reference).

In pure nitrides and carbonitrides (with low carbon content) films, columnar growth is usually reported in cross sectional images for coatings with 0 at. % of Ag. Thus, for low silver content (< 8 at.%) [13, 22] the films maintain columnar growth with very well-defined columns, as observed in Figure 2-3 a and b. As silver increases, the columnar growth is gradually destroyed and a granular aspect is obtained [13, 23, 49, 54-55, 61-62, 114], as shown in Figure 2-4. The effect of silver should be related with the interruption of the columnar growth due to silver segregation to the grain and column boundaries. Large agglomerates can, then, be formed, obstructing the continuity of the column and promoting the re-nucleation of the nitrides around the silver particles. On the other hand, for carbonitrides and carbides coatings, the increase of the amorphous carbon phase for

higher Ag contents, also contributes to the loss of the columnar growth of the films. In the same way, carbon phases can surround the ceramic matrix grains / Ag crystallites and form a composite-like configuration.

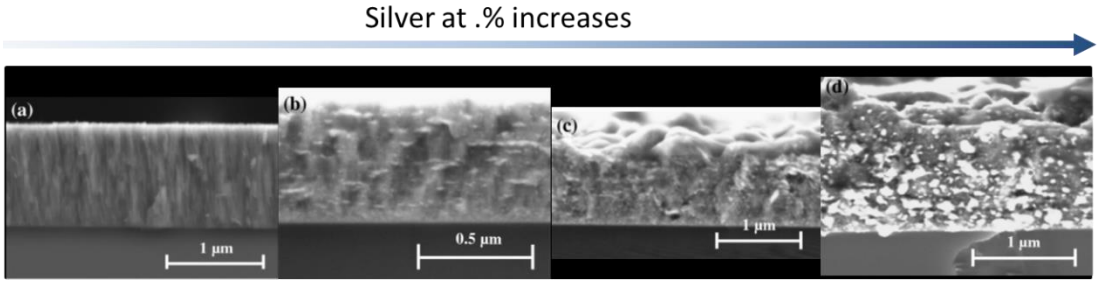

Figure 2-4 Cross-section SEM images for TiSiC-Ag films with increasing silver content [54] (adapted from the corresponding reference).

For C-based matrices, the addition of the silver modify the coatings morphology from featureless to a more granular-like pattern, responsible for the increase of the surface roughness of the films [10].

These monotonous trends cannot be applied to the coatings with oxide matrices for which the effect of silver in the morphology is no conclusive. Huang et al. [88], for instance, have shown that the incorporation of silver in ZrO_2 films produces their densification, with the transformation of the well-defined columns to a denser granular structure, with particles between 10 and 30 nm. However, for ZnO and ZrON coatings, the surface of the films showed more defects as the silver is introduced [75, 82, 85].

Silver surface segregation has been commonly reported for most of the matrices induced by changes in the Ag power (or silver content), bias voltage and deposition or annealing temperature, as shown in Figure 2-5. The segregation phenomena is discussed in detail in the following sections.

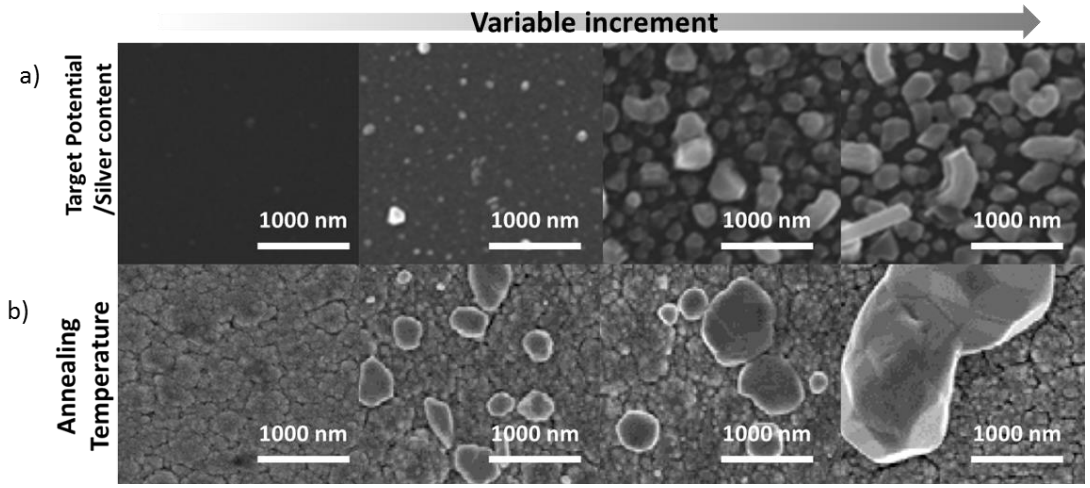

Figure 2-5 Evolution of silver segregation as a function of a) the silver target power or silver content in CrAlN-Ag [20] , b) the annealing temperature in TiN-Ag [13] (adapted from the corresponding reference).

2.3.3.2 Silver segregation

In general, for different types of matrices, self-assembled silver nanoparticles are shown on the surface [8, 13, 15, 17-18, 27, 35-37, 39, 49-50, 52, 79, 94, 111, 114]. The form of the nanoparticles varied from lamellar [27], small dots (<20 nm) [12, 39, 49, 52, 94, 109, 111, 114], rods and spherical [36-37]; the number and distribution are dependent on the silver content or power density on the silver target: larger silver particles are achieved by increasing the noble metal content in the matrix [13, 15, 17, 35, 38, 50, 103], see Figure 2-5a. A synergetic analysis with SEM, XRD and TEM allows concluding that the silver nanoparticles are composed by several crystals [67]. For low Ag content, the segregation is less perceptible, indicating that a threshold content is required for agglomeration starting; however, this threshold is dependent on the matrix, being difficult to determine from different authors and technique used, and therefore a systematic study is needed to be able to determine the evolution of the silver content threshold to promote the agglomeration, as a function of the matrices type.

Song et al. [101] have shown a dependency of the silver agglomeration and the substrate bias potential for TiO_2: by applying -100 V to the substrates, a higher number of particles is observed when compared to unbiased depositions. In the latter case, Ag-particles are not well defined.

Thermal annealing has been often used to enhance Ag segregation and agglomeration in Ag-ceramic films. In fact, the temperature improves the mobility of silver, promoting its diffusion from the films to the surface, as well as the aggregation and the crystal growth on the surface [4, 12, 19-21, 26-27]. Silver particles with a very wide range of sizes are observed on the coating surface deposited with the substrate heated at different temperatures. Mulligan et al. [24-25] have reported that the silver nanoparticles are well distributed in the coatings at 500 °C, but segregate to the

surface when larger temperature are used (600 °C and 700 °C). Similar behavior are observed by other authors either by changing the deposition temperature or annealing the samples at different temperatures, from a few degrees up to 1000 °C. The segregation / coalescence / agglomeration process is strongly dependent on the temperature and the silver content. The thermal energy, provided by either the annealing process or the deposition at high temperature, gives mobility to the silver species [86], being thermal treatment more efficient than the deposition with high temperature [25].

The silver segregation to the surface may be explained by the need to reduce the larger surface energy of smaller particles, promoting the agglomeration of the metal particles. In a first step, during the deposition process, a constant flow of sputtered species from the target are deposited over the previous layer of material, enrobing the existing silver particles and preventing them to agglomerate, by limiting their mobility. However, in a second step when no new species are arriving to the growing film, the mobility is less restricted, allowing the silver nanoparticles to move over the free surface, leading to their agglomeration and reducing the surface energy [67, 115]. In a third step, if favorable conditions exist, Ag nanoparticles laying in grain and/or column boundaries inside the film, are segregated to the surface, increasing the size of the aggregates (in their different shapes), always driven by the decrease of the surface energy. This process is enhanced by the low reactivity of the silver with the matrix, which prevents the formation of strong bonds between the ceramic and silver, and allows its easier mobility. This hypothesis is, to some extent, corroborated by an experimental outcome, which showed that applying a barrier layer of the same ceramic matrix on top of the surface, the silver aggregation can be partially controlled [25, 67, 80]. The efficiency of this layer has been shown to depend on its thickness [27] and morphology [103], since thinner or columnar films offer less barrier properties than thicker or dense films. The silver segregation was also observed to be reduced when silver establish chemical bonds with elements of the films, such S or Ti [29, 116], supporting that the low affinity between Ag and matrices, such as nitrides or C-based coatings [8] facilitates the silver mobility and aggregation.

The morphology of the coatings plays a crucial role in this silver segregation, since it determines the diffusion paths of silver. One of the most common morphologies in these films are columnar-like and granular-like, which possess clear diffusion paths that facilitate the silver diffusion and segregation to the surface [19, 26]. The accumulation of silver in the boundary regions generates

pressure inside the diffusion path that needs to be released. As a consequence, the silver that filled the channels [26] moves to more open spaces (outer column boundaries) and exits to the surface of the material. This process is, then, enhanced for either higher energy of the species (high temperatures) or larger amounts of Ag particles in the boundary regions (diffusion path). The latter explains why for low silver content the agglomeration is hard to be observed, since less silver areas are interconnected, reducing the transport rate [26].

The lateral diffusion has been demonstrated in cross-section analyses, evidencing the mobility of silver in the films [86], not only on the free surface but also inside the films [21, 27]. In fact, studies have shown that after few hours of annealing, a continuous top layer of silver is formed that completely cover the surface [12, 21, 86].

Silver aggregates are observed on the surface, growing in size and reducing in number as the temperature increases, such growth resembling the Ostwald ripening process [13, 36-37, 59, 78, 80, 93], as shown in Figure 2-5b. When the films are deposited onto substrates with rough topography (i.e. unpolished stainless steel) the silver segregation and agglomeration is more pronounced on the topographical features of the substrate [100], evidencing that silver diffuses first at free surfaces in the interior of the films (less dense column boundaries originated by shadowing film growth) and then segregates. The images also evidenced that the silver not only agglomerates, but coalesces forming large grains instead of silver nanoparticles agglomerates [13]. Additionally, Mulligan et al. [27] have demonstrated that, for CrN-Ag films, the silver diffusion occurring from the inner part of the films, leaves a porous microstructures behind, as shown in Figure 2-6.

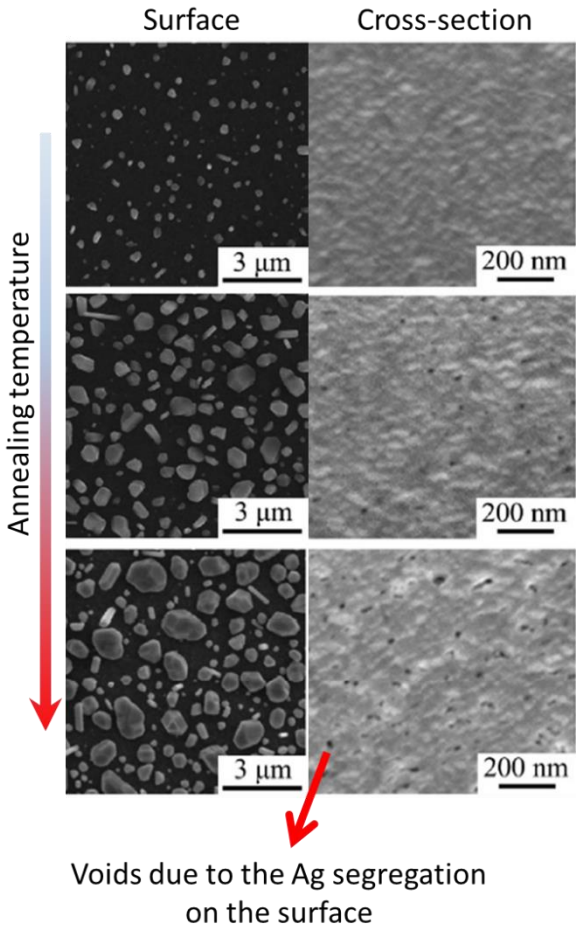

Figure 2-6 Silver segregation effect on the surface and cross-section morphology in CrN-Ag [27] (adapted from the corresponding reference).

The silver agglomeration at the surface has been also observed in cross sectional images by TEM images [16], shown in Figure 2-7.

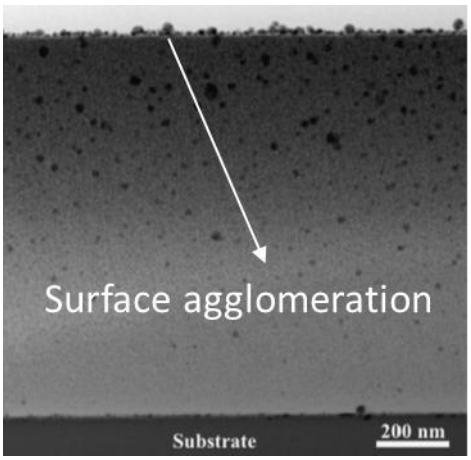

Figure 2-7 Silver surface agglomeration observed by TEM or STEM imagining for a) DLC-Ag [10] (adapted from the corresponding reference).

2.3.3.3 Roughness

The topography changes of the films are highly related to the silver diffused to the surface, which promotes an overall increase of the surface roughness, as reported by [6, 8-9, 43, 79, 90]. For high adatoms mobility depositions, the fast diffusion of silver gives rise to a more granular-like morphology as silver is increased [10, 79, 105]. However, when silver content is not sufficient to form large agglomerates, the incorporation of silver induces a reduction of the roughness of the coatings, due to the refinement of the structure [3, 8, 15, 45, 61] and the silver segregation to the grain and columns boundaries [15, 57, 61]. Both scenarios are schematically shown in Figure 2-8.

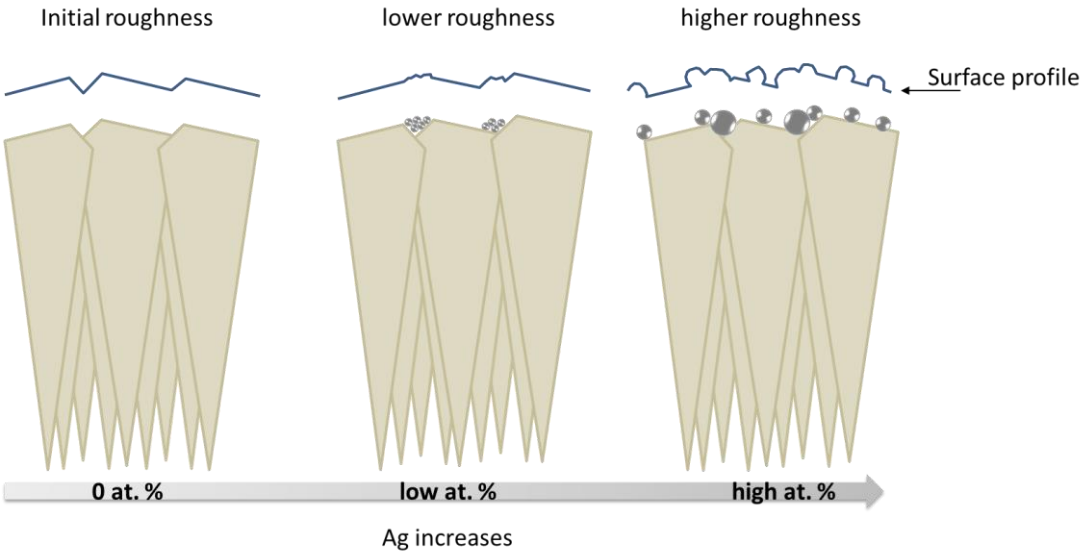

Figure 2-8 Surface roughness scheme as a function of silver content.

2.3.3.4 Contact angle

The contact angle is used to determine the surface energy of the samples, which may provide useful information about the samples wettability and interaction with the environment (i.e. in biological test, it provides information about the interaction between the surface and the cells or biomolecules). The wettability is known to be mainly dependent on the chemical and topographical properties of the surface. Thus, the roughness and type of matrices are expected to control the hydrophobicity of the coatings. The materials are usually considered hydrophilic when the contact angle with water is below 65 degrees and hydrophobic for values above this contact angle [117]. From a chemical point of view, silver surfaces are known to be hydrophobic in nature, independently of its roughness; however, in ceramic matrices the contact angle depends on the compound (nitride, carbonitride, carbide, oxide) and the transition metal. The roughness, as discussed above, is altered by the silver content and its ability to form particles on the film surface. Unfortunately, the roughness is not always possible to be controlled, hindering the

analysis about its influence on the wettability of the coatings. Thus, it would be inaccurate to generalize the effect of silver in the contact angle of the matrices. Figure 2-9 summarizes the contact angle values measured for several ceramic-Ag coatings as a function of five groups of silver content [10, 33, 57-58, 75, 88, 111]. No distinguishable tendency is observed as silver is incorporated; both reduction and increment of the hydrophobic character is observed. The highest contact angles are reported for ZrCN and TiCN, attaining values closed to 120°, while TiN and TiO_2 have the lowest values, both with and without silver.

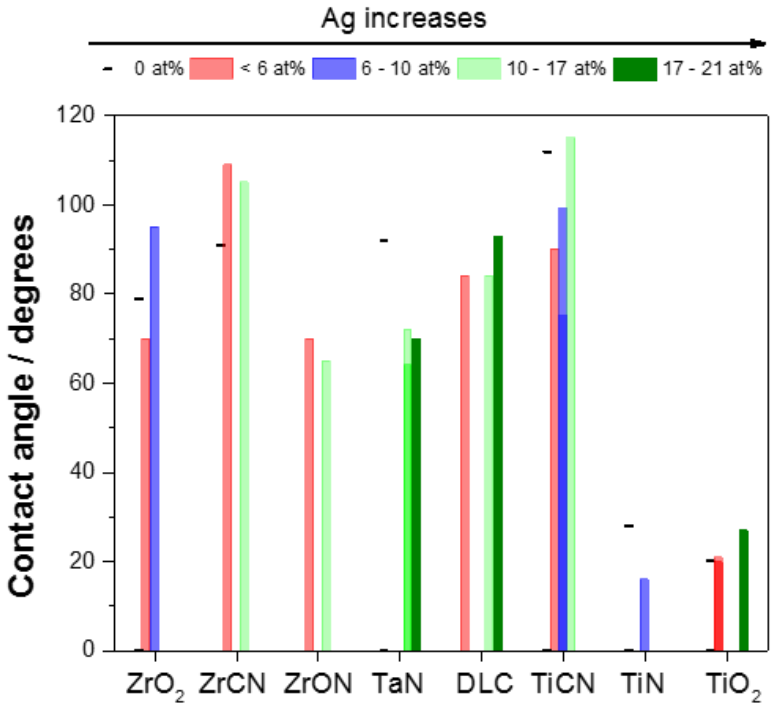

Figure 2-9 contact angle of ceramic-Ag coatings measure with water reported in ZrO_2-Ag [88], ZrCN-Ag [111], ZrON-Ag [75], TaN-Ag [33], DLC-Ag [10], TiCN-Ag [15, 57], TiN-Ag [42], TiO_2-Ag [100].

2.4 Functional properties

2.4.1 Mechanical properties

2.4.1.1 Residual stress

The stress in PVD films is usually of compressive type, due to either the difference in thermal expansion coefficient values, between the substrate and the films, or its final cross section morphology (Figure 2-10). Figure 2-10a shows a scheme of a system (coating-substrate) without any residual stress; a red square was drawn to show what is occurring when compressive residual stress exists (Figure 2-10b). Due to the high contraction of the substrate, the film is compressed following the direction parallel to the substrate and, then, the rectangle expands in

the perpendicular direction. The effect of the morphology is schematized in Figure 2-10c and d. If a column is perfectly isolated, no stress is present. If the proximity between columns increases, attractive forces are established between columns originating tensile stresses. If the columns are in close contact, compressive stresses are generated.

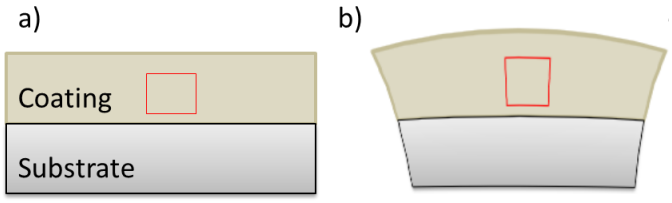

Figure 2-10 Compressive stress of PVD coatings a) coating without stress, b) coating with compressive stress.

When silver is incorporated, the compressive stress is released due to the plastic deformation of the soft metallic phase [27], as schematically shown in Figure 2-11. In fact, this effect is in the basis of the purposes to incorporate silver in DLC coatings, which helps to increase the adhesion properties of the coatings by reducing the compressive stress [7, 52, 65, 74].

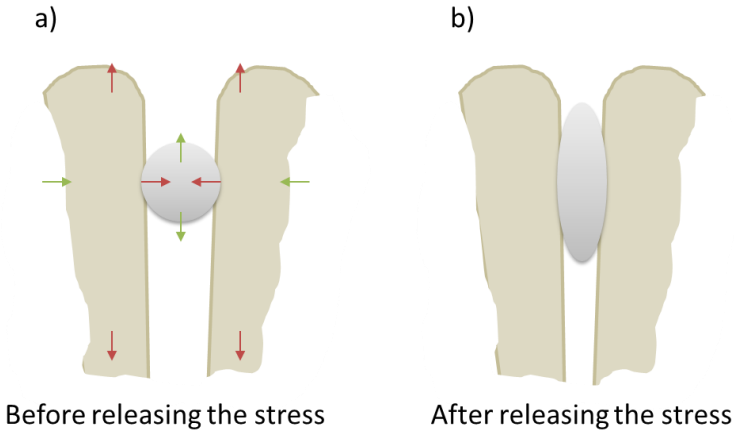

Figure 2-11 Scheme of silver effect on the compressive residual stress of ceramic-Ag coatings.

2.4.1.2 Hardness

In general, an increase of silver produces a reduction of the hardness and Young modulus of the coatings as shown in Figure 2-12, Figure 2-13 and Figure 2-14. Some researchers have shown that, for low silver content, the hardness of MeN can be increased due to the grain refinement of the structure, hindering dislocation motion and avoiding crack development at the interfaces. The silver content threshold, up to which this trend is verified, depends on the type

of matrixes, being reported for CrN < 5 at% [20], ZrN between 5 and 12 at% [45], TaN 2 to 15 at% and TiN <5 at%.

As silver content continuously increases, more silver segregates to the grain boundaries, enhancing the ductility in those regions and facilitating both the grain boundary sliding and the reduction of the residual stress of the coatings, with the consequent deterioration of the system hardness.

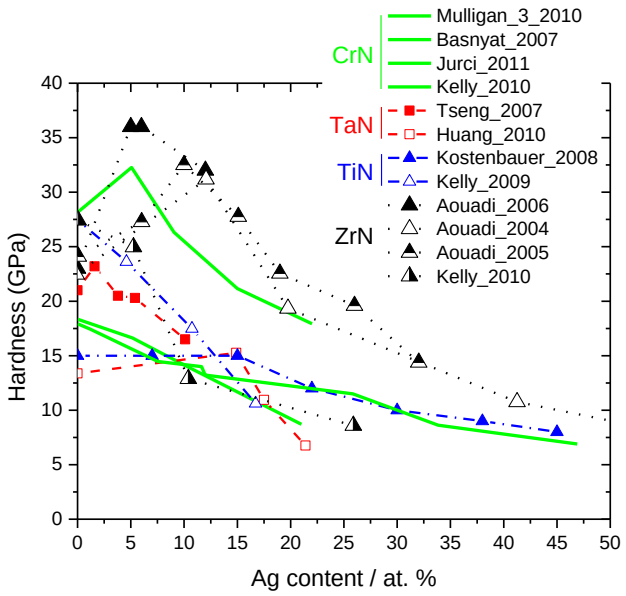

Figure 2-12 Hardness of MeN-Ag coatings as a function of the silver content [5-6, 20, 22-24, 33, 35-36, 39, 45-48, 81]. For hardness values reported in HK a conversion factor was used to approximate the values to GPa (100 HK/GPa).

The increase in the deposition temperature can give rise to higher hardness of the films. Some authors explains this trend by the segregation of Ag-phases, originating pure MeN phases, free of silver, that possess higher hardness [24, 35-36]. However, difficulties have been reported for measuring the hardness of the system, after high temperature deposition or thermal treatment, since silver tends to segregate to the surface and Ag-rich regions can mislead the measured values [6].

In C-based-Ag coatings, the hardness depends on the ratio between the sp^2 and sp^3 carbon bonds, which can be altered as silver is added to the films (see above discussion of Raman and XPS results). Thus, the hardness is expected to decrease with sp^2/sp^3 ratio increase, trend shown when silver content increases [3, 7-8, 18, 74], as shown in Figure 2-13. However, some reports have stated that, for low content of silver (between 3 and 10 at%), the hardness can follow an

opposite trend [3, 7], in agreement with the increment of sp^3 bonds in the films, as demonstrated by Raman spectroscopy.

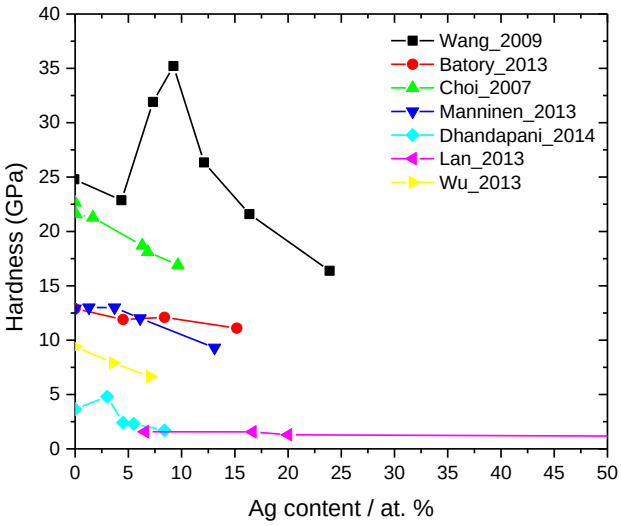

Figure 2-13 Hardness of C-based-Ag coatings as a function of the silver content [3, 7-8, 10, 18, 65, 74].

The analysis of hardness for MeCN-Ag films is more complex since, when silver is added to MeCN matrices, the amorphous carbon phase content can appear or increase [11, 15, 57, 62, 114], as previously discussed. Therefore, a mixture of MeCN crystalline, amorphous carbon and silver nanocrystalline phases is created each one with specific mechanical properties, which determine the final hardness of the system.

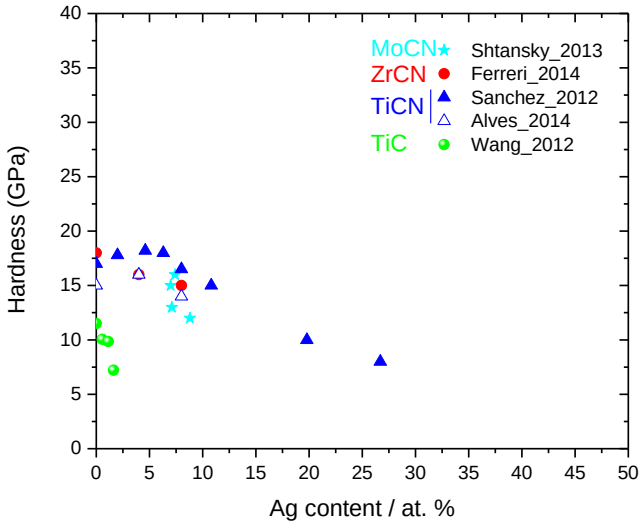

Figure 2-14 Hardness of MeCN-Ag and MeC-Ag coatings as a function of the silver content [15, 56-57, 62].

Finally, oxides such yttria-stabilized zirconia show the same behavior as reported in previous systems [12] [86], where the hardness of the films is reduced as the silver is increased. A particular behavior is found for WS_2-Ag systems where the hardness increases as silver is incorporated. In these films, the microstructure is the dominant factor controlling the hardness of the films since when the silver is added, densification of the film is attained and, thus, the reduction of the porosity helps preventing the plastic deformation due to indentations [107].

2.4.2 Tribological properties

The combination of a hard material with enhanced wear resistance with silver as a lubricating solid with high thermochemical stability, is one of the main purposes of depositing ceramic-Ag coatings. This is the reason why the majority of tribological studies are carried out in dry conditions. However, due to the potential of these films for other applications, other testing conditions, such as simulated human body fluids, have also been reported. This procedure will allow to evaluate the ability of these systems to support saline and biological environments in order to explore the known antimicrobial performance of silver.

The tribological performance of ceramic-Ag films, depends not only on the silver content, but it is also highly correlated with the ceramic matrix and the testing conditions (e.g. lubricant and counterpart). Hence, the tribological behavior of ceramic-Ag films, grouped by nitrides, carbides, carbonitrides, C-based coatings and oxides, tested under and specific conditions, is summarized in Table 2-3 and Table 2-4.

2.4.2.1 Coefficient of friction (COF)

2.4.2.1.1 Transition metal nitrides matrices (MeN-Ag)

All the studies found for MeN-Ag films, deposited by magnetron sputtering, report tribological tests that have been performed in dry conditions, at different temperatures and counterparts. A summary of the experimental conditions and achieved results is shown in Table 2-3. The table is ordered by the type of ceramic matrix.

Table 2-3 Tribological test condition, COF and wear rate reported for MeN-Ag. All the rest were reported at dry conditions.

Matrix	Test	Counterpart	Temperature [°C]	Humidity [%]	Applied load [N]	COF	Wear rate X 10^{-6} [$mm^3 N^{-1} m^{-1}$]
CrN [26]	Reciprocating multipass scratch method	Rockwell type diamond	RT	40-45	1	0.04 - 0.11	0.4 to 0.19 µm/100 cycles
CrN [25]	Ball on disk	Alumina balls	550	35-45	5	0.2 to 0.4	10.2 to 3.2
CrN [25]	Ball on disk	Alumina balls	450, 550 and 650	NM	5	0.16-0.54	4 to 47
CrN [25]	Ball on disk	Alumina balls	RT	35-45	5	0.5 to 0.8	7 to 100
CrN [25]	Ball on disk	100Cr6 steel	RT	35-45	15	0.47 to 0.8	2.3 to 9.9
CrN [25]	Ball on disk	Alumina balls	25 to 400 at 10 °C min^{-1} 400 to700 at 5 °C min^{-1}		15	0.05 to 0.8	NA
CrN [21]	Ball on disk	100Cr6 steel	RT, 400 and 600	NM	2	0.23 to 0.75	NM
CrN [20]	Ball on disk	Alumina	RT	40	2	0.23 to 0.83	0.054 to 0.4
CrN [22]	Pin on disk	Alumina	RT and 500	NM	1	0.169 to 0.389	(7.4 to 289.4) x 10^{-7}
CrN [5]	Reciprocating sliding wear tester	S45C	NM	NM	100	0.3 to 0.65 *	0.4 to 0.72 um
MoN [28]	Ball on disk	Alumina, 440C, Si_3N_4	RT	50 and Dry N_2	1	0.28 to 1.06	300 to 800
MoN [28]	Ball on disk	Si_3N_4	350 and 600	50 and Dry N_2	1	0.1 to 0.8	8 to 500
MoN [29]	Ball on disk	Si_3N_4	RT, 350 and 600	<0.4	1	0.1 to 0.8	0.8 to 90
MoN [30]	Ball on disk	Alumina	RT, 100, 250, 400	50	1	0.3 to 0.8	NM
NbN [31]	Ball on disk	Si_3N_4	RT, 350 and 750, 1000	60	1	0.27 to 0.35	NM
TaN [37]	Pin on disk	Alumina	NM	NM	1 or 5	0.7 to 1.2	(0.7 to 6) x10^{-6} $mm^3 m^{-1}$ *
TiN [6]	Ball on disc	Alumina	RT, 200, 300 and 500	30 to 40	1	0.15 to 0.7	NM
TiN [39]	Thrust washer wear testing	100Cr6 steel	NM	NM	20	0.31 to 0.36	NM
VN [43]	Ball on disk	Si_3N_4	RT, 350 , 700 and 1000	60	2	0.12 to 0.9	NM
ZrN [48]	Ball on disk	440C	23	50	5	NM	1.8x10^{-3} mm^3
ZrN [45]	Ball on disk	440C	23	50	5	0.65 to 0.09	27x10^{-3} mm^3
ZrN, CrN and TiN [23]	Thrust washer wear testing	100Cr6 steel	RT	NM	NM	0.11 to 0.188 ZrN 0.13 to 0.17 CrN 0.16 to 0.167 TiN*	NM
*** Approximated value; NM= not mentioned; RT = Room temperature**							

In dry conditions, the segregation of silver to the surface is one of the key parameters controlling the self-lubricating features of the ceramic-Ag coatings. Therefore, the deposition and annealing conditions, as well as the tribological test parameters, that can modify the segregation activity, must be considered. As previously discussed, the morphology of the films strongly changes when annealing treatment is applied, allowing the silver to segregate to the surface, forming islands that can act as lubricant during the tribological test, explaining the reduction of the COF when high temperatures are applied [21-22, 25, 36-37, 43]. The reduction of the COF at high temperatures is attributed to the low shear strength of Ag at high temperatures. In fact, the reduction of COF has been also reported for larger silver content at room temperature testing [20, 23, 26, 31, 36-37], when compared to the pure MeN matrix.

The deposition temperature is another important variable in the silver segregation. Some studies have described a very simple mathematical relationship between the deposition temperature and the testing temperature in order to be able to control the silver diffusion to the surface to act as self-lubricant material. For example, Mulligan et al. [25] have proposed that the difference between the deposition temperature (T_d) and test temperature (T_t) (T_t-T_d), works as a parameter to evaluate the efficiency of the silver lubrication. They demonstrated that when the test is carried out at higher temperature than the deposition ($T_t > T_d$) the lubricant effect of the silver is evidenced; however, it works only during certain number of cycles until the silver is depleted and consequently rising the COF up to MeN values. When $T_t < T_d$, the coefficient of friction is constant and may be located below or above the MeN COF depending on the amount of silver, as schematized in Figure 2-15.

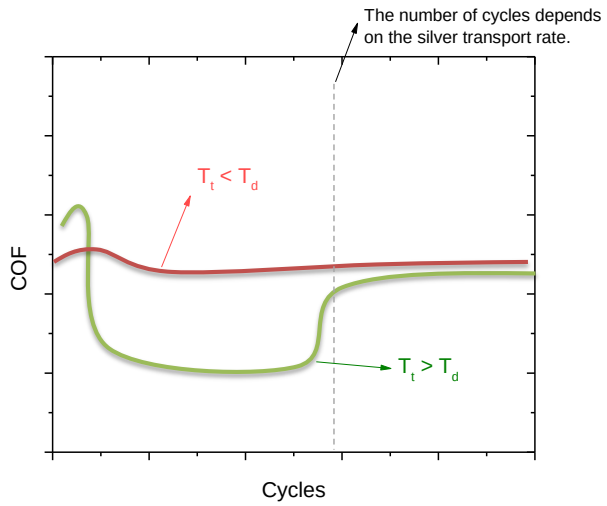

Figure 2-15 Scheme of the COF dependency with the test and deposition temperature.

For very large content of silver some authors have reported higher COF [20], which may be associate to a more unstable porous matrix (Figure 2-6) that remain below the top layer due to the silver diffusion and segregation. Thus, the mechanical solicitation collapse the pores and disintegrate part of the film (the topmost layer), increasing the COF.

When tests are performed at high temperature another factor can influence the friction behavior of the coatings. In fact, some matrices can react with silver at high temperatures to form complex oxides, such as silver molybdate (in MoN-Ag films) [28-29, 81] or silver niobate (for NbN-Ag) [31], which are responsible for the reduction of the COF. Moreover, they can prevent the depletion of silver, since it will be incorporated in the lubricious oxides, allowing maintaining the COF constant at low values for a much larger number of cycles.

A comparison between the coefficient of friction and the MeN matrix in the coating is presented in Figure 2-16. Although different counterparts, normal loads, and test temperatures have been used, the graph provide indicative ranges of values for the COF, attained in these systems.

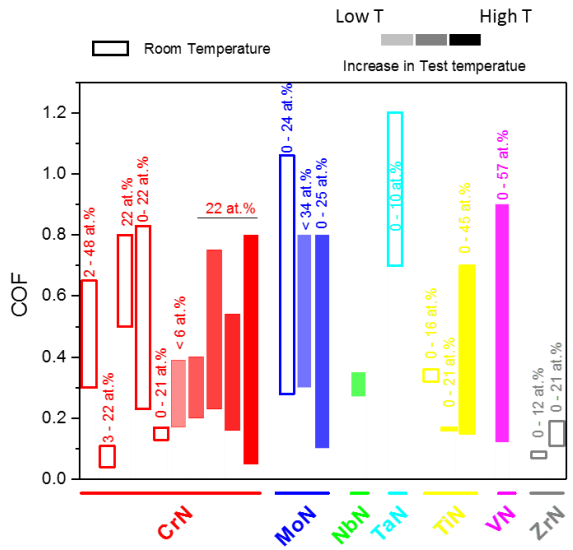

Figure 2-16 COF reported in the literature (Table 2-3) for different MeN-Ag coatings. Different columns for the same material correspond to different references. The intensity of the color for each column represent the low (less intense color) to high (more intense color) testing temperature. The atomic percentages located over the columns represent the range of silver content in the studies.

2.4.2.1.2 Carbon containing matrices (MeC-Ag, MeCN-Ag and a-C-Ag)

For C-based-Ag films, no common behavior is observed due to silver incorporation. The different test conditions are summarized in Table 2-4. Some studies reported that the COF of C-based-Ag coatings is always higher when compared to pure a-C coatings [18], independently of the silver

content, whereas others report a reduction of the COF for low silver content (<4.5 at%) [3]. For high silver content films, significant instabilities of the COF are observed [3, 18, 72], due to the segregation of silver and the consequent degradation of the film left beneath with a porous structure. The easy degradation of the film gives rise to oscillations in the friction coefficient.

The experimental parameters for MeC and MeCN matrices are also summarized in Table 2-4. A threshold silver content is necessary to promote enough silver agglomeration on the material surface to allow the reduction of the COF, at room temperature [50, 55]. As for DLC, the beneficial effect of silver only takes place up to a certain amount, but for further increment in the silver content some systems showed a deterioration of the COF [50, 52]. As already referred, the reduction of the friction coefficient may also be due to the increase of the amorphous carbon, induced by the increase in the Ag content [56-57], which is known to act as self-lubricant material.

Table 2-4 Tribological test condition, COF and wear rate reported for MeC, MeCN and DLC coatings.

	Test	Lubricant	Counter body	Temperature [°C]	Humidity [%]	Applied load [N]	COF	WEAR rate X 10^{-6} [$mm^3 N^{-1} m^{-1}$]
C-based [66]	Ball on disk	Dry	AISI 52100	RT	40-50	5	0.25 to 0.7	NM
C-based [18]	pin on disk	Dry	Zirconia	RT	40	10 18	0.06 to 0.2	0.05 to 0.2
C-based [72]	Reciprocating pin on disk	Dry	AISI 52100	RT	30	1	0.2 to 0.3	NM
C-based [3]	Reciprocating test	NM	Alumina	RT	40	0.01	0.16 to 0.6	0.002 to 19.60 um^3/cycle mN
C-based [74]	Ball on disk	vacuum	GCr15	RT	NA	5	0.005	NM
SiC [50]	Ball on flat	Dry	440C	NM	Vacuum	1	0.125 to 0.39	NM
TiC [51]	Ball on flat	Dry	440C	RT	Vacuum	1	0.25 to 0.75	NM
TiC [52]	Ball on flat	Dry	CCr15	RT	NM and Vacuum	1	0.04 to 0.3	0.1 to 0.8
HfC [50]	Ball on flat	Dry	440C	NM	Vacuum	1	0.17 to 0.45	NM
MoCN [56]	Ball on disk	Dry	Alumina and cemented carbide	25, 500 and 700	60% (RT)	1	0.25 to 0.9*	NM
TiCN [57]	Pin on disk	Dry, HBSS and HBSS+BSA	Alumina	RT	35	2	NM	0.15 to 0.21
TiCN [60]	Reciprocating test	Fetal bovine serum	Alumina	NM	NM	0.5	0.3 *	1 to 9

*** Approximated value; NM= not mentioned; RT = Room temperature**

MeCN-Ag systems have been tested in lubricated environments using albumin containing solution. In these studies, the incorporation of silver did not give rise to an evident lubrication enhancement, being the reduction of the COF attributed to a protein protective layer formed in the sliding contact [57].

Figure 2-17 summarizes the coefficient of friction reported for a-C-Ag, MeC-Ag and MeCN-Ag coatings reported in Table 2-4. In general terms, it may be observed that and COF have lower intervals, demonstrating the influence of the carbon phases in friction behavior of the systems.

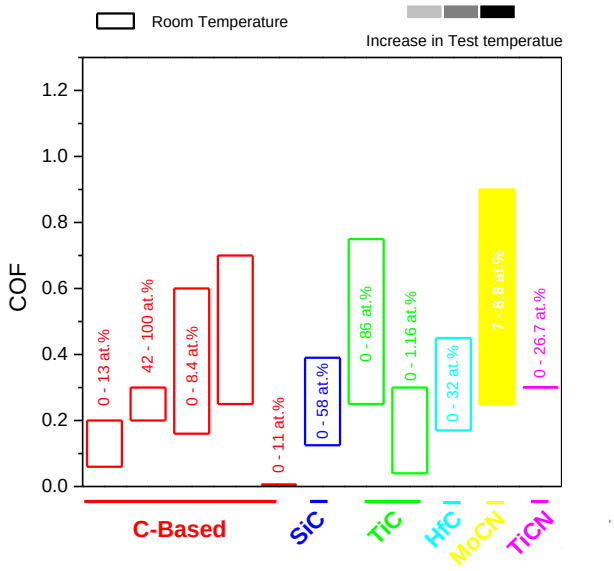

Figure 2-17 COF reported in the literature for C-based-Ag, MeC-Ag and MeCN-Ag coatings (Table 2-4). Different columns for the same material correspond to different references. The intensity of the color for each column represent from low (less intense color) to high (more intense color) testing temperature. The atomic percentages located over the columns represent the range of silver content in the studies.

2.4.2.1.3 Oxides and other matrices

These matrices showed also a reduction of the COF due to the incorporation of silver [12, 97]. Two systems will be highlighted as follows.

- Yttria-stabilized zirconia (YSZ) with silver showed that, for temperatures from 300 °C to 500 °C, increasing the silver resulted in a reduction of COF. For higher temperatures (700 °C) the COF stabilizes at 0.8. The out diffusion of silver from the ceramic matrix, forms a lubricious layer on the contact decreasing the friction. For higher temperature (700 °C) the silver becomes very soft being pushed easily out of the sliding contact reducing its ability to lubricate [12]. To avoid the quick depletion of silver, Hu et al. [86] produced a multilayered system with TiN as barrier layer,

allowing the control of silver diffusion. The COF could be kept at low values for more than 25000 cycles when compared to the monolithic layer that only could withstand 4500 cycles.

- WS_2-Ag films with 40 at% of silver improved the tribological behavior compared to pure WS_2 in air and vacuum condition. The incorporation of silver improved the mechanical properties of WS_2, and thus, the wear track showed less debris and higher resistance to crack nucleation and propagation [106]. The COF starts at similar values but decreases abruptly for the films containing silver after a few cycles (<1000). In humid air, the lower COF are maintained for all silver content, when compared to WS_2, but they are higher when the tests are performed in vacuum [107-108].

2.4.2.2 WEAR

The wear resistance of the ceramic-Ag systems depends on the Ag depletion time. In a first phase, the wear rate is rather low due to the lubrication effect of the silver. However, after the solid lubricant (silver) is worn-out an unstable porous structure underneath the surface is created, leading to the quick destruction of the coating and an enormous increase in the wear rate. Thus, the stability of the coatings will define the segregation, which when in large amount may provoke the failure and the increase of the wear rates of the system [25].

In the literature, contradictory results regarding the wear rate can be found, depending on the silver content and the testing temperature and their influence on the stability of the coating. Hence, the wear rate can be reduced [26, 57] or increased [3, 15, 18, 20, 57]. Kelly et al., for example, demonstrated that ZrN-Ag and TiN-Ag showed no wear when Ag=0 at%, increasing for higher silver content, while CrN-Ag showed lower values of wear for silver content <11 at. %, then increasing for higher Ag contents [23].

In other studies, ZrN-Ag and TaN-Ag wear rates did not follow a clear tendency with the incorporation of silver, but evidencing a reduction of the wear rate when compared to the pure nitrides [36-37, 47]. In relation to the effect of the testing temperature increment, in some cases, a reduction of the wear rates is achieved [21, 28, 36-37], due to the efficient lubrication of silver. Although, in other cases, an increase of the wear rates is observed due to the loss of integrity of the coatings [6, 25, 108]. The values of the wear rate are varied from 10^{-13} to 10^{-3} mm^3 $N^{-1}m^{-1}$; a summary of the tribological results is shown in Table 2-3 and Table 2-4.

2.4.3 Electrochemical properties

A limited number of studies have been published regarding the electrochemical behavior of ceramic-Ag films produced by magnetron sputtering. Among them, the majority of the reports is carried out for saline solution with concentration isotonic to seawater or human body fluids. The electrochemical characterization helps to understand the ability of the coatings either to withstand certain liquid environments or to predict their behavior and possible duration in harsh environments. A variety of tests can be considered among which the most commons are the potentiodynamic test (PT) and the electrochemical impedance spectroscopy (EIS). The studies strongly depend on the substrate and environment selected for the assays which are depending on the final application of the system. Table 2-5 shows a summary of the general test conditions for such evaluation.

Table 2-5 Electrochemical test parameters used in ceramic-Ag films

	Test	REF	Aux	Area [cm²]	Electrolyte	Substrate
DLC [3]	PT EIS	SCE	NM	NM	3.5% NaCl	SS316L
TiCaPCON [109]	PT	Ag/AgCl	Pt	1	Saline solution 37 °C	Si
TiN [40]	CV EIS	SCE	Pt	NM	Sweat solution with 4.7 pH	Glass
ZnS [104]	Photocurrent	Ag/AgCl	Pt	1	K_2SO3 Na_2S	NM
ZrCN [111]	PT EIS	SCE	Pt	0.44	NaCl 0.9 % 37 °C	SS316L
ZrCN [61]	PT EIS	SCE	Pt	1.7	NaCl 0.9 % 37 °C	SS316L
ZrN [48]	PT	SCE	Graphite	1	3.5 % NaCl 37 °C	NM

Taking into consideration that ceramic-Ag films form separate phases, including crystalline and/or amorphous ceramic and metallic silver, the corrosion potential and the open circuit potential of the coatings, behave as predicted by the mixing potential theory, in which for two conductive phases in electrical contact, the resulting OCP is located between the OCP of both phases. Therefore, OCP and/or corrosion potential of a ceramic-Ag system will be located between the ceramic OCP and the metallic silver. In the majority of the cases, the matrix possesses lower OCP when compared to silver, such as for ZrN [48], DLC [3] and ZrCN [61], and thus, the corrosion potential of the films tends to increase when silver is incorporated to the coatings. On the other hand, for matrixes with higher reduction potentials, such as TiN [40], the OCP decreases when silver is introduced to the system. The variation of the OCP is not monotonic

with the silver incorporation, since the OCP is an intensive property, which does not depend on the amount of the phases.

The corrosion resistance, represented by either the inverse of the density current for potentiodinamic test or the polarization resistance in the EIS, is usually reported to decrease as silver content increases in the films [40, 48, 109]. The deterioration of the electrochemical properties of the films is associated to the increase of a more electrochemical active phase (Ag), when compared to ceramic counterpart, but additionally silver may potentiate the oxidation of the metal in the ceramic matrix. In simpler electrolytes, such as NaCl, the oxidation of silver is expected due to the high affinity of Ag to Cl to form AgCl; however, no evidence has been found in most of the literature about the precipitation of such phase.

For low silver content, an improvement in the corrosion resistance of the coatings has also been reported. Dhandapani et al. [3], for instance, showed a reduction of the density current as silver is increased in C-based matrix up to ~ 8 at%, from which the corrosion resistance is deteriorated; the improvements in the corrosion resistance is hypothetically due to the increase in the sp^2/sp^3 ratio.

2.4.3.1 Silver ion release

Silver ion release is one of the main phenomena reported to be important to attain antibacterial behavior and to understand the electrochemical activity of the coatings. We have demonstrated that such metal ion release is dependent on the electrolyte in which the films are immersed, due to the different electrochemical reactions that may be promoted by the component of the electrolytes [63]. Therefore, in order to elucidate the behavior of the silver ionization for specific application, it is essential to mimic the condition of the environment. Nonetheless, limitations such as reactivity and/or precipitation of silver compounds may prevent the correct determination of silver ion release in complex environments.

The silver ion release has been reported to be dependent on the silver content, but with contradictory behaviors. Song et al. [101], for example, have shown that for lower silver content, higher silver release is observed, while for similar systems the silver increase in the films promotes more ion release to the media as reported by [99]. This contradictory results may indicate that it is not only the silver content that controls the silver ion release, but other parameters, such as the silver nanoparticles size, the electrochemical galvanic couples formed between the silver and the matrix or the initial oxidized state of silver may also influence the

process. The increase of the silver particles size by annealing treatment leads to a decrease on the silver ion release, possibly explained by the decrease of the surface area of the silver nanoparticles [93]

Most of the reports assesses the Ag^+ release in simple solutions, such as distilled water, NaCl at low concentrations or acid environment, in order to avoid the increase of the complexity brought by extra variables; however, care must be taken when comparing the results with those occurring in environments characteristic of the final application. Independently of the electrolyte, a common behavior has been observed. Silver is rapidly released in the first hours of immersion, reaching a plateau-like behavior after this time, releasing very low or none silver ions, as schematized in Figure 2-18 [98-99, 111].

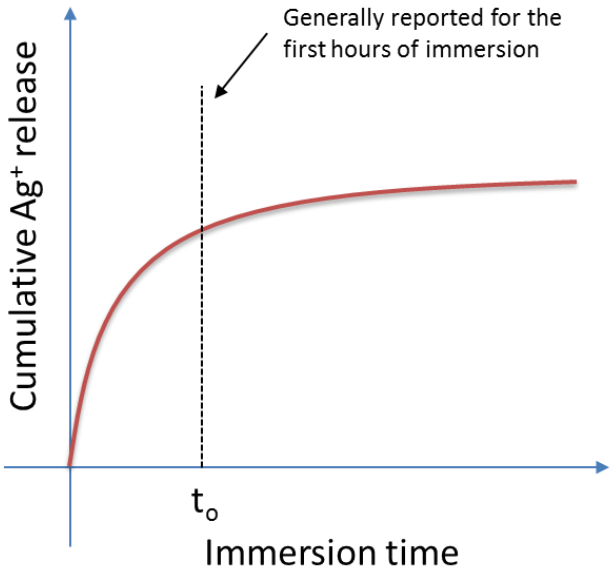

Figure 2-18 Schematic silver ion release as a function of ceramic-Ag immersion time in an electrolyte.

Such behavior may be attributed to two phenomena:

a) The formation of passive films on the surface of the material, or on the silver crystals, that prevent the silver release. Hypothetically, the passive films may be formed by $AgCl^+$; however, no evidence of such compound has been provided in the literature; other passivation forms such as silver oxides and sulfides, among others, can also be considered [41].

b) The release of chemisorbed silver ions on the silver nanoparticles surface, dropping the release rate of the chemisorbed species with time. This behavior was found in composite samples [111, 118] and in pure nanoparticles in natural waters [119].

These two scenarios may be optimal for antibacterial short term application since the silver release in the first hours will control the possible bacteria adhesion while maintain low silver release to reduce toxicity effect. However, in order to exploit the materials for long term applications, solutions should be provided in order to keep silver ion release along the time.

The comparison between the silver ion release and the antibacterial effect cannot be directly performed, since in most of the reports different electrolytes are used in both, antibacterial and silver ion release, tests. Furthermore, very often dimensions of the samples are not provided; e.g. silver release in a maximum period of 30 days has been reported to be in the order of ppb; however, no specifications of the size of the immersed sample, to determine either the silver release per area of the sample or the total amount of silver release in grams, are given.

From the contamination point of view, the low silver release and the reduction of the silver after few hours of immersion can represent a benefit to the use of ceramic-Ag coatings in the cases where Ag release is undesirable as, for example, filters or bearing surfaces in contact with fluids. In other cases, the low silver activity can also be exploited as a self-controlled release mechanism if the release is controlled by an activation process (i.e. electrically, mechanically, chemically, among others).

In conclusion, in order to better understand the behavior of ceramic-Ag coatings immersed in electrolyte, more studies are required, particularly concerning the Ag^+ dependency of the matrix (MeN, MeCN, MeC, etc) and electrolyte, as well as of the importance of the activation processes for the kinetic release control. Only with a deeper study, the use of these coatings for applications involving silver ion release can be envisaged. Part of these studies are covered in the results of these thesis and will be discussed in Chapter VIII.

2.4.4 Biological properties

2.4.4.1 Biocompatibility

In order to be able to apply these types of material in medical devices, such the ones reported in these thesis, biocompatibility of the system must be ensure. However, only few studies of ceramic-Ag films deposited by magnetron sputtering report the cytotoxicity and biocompatibility

of the materials. All the reports agree that below a certain value of silver content the cytotoxicity levels of the ceramic-Ag coatings are insignificant. The absolute amount of silver necessary to produce cytotoxicity is not clearly defined, and it is probably dependent on the matrix. For instance, no significant cytotoxicity is observed on ceramic-Ag films for human gingival fibroblast for surfaces with less than 12 at% of silver in ZrON matix [75], or TaN-Ag films with less than 21 at% of silver [33]. In TiCN-Ag films our group have reported low cytotoxicity (<20 at%) in coatings silver content up to 27 at% and less than 10 % of fibroblast 3T3 cells die when the silver is maintained below 20 at% [15], similar to TiO2-Ag films [99, 101]. However, despite of the fact that the samples are not cytotoxic some groups have demonstrated that from certain silver content (> 4 at%), a significant inhibitory effect of osteoblastic differentiation [109].

2.4.4.2 Antibacterial properties

Antimicrobial effect of silver has been extensively reported in different types of materials containing silver nanoparticles and for a large number of application. One of the advantages of ceramic-Ag coatings is the local effect of the bactericidal agent, which is expected to be released directly at the site where the effect is needed, minimizing the risk of reaching concentrations that can cause harmful side reactions. The two main factors responsible for the antimicrobial capabilities of silver are: (i) the amount of silver ions release and, (ii) the silver nanoparticles activity, which depends on their sizes and shapes. These factors are directly related with the mechanisms controlling bacteria spreading, respectively: (i) Ag^{+} is known to interact with the cell thiol groups, binding to the main functional groups in some components such enzymes, and avoids bacterial division, damaging the cell envelope [120], while (ii) the particles disrupt the cell membrane, killing the bacterium[121]. In this basis, to properly determine the antibacterial effect of the films, different kinds of experiments are designed.

Nonetheless, the large variety of test and condition used in the determination of the antibacterial effectivity of the ceramic-Ag coatings, make it difficult to perform a proper comparison and extract general conclusion of such behavior. In fact, contradictory results are found in the literature in relation to the antibacterial effectiveness of ceramic-Ag coatings.

For instance, Kelly et al. [23], reported antibacterial effect of ZrN-Ag, TiN-Ag and CrN-Ag for *P. Aeruginosa*, however in their results even the pure nitride matrices present the antibacterial effect using a Nitro Blue-Tetrazolium test (NBT). This method was also used to determine the *S. aureus* susceptibility to the antibacterial effect of these three coatings, finding that a silver

increase on the surface resulted in a decrease in the colony forming units for all the matrices. They also report opposite results using a zone of inhibition method (ZOI), where for ZrN-Ag and CrN-Ag an increase of the inhibition zone is identified as silver increase, but not ZOI is observed for TiN-Ag [23, 39]. Similarly, Wickens et al. [49] state that as silver increase in the coatings, the respiring colonies on the surface significantly decreased in ZrN-Ag coatings compared to pure ZrN coatings for *S. aureus* and *S. epidermidi*, increasing the dead cell as the silver increased.

Huang et al. demonstrated by fluorescence test in TaN-Ag films with silver content of 14 and 17 at% that bacteria adhesion increase with respect to pure TaN coatings, but with a reduction of the hydrophobicity of the films. When silver is added to 24 at% (which in the surface images showed enough silver on the surface), the adhere bacteria is reduced and the viability test showed no bacteria in the vicinity of the samples, in contrast with Ti and TaN, which showed some bacteria [33]. In the same system [32], only samples with 10 at% showed antibacterial effect for *E. Coli*. However, after annealing treatment, which is expected to promote silver segregation to the surface, all the samples (1.6 and 3.4 at%) revealed antibacterial effectivity, indicating that the silver on the surface may be a key factor on the antibacterial effect. Similar results are reported by [78] in TaON-Ag samples.

On the other hand, Carvalho et al. demonstrated lack of antibacterial activity of TiCN-Ag [15], proposing that the increase of contact zone between the bacteria and the surface due to the changes promote by silver on the morphology and the lack of silver ion release may be responsible for the non-antibacterial effect of the films using the CFUs methods [15].

Finally some studies have reported the antibacterial capabilities of ceramic-Ag films deposited by magnetron sputtering, without a specific explanation of the mechanisms [10, 48, 88, 92, 102]. Balagna et al. [92] have demonstrated that the ZOI dimension depends on the sensitivity of the bacteria, testing *E. coli, B. cereus, S. aureus* and *Morganella*. And that the aging of the samples affect the antifungal activity, but not the antimicrobial activity of the samples.

2.5 References

1. Manninen, N. K.; Calderón V, S.; Almeida Alves, C. F.; Carvalho, S.; Cavaleiro, A., Influence of Hydrogen Incorporation and Coating Thickness on the Corrosion Resistance of Carbon Based Coatings Deposited by Magnetron Sputtering. *Surface and Coatings Technology* **2015,** *275* (0), 127-132.

2. Van der Donck, T.; Muchlado, M.; Zein Eddine, W.; Achanta, S.; Carvalho, N. J. M.; Celis, J. P., Effect of Hydrogen Content in a-C:H Coatings on Their Tribological Behaviour at Room Temperature up to 150 °C. *Surface and Coatings Technology* **2009,** *203* (22), 3472-3479.

3. Dhandapani, V. s.; Thangavel, E.; Arumugam, M.; Shin, K. S.; Veeraraghavan, V.; Yau, S. Y.; Kim, C.; Kim, D.-E., Effect of Ag Content on the Microstructure, Tribological and Corrosion Properties of Amorphous Carbon Coatings on 316l Ss. *Surface and Coatings Technology* **2014,** *240* (0), 128-136.

4. Onoprienko, A. A.; Danylenko, M. I., Annealing Effects in Ag-Doped Amorphous Carbon Films Deposited by Dc Magnetron Sputtering. *Surface and Coatings Technology* **2012,** *206* (16), 3450-3453.

5. Yao, S. H.; Su, Y. L.; Kao, W. H., Effect of Ag/W Addition on the Wear Performance of Crn Coatings Prepared by Rf Unbalanced Magnetron Sputtering. *Materials Science and Engineering: A* **2005,** *398* (1–2), 88-92.

6. Köstenbauer, H.; Fontalvo, G.; Mitterer, C.; Keckes, J., Tribological Properties of Tin/Ag Nanocomposite Coatings. *Tribology Letters* **2008,** *30* (1), 53-60.

7. Wang, C.; Yu, X.; Hua, M., Microstructure and Mechanical Properties of Ag-Containing Diamond-Like Carbon Films in Mid-Frequency Dual-Magnetron Sputtering. *Applied Surface Science* **2009,** *256* (5), 1431-1435.

8. Batory, D.; Reczulska, M. C.; Kolodziejczyk, L.; Szymanski, W., Gradient Titanium and Silver Based Carbon Coatings Deposited on Aisi316l. *Applied Surface Science* **2013,** *275* (0), 303-310.

9. Chen, S.-Y.; Ou, K.-L.; Huang, W.-C.; Chu, K.-T.; Ou, S.-F., Phase Transformation of Diamond-Like Carbon/Silver Composite Films by Sputtering Deposition. *Ceramics International* **2013,** *39* (3), 2575-2580.

10. Lan, W.-C.; Ou, S.-F.; Lin, M.-H.; Ou, K.-L.; Tsai, M.-Y., Development of Silver-Containing Diamond-Like Carbon for Biomedical Applications. Part I: Microstructure Characteristics, Mechanical Properties and Antibacterial Mechanisms. *Ceramics International* **2013,** *39* (4), 4099-4104.

11. Calderon V, S.; Oliveira, J. C.; Evaristo, M.; Cavaleiro, A.; Carvalho, S., Prediction of Optimized Composition for Enhanced Mechanical and Electrochemical Response of Zr-C-N-Ag Coatings for Medical Devices. *Applied Surface Science* **2014,** *320* (0), 570-580.

12. Muratore, C.; Voevodin, A. A.; Hu, J. J.; Jones, J. G.; Zabinski, J. S., Growth and Characterization of Nanocomposite Yttria-Stabilized Zirconia with Ag and Mo. *Surface and Coatings Technology* **2005,** *200* (5–6), 1549-1554.

13. Pedrosa, P.; Machado, D.; Lopes, C.; Alves, E.; Barradas, N. P.; Martin, N.; Macedo, F.; Fonseca, C.; Vaz, F., Nanocomposite Ag:Tin Thin Films for Dry Biopotential Electrodes. *Applied Surface Science* **2013,** *285, Part A* (0), 40-48.

14. Liu, M.; Bao, S.; Yang, G.; Lu, L.; Cheng, S.; Qu, S.; Yu, W.; Ma, C.; Zhang, Q., Self-Assembled Zno/Ag Nanocomposite Thin Films with Enhanced Multiple-Phonon Resonant Raman Scattering. *Materials Letters* **2014,** *115* (0), 172-175.

15. Isabel, C.; Mariana, H.; João Carlos, O.; Cristiana Filipa Almeida, A.; Ana Paula, P.; Sandra, C., Influence of Surface Features on the Adhesion of Staphylococcus Epidermidis to Ag–Ticn Thin Films. *Science and Technology of Advanced Materials* **2013,** *14* (3), 035009.

16. Sella, C.; Chenot, S.; Reillon, V.; Berthier, S., Influence of the Deposition Conditions on the Optical Absorption of Ag–Sio2 Nanocermet Thin Films. *Thin Solid Films* **2009,** *517* (20), 5848-5854.

17. Manninen, N.; Galindo, R. E.; Benito, N.; Figueiredo, N.; Cavaleiro, A.; Palacio, C.; Carvalho, S., Ag–Ti (C, N)-Based Coatings for Biomedical Applications: Influence of Silver Content on the Structural Properties. *Journal of Physics D: Applied Physics* **2011,** *44* (37), 375501.

18. Manninen, N. K.; Ribeiro, F.; Escudeiro, A.; Polcar, T.; Carvalho, S.; Cavaleiro, A., Influence of Ag Content on Mechanical and Tribological Behavior of Dlc Coatings. *Surface and Coatings Technology* **2013,** *232* (0), 440-446.

19. Siozios, A.; Zoubos, H.; Pliatsikas, N.; Koutsogeorgis, D. C.; Vourlias, G.; Pavlidou, E.; Cranton, W.; Patsalas, P., Growth and Annealing Strategies to Control the Microstructure of Aln:Ag Nanocomposite Films for Plasmonic Applications. *Surface and Coatings Technology* **2014,** *255* (0), 28-36.

20. Basnyat, P.; Luster, B.; Kertzman, Z.; Stadler, S.; Kohli, P.; Aouadi, S.; Xu, J.; Mishra, S. R.; Eryilmaz, O. L.; Erdemir, A., Mechanical and Tribological Properties of Craln-Ag Self-Lubricating Films. *Surface and Coatings Technology* **2007,** *202* (4–7), 1011-1016.

21. Incerti, L.; Rota, A.; Valeri, S.; Miguel, A.; García, J. A.; Rodríguez, R. J.; Osés, J., Nanostructured Self-Lubricating Crn-Ag Films Deposited by Pvd Arc Discharge and Magnetron Sputtering. *Vacuum* **2011,** *85* (12), 1108-1113.

22. Jurči, P.; Dlouhý, I., Coating of Cr–V Ledeburitic Steel with Crn Containing a Small Addition of Ag. *Applied Surface Science* **2011,** *257* (24), 10581-10589.

23. Kelly, P. J.; Li, H.; Benson, P. S.; Whitehead, K. A.; Verran, J.; Arnell, R. D.; Iordanova, I., Comparison of the Tribological and Antimicrobial Properties of Crn/Ag, Zrn/Ag, Tin/Ag, and

Tin/Cu Nanocomposite Coatings. *Surface and Coatings Technology* **2010,** *205* (5), 1606-1610.

24. Mulligan, C. P.; Blanchet, T. A.; Gall, D., Crn–Ag Nanocomposite Coatings: Effect of Growth Temperature on the Microstructure. *Surface and Coatings Technology* **2008,** *203* (5–7), 584-587.

25. Mulligan, C. P.; Blanchet, T. A.; Gall, D., Crn–Ag Nanocomposite Coatings: High-Temperature Tribological Response. *Wear* **2010,** *269* (1–2), 125-131.

26. Mulligan, C. P.; Gall, D., Crn–Ag Self-Lubricating Hard Coatings. *Surface and Coatings Technology* **2005,** *200* (5–6), 1495-1500.

27. Papi, P. A.; Mulligan, C. P.; Gall, D., Crn–Ag Nanocomposite Coatings: Control of Lubricant Transport by Diffusion Barriers. *Thin Solid Films* **2012,** *524* (0), 211-217.

28. Aouadi, S.; Paudel, Y.; Luster, B.; Stadler, S.; Kohli, P.; Muratore, C.; Hager, C.; Voevodin, A., Adaptive Mo2n/Mos2/Ag Tribological Nanocomposite Coatings for Aerospace Applications. *Tribology Letters* **2008,** *29* (2), 95-103.

29. Aouadi, S. M.; Paudel, Y.; Simonson, W. J.; Ge, Q.; Kohli, P.; Muratore, C.; Voevodin, A. A., Tribological Investigation of Adaptive Mo2n/Mos2/Ag Coatings with High Sulfur Content. *Surface and Coatings Technology* **2009,** *203* (10–11), 1304-1309.

30. Gulbiński, W.; Suszko, T., Thin Films of Mo2n/Ag Nanocomposite—the Structure, Mechanical and Tribological Properties. *Surface and Coatings Technology* **2006,** *201* (3–4), 1469-1476.

31. Stone, D. S.; Migas, J.; Martini, A.; Smith, T.; Muratore, C.; Voevodin, A. A.; Aouadi, S. M., Adaptive Nbn/Ag Coatings for High Temperature Tribological Applications. *Surface and Coatings Technology* **2012,** *206* (19–20), 4316-4321.

32. Hsieh, J. H.; Tseng, C. C.; Chang, Y. K.; Chang, S. Y.; Wu, W., Antibacterial Behavior of Tan–Ag Nanocomposite Thin Films with and without Annealing. *Surface and Coatings Technology* **2008,** *202* (22–23), 5586-5589.

33. Huang, H.-L.; Chang, Y.-Y.; Lai, M.-C.; Lin, C.-R.; Lai, C.-H.; Shieh, T.-M., Antibacterial Tan-Ag Coatings on Titanium Dental Implants. *Surface and Coatings Technology* **2010,** *205* (5), 1636-1641.

34. Park, I.-S.; Park, S.-Y.; Jeong, G.-H.; Na, S.-M.; Suh, S.-J., Fabrication of Ta3n5–Ag Nanocomposite Thin Films with High Resistivity and near-Zero Temperature Coefficient of Resistance. *Thin Solid Films* **2008,** *516* (16), 5409-5413.

35. Tseng, C. C.; Hsieh, J. H.; Jang, S. C.; Chang, Y. Y.; Wu, W., Microstructural Analysis and Mechanical Properties of Tan–Ag Nanocomposite Thin Films. *Thin Solid Films* **2009,** *517* (17), 4970-4974.

36. Tseng, C. C.; Hsieh, J. H.; Wu, W.; Chang, S. Y.; Chang, C. L., Emergence of Ag Particles and Their Effects on the Mechanical Properties of Tan–Ag Nanocomposite Thin Films. *Surface and Coatings Technology* **2007,** *201* (24), 9565-9570.

37. Tseng, C. C.; Hsieh, J. H.; Wu, W.; Chang, S. Y.; Chang, C. L., Surface and Mechanical Characterization of Tan–Ag Nanocomposite Thin Films. *Thin Solid Films* **2008,** *516* (16), 5424-5429.

38. de los Arcos, T.; Oelhafen, P.; Aebi, U.; Hefti, A.; Düggelin, M.; Mathys, D.; Guggenheim, R., Preparation and Characterization of Tin–Ag Nanocomposite Films. *Vacuum* **2002,** *67* (3–4), 463-470.

39. Kelly, P. J.; Li, H.; Whitehead, K. A.; Verran, J.; Arnell, R. D.; Iordanova, I., A Study of the Antimicrobial and Tribological Properties of Tin/Ag Nanocomposite Coatings. *Surface and Coatings Technology* **2009,** *204* (6–7), 1137-1140.

40. Pedrosa, P.; Lopes, C.; Martin, N.; Fonseca, C.; Vaz, F., Electrical Characterization of Ag:Tin Thin Films Produced by Glancing Angle Deposition. *Materials Letters* **2014,** *115* (0), 136-139.

41. Rtimi, S.; Baghriche, O.; Sanjines, R.; Pulgarin, C.; Ben-Simon, M.; Lavanchy, J. C.; Houas, A.; Kiwi, J., Photocatalysis/Catalysis by Innovative Tin and Tin-Ag Surfaces Inactivate Bacteria under Visible Light. *Applied Catalysis B: Environmental* **2012,** *123–124* (0), 306-315.

42. Skovager, A.; Whitehead, K.; Wickens, D.; Verran, J.; Ingmer, H.; Arneborg, N., A Comparative Study of Fine Polished Stainless Steel, Tin and Tin/Ag Surfaces: Adhesion and Attachment Strength of Listeria Monocytogenes as Well as Anti-Listerial Effect. *Colloids and Surfaces B: Biointerfaces* **2013,** *109* (0), 190-196.

43. Aouadi, S. M.; Singh, D. P.; Stone, D. S.; Polychronopoulou, K.; Nahif, F.; Rebholz, C.; Muratore, C.; Voevodin, A. A., Adaptive Vn/Ag Nanocomposite Coatings with Lubricious Behavior from 25 to 1000 °C. *Acta Materialia* **2010,** *58* (16), 5326-5331.

44. Aouadi, S. M.; Bohnhoff, A.; Sodergren, M.; Mihut, D.; Rohde, S. L.; Xu, J.; Mishra, S. R., Tribological Investigation of Zirconium Nitride/Silver Nanocomposite Structures. *Surface and Coatings Technology* **2006,** *201* (1–2), 418-422.

45. Aouadi, S. M.; Bohnhoff, A.; Amriou, T.; Williams, M.; Hilfiker, J. N.; Singh, N.; Woollam, J. A., Vacuum Ultra-Violet Spectroscopic Ellipsometry Study of Single- and Multi-Phase Nitride Protective Films. *Journal of Physics: Condensed Matter* **2006,** *18* (32), S1691.

46. Aouadi, S. M.; Debessai, M.; Filip, P., Zirconium Nitride/Silver Nanocomposite Structures for Biomedical Applications. *Journal of Vacuum Science & Technology B* **2004,** *22* (3), 1134-1140.

47. Aouadi, S. M.; Shreeman, P. K.; Ge, Q.; Xu, J.; Mishra, S. R., Correlation between Interfacial Electronic Structure and Mechanical Properties of Zrn–Me (Me□Ag, Au, or Pd) Nanocomposite Films. *Applied Physics Letters* **2005,** *87* (4), 041902-1.

48. Kertzman, Z.; Marchal, J.; Suarez, M.; Staia, M. H.; Filip, P.; Kohli, P.; Aouadi, S. M., Mechanical, Tribological, and Biocompatibility Properties of Zrn-Ag Nanocomposite Films. *Journal of Biomedical Materials Research Part A* **2008,** *84A* (4), 1061-1067.

49. Wickens, D. J.; West, G.; Kelly, P. J.; Verran, J.; Lynch, S.; Whitehead, K. A., Antimicrobial Activity of Nanocomposite Zirconium Nitride/Silver Coatings to Combat External Bone Fixation Pin Infections. *International Journal of Artificial Organs* **2012,** *35* (10), 817-825.

50. Krzanowski, J. E.; Endrino, J. L.; Nainaparampil, J. J.; Zabinski, J. S., Composite Coatings Incorporating Solid Lubricant Phases. *Journal of Materials Engineering and Performance* **2004,** *13* (4), 439-444.

51. Endrino, J. L.; Nainaparampil, J. J.; Krzanowski, J. E., Microstructure and Vacuum Tribology of Tic–Ag Composite Coatings Deposited by Magnetron Sputtering-Pulsed Laser Deposition. *Surface and Coatings Technology* **2002,** *157* (1), 95-101.

52. Wang, Y.; Wang, J.; Zhang, G.; Wang, L.; Yan, P., Microstructure and Tribology of Tic(Ag)/a-C:H Nanocomposite Coatings Deposited by Unbalanced Magnetron Sputtering. *Surface and Coatings Technology* **2012,** *206* (14), 3299-3308.

53. Sarius, N. G.; Lauridsen, J.; Lewin, E.; Lu, J.; Högberg, H.; Öberg, Å.; Ljungcrantz, H.; Leisner, P.; Eklund, P.; Hultman, L., Ni and Ti Diffusion Barrier Layers between Ti–Si–C and Ti–Si–C–Ag Nanocomposite Coatings and Cu-Based Substrates. *Surface and Coatings Technology* **2012,** *206* (8–9), 2558-2565.

54. Eklund, P.; Joelsson, T.; Ljungcrantz, H.; Wilhelmsson, O.; Czigány, Z.; Högberg, H.; Hultman, L., Microstructure and Electrical Properties of Ti–Si–C–Ag Nanocomposite Thin Films. *Surface and Coatings Technology* **2007,** *201* (14), 6465-6469.

55. Endrino, J. L.; Nainaparampil, J. J.; Krzanowski, J. E., Magnetron Sputter Deposition of Wc–Ag and Tic–Ag Coatings and Their Frictional Properties in Vacuum Environments. *Scripta Materialia* **2002,** *47* (9), 613-618.

56. Shtansky, D. V.; Bondarev, A. V.; Kiryukhantsev-Korneev, P. V.; Rojas, T. C.; Godinho, V.; Fernández, A., Structure and Tribological Properties of Mocn-Ag Coatings in the Temperature Range of 25–700 °C. *Applied Surface Science* **2013,** *273* (0), 408-414.

57. Alves, C. F. A.; Oliveira, F.; Carvalho, I.; Piedade, A. P.; Carvalho, S., Influence of Albumin on the Tribological Behavior of Ag–Ti (C, N) Thin Films for Orthopedic Implants. *Materials Science and Engineering: C* **2014,** *34* (0), 22-28.

58. Carvalho, I.; Galindo, R. E.; Henriques, M.; Palacio, C.; Carvalho, S., Influence of Culture Media on the Physical and Chemical Properties of Ag–Ticn Coatings. *Journal of Physics D: Applied Physics* **2014,** *47* (33), 335401.

59. Escobar Galindo, R.; Manninen, N. K.; Palacio, C.; Carvalho, S., Advanced Surface Characterization of Silver Nanocluster Segregation in Ag–Ticn Bioactive Coatings by Rbs, Gdoes, and Arxps. *Analytical and Bioanalytical Chemistry* **2013,** *405* (19), 6259-6269.

60. Sánchez-López, J. C.; Abad, M. D.; Carvalho, I.; Escobar Galindo, R.; Benito, N.; Ribeiro, S.; Henriques, M.; Cavaleiro, A.; Carvalho, S., Influence of Silver Content on the Tribomechanical Behavior on Ag-Ticn Bioactive Coatings. *Surface and Coatings Technology* **2012,** *206* (8–9), 2192-2198.

61. Calderon Velasco, S.; Lopez, V.; Almeida Alves, C. F.; Cavaleiro, A.; Carvalho, S., Structural and Electrochemical Characterization of Zr–C–N–Ag Coatings Deposited by Dc Dual Magnetron Sputtering. *Corrosion Science* **2014,** *80* (0), 229-236.

62. Ferreri, I.; Lopes, V.; Calderon V, S.; Tavares, C. J.; Cavaleiro, A.; Carvalho, S., Study of the Effect of the Silver Content on the Structural and Mechanical Behavior of Ag–Zrcn Coatings for Orthopedic Prostheses. *Materials Science and Engineering: C* **2014,** *42* (0), 782-790.

63. Calderon V, S.; Ferreri, I.; Galindo, R. E.; Henriques, M.; Cavaleiro, A.; Carvalho, S., Electrochemical Vs Antibacterial Characterization of Zrcn-Ag Coatings. *Surface and Coatings Technology* **2015,** *275* (0), 357-362.

64. Ahmed, S. F.; Moon, M.-W.; Lee, K.-R., Effect of Silver Doping on Optical Property of Diamond Like Carbon Films. *Thin Solid Films* **2009,** *517* (14), 4035-4038.

65. Choi, H. W.; Choi, J.-H.; Lee, K.-R.; Ahn, J.-P.; Oh, K. H., Structure and Mechanical Properties of Ag-Incorporated Dlc Films Prepared by a Hybrid Ion Beam Deposition System. *Thin Solid Films* **2007,** *516* (2–4), 248-251.

66. Lungu, C. P., Nanostructure Influence on Dlc-Ag Tribological Coatings. *Surface and Coatings Technology* **2005,** *200* (1–4), 198-202.

67. Manninen, N. K.; Galindo, R. E.; Carvalho, S.; Cavaleiro, A., Silver Surface Segregation in Ag-Dlc Nanocomposite Coatings. *Surface and Coatings Technology* **2015,** *267* (0), 90-97.

68. Meškinis, Š.; Čiegis, A.; Vasiliauskas, A.; Tamulevičienė, A.; Šlapikas, K.; Juškėnas, R.; Niaura, G.; Tamulevičius, S., Plasmonic Properties of Silver Nanoparticles Embedded in Diamond Like Carbon Films: Influence of Structure and Composition. *Applied Surface Science* **2014,** *317* (0), 1041-1046.

69. Meškinis, Š.; Vasiliauskas, A.; Šlapikas, K.; Gudaitis, R.; Andrulevičius, M.; Čiegis, A.; Niaura, G.; Kondrotas, R.; Tamulevičius, S., Bias Effects on Structure and Piezoresistive Properties of Dlc:Ag Thin Films. *Surface and Coatings Technology* **2014,** *255* (0), 84-89.

70. Tamulevičius, S.; Meškinis, Š.; Šlapikas, K.; Vasiliauskas, A.; Gudaitis, R.; Andrulevičius, M.; Tamulevičienė, A.; Niaura, G., Piezoresistive Properties of Amorphous

Carbon Based Nanocomposite Thin Films Deposited by Plasma Assisted Methods. *Thin Solid Films* **2013,** *538* (0), 78-84.

71. Morrison, M. L.; Buchanan, R. A.; Liaw, P. K.; Berry, C. J.; Brigmon, R. L.; Riester, L.; Abernathy, H.; Jin, C.; Narayan, R. J., Electrochemical and Antimicrobial Properties of Diamondlike Carbon-Metal Composite Films. *Diamond and Related Materials* **2006,** *15* (1), 138-146.

72. Takeno, T.; Saito, H.; Goto, M.; Fontaine, J.; Miki, H.; Belin, M.; Takagi, T.; Adachi, K., Deposition, Structure and Tribological Behavior of Silver–Carbon Nanocomposite Coatings. *Diamond and Related Materials* **2013,** *39* (0), 20-26.

73. Tamulevičius, T.; Tamulevičienė, A.; Virganavičius, D.; Vasiliauskas, A.; Kopustinskas, V.; Meškinis, Š.; Tamulevičius, S., Structuring of Dlc:Ag Nanocomposite Thin Films Employing Plasma Chemical Etching and Ion Sputtering. *Nuclear Instruments and Methods in Physics Research Section B: Beam Interactions with Materials and Atoms* **2014,** *341* (0), 1-6.

74. Wu, Y.; Chen, J.; Li, H.; Ji, L.; Ye, Y.; Zhou, H., Preparation and Properties of Ag/Dlc Nanocomposite Films Fabricated by Unbalanced Magnetron Sputtering. *Applied Surface Science* **2013,** *284* (0), 165-170.

75. Chang, Y.-Y.; Huang, H.-L.; Chen, Y.-C.; Weng, J.-C.; Lai, C.-H., Characterization and Antibacterial Performance of Zrno–Ag Coatings. *Surface and Coatings Technology* **2013,** *231* (0), 224-228.

76. Rtimi, S.; Baghriche, O.; Sanjines, R.; Pulgarin, C.; Bensimon, M.; Kiwi, J., Tion and Tion-Ag Sputtered Surfaces Leading to Bacterial Inactivation under Indoor Actinic Light. *Journal of Photochemistry and Photobiology A: Chemistry* **2013,** *256* (0), 52-63.

77. Hsieh, J. H.; Chang, C. C.; Chang, Y. K.; Cherng, J. S., Photocatalytic and Antibacterial Properties of Taon–Ag Nanocomposite Thin Films. *Thin Solid Films* **2010,** *518* (24), 7263-7266.

78. Hsieh, J. H.; Chang, C. C.; Li, C.; Liu, S. J.; Chang, Y. K., Effects of Ag Contents on Antibacterial Behaviors of Taon–Ag Nanocomposite Thin Films. *Surface and Coatings Technology* **2010,** *205, Supplement 1* (0), S337-S340.

79. Barshilia, H. C.; Kumar, P.; Rajam, K. S.; Biswas, A., Structure and Optical Properties of Ag–Al2o3 Nanocermet Solar Selective Coatings Prepared Using Unbalanced Magnetron Sputtering. *Solar Energy Materials and Solar Cells* **2011,** *95* (7), 1707-1715.

80. Tu, C. J.; Gao, J. H.; Hui, S.; Lou, D.; Zhang, H. L.; Liang, L. Y.; Jin, A. P.; Zou, Y. S.; Cao, H. T., Alloyed Nanoparticle-Embedded Alumina Nanocermet Film: A New Attempt to Improve the Thermotolerance. *Applied Surface Science* **2015,** *331* (0), 285-291.

81. Bian, H. Q.; Ma, S. Y.; Li, F. M.; Zhu, H. B., Influence of Zno Buffer Layer on Microstructure and Raman Scattering of Zno:Ag Film on Si Substrate. *Superlattices and Microstructures* **2013,** *58* (0), 171-177.

82. Duan, L.; Gao, W.; Chen, R.; Fu, Z., Influence of Post-Annealing Conditions on Properties of Zno:Ag Films. *Solid State Communications* **2008,** *145* (9–10), 479-481.

83. Duan, L.; Yu, X.; Ni, L.; Wang, Z., Zno:Ag Film Growth on Si Substrate with Zno Buffer Layer by Rf Sputtering. *Applied Surface Science* **2011,** *257* (8), 3463-3467.

84. Jeong, S. H.; Yoo, D. G.; Kim, D. Y.; Lee, N. E.; Boo, J. H., Physical Properties and Etching Characteristics of Metal (Al, Ag, Li) Doped Zno Films Grown by Rf Magnetron Sputtering. *Thin Solid Films* **2008,** *516* (19), 6598-6603.

85. Liang, Y.-C.; Deng, X.-S., Structure Dependent Luminescence Evolution of C-Axis-Oriented Zno Nanofilms Embedded with Silver Nanoparticles and Clusters Prepared by Sputtering. *Journal of alloys and compounds* **2013,** *569* (0), 144-149.

86. Hu, J. J.; Muratore, C.; Voevodin, A. A., Silver Diffusion and High-Temperature Lubrication Mechanisms of Ysz–Ag–Mo Based Nanocomposite Coatings. *Composites Science and Technology* **2007,** *67* (3–4), 336-347.

87. Muratore, C.; Voevodin, A. A.; Hu, J. J.; Zabinski, J. S., Tribology of Adaptive Nanocomposite Yttria-Stabilized Zirconia Coatings Containing Silver and Molybdenum from 25 to 700 °C. *Wear* **2006,** *261* (7–8), 797-805.

88. Huang, H.-L.; Chang, Y.-Y.; Weng, J.-C.; Chen, Y.-C.; Lai, C.-H.; Shieh, T.-M., Anti-Bacterial Performance of Zirconia Coatings on Titanium Implants. *Thin Solid Films* **2013,** *528* (0), 151-156.

89. Zhou, P.; You, H.-Y.; Jia, J.-H.; Li, J.; Han, T.; Wang, S.-Y.; Zhang, R.-J.; Zheng, Y.-X.; Chen, L.-Y., Concentration and Size Dependence of Optical Properties of Ag:Bi2o3 Composite Films by Using the Co-Sputtering Method. *Thin Solid Films* **2004,** *455–456* (0), 605-608.

90. Ashok Kumar Reddy, Y.; Sivasankar Reddy, A.; Sreedhara Reddy, P., Effect of Oxygen Partial Pressure on the Properties of Nio–Ag Composite Films Grown by Dc Reactive Magnetron Sputtering. *Journal of alloys and compounds* **2014,** *583* (0), 396-403.

91. Balagna, C.; Perero, S.; Ferraris, S.; Miola, M.; Fucale, G.; Manfredotti, C.; Battiato, A.; Santella, D.; Vernè, E.; Vittone, E.; Ferraris, M., Antibacterial Coating on Polymer for Space Application. *Materials Chemistry and Physics* **2012,** *135* (2–3), 714-722.

92. Ferraris, M.; Balagna, C.; Perero, S.; Miola, M.; Ferraris, S.; Baino, F.; Battiato, A.; Manfredotti, C.; Vittone, E.; Vernè, E., Silver Nanocluster/Silica Composite Coatings Obtained by Sputtering for Antibacterial Applications. *IOP Conference Series: Materials Science and Engineering* **2012,** *40* (1), 012037.

93. Ferraris, M.; Perero, S.; Miola, M.; Ferraris, S.; Gautier, G.; Maina, G.; Fucale, G.; Verne, E., Chemical, Mechanical, and Antibacterial Properties of Silver Nanocluster–Silica Composite Coatings Obtained by Sputtering. *Advanced Engineering Materials* **2010,** *12* (7), B276-B282.

94. Ferraris, S.; Perero, S.; Miola, M.; Vernè, E.; Rosiello, A.; Ferrazzo, V.; Valletta, G.; Sanchez, J.; Ohrlander, M.; Tjörnhammar, S.; Fokine, M.; Laurell, F.; Blomberg, E.; Skoglund, S.; Odnevall Wallinder, I.; Ferraris, M., Chemical, Mechanical and Antibacterial Properties of Silver Nanocluster/Silica Composite Coated Textiles for Safety Systems and Aerospace Applications. *Applied Surface Science* **2014,** *317* (0), 131-139.

95. Nikolaeva, M.; Sendova-Vassileva, M.; Malinovska, D.; Sarov, Y.; Pivin, J. C., Ion Beam Assisted Formation of Ag Nanoparticles in Sio2 and Their Optical Properties. *Nuclear Instruments and Methods in Physics Research Section B: Beam Interactions with Materials and Atoms* **2002,** *193* (1–4), 867-870.

96. Singh, F.; Gautam, S. K.; Kulriya, P. K.; Pivin, J. C., In Situ X-Ray Diffraction Study of the Growth of Silver Nanoparticles Embedded in Silica Film by Ion Irradiation: The Effect of Volume Fraction. *Nuclear Instruments and Methods in Physics Research Section B: Beam Interactions with Materials and Atoms* **2013,** *311* (0), 5-9.

97. Adochite, R. C.; Munteanu, D.; Torrell, M.; Cunha, L.; Alves, E.; Barradas, N. P.; Cavaleiro, A.; Riviere, J. P.; Le Bourhis, E.; Eyidi, D.; Vaz, F., The Influence of Annealing Treatments on the Properties of Ag:Tio2 Nanocomposite Films Prepared by Magnetron Sputtering. *Applied Surface Science* **2012,** *258* (8), 4028-4034.

98. Hrkac, T.; Röhl, C.; Podschun, R.; Zaporojtchenko, V.; Strunskus, T.; Papavlassopoulos, H.; Garbe-Schönberg, D.; Faupel, F., Huge Increase of Therapeutic Window at a Bioactive Silver/Titania Nanocomposite Coating Surface Compared to Solution. *Materials Science and Engineering: C* **2013,** *33* (4), 2367-2375.

99. Jamuna-Thevi, K.; Bakar, S. A.; Ibrahim, S.; Shahab, N.; Toff, M. R. M., Quantification of Silver Ion Release, In vitro Cytotoxicity and Antibacterial Properties of Nanostuctured Ag Doped Tio2 Coatings on Stainless Steel Deposited by Rf Magnetron Sputtering. *Vacuum* **2011,** *86* (3), 235-241.

100. Navabpour, P.; Ostovarpour, S.; Hampshire, J.; Kelly, P.; Verran, J.; Cooke, K., The Effect of Process Parameters on the Structure, Photocatalytic and Self-Cleaning Properties of Tio2 and Ag-Tio2 Coatings Deposited Using Reactive Magnetron Sputtering. *Thin Solid Films* **2014,** *571, Part 1* (0), 75-83.

101. Song, D.-H.; Uhm, S.-H.; Kim, S.-E.; Kwon, J.-S.; Han, J.-G.; Kim, K.-N., Synthesis of Titanium Oxide Thin Films Containing Antibacterial Silver Nanoparticles by a Reactive Magnetron Co-Sputtering System for Application in Biomedical Implants. *Materials Research Bulletin* **2012,** *47* (10), 2994-2998.

102. Song, D.-H.; Uhm, S.-H.; Lee, S.-B.; Han, J.-G.; Kim, K.-N., Antimicrobial Silver-Containing Titanium Oxide Nanocomposite Coatings by a Reactive Magnetron Sputtering. *Thin Solid Films* **2011,** *519* (20), 7079-7085.

103. Xiong, J.; Ghori, M. Z.; Henkel, B.; Strunskus, T.; Schürmann, U.; Kienle, L.; Faupel, F., Controlling Surface Segregation of Reactively Sputtered Ag/Tiox Nanocomposites. *Acta Materialia* **2014,** *74* (0), 1-8.

104. Huang, C.-M.; Cheng, K.-W.; Jhan, Y.-R.; Chung, T.-W., Preparation of Visible-Light-Active Ag and in-Doped Zns Thin Film Photoelectrodes by Reactive Magnetron Co-Sputtering. *Thin Solid Films* **2007,** *515* (20–21), 7935-7944.

105. Song, X.; Shi, S.; Cao, C.; Chen, X.; Cui, J.; He, G.; Sun, Z., Effect of Ag-Doping on Microstructural, Optical and Electrical Properties of Sputtering-Derived Zns Films. *Journal of alloys and compounds* **2013,** *551* (0), 430-434.

106. Wang, Q.; Tu, J. P.; Zhang, S. C.; Lai, D. M.; Peng, S. M.; Gu, B., Effect of Ag Content on Microstructure and Tribological Performance of Ws2–Ag Composite Films. *Surface and Coatings Technology* **2006,** *201* (3–4), 1666-1670.

107. Xu, S.; Gao, X.; Hu, M.; Sun, J.; Wang, D.; Zhou, F.; Weng, L.; Liu, W., Morphology Evolution of Ag Alloyed Ws2 Films and the Significantly Enhanced Mechanical and Tribological Properties. *Surface and Coatings Technology* **2014,** *238* (0), 197-206.

108. Zheng, X. H.; Tu, J. P.; Lai, D. M.; Peng, S. M.; Gu, B.; Hu, S. B., Microstructure and Tribological Behavior of Ws2–Ag Composite Films Deposited by Rf Magnetron Sputtering. *Thin Solid Films* **2008,** *516* (16), 5404-5408.

109. Shtansky, D. V.; Batenina, I. V.; Kiryukhantsev-Korneev, P. V.; Sheveyko, A. N.; Kuptsov, K. A.; Zhitnyak, I. Y.; Anisimova, N. Y.; Gloushankova, N. A., Ag- and Cu-Doped Multifunctional Bioactive Nanostructured Ticapcon Films. *Applied Surface Science* **2013,** *285, Part B* (0), 331-343.

110. Krzanowski, J. E., Phase Formation and Phase Separation in Multiphase Thin Film Hard Coatings. *Surface and Coatings Technology* **2004,** *188–189* (0), 376-383.

111. Calderon V, S.; Galindo, R. E.; Oliveira, J. C.; Cavaleiro, A.; Carvalho, S., Ag+ Release and Corrosion Behavior of Zirconium Carbonitride Coatings with Silver Nanoparticles for Biomedical Devices. *Surface and Coatings Technology* **2013,** *222* (0), 104-111.

112. Garcia-Zarco, O.; Rodil, S. E.; Camacho-López, M. A., Deposition of Amorphous Carbon–Silver Composites. *Thin Solid Films* **2009,** *518* (5), 1493-1497.

113. Machado, D.; Pedrosa, P.; Fonseca, C.; Martin, N.; Vaz, F., Structural and Morphological Changes in Ag: Tin Nanocomposite Films Promoted by in-Vacuum Annealing. *Journal of Nano Research* **2013,** *25*, 67-76.

114. Calderon V, S.; Sánchez-López, J. C.; Cavaleiro, A.; Carvalho, S., Biotribological Behavior of Ag–Zrcxn1−X Coatings against Uhmwpe for Joint Prostheses Devices. *Journal of the Mechanical Behavior of Biomedical Materials* **2015,** *41* (0), 83-91.

115. Chakravadhanula, V. S. K.; Mishra, Y. K.; Kotnur, V. G.; Avasthi, D. K.; Strunskus, T.; Zaporotchenko, V.; Fink, D.; Kienle, L.; Faupel, F., Microstructural and Plasmonic Modifications in Ag–Tio2 and Au–Tio2 Nanocomposites through Ion Beam Irradiation. *Beilstein Journal of Nanotechnology* **2014,** *5*, 1419-1431.

116. Marques, S. M.; Manninen, N. K.; Ferdov, S.; Lanceros-Mendez, S.; Carvalho, S., Ti1−Xagx Electrodes Deposited on Polymer Based Sensors. *Applied Surface Science* **2014,** *317* (0), 490-495.

117. Lei Jiang, L. F., *Bioinspired Intelligent Nanostructured Interfacial Materials*. World scientific publishing: Singapore, **2010**; p 339.

118. Akhavan, O.; Ghaderi, E., Capping Antibacterial Ag Nanorods Aligned on Ti Interlayer by Mesoporous Tio2 Layer. *Surface and Coatings Technology* **2009,** *203* (20-21), 3123-3128.

119. Dobias, J.; Bernier-Latmani, R., Silver Release from Silver Nanoparticles in Natural Waters. *Environmental Science & Technology* **2013,** *47* (9), 4140-4146.

120. Jung, W. K.; Koo, H. C.; Kim, K. W.; Shin, S.; Kim, S. H.; Park, Y. H., Antibacterial Activity and Mechanism of Action of the Silver Ion in Staphylococcus Aureus and Escherichia Coli. *Applied and environmental microbiology* **2008,** *74* (7), 2171-2178.

121. Sondi, I.; Salopek-Sondi, B., Silver Nanoparticles as Antimicrobial Agent: A Case Study on E. Coli as A model for Gram-Negative Bacteria. *Journal of Colloid and Interface Science* **2004,** *275* (1), 177-182.

PRODUCTION AND CHARACTERIZATION OF ZrCN-Ag COATINGS DEPOSITED BY MAGNETRON SPUTTERING

CHAPTER III – Sample Preparation and Characterization Techniques

The following chapter is partially based on the results published in: S. Calderon V, R.E. Galindo, J.C. Oliveira, A. Cavaleiro, S. Carvalho, Ag+ release and corrosion behavior of zirconium carbonitride coatings with silver nanoparticles for biomedical devices, Surface and Coatings Technology, 222 (2013) 104-111.

3 Introduction

All the films in this study were deposited by magnetron sputtering and a wide range of characterization techniques were used, including X-ray photoelectron spectroscopy (XPS), electron probe microanalysis (EPMA), glow discharge optical emission spectroscopy (GD-OES), scanning electron microscopy (SEM), transmission electron microscopy (TEM), Raman spectroscopy, electrochemical impedance spectroscopy (EIS), inductively coupled plasma optical emission spectroscopy (ICP-OES), among other. In this chapter the different methodologies used for the coatings preparation are discussed and a brief description of the methods and techniques used for their characterization is performed.

3.1 Reactive magnetron sputtering

Reactive magnetron sputtering is a widely used physical vapor deposition (PVD) technique to deposit ceramic films of transition metal nitrides and carbonitrides family (MeCN, Me = transition metal), due to its versatility. The high number of deposition parameters possible to be varied allows to produce a large spectrum of coatings, with different chemical composition, structure and properties, without the need of hazardous chemicals and high temperatures.

In magnetron sputtering an electric field is created between two plates (electrodes) within a vacuum chamber. A non-reactive gas (usually Ar) is introduced in the chamber, which ionizes positively due to the electric field and bombards the negative pole of the electric field, the cathode of the discharge. The collision of Ar^+ ions with the material located in the cathode, known as target, ejects atoms/molecules from the surface towards the substrates. This system is schematically shown in Figure 3-1.

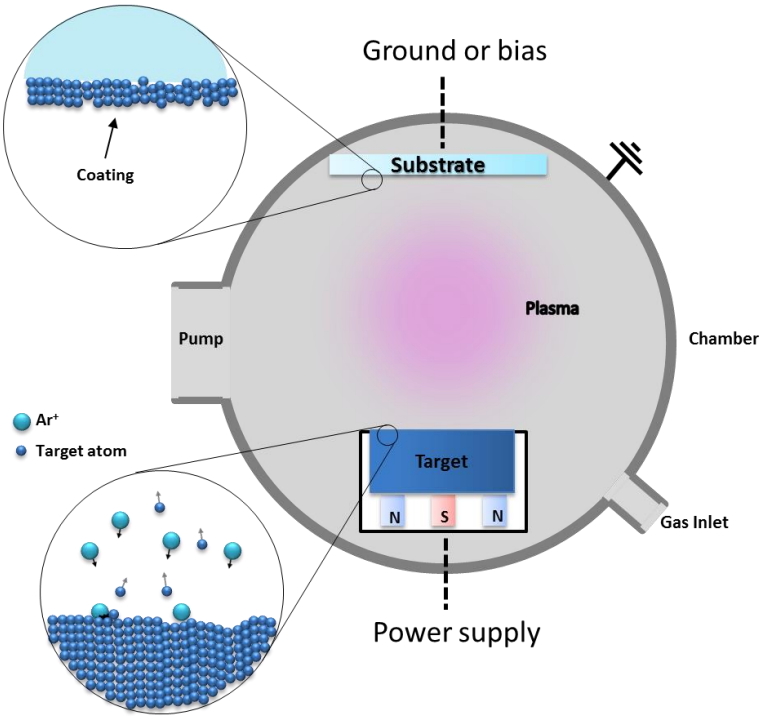

Figure 3-1 Magnetron sputtering system scheme.

The ionization and collision rate of argon in diode sputtering systems is generally low, resulting in very slow deposition rates and poor film densities. Thus, a variation to the sputtering technique was introduced in the 1930s, in order to increase the ionization rate in the vicinity of the target and increase the deposition rate of the films. This modification consists on a magnet set placed beneath the target, composing the magnetron, providing a magnetic field to trap the secondary electrons emitted by the target in the discharge, producing an augment in the ionization of the argon and, consequently, of the bombardment.

Magnetron sputtering can be of unbalanced and balanced type, which referred to the magnitude of the magnetic field between the poles of the magnets that conform the magnetron. Balanced magnetrons possess the same strength in the magnetic field between the south and north poles of the magnets, making that the field lines close between these poles, while the unbalanced magnetron has a strengthen magnetic field in the poles located in the exterior of the magnetron to allow the magnetic field lines to be directed towards the substrate. These two types of magnetron are schematized in Figure 3-2.

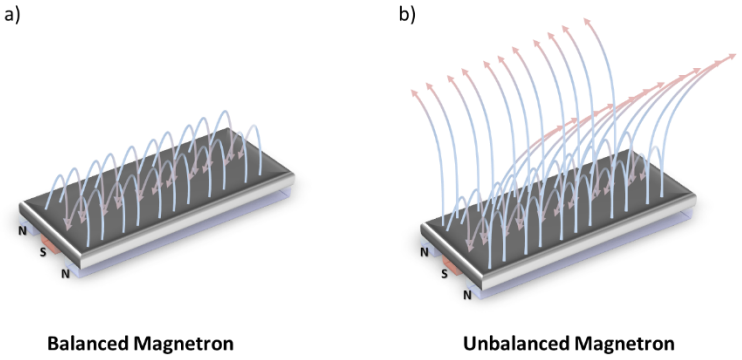

Figure 3-2 Type of magnetrons a) balanced magnetron and b) unbalanced magnetron.

In addition to the magnetic field balancing, the film deposition can be modified by altering several parameters in the production process such as the number of magnetrons, the type of power supply, the distance between the magnetron and the substrate, the pressure in the chamber (known as discharge pressure), the temperature of the chamber/substrate, among other, making this technique very versatile. Moreover, the addition of reactive gases, in order to form different compounds, is another variation of the technique, which creates countless possibilities to modify the chemical, structural and morphological properties of the films.

The electric field to establish the discharge may be applied by different types of power supplies such as radio frequency, direct current, pulsed or microwave, depending on the target conductivity, due to either the insulating properties of the material itself or its tendency to react with the injected gas, in a reactive processes, known as poisoning.

The temperature in this process plays the role of providing kinetic energy to the species being deposited, adding mobility to the adatoms at the surface with the consequent modification of the morphology and structure of the films.

Finally, an additional bias potential can be applied to the substrate to make Ar^+ ions to collide to the substrate surface and produce significant changes in the morphology, structure and composition of the films, by adding energy to the species deposited or re-sputtering some species form the growing film.

3.2 Samples deposition

3.2.1 Magnetron sputtering system

In this project, the coatings were deposited onto 316L stainless steel and Si (100) in a dual magnetron sputtering chamber, using unbalanced magnetrons in a closed field configuration. Each magnetron was connected to a direct current (DC) power supply and provided with a highly pure target of 100 × 200 × 6 mm^3. The magnetrons are located in opposite direction pointing towards an octahedron rotational substrate holder placed at the center of the chamber, 70 mm apart. The chamber is equipped with two shutters located in front of the magnetrons for target and substrate cleaning, avoiding cross contamination. A scheme of the magnetron sputtering system is provided in Figure 3-3.

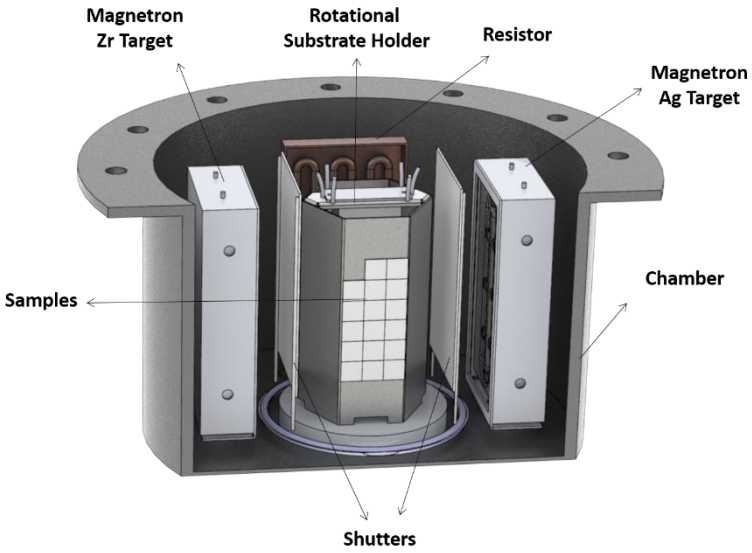

Figure 3-3 Dual magnetron sputtering system.

The films were prepared in an Ar + C_2H_2 + N_2 atmosphere, at base pressure of the order of 10^{-4} Pa and working pressure of 10^{-1} Pa. These gases are inserted through a pipe surrounding the perimeter of the cylindrical chamber to ensure environment homogeneity. The composition of the films can be varied by modified the amount of gases introduced to the chamber, as well as the current density applied to the targets.

As it was already mentioned the bias voltage, substrate rotation speed and chamber temperature may also influence the characteristics of the films. However, they were maintained constant during the project having been selected based on the group experience on similar systems such as ZrCN, TiCN and TiCN-Ag.

Two set of targets were evaluated. Firstly, a pure Zr target and a modified Zr target with silver pellets on the erosion zone (Zr-Ag) were used to control the composition of the films. The final amount of silver in the films was controlled by modifying either the density current of the Zr-Ag target or the number of Ag pellets on its surface. For the second configuration, a pure Zr and a pure Ag target were used, being the control of the silver content achieved by simply modifying the current density (or power) applied to them. Preliminary studies, shown in this chapter to study the samples homogeneity, were performed with the first targets configuration, whereas the latter set up was selected to study more in detail the films. In this case, the silver control is facilitated, reducing the compositional changes in the films originated in target modifications, such as silver poisoning of the Zr areas of the target and/or losing of pellets during the deposition. Nonetheless, the same variety of phases, structures and morphologies are identified in any of those target arrangements[1].

3.2.2 Samples homogeneity

In order to ensure the reproducibility of the samples some preliminary tests were carried out to study the effect of the samples position on the substrate holder. The substrate holder possesses six faces identified with letters from A to F, each of these phases was subdivided in 3 zones, 1,2 and 3, as shown in Figure 3-4. The samples were disposed using a matrix-like configuration, in a three columns / six rows arrangement in each face. Then, the deposition rate and the chemical composition of the coating was evaluated for the different positions and faces.

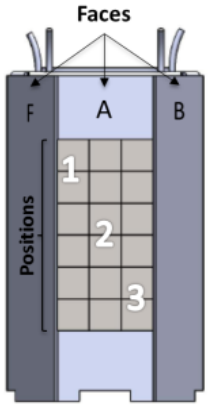

Figure 3-4 Substrate holder.

Figure 3-5 shows the deposition rate values calculated for samples placed in different zones and faces of the substrate holder. The location of the samples in different faces, always positioned in the same zone of the face (A2 to F2), does not influence the deposition rate, with

all values inside the statistical error bar. This would be expected since the rotation of the substrate holder allows a homogeneous growth, independently of the rotation speed. On the other hand, in the same face, small differences are observed, with slightly higher deposition rate values in the middle in relation to the border zones. These small differences are not critical for most of the characterization performed in the aim of this work, since coatings with more than 1 μm are usually utilized.

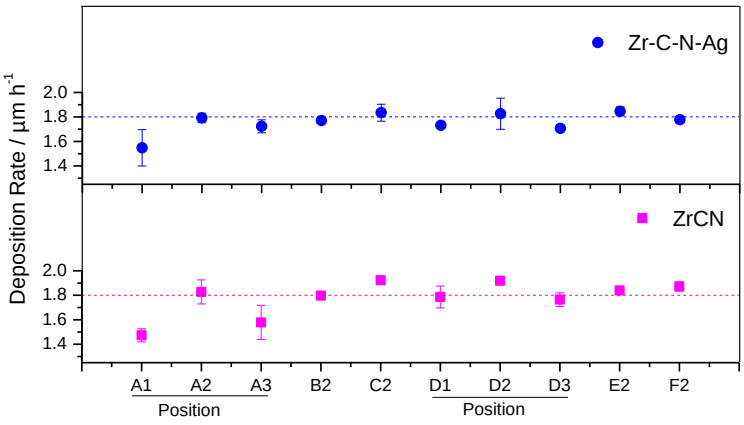

Figure 3-5 Deposition rates as a function of the substrate position in the substrate holder.

GD-OES compositional profiles do not show significant difference between the samples. Figure 3-6 depicts the GD-OES profile for a ZrCN-Ag coating in two different positions within the substrate holder, revealing homogeneous composition in-depth profile. Comparing the Zr signal in different faces and same position, for instance, an increase of less than 4 at. % is noticed. On the same basis, comparing different position within the same face, from a position near to the bottom of the substrate holder moving toward the center, the Zr variation was not significant (Figure 3-6b). Moreover, silver shows a constant distribution throughout the film. These results demonstrate a homogenous environment within the chamber.

Based on these results of composition and deposition rate, the samples were maintained in the matrix-like configuration; nonetheless, in order to reduce the possible influence of the positions of the substrates, for further depositions, the top and bottom row were remove, leaving a matrix of 3 x 4 samples.

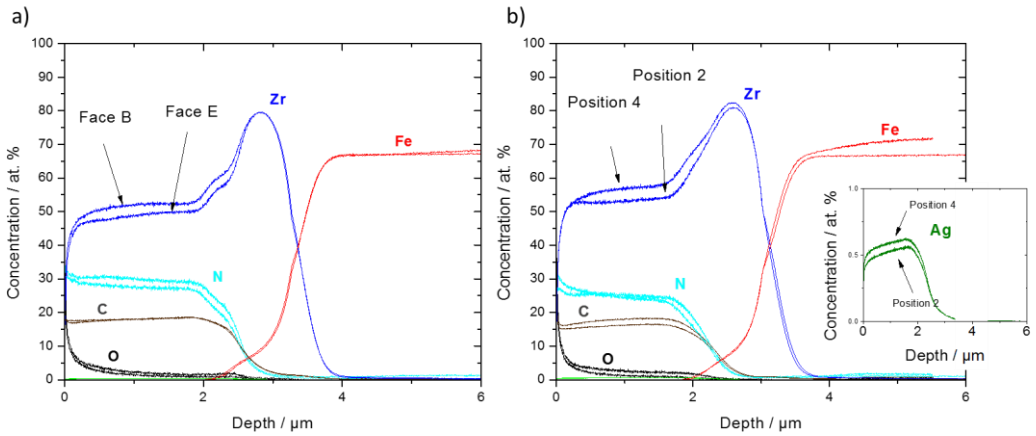

Figure 3-6 GD-OES profiles comparison between a) faces and b) positions within the substrate holder.

3.2.3 Substrate preparation

Stainless steel substrates grade 316L with the composition of Fe 68.40 wt% , Cr 16.40 wt%, Ni 11.1 wt%, Mo 2.28 wt%, Mn 1.3 wt%, Si 0.39 wt%, P = 0.06 wt%, and C < 0.03 wt%, were used as example of a widely used material for surgical and prosthetic devices. Two surface finishing grades were used, a type 2B, which correspond to a mill finish, produced during the steel production process, and cold-rolling with a final light rolling pass with surface roughness of 60 nm; and a finely polished surface with surface roughness close to 8 nm. The latter was attained by grinding using emery paper from 240 to 2400 grit, and then, mirror polished with a diamond solution. Additionally, wafers of single crystal Si (100) (p-type/B, 1-100 Ohm cm) cut in 1 x 1 cm^2 were utilized for structural and morphological characterization.

Before deposition, all the substrates were cleaned using ultrasonic baths in distilled water, ethanol and acetone, each during 10 min, in order to remove dust and impurities. Additionally, the substrates were in-situ cleaned by Ar^+ etching, using a pulsed-DC power supply, operated at 0.48 A and 180 sccm of Ar, attaining 1 Pa of working pressure.

3.3 Design of experiments

Due to the large number of variable and responses that may affect the production process of the coatings, the Zr-C-N-Ag films were deposited following a design of experiments, known as response surface methodology. This procedure allows to select a set of samples that can be fully characterized in terms of chemical, structural, morphological, mechanical, tribological and electrochemical properties, giving indications about the influence of the processing variables.

3.3.1 Response surface methodology

Response surface methodology (RSM) is a mathematical technique used to evaluate the statistical influence of processing parameters on selected properties [2-4]. Three processing parameters are selected in such a way that three levels are determined for each variable. These levels are identified as -1, 0 and 1 and correspond to the lower, intermediate and higher values of such variable, respectively. These are added to a 2^3 central composite design accordingly to the Table 3-1.

Table 3-1 Central composite design

	VARIABLE 1	VARIABLE 2	VARIABLE 3
SAMPLE 1	-1	-1	-1
SAMPLE 2	-1	1	-1
SAMPLE 3	-1	0	0
SAMPLE 4	-1	-1	1
SAMPLE 5	-1	1	1
SAMPLE 6	0	0	-1
SAMPLE 7	0	-1	0
SAMPLE 8	0	0	0
SAMPLE 9	0	0	0
SAMPLE 10	0	0	0
SAMPLE 11	0	1	0
SAMPLE 12	0	0	1
SAMPLE 13	1	-1	-1
SAMPLE 14	1	1	-1
SAMPLE 15	1	0	0
SAMPLE 16	1	-1	1
SAMPLE 17	1	1	1

This procedure allows obtaining an empirical model in which an equation derived from the data defines the relationship between the properties and the deposition parameters. The statistical significance of the regression coefficients is determined by the Student's t test at 5 % probability level (p<0.05). The proportion of variance explained by the models is given by the multiple coefficient of determination, R^2.

A complete quadratic model is used to fit the results of the responses and the models are simplified by eliminating the terms without statistical significance. Statistical analysis of the data, as well as the determination of the conditions able to maximize the films performance were carried out using the software Statistica (version 8.0), and Design expert (version 7.0).

In this work, RSM was used to correlate the production parameters gas fluxes and current density of Ag target (independent variables), with the composition and three functional properties of the films, dependent variables or responses, shown in Table 3-2.

Table 3-2 Variable and responses for the surface response methodology.

VARIABLES	VALUES			RESPONSES							
	-1	0	1	Zr	N	C	Ag	O	Hardness	Corrosion resistance	Adhesion
				At %					GPa	MΩ	N
Ag density current [mA cm^{-2}]	0.25	0.5	0.75								
C2H2 flux [sccm]	1.2	2.4	3.6								
N2 Flux [sccm]	3	6	9								

3.4 Sample characterization

Most of the structural, chemical and morphological characterization technique used in this project may be explained by the interaction between electrons or X-rays and matter. Below, these types of interaction and the equipment used are described, focusing on the experimental procedure and sample preparation for each technique, instead of on the principle that describe the technique. Moreover, the techniques that does not fit in these interactions are explained independently.

3.4.1 Electron and matter interaction

The interaction between electrons and matter produces a variety of radiation that can be collected to determine the samples structure, chemical composition, morphology, among other (Figure 3-7). When an electron beam interacts with a specific atom, it produce an energy exchange that produce a large variety of phenomena. If the beam collides with a low-energetic electron from an atom can remove it, known as a secondary electron (Figure 3-7b). Such electrons are used to generate images in scanning electron microscopes (SEM) and, due to their low energy, they are emanating from the near surface of the sample, providing information about the morphology of the material. However, if the beam does not interact with the electronic cloud and crosses very close to the nucleus, some incident electrons are backscattered out of the surface (Figure 3-7c), generating images highly dependent on the mass of the atom. In fact, heavier elements, backscatter more efficiently, appearing brighter than lighter elements in a backscattered electron image. When the secondary electrons are produced, electronic transition between the energy levels of the atom can occur, producing characteristic X-rays, typical of each element. The transitions may occurs for different energy levels (K, L, M, etc), and give information about the composition of the material. This phenomenon is supporting the electron

probe microanalysis techniques using either energy dispersive spectroscopy (EDS) or wavelength dispersive spectroscopy (WDS).

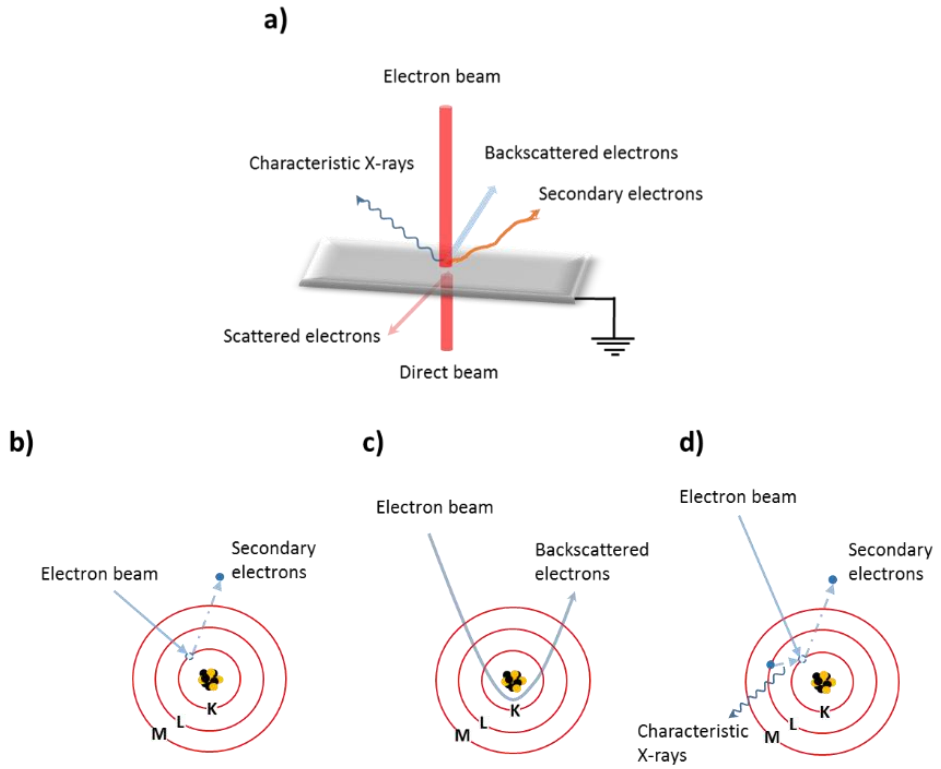

Figure 3-7 Interaction between an electron beam and matter.

On the other hand, when the electron beam is focused in very thin samples (< 500 nm) the electrons can be transmitted, and thus, the information of the material can be collected giving rise to the transmission electron microscopy. In such case, the electrons suffer scattering depending on the interaction between the electron beam and the cloud of electrons or nucleus, resulting in low angle non-uniform distribution of transmitted electrons. The different distribution of scattering gives rise to TEM images (spatial distribution) or diffraction patterns (angular distribution). In the latter, using circular apertures that select only the desired transmitted electrons, information about the atomic structural arrangement can be achieved, technique known as selected area diffraction (SAD).

3.4.2 X-rays and matter interaction

Similarly to electrons, when X-rays interact with matter produce a variety of radiations that may be used to characterize the materials in terms of structure and chemical composition. For X-ray interaction, only two methods were used in this project, X-ray photoelectron spectroscopy (XPS) and X-ray diffraction (XRD). The first one takes advantage of the photoelectric effect, in which

by irradiating a material with electromagnetic radiation, electrons of the material are exited and emitted out of the material, as schematized in Figure 3-8. These electrons are collected and their energy is measured. The kinetic energy of these emitted electrons is characteristic of the element from which the photoelectron originates, while the position and intensity of the peaks in an energy spectrum provide the chemical state of the elements.

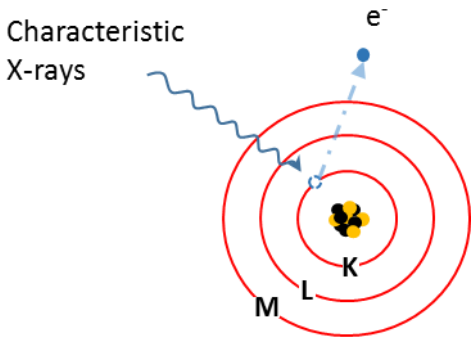

Figure 3-8 Scheme of X-ray photoelectron generation

On the other hand, X-ray diffraction is a coherent scattering effect from atoms in the material. The scattering may undergo constructive and destructive interference in regular structure or crystalline materials, producing a spectrum known as diffraction pattern. The diffraction of X-rays by crystals is described by Bragg's Law and the angles of possible diffractions depend on the size and shape of the unit cell of the material.

3.4.3 Equipment and sample preparation

3.4.3.1 Scanning electron microscopy (SEM) and energy dispersive electron spectroscopy (EDS).

A high resolution NanoSEM - FEI Nova 200 scanning electron microscope, equipped with a secondary electron detector, backscattered electron and energy dispersive spectrometer was used to analyze the surface and cross-section morphologies of the coatings. The surface of the coatings was observed when they were deposited onto both substrates, 316L SS and Si, being the results indifferently presented throughout the document, when no significant differences are noticeable. Cross-section images were acquired mainly on coatings deposited on Si, due to the ease of sample preparation; however, tests were carried out in order to ensure that the morphology of the coatings is only marginally affected by the substrate, as shown in Figure 3-9.

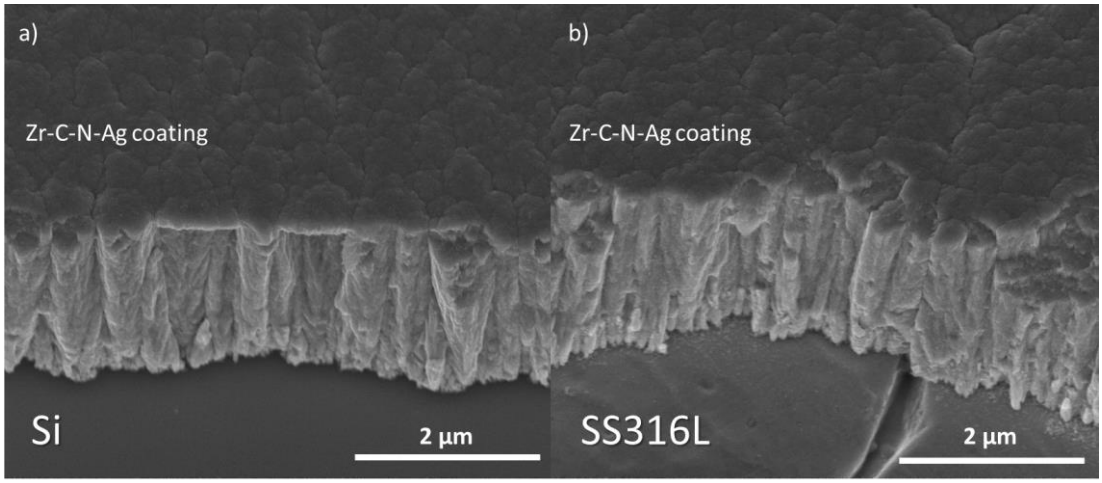

Figure 3-9 Cross-section SEM images of a Zr-C-N-Ag coating on a) silicon and b) stainless steel 316L.

Energy dispersive X-ray spectroscopy was utilized at an acceleration voltage of 10 keV, in both spot and area analyses. This condition ensure that the electron beam did not reach the substrates in any of the studied coatings.

3.4.3.2 Electron probe microanalysis (EPMA)

A Cameca SX 50 electron probe micro-analyzer (EPMA), equipped with wavelength energy spectrometry was used to determine the bulk composition of the coatings. The accelerating voltage of the electron beam was 10 kV and the current 40 nA. A statistical analysis of 5 randomly selected spots in each sample was performed. The experimental error associated with this technique was determined to be less than 1.2 at % in all the elements evaluated.

3.4.3.3 Transmission electron microscopy (TEM) and high resolution TEM (HR-TEM)

A JEM 2010F transmission electron microscope, operating at 200 kV, equipped with an EDS system, was used to acquire TEM and high-resolution TEM (HR-TEM) images of the surface in cross-section. The HR images were recorded around Scherzer defocus, i.e. −64 nm. Fast Fourier transformation (FFT) was carried out using a digital micrograph software package (Gatan, USA), when needed, as schematically shown in Figure 3-10. This process helps to determine the crystalline patterns and the interplanar distance of the crystalline phases, having been used to distinguish the Ag and ZrCN crystalline phases. Briefly, a FFT is applied to the HR-TEM image to obtain the digital diffraction pattern (Figure 3-10b); the diffraction pattern is indexed and the desired diffraction spots are selected to carry out an inverse FFT (shown in Figure 3-10c). Finally, the average distance between the line patterns is measured and attributed to a specific interplanar distance of a crystalline phase.

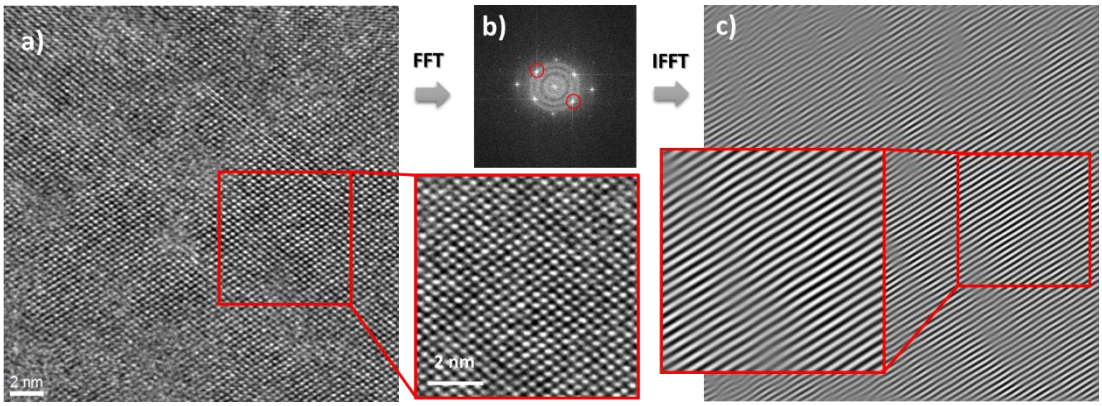

Figure 3-10 FFT on a HR-TEM image for Si wafer used as substrates.

The samples were prepare by the cross-section methodology, schematized in Figure 3-11. Briefly, the samples are cut in two slices of 1 to 2 mm, glued with an epoxy resin (Gatan G2) and cured at 90 ◦C. Thereafter, the stacked samples are placed in a brass tube, filled with the resin and cured at 90 ◦C. The tube is cut into disks using a diamond saw and grinded and polished to a thickness of 90 µm. Finally, the samples are dimpled to a thickness of 10 µm and ion polished to the desired thickness.

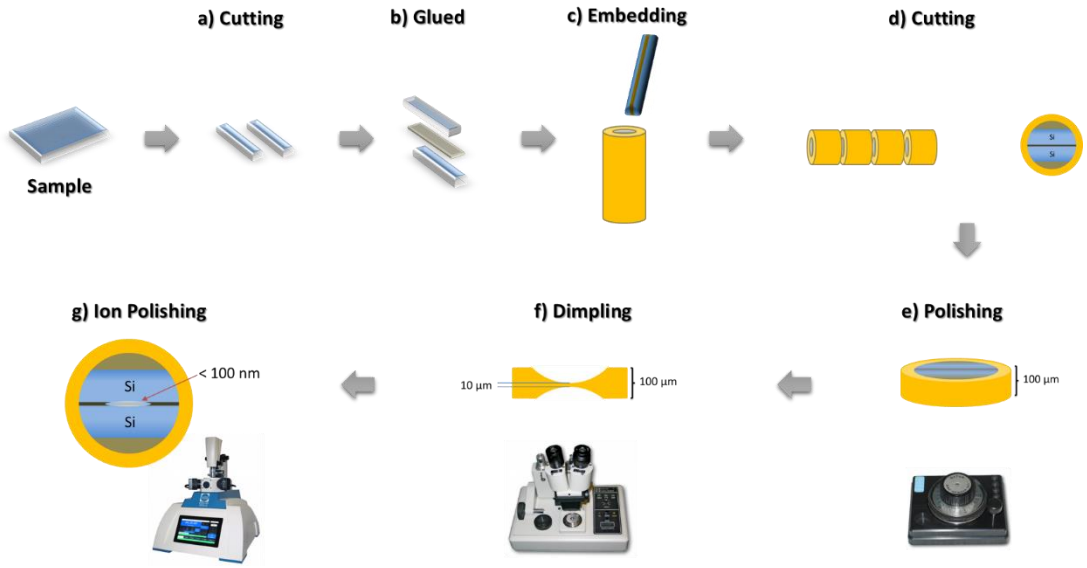

Figure 3-11 Cross-section sample preparation

3.4.3.4 Selected area electron diffraction (SAED)

The diffraction pattern were collected using two aperture sizes in order to identify inhomogeneous crystalline phase distribution. However, for all the samples, the patterns were similar in both apertures. Digital micrograph software package (Gatan, USA) was used to treat the diffraction patterns (by taking the reciprocal cube root), in order to reveal the weak reflections (Figure 3-12b) using the DiffTool package. In addition, the theoretical rings

of $ZrC_{0.5}N_{0.5}$ and Ag crystalline phases were drawn over the patterns in order to identify the phases (Figure 3-12c).

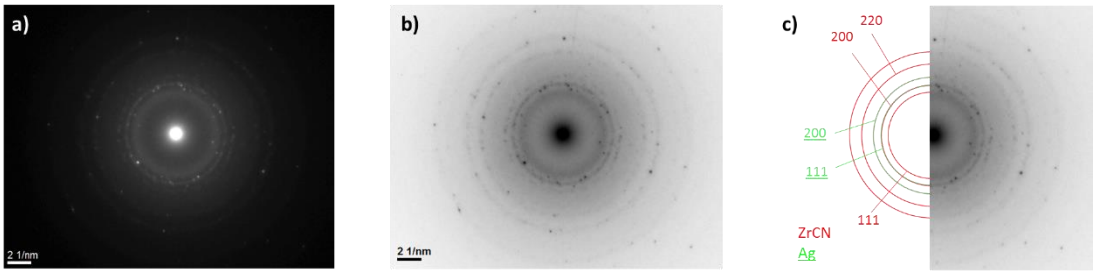

Figure 3-12 a) Diffraction pattern of a Zr-C-N-Ag coating, b) after revealing weak diffraction

3.4.3.5 X-ray photoelectron spectroscopy (XPS)

A Kratos AXIS Ultra HSA X-ray photoelectron spectrometer, with VISION software for data acquisition and CASAXPS software for data analysis. The analyses were carried out with a monochromatic Al Kα X-ray source (1486.7 eV), operating at 15kV (150 W), in FAT mode (Fixed Analyser Transmission), with a pass energy of 40 eV for regions ROI and 80 eV for survey. Data acquisition was performed with a pressure lower than 1 x 10^{-6} Pa, and a charge neutralization system was used. The effect of the electric charge was corrected by reference to the carbon peak (285 eV).

The analyses were performed with and without ion bombardment in order to obtain information about the surface and the bulk of the coating. Ion bombardment was carried out using a Kratos Mini Beam I with an Ar^+ beam energy of 2 keV. The ion beam current density 0.232 A m^{-2}. Those experimental conditions lead to an ion beam with a flat profile ~3 × 3 mm^2.

The deconvolution of the peaks was carried out using CasaXPS program, in which the peak fitting is performed using Gaussian-Lorentzian peak shape and Shirley type background subtraction.

3.4.3.6 X-ray diffraction (XRD)

X-ray diffraction was performed in a PANalytical XPert PRO micro-diffractometer with Cu Kα (1.540598 Å) radiation in a grazing angle mode at 1° incidence angle, using a parallel beam configuration with scan steps of 0.025 ◦ and 3 seconds per step. The deconvolution of the peaks was carried out by Fityk v.0.9.8 using a Voight peak shape. The grain size of the crystalline phases was determine by Sherrer formula, as shown in Equation 3-1

Equation 3-1 $$Grain\ size = \frac{k\lambda}{B\cos\theta}$$

where k is a constant related to the shape factor, which depends on the lattice structure (0.89 for cubic structures), λ is the X-ray wavelength used in the experiment, B is the peak broadening at half maximum intensity in radians and θ is the Bragg angle.

3.4.3.7 Glow discharge optical emission spectroscopy

Glow discharge optical emission spectroscopy uses a plasma discharge generated in an argon atmosphere, which produces the sputtering of the sample. The discharge process may be compared to a sputtering process, where the target of the sputtering process is the sample to be analyzed. In this technique, instead of depositing the sputtering species, a coupled spectrometer collets the light emitted by the species. Characteristic lines (wavelengths) for each element are measured and the intensities (number of photons) are directly proportional to the amount of the elements present in the discharge. The Ar ions remove the material from the sample surface, in a selected area, creating a crater, schematically shown in Figure 3-13d. The profile composition of the samples is achieved as the crater goes deeper. The shape of the crater is important on the resolution of the technique; the deeper the crater, the lower the accuracy of the technique. An ideal crater shape (Figure 3-13a) would give information about the elements at a nanometric layer scale. However, as the crater shape changes from the ideal shape to the experimental one, the signal of the elements is mixed between layers, depending on the convexity of the surface (Figure 3-13b and Figure 3-13c).

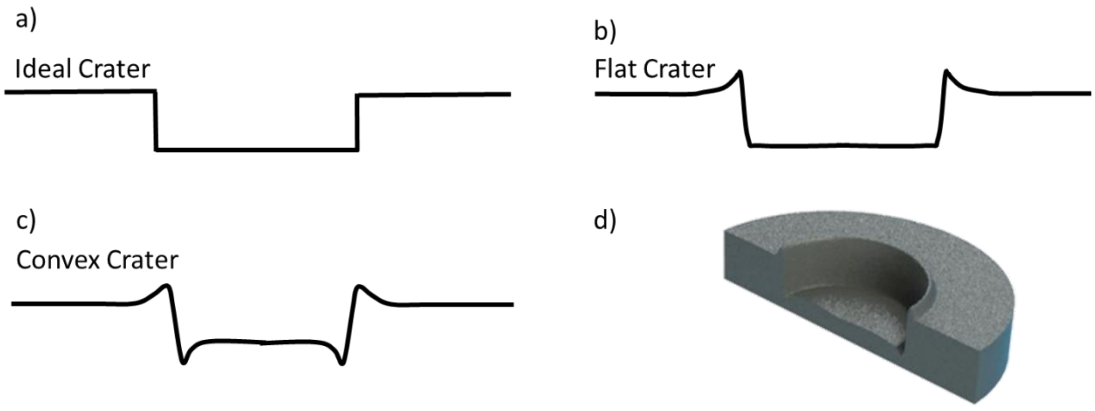

Figure 3-13 Crater after GD-OES analysis

In this work, a glow discharge optical emission spectrometer GD-OES - Jobin Yvon RF GD Profiler was used. The apparatus is equipped with a 4 mm diameter anode and operating at a typical radio frequency discharge pressure of 650 Pa and a power of 40 W. The emission lines detected were oxygen (130 nm), nitrogen (149 nm), carbon (156 nm), silver (328 nm), nickel (341 nm),

chromium (425), zirconium (339 nm) and iron (271 nm). The calibration of light elements, such as N, was carried out as explained in [5]. The calibration of oxygen and carbon were carried out with standard materials. Special care was taken with the carbon quantification in order to take into account the lack of standards with large amount of carbon and large sputtering rates in the GD-OES process, as the ones presented in this work.

3.4.3.8 Raman spectroscopy

Raman spectroscopy is based on the variation of the photons frequency of monochromatic light (laser source), known as inelastic scattering, upon the interaction with the sample. Photons of the light source are absorbed by the sample and then reemitted. Frequency of the reemitted photons is shifted up or down in comparison with original monochromatic frequency (Raman effect). This shift provides information about vibrational, rotational and other low frequency transitions in molecules.

Raman spectra measurements (200–2000 cm^{-1}) were carried out using a LabRAM Horiba Jobin Yvon spectrometer equipped with a CCD (charge-coupled device) detector and a He–Ne laser (532 nm) at 5 mW before and after the tribological testing, to detect alterations on the chemical structure of the films.

3.4.4 Functional characterization

3.4.4.1 Mechanical characterization

3.4.4.1.1 Adhesion

In order to assess the integrity of the coatings, on the stainless steel 316L substrates, scratch testing based on the standard EN-1071-3[1] [5] was performed. This test consists on producing a scratch on the coating surface with a diamond stylus with increasing applied load, as schematically shown in Figure 3-14. The elastic and plastic failure of the films, created due to the indentation stress, frictional stress and the internal residual stress of the coatings, are afterwards observed in the microscope. The normal load at which the failure occurs is known as the critical load. The first cohesive failure observed in the coatings is identify as Lc1, while the load at which the detachment of 50% of the films occurs was considered as Lc2.

[1] Advanced technical ceramics - Methods of test for ceramic coatings - Part 3: Determination of adhesion and other mechanical failure modes by a scratch test.

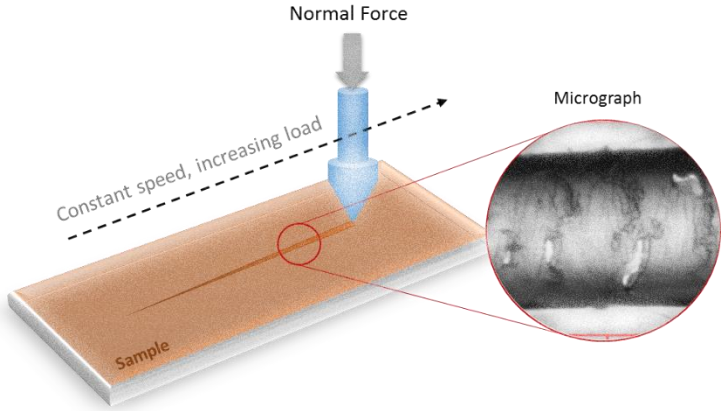

Figure 3-14 Schematic principle of the scratch test

The adhesion of the coatings was accessed by scratch-testing technique using a Revetest CSM Instruments. The load was increased linearly from 0 up to 100 N using a Rockwell C indenter tip with a radius of 200 μm, loading speed of 100 N/min and scratch speed of 10 mm/min. The critical loads (Lc) values corresponding to the different failure mechanisms (adhesive/cohesive) were measured by analyzing the failures events in the scratch track by optical microscopy.

3.4.4.1.2 Nanoindentation - Hardness

The hardness was evaluated by a MicroMaterials Nanotest system, using a nanoindentation technique. Briefly, it consists on performing indentation on the material surface with a diamond indenter, with a known geometry and mechanical properties (Berkovich indenter). The required load is defined and a curve of the penetration depth vs applied load is obtained, as shown in Figure 3-15.

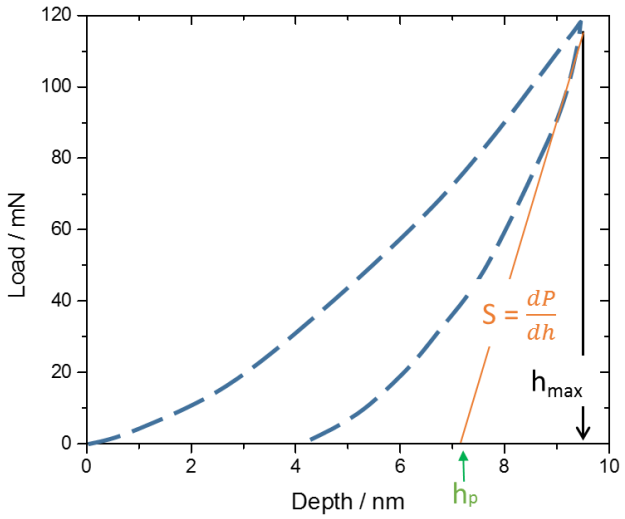

Figure 3-15 Applied load vs penetration depth.

Hardness is calculated using Equation 3-2 [6].

Equation 3-2

$$H = \frac{P_{max}}{A} = \frac{P_{max}}{C h_p^2}$$

where H is the hardness, P_{max} is the maximum load applied A is the residual indentation area, which may be related to the residual depth (h_p) and a C constant, that depends on the indenter geometry.

The tests were carried out at 5 mN, and the indenter was maintained 5 s at maximum load and 30 s at a low load, during unloading, for thermal drift correction. The loading and unloading rates were maintained equal to 0.167 mN s^{-1}. The values reported are an average of 16 measurements.

3.4.4.2 Tribological characterization

To replicate the hip or knee joint prosthesis, it is necessary to simulate the sliding movement of the joints. For this type of experiments a joint simulator is required and a large number of resource consuming experiments is needed. In order to initially assess the ability of the coatings to withstand the mechanical loading, against one of the most used counterparts in orthopedic prosthesis (ultra-high molecular weight polyethylene), a simpler test can be used. Therefore, in this study a linear reciprocating motion was selected based on the standard ASTM F732[7], with some modifications. Such standard describes a laboratory method for evaluating the friction and wear properties for bearing surfaces of human total joint replacement prostheses, which

experience only linear reciprocating motion, such as hinged joints, trunnion bearings, axle bearings, some mobile bearing knee applications.

The reciprocating tests were carried out using 10 mm ultrahigh molecular weight polyethylene (UHMWPE CHIRULEN 1020) balls in 30 ml of Hank´s balanced salt solution (HBSS) with 10 g L^{-1} of albumin from bovine serum (BSA) at 37 °C in a CSM ball-on-disk tribometer (Figure 3-17). The test parameters were set to 10 N of applied load; 20 mm/s of linear speed; 10 mm track length; 80000 cycles of duration at 1 Hz of acquisition rate. Under these conditions, the corresponding initial Hertzian contact pressure was calculated to be 40 MPa.

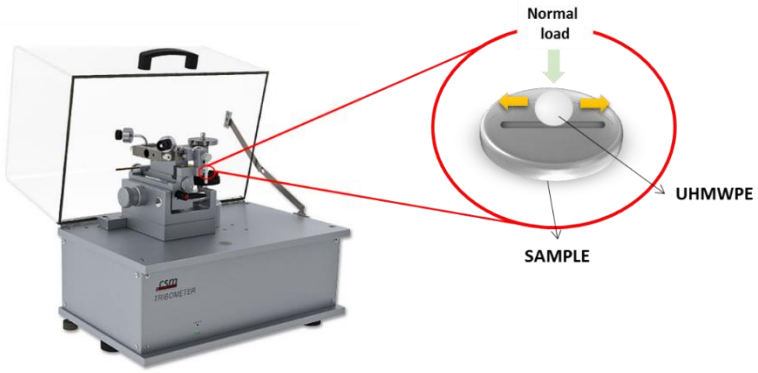

.

Figure 3-16 CSM ball-on-disk tribometer and the schematic reciprocating motion.

The friction coefficient is measured and the specific UHMWPE wear rate was calculated as the volume of the spherical cap corresponding to the worn area measured on the ball (Figure 3-17), divided by the applied load and the total sliding distance. The wear rate is believed to be overestimated since the surface of the UHMWPE is composed of plastically deformed microscopic crests which impede the exact definition of the crater borders. However, the estimation and trends achieved with this procedure is in a very good agreement with the tendency achieved by the measurements of the material weight losses. However, the latter values were not reported since they are of the same order of magnitude of the equipment detection limits (~10^{-4} g).

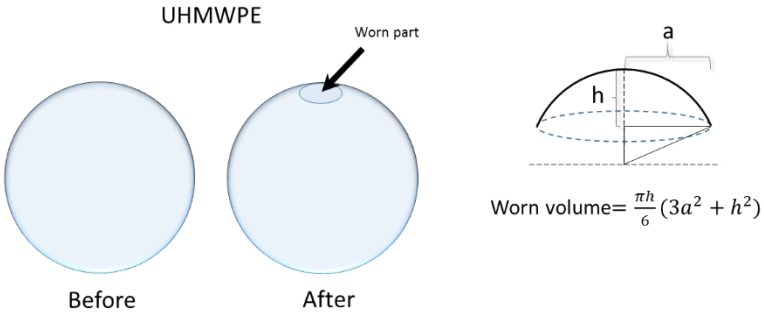

Figure 3-17 scheme of the UHMWPE ball before and after the tribological tests, and the calculus for the worn volume.

3.4.4.3 Electrochemical characterization

Taking into consideration that the coatings are designed to be used in contact with human fluids, more specifically, the synovial fluid, their electrochemical corrosion resistance was evaluated by different electrochemical techniques.

An electrochemical corrosion process may be simplified as a charge and mass transference process in which an anode is oxidized and a cathode is reduced. Then, to measure the corrosion process of the materials in an electrolyte, the charge transfer in an electrochemical cell (electrolyte + sample) must be measured. This can be achieved by using DC and AC techniques, including potentiodynamics curves and electrochemical impedance spectroscopy, after applying a potential. These techniques allow to perform an exhaustive investigation of the corrosion process to obtain the mechanistic/kinetic behavior of the material. Moreover, by fitting the EIS data, a set of parameters can be correlated with the coating morphology and structure as well as with the corrosion of the substrate.

Potentiodynamic tests are known to be destructive due to the very high potential values used, while the EIS small amplitude signals do not significantly disturb the properties being measured. Therefore, a quasi-stable state is allowed to measure the system, as well as measurements are permitted to be taken in unlikely electrolytes. This technique also allows to show details of the corrosion mechanism which are often hidden in DC tests.

3.4.4.3.1 Electrochemical cell

In this project, a custom made electrochemical cell was designed and built. The cell consists of an acrylic container, provided with a water jacket to control the temperature of the experiments (Figure 3-18). The sample is held vertically in order to avoid that the corrosion products could block the development of the corrosion process. The reference electrode (saturated calomel

electrode) and the auxiliary electrode (platinum electrode) are placed on two windows located in the top cover of the cell.

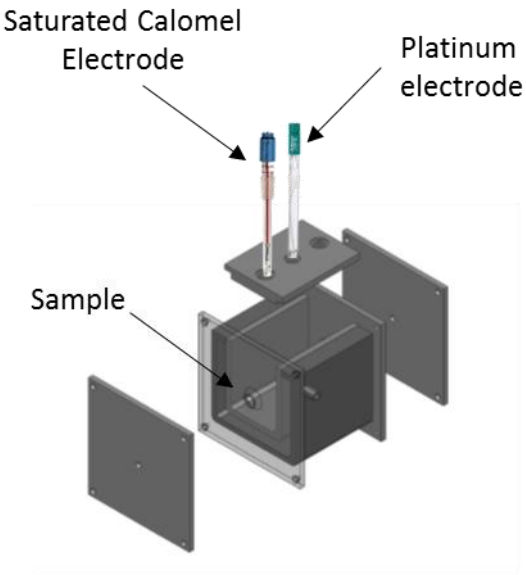

Figure 3-18 electrochemical cell

3.4.4.3.2 Potentiodynamic curves

The potentiodynamic polarization tests allow the system to vary the potential of the cell being the sample used as the cathode or the anode of the electrochemical cell, depending on the applied potential. When a potential is applied below the open circuit potential of the system (sample-electrolyte), cathodic reaction determine the current of the cell, while by increasing the potential above the open circuit value, anodic reactions dominate the cell. Hence, knowing the composition of the electrolyte and the samples, it is possible to determine the type of the reaction occurring in the cell. Figure 3-19 shows a characteristic potentiodynamic curve of stainless steel 316L, which is known to resist corrosion due to the formation of a passive chromium oxide layer on the surface. The formation of such layer can be demonstrated by the passive zone shown in Figure 3-19, which became unstable for high potentials around 600 mV in this electrolyte (Hank's balanced salt solution with 10 g L^{-1} of bovine serum albumin (BSA) at 37 °C); this potential is known as the breakdown potential and corresponds to localized corrosion of the stainless steel, which is one of its main causes of failure, in terms of corrosion. From these curves, and knowing the types of reactions occurring, a corrosion rate may be calculated, which is directly proportional to the density current observed in the curve. However, for such calculation, the exact reaction must be known, but due to the complexity of the

electrolyte and the structure of the films, the curves were used only as qualitative evaluation of the corrosion rate. Thus, three parameters will be taken into consideration for the sample analysis, as follows: (i) an increase on the density current in the curves indicates a larger corrosion rate; (ii) a variation of the breakdown potential provides information about the susceptibility of the system to localized corrosion due to pitting, and (iii) the corrosion potential variation indicates the thermodynamic tendency of the system to corrode.

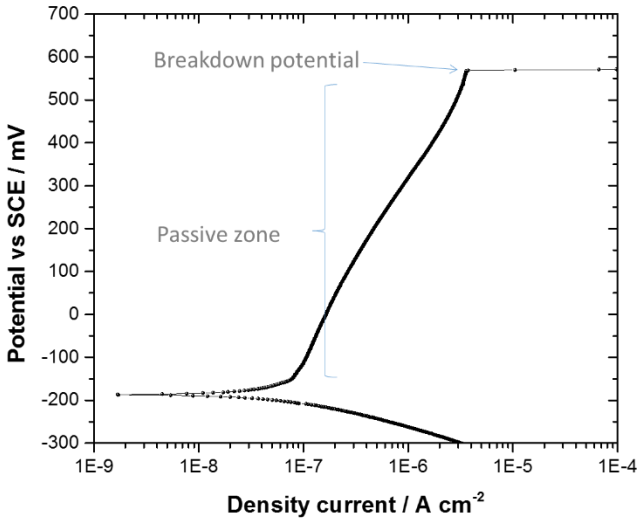

Figure 3-19 Potentiodynamic curve for SS316L in a saline solution

Potentiodynamic tests were performed at two stages: as-deposited and 336h after immersion in HBSS + A. A scanning rate of 60 mV/min from -300 mV vs. OCP to +1000 mV vs. SCE was used.

3.4.4.3.3 Electrochemical impedance spectroscopy

For EIS testing a very small single-sine AC perturbation (10 mV) is applied at the open circuit potential of the electrochemical cell described above, and the response (current) is measured. This perturbation allows to measure the impedance of the system and to model it through an equivalent electric circuit, using mainly resistors and capacitors as components. Such circuit allows to describe the different types of charge transfer mechanisms that occur in the system. In thin protective films a Randles equivalent circuit is commonly used (cf. Figure 3-20a). The capacitance element is replaced by a constant phase element, in order to consider the surface roughness and heterogeneities [8-10], and represents the accumulation of charge on the surface of

the electrode and the capacitance offered by the coatings. Rp, on the other hand, represents the polarization resistance element, which indicates the charge transfer resistance of the material. Nonetheless, when the coatings are particularly electrochemical porous, a second equivalent circuit better represents the system. In this case, the pores of the coatings provide the impedance response in the system, creating a second time constant that corresponds to the capacitance and the resistance of the film and pores, respectively. The second system represents the double layer capacitance and the transfer resistance between the electrolyte and the substrate inside the pore.

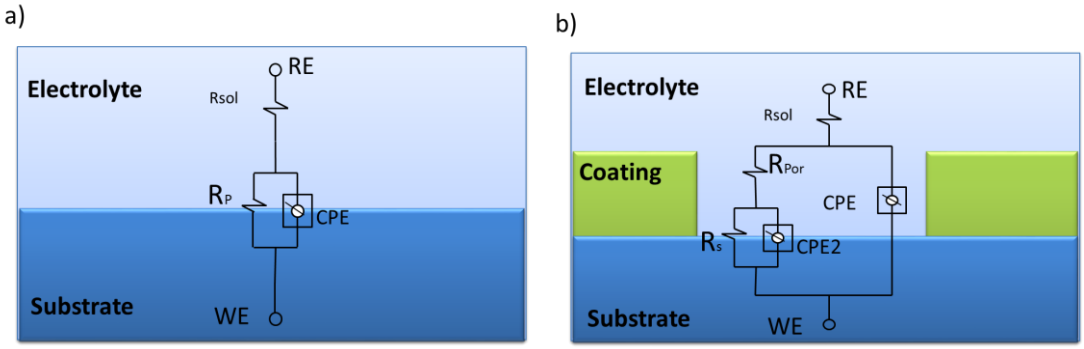

Figure 3-20 Equivalent electrical circuit used for modeling the impedance of the samples

The tests were carried out at open circuit potential, for frequencies ranging from 100 kHz to 5 mHz, with a 10 mV (rms) AC perturbation, using EIS300 software in a Gamry potentiostat REF600.

All electrochemical experiments were performed in the classic three electrodes corrosion cell described above, in Hank's balanced salt solution (0.137 M NaCl, 5.4 mM KCl, 0.25 mM Na_2HPO_4, 0.44 mM KH_2PO_4, 1.3 mM $CaCl_2$, 1.0 mM $MgSO_4$ and 4.2 $NaHCO_3$) with 10 g L^{-1} of bovine serum albumin (BSA) at 37 °C with stabilized pH to 7.0 ± 0.2 in equilibrium with air.

Simulation of the experimental data was also performed with Gamry software. The samples with best corrosion resistance properties were utilized for immersion tests in order to observe the evolution of the electrochemical parameters for 15 days.

The results of the electrochemical tests were calculated as the average and standard deviations of at least three separated samples. All the potentials are expressed with respect to SCE electrode.

3.4.4.4 Contact angle

The surface free energy and the hydrophobicity parameters of surfaces were determined by the sessile drop contact angle technique, by means of an OCA 15 Plus device. In these measurements a low volume drop of a liquid is used, in order to provide a solid/liquid, liquid/gas and solid/gas interfaces. The free energies may be determined by using the Young-Dupre equation (Equation 3-3).

Equation 3-3 $$\gamma_L(1+cos\theta) = 2\left(\sqrt{\gamma_S{}^{LW}\gamma_L{}^{LW}} + \sqrt{\gamma_S{}^{+}\gamma_L{}^{-}} + \sqrt{\gamma_S{}^{-}\gamma_L{}^{+}}\right.$$

where, γ^{LW} is the apolar Lifshitz-van der Waals component of the surface tension of the solid or liquid used, while and the γ- and , γ+ are the polar component, which correspond to the acid-base interaction.

The measurements were performed at room temperature, using 2 μL of water, formamide and α-bromonaphtalene with known surface energy components, as reference liquids. The surface tension parameters were calculated using the Van Oss approach [11].

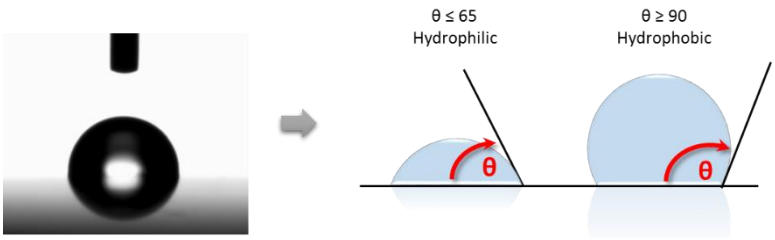

Figure 3-21 Contact angle scheme for hydrophobic and hydrophilic materials

3.4.4.5 Silver ion release

The silver ion release from the samples, when immersed in a saline solution, was evaluated by inductively coupled plasma optical emission spectroscopy (ICP-OES). In this equipment a liquid sample is introduce into a nebulizer, which converts it into very fine droplets of the aerosol and sprayed them into a plasma torch, where an RF Ar plasma excites the sample moving electrons from the ground-state higher energy levels. Some electrons fall to the ground state, emitting wavelength-specific photons that are characteristic of the element of interest. Similarly to the GD-OES, the intensity of the light emitted by each element in the plasma is proportional to the amount of the element present in the sample.

For the experiments, 4 cm^2 samples were immersed into a 50 ml vessel, containing 30 ml of 0.9% NaCl at room temperature. Thereafter, 1.5 ml of the solution was taken out at different

times and reserved at dark for ICP-OES analysis. Before the analysis, the samples are diluted in 4.5 ml of HNO_3.

Tests were carried out in an ICP spectrometer PERKIN ELMER OPTIMA 8000, within a period of 30 days. In order to avoid silver precipitation, the solution was maintained in the dark until ICP evaluation. Two calibration curves were prepared using a silver standard solution for ICP (silver, plasma standard solution, specpure, Ag 1000 µg ml-1). The first calibration curve was prepared in HNO_3 acid, due to the fact that this is the matrix in which the silver standard solution is stabilized. The second calibration curve was prepared in NaCl 0.9 % in order to mimic the experimental conditions used for the samples. Both calibration curves are shown in Figure 3-22, demonstrating linear behavior in the concentration studied.

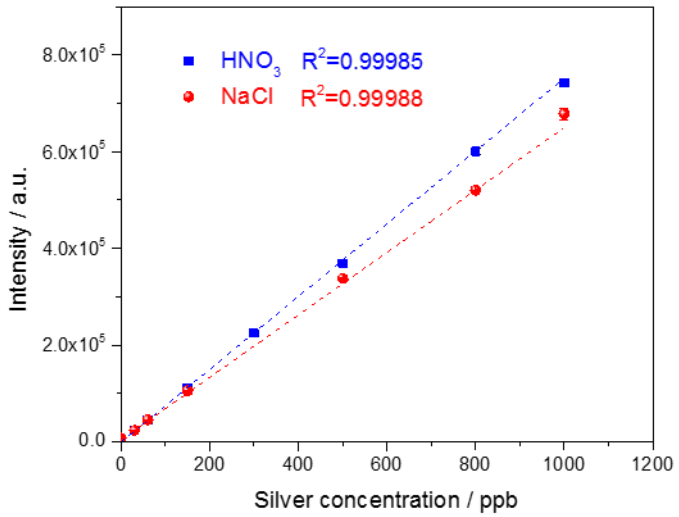

Figure 3-22 ICP calibration curves in nitric acid and sodium chloride.

The presence of Zr ions was also evaluated in the solution after immersion, and both calibration curves were also prepared, however, no presence of Zr was detected in the solution after 336 hours of immersion.

3.4.4.6 Antibacterial test

The antibacterial properties of the coating were assessed by means of the zone of inhibition (ZOI) test [12]. A single colony of *Staphylococcus epidermidis* (*S. epidermidis*, IE186 strain) was inoculated in 20 ml of Tryptic Soy Broth (TSB, Merck) for 18 h, at 37 °C, and 120 rpm. The inoculum bacteria concentration was adjusted to a concentration of *S. epidermidis* $1x10^7$ colony forming units (cfu) m L^{-1} by correcting the optical density (OD) to 1.0 at 640 nm. The cellular

suspension was added to cooled (50 °C) TSB agar (Merck) (TSA) (1:14 ml) and placed into sterile plastic Petri dishes. After medium solidification, samples of ~ 1 cm^2 (previously sterilized in UV light 15 min) were placed on the agar plates and cultured for 24 h, at 37 °C. After the incubation period, images of the Petri dishes were acquire by an Image Lab™ software and the ZOI was measured using ImageJ software, as schematically shown in Figure 3-23.

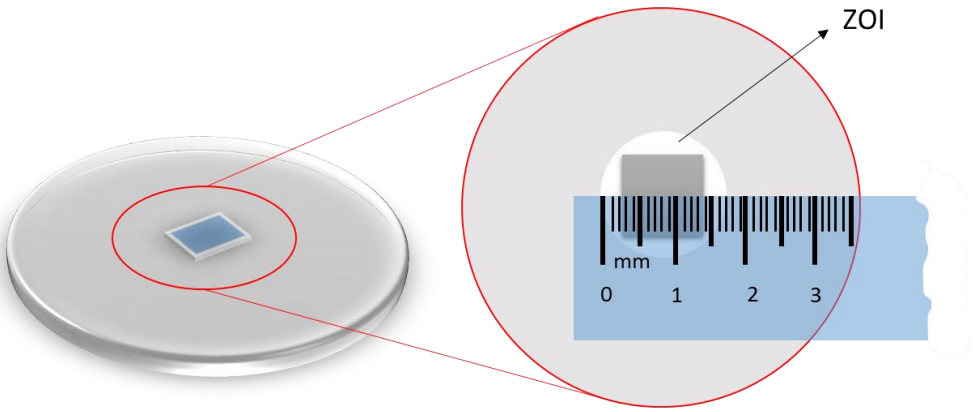

Figure 3-23 Scheme of the ZOI and it size determination

3.5 References

1. Calderon V, S.; Galindo, R. E.; Benito, N.; Palacio, C.; Cavaleiro, A.; Carvalho, S., Ag+ Release Inhibition from Zrcn–Ag Coatings by Surface Agglomeration Mechanism: Structural Characterization. *Journal of Physics D: Applied Physics* **2013,** *46* (32), 325303.

2. Adamczyk, J.; Horny, N.; Tricoteaux, A.; Jouan, P. Y.; Zadam, M., On the Use of Response Surface Methodology to Predict and Interpret the Preferred C-Axis Orientation of Sputtered Aln Thin Films. *Applied Surface Science* **2008,** *254* (6), 1744-1750.

3. Tien, C.-L.; Lin, S.-W., Optimization of Process Parameters of Titanium Dioxide Films by Response Surfaces Methodology. *Optics Communications* **2006,** *266* (2), 574-581.

4. Chou, W.-J.; Sun, C.-H.; Yu, G.-P.; Huang, J.-H., Optimization of the Deposition Process of Zrn and Tin Thin Films on Si(1 0 0) Using Design of Experiment Method. *Materials Chemistry and Physics* **2003,** *82* (1), 228-236.

5. Escobar Galindo, R.; Manninen, N. K.; Palacio, C.; Carvalho, S., Advanced Surface Characterization of Silver Nanocluster Segregation in Ag–Ticn Bioactive Coatings by Rbs, Gdoes, and Arxps. *Analytical and Bioanalytical Chemistry* **2013,** *405* (19), 6259-6269.

6. Shuman, D. J.; Costa, A. L. M.; Andrade, M. S., Calculating the Elastic Modulus from Nanoindentation and Microindentation Reload Curves. *Materials Characterization* **2007,** *58* (4), 380-389.

7. Pedrosa, P.; Machado, D.; Lopes, C.; Alves, E.; Barradas, N. P.; Martin, N.; Macedo, F.; Fonseca, C.; Vaz, F., Nanocomposite Ag:Tin Thin Films for Dry Biopotential Electrodes. *Applied Surface Science* **2013,** *285, Part A* (0), 40-48.

8. Liu, C.; Bi, Q.; Leyland, A.; Matthews, A., An Electrochemical Impedance Spectroscopy Study of the Corrosion Behaviour of Pvd Coated Steels in 0.5 N Nacl Aqueous Solution: Part Ii.: Eis Interpretation of Corrosion Behaviour. *Corrosion Science* **2003,** *45* (6), 1257-1273.

9. Ramírez, G.; Rodil, S.; Muhl, S.; Turcio-Ortega, D.; Olaya, J.; Rivera, M.; Camps, E.; Escobar-Alarcón, L., Amorphous Niobium Oxide Thin Films. *Journal of Non-Crystalline Solids* **2010,** *356* (50), 2714-2721.

10. Assis, S. L. d.; Wolynec, S.; Costa, I., Corrosion Characterization of Titanium Alloys by Electrochemical Techniques. *Electrochimica Acta* **2006,** *51* (8), 1815-1819.

11. Van Oss, C. J.; Chaudhury, M. K.; Good, R. J., Interfacial Lifshitz-Van Der Waals and Polar Interactions in Macroscopic Systems. *Chemical Reviews* **1988,** *88* (6), 927-941.

12. Kelly, P. J.; Li, H.; Benson, P. S.; Whitehead, K. A.; Verran, J.; Arnell, R. D.; Iordanova, I., Comparison of the Tribological and Antimicrobial Properties of Crn/Ag, Zrn/Ag, Tin/Ag, and Tin/Cu Nanocomposite Coatings. *Surface and Coatings Technology* **2010,** *205* (5), 1606-1610.

CHAPTER IV- Optimized Composition for Enhanced Mechanical and Electrochemical Response of ZrCN-Ag Coatings

The following chapter is partially based on the results published in: S. Calderon V, J.C. Oliveira, M. Evaristo, A. Cavaleiro, S. Carvalho, Prediction of optimized composition for enhanced mechanical and electrochemical response of Zr-C-N-Ag coatings for medical devices, Applied Surface Science, 320 (2014) 570-580.

4 Introduction

Prior to a detailed evaluation of the ZrCN-Ag coatings properties, it is necessary to understand the coating production process, and determine the influence of the process parameters on the main characteristics of the coatings. However, before long time consuming experiments, such as tribological tests, electrochemical immersion tests and silver ion release, a rapid evaluation of the coatings properties must be carried out in order to determine a set of production variables, to obtain the desire composition to be assessed in the experimental procedure that consume more resources. As a result, the films have been produced in a large range of condition and the best mechanical and electrochemical performance have been identify.

The variables to be altered were selected taking into consideration that, in previous research, it has been demonstrated that the properties of transition metal carbonitride can be tailored depending on the stoichiometry of the MeCN phase [1-9], as previously mentioned in Chapter II of the thesis. In addition, the necessity of adding Ag to the $ZrC_{1-x}N_x$ matrix, to attain the antibacterial effect, is expected to promote further modification to the structural, chemical, mechanical and electrochemical performance.

Our group, for instance, has previously reported that adding more than 6.3 at. % silver to a TiCN coating, the mechanical and tribological properties are reduced due to the predominant soft metallic phase [10-11]. In spite of the similarities between ZrCN-Ag and TiCN-Ag systems, for the first one, no optimization processes have been carried out to determine the best compromise between the mechanical and the electrochemical properties, as a function of either the composition or, mainly, the amount of an immiscible metallic phase as silver. Hence, proper conditions to maintain or enhance those features in the system will be determined.

This chapter provides information about the optimization process regarding the composition of the films such as the amount of silver, carbon and nitrogen incorporated into the quaternary system Zr-C-N-Ag to obtain the best performance, at laboratorial level, concerning mechanical and corrosion tests. Proper adhesion is also envisaged for the coatings to withstand mechanical loading. The optimization process is performed by a response surface methodology, which has been successfully applied as optimization method for physical vapor deposition processes [12-14].

4.1 Optimization process

Response surface methodology was used to correlate the Ag target current density and the reactive gas fluxes (independent variables), with the composition, hardness, corrosion resistance and adhesion of the film (dependent variables or responses). The responses were evaluated as previously described in chapter III. Briefly, the coatings chemical composition was analyzed by electron probe micro-analyzer (EPMA), the corrosion behavior was assessed by electrochemical impedance spectroscopy (EIS) in Hank's balanced salt solution with 10 g/L of albumin at 37 °C with stabilized pH (7.0-7.5) after 1h of open circuit potential stabilization. The adhesion of the coatings was accessed by scratch-testing technique, the hardness was evaluated by nano-indentation technique[2]. Each independent variable was set as shown in Table 4-1, which also presents the monitored variables such targets potential, base pressure, working pressure, etc.

Additionally to the responses, the structure of the coatings was studied by X-ray diffraction and the thicknesses were evaluated by the Calotest method. The results for the composition and all the functional properties evaluated are presented in Table 4-2.

Table 4-1 Coatings deposition parameters and sputtering process variables.

Sample	Ag Current density [mA cm^{-2}]	C_2H_2 [sccm]	N_2 [sccm]	Time [s]	Base Pressure [1x10^{-4} Pa]	Working Pressure [1x10^{-1} Pa]	Ag Potential [V]	Zr Potential [V]	Total Power [W cm^{-2}]	Substrate Current [mA]
ZrCN8	0.25	1.2	3	4005	4.3	6	282	303	3.14	107
ZrCN14	0.25	1.2	9	4005	3.1	6.5	285	328	3.39	120
ZrCN1	0.25	2.4	6	4005	4.5	6.5	306	332	3.44	111
ZrCN9	0.25	3.6	3	4005	3.3	6.5	312	318	3.30	117
ZrCN15	0.25	3.6	9	4005	3.9	7.1	291	348	3.61	115
ZrCN6	0.5	1.2	6	3720	4.3	6.2	313	309	3.29	110
ZrCN10	0.5	2.4	3	3720	4.2	6.2	358	319	3.42	110

[2] For a more detailed description of the techniques please see chapter III.

Sample	Ag Current density [mA cm^{-2}]	C_2H_2 [sccm]	N_2 [sccm]	Time [s]	Base Pressure [1x10^{-4} Pa]	Working Pressure [1x10^{-1} Pa]	Ag Potential [V]	Zr Potential [V]	Total Power [W cm^{-2}]	Substrate Current [mA]
ZrCN12	0.5	2.4	6	3720	2.5	6.6	320	325	3.46	111
ZrCN19	0.5	2.4	6	3720	4.5	6.6	315	332	3.53	120
ZrCN2	0.5	2.4	6	3720	6	6.5	340	328	3.49	110
ZrCN16	0.5	2.4	9	3720	3.1	6.9	321	337	3.58	119
ZrCN7	0.5	3.6	6	3720	3.6	6.9	337	328	3.50	114
ZrCN11	0.75	1.2	3	3465	2.4	6	355	315	3.46	113
ZrCN17	0.75	1.2	9	3465	4.5	6.6	342	325	3.55	116
ZrCN3	0.75	2.4	6	3465	4.3	6.6	361	324	3.55	114
ZrCN13	0.75	3.6	3	3465	4	6.5	356	335	3.66	113
ZrCN18	0.75	3.6	9	3465	3.3	7.1	348	345	3.76	123

4.2 Results and discussion

4.2.1 Sputtering Process

Table 4-1 summarizes the main deposition conditions and some important parameters of the discharge during the films production.

The Zr target potential largely depends on the nitrogen and acetylene reactive gases, which gradually poison the target with increasing fluxes. As shown in Figure 4-1a, the zirconium target potential exhibited a linear correlation with both gas fluxes. The silver target potential, on the other hand, only depends on the current density applied to the silver target, as shown in Figure 4-1b.

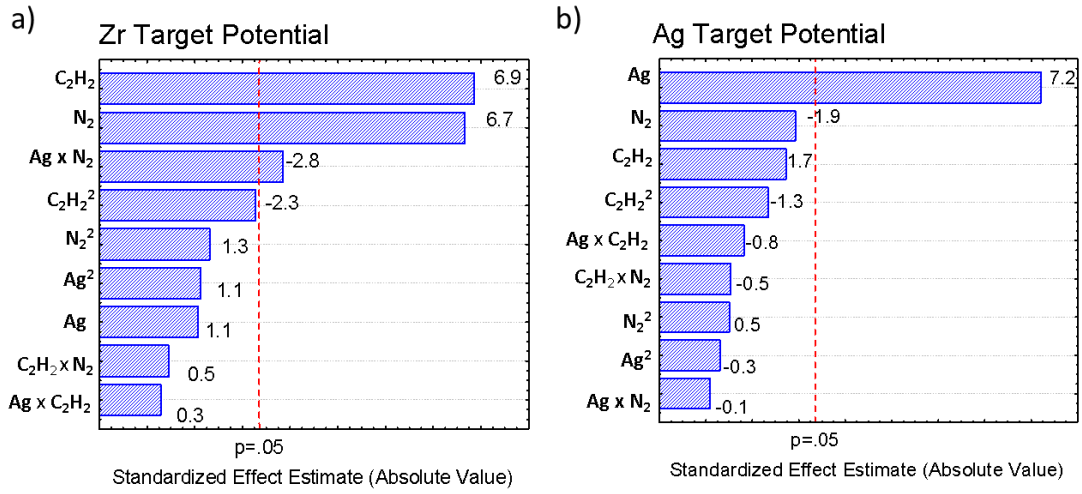

Figure 4-1 Pareto charts for the effects of silver current density, nitrogen flux and acetylene flux on the targets potential during the sputtering process. a) Zr target potential and b) Ag target potential. Ag represents the current density applied to the silver target, N_2 the flux of nitrogen and C_2H_2 the flux of acetylene.

Table 4-2 summarizes the values of the main properties measured in the films. The thickness of the films varied between 1.1 and 2.0 µm for most of the coatings (corresponding to deposition rates between 1.0 and 2.1 µm h^{-1}). The films deposited at the highest current density on the silver target and the highest acetylene flux exhibited the highest depositions rates (samples ZrCN3 and ZrCN13).

The films chemical composition measured by EPMA (shown in Table 4-2) was statistically modeled in order to evaluate the influence of the deposition conditions on the incorporation of zirconium, carbon, nitrogen, silver and residual oxygen in the films. The resulting Pareto diagrams are shown in Figure 4-2.

Table 4-2 Coatings thicknesses, depositions rates, composition and functional properties.

Sample	J_{Ag} [mA cm^{-2}]	C_2H_2 [sccm]	N_2 [sccm]	Th [µm]	DR [µm h^{-1}]	Zr [at. %]	C [at. %]	N [at. %]	Ag [at. %]	O [at. %]	Hardness [GPa]	Rp [kΩ cm^{-2}]	Lc_2 [N]
ZrCN8	0.25	1.2	3	1.8	1.7	46.3	17.6	24.3	5.7	6.0	18.6 ± 2.2	5922 ± 225	42.9 ± 2.3
ZrCN14	0.25	1.2	9	1.1	1	31.8	18.0	39.6	6.9	3.8	11.5 ± 0.8	3290 ± 608	19.7 ± 0.9
ZrCN1	0.25	2.4	6	1.5	1.3	33.2	29.2	30.9	1.3	5.4	14.5 ± 1.5	5826 ± 600	38.3 ± 2.6
ZrCN9	0.25	3.6	3	1.9	1.7	35.8	37.3	18.3	0.1	8.4	12. ± 1.1	817 ± 59	45.8 ± 2.8
ZrCN15	0.25	3.6	9	1.4	1.3	20.0	40.9	32.8	3.9	2.4	9.0 ± 0.8	4217 ± 513	10.1 ± 0.5
ZrCN6	0.5	1.2	6	1.3	1.3	25.6	15.3	23.8	15.5	19.8	7.7 ± 0.4	132 ± 3	56.5 ± 8.4
ZrCN10	0.5	2.4	3	1.6	1.5	34.5	29.5	18.3	9.0	8.8	13.4 ± 1.2	1535 ± 429	59.4 ± 4.9

Sample	J_{Ag} [mA cm^{-2}]	C_2H_2 [sccm]	N_2 [sccm]	Th [µm]	DR [µm h^{-1}]	Zr [at. %]	C [at. %]	N [at. %]	Ag [at. %]	O [at. %]	Hardness [GPa]	Rp [kΩ cm^{-2}]	Lc_2 [N]
ZrCN12	0.5	2.4	6	1.2	1.2	22.9	26.5	24.1	12.9	13.7	8.0 ± 0.4	539 ± 25	90.3 ± 5.6
ZrCN19	0.5	2.4	6	1.6	1.5	22.6	27.0	25.3	12.9	12.3	8.9 ± 0.9	490 ± 27	66.5 ± 6.8
ZrCN2	0.5	2.4	6	2	2	21.9	24.7	19.3	13.4	20.7	7.3 ± 0.9	252 ± 37	> 100
ZrCN16	0.5	2.4	9	1.5	1.4	20.5	27.0	30.2	13.3	8.9	7.4 ± 0.8	620 ± 118	89.2 ± 2.1
ZrCN7	0.5	3.6	6	1.5	1.4	17.5	33.1	18.3	12.7	18.4	7.3 ± 0.5	1022 ± 94	75.4 ± 0.9
ZrCN11	0.75	1.2	3	2	2.1	37.9	15.8	20.2	19.8	6.4	12.2 ± 1.1	208 ± 42	44.3 ± 2.0
ZrCN17	0.75	1.2	9	1.8	1.8	19.0	9.2	3.2	29.0	39.5	3.0 ± 0.3	-	30.0 ± 2.1
ZrCN3	0.75	2.4	6	3.2	3.3	19.0	16.4	4.6	20.3	39.8	2.9 ± 0.2	51 ± 7	35.9 ± 3.0
ZrCN13	0.75	3.6	3	2.6	2.7	18.8	24.1	7.2	11.6	38.4	3.0 ± 0.2	50 ± 13	36.7 ± 3.0
ZrCN18	0.75	3.6	9	2	2.1	14.8	21.3	8.5	21.1	34.3	1.9 ± 0.1	-	30.0 ± 3.2

J_{Ag} = Silver target current density; Th = Thickness; DR= Deposition Rate.

Zirconium content is highly dependent on three parameters (i) the nitrogen flux, due to the high reactivity between these two species; the larger the nitrogen flux, the higher the Zr target poisoning is, reducing the incorporation of Zr into the coating; (ii) the silver current density since increasing the silver current density, the relative zirconium content tends to decrease, despite of the constant value of the Zr current density; (iii) The acetylene flux play a similar that the N_2 since the carbon species react with the Zr to form carbides or carbonitrides.

Nitrogen and carbon are strongly affected by the silver current density, due to its effect on decreasing zirconium species: with less zirconium available lower gases react with it.

Finally, silver content mainly depends on the silver current density, as expected. Nonetheless, the nitrogen and carbon also affect the Ag incorporation, due to the negative effect on the Zr, and additionally, the increment of the amorphous carbon phases due to carbon (as will be later explained) the relative content of silver is reduced by the acetylene flux.

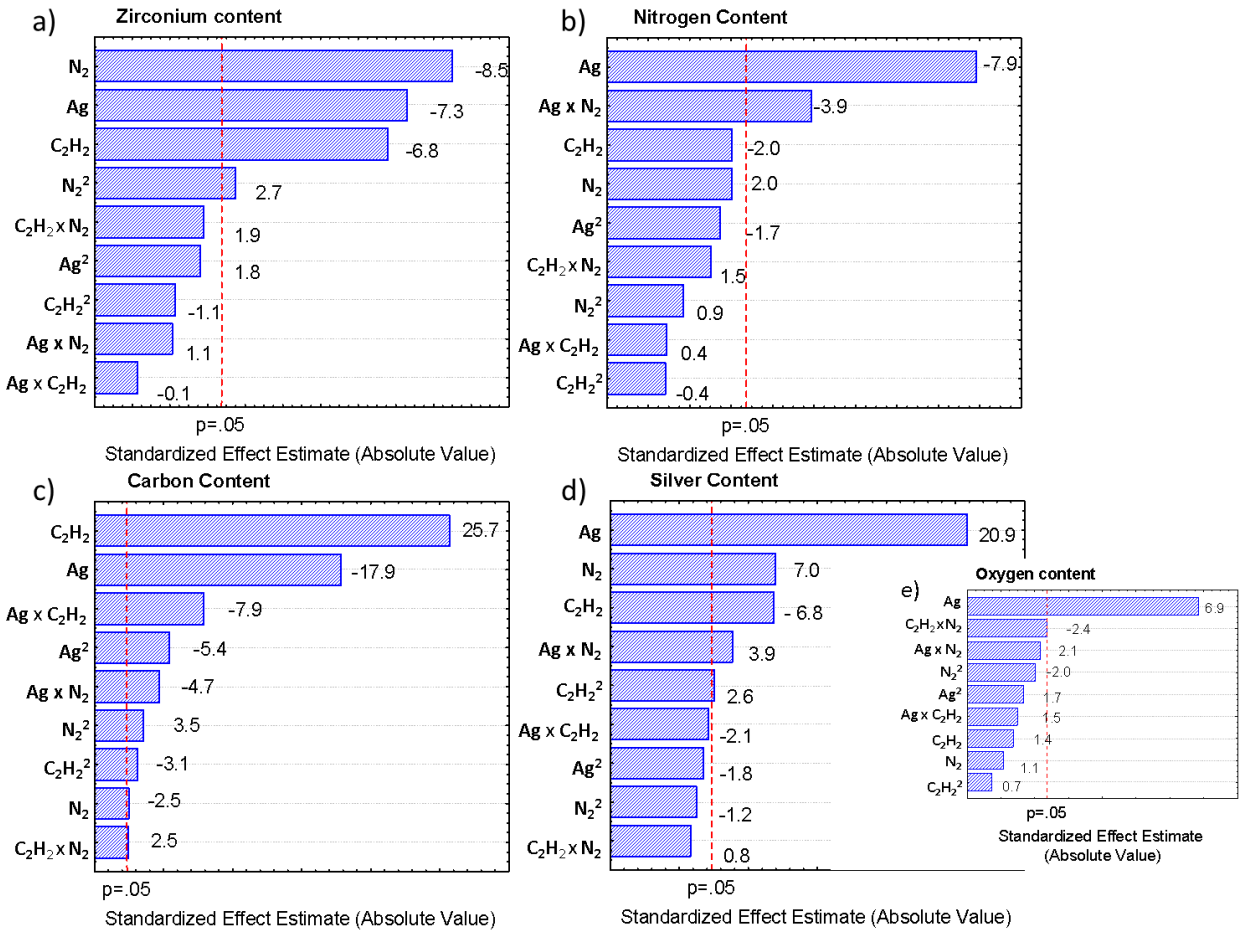

Figure 4-2 Pareto charts for the effect of silver current density (Ag), nitrogen flux (N_2) and acetylene flux (C_2H_2) on the elemental composition of the films.

An unexpected increase in the residual oxygen content of the samples due to the intensification of the silver current density was observed. As shown in Table 4-2, the oxygen content for the samples deposited at the highest silver content reaches about 40 at. %. This is an extremely high value considering that no oxygen was purposely introduced in the deposition chamber. The oxygen content revealed a strong positive correlation with the silver current density applied to the target.

Several steps were developed in order to elucidate this result. Firstly, gas leaks in the deposition chamber were discarded since the Zr interlayer, in the films with high content of oxygen, has very low residual oxygen content, as shown by energy dispersive X-ray spectroscopy in Figure 4-3. Secondly, targets contamination was discarded since pure Ag and Zr films, produced using similar deposition conditions, only have 3.5 and 2.7 at. % of O, respectively. Thirdly, ZrC_xN_{1-x} films were deposited without silver addition, using similar deposition conditions to the ones used in this report. In all cases, the oxygen contamination was less than 5 at. %. Finally, ZrCN-Ag

films were deposited using a different sputtering configuration. Two Zr targets were mounted in the deposition chamber and Ag pellets were placed on the erosion track of one of the targets. Also with this configuration, the oxygen content in the films increased with increasing the current applied to the Zr-Ag target, reaching values around 30 at. %.

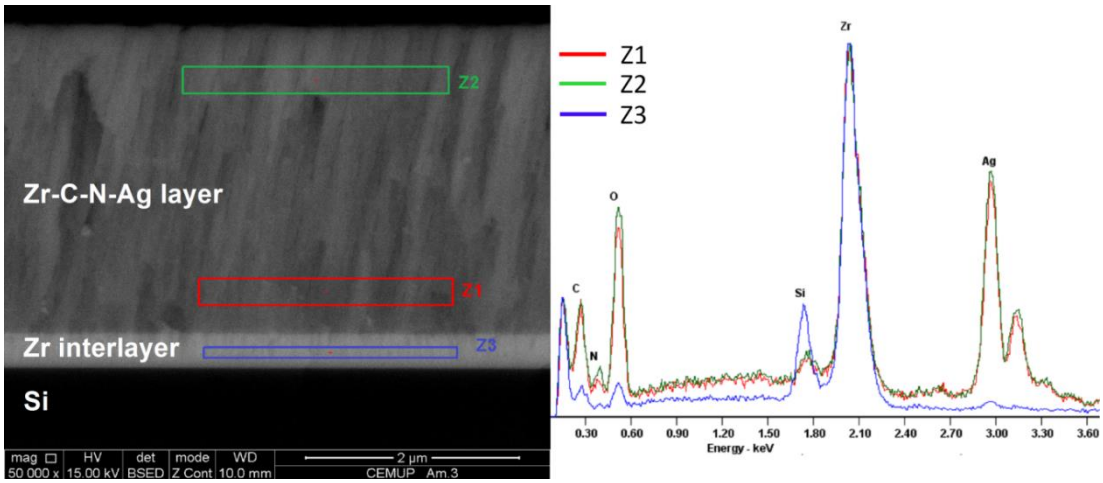

Figure 4-3 a) SEM cross section image for a selected sample produce at the highest Ag current density (ZrCN3) with three marked zones, where EDS was performed and b) EDS spectra for the three zones shown in the SEM image.

Thus, it is believed that during the sputtering process, the silver atoms, in combination with the C_2H_2 + N_2 flux on the plasma, may act as catalyzers accelerating Zr oxidation and consuming the residual oxygen more rapidly compared to the low silver content films. Such process may even occur at the surface, on which the contact between Ag and Zr may accelerate the Zr oxidation assisted by the bias potential applied to the substrates. Consequently, the samples with high content of oxygen were also considered for the statistical model, once the oxygen incorporation seems to be a consequence of the deposition parameters.

Accordingly to preliminary studies commented in chapter III and published in [15], ZrCN-Ag films are composed by a variety of phases, including ZrC_xN_{1-x}, amorphous carbon-base, metallic silver and ZrO_2 phases. In order to take into consideration how these phases affect the properties of the material, a rough calculation of their content through EPMA results has been carried out taking into account the following considerations. Firstly, the most probable oxide formed in reactive magnetron sputtering with similar deposition condition is ZrO_2 [16], which is energetically the most favorable to form when compared to the nitride or the cabonitride [17], and thus, the oxygen detected by EPMA is completely assigned to the ZrO_2 phase, estimating Zr as 1/2 of the oxygen content in such phase. The remaining Zr ([Zr]-[O]/2) is considered to be entirely

associated to ZrC_xN_{1-x}, which in turn, possesses a ratio (C+N)/Zr equal to unity. Finally, the remaining C and N will compose the amorphous carbon-based phase in the material. It is assumed that the silver content stays constant, due to its low reactive behavior. The results of these considerations are presented in Figure 4-4.

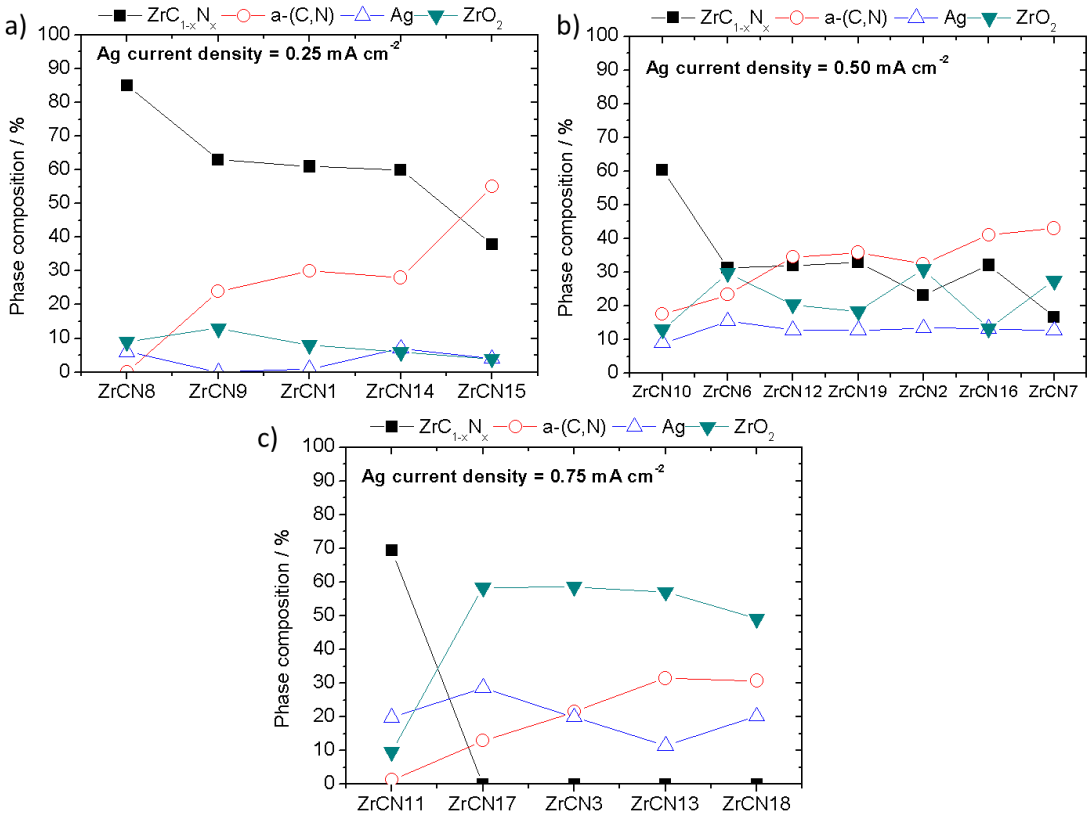

Figure 4-4 Phase composition calculated from EPMA analysis, grouped by the current density applied to the silver target. a) 0.25 mA cm^{-2}, b) 0.50 mA cm^{-2} and c) 0.75 mA cm^{-2}.

4.2.2 Structural Characterization

Figure 4-5 shows the XRD spectra of the films for different current density applied to the silver target, organized by the amount of Zr. The ZrC_xN_{1-x} crystalline phase has been identified as a ZrC_xN_{1-x} solid solution with face-centered cubic (FCC) crystalline structure B1-NaCl type (ICDD-00-065-8779 for x= 0.5). This solid solution is constituted by two isomorphous phases, ZrN and ZrC, which interplanar distances depends on the carbon and nitrogen content in the phases. The higher the amount of carbon the larger the interplanar distance is, due to the higher atomic radii of carbon. As a results, a shift on the diffraction peak can be observed to lower angles depending on the carbon/nitrogen content in the phase.

Silver crystalline phase, on the other hand, is also associated to a FCC structure (ICDD- 00-087-0719).

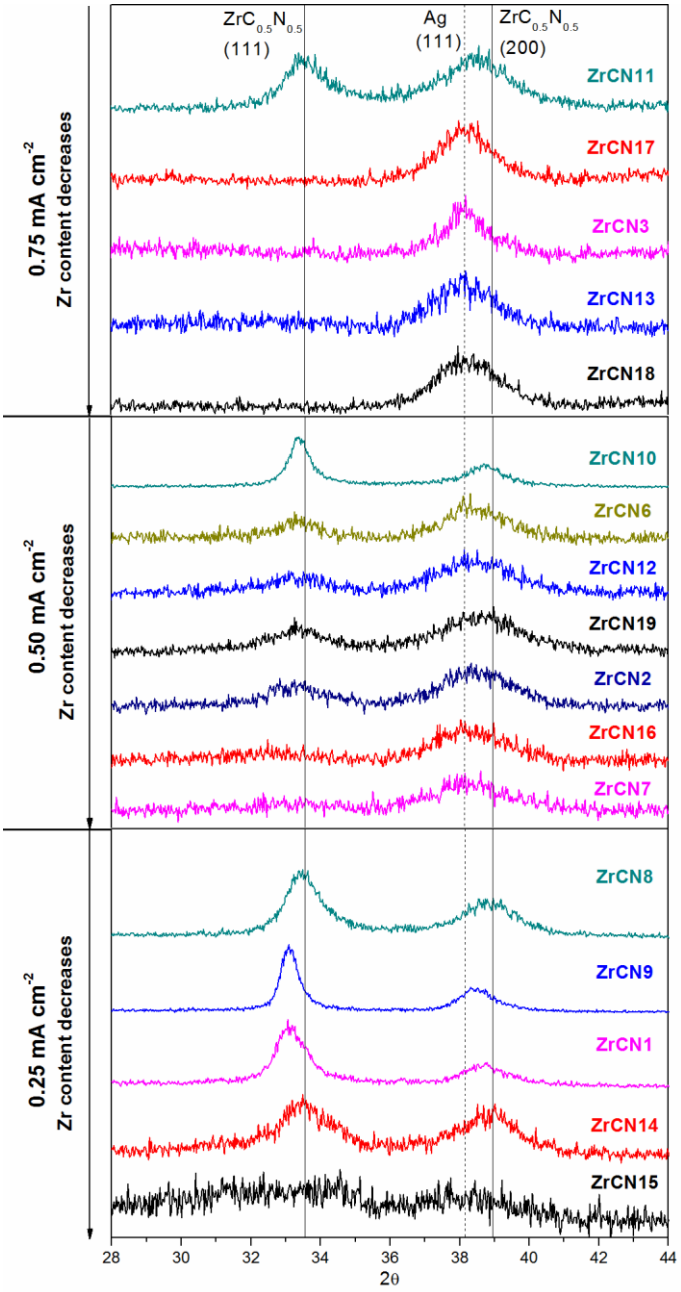

Figure 4-5 X-ray diffraction patterns of the Zr-C-N-Ag coatings. The patterns are grouped by the silver current density applied to the Ag target (0.25, 0.50 and 0.75 mA cm^{-2}) and ordered by zirconium content for each group.

For the lower current density, the structural assessment reveals the ZrC_xN_{1-x} crystalline phase located at different diffraction angles, depending on the carbon content of each coating. For the lowest acetylene flux (1.2 sccm - ZrCN8 and ZrCN14 samples) the ZrC_xN_{1-x} peaks are positioned very close as the $ZrC_{1-x}N_x$ standard. With increasing the C_2H_2 flux, the peaks shift toward lower

angles, closer to the ZrC standard position (ICDD card ICDD- 00-035-0784) meaning that C/N ratio increases in the structure. ZrCN15, on the other hand, was deposited in a very rich nitrogen and acetylene atmosphere, and hence, more amorphous carbon-based phase (a-(C,N)) is formed (Figure 4-4a), hampering the crystallization of ZrC_xN_{1-x} phases and explaining the amorphous character of that coating. In any of these films the silver crystalline phase is evidenced; however, due to its non-carbide and nitride forming characteristics [18], silver nanoparticles are expected to be embedded into the $ZrC_{1-x}N_x$ + a-(C,N) matrix.

For intermediate current density (0.50 mA cm^{-2}), the crystallinity of the $ZrC_{1-x}N_x$ phase on the films is decreased and the silver metallic phase starts to appear. ZrCN10, in contrast, exhibits a well-defined $ZrC_{1-x}N_x$ phase due to the low reactive gases fluxes utilized, low Ag and O contents, and therefore, less amount of phases interfering in the $ZrC_{1-x}N_x$ nucleation and growing.

Higher Ag current density gives rise to films with a clear FCC silver phase without any sign of the $ZrC_{1-x}N_x$ phase, excepting for ZrCN11 in accordance with the phase calculation, as shown in Figure 4-4. The distinctive case of ZrCN11, for which despite of the high current density in the Ag target both $ZrC_{1-x}N_x$ and metallic Ag phase are formed, is explained by the low reactive gases fluxes used in this deposition, avoiding large Zr target poisoning and permitting higher Zr sputtering yield, and thus, the formation of the $ZrC_{1-x}N_x$ phase. For this range of silver current densities, the largest residual oxygen is found, with an O/Zr ratio close to 2, and thus, amorphous ZrO_2 is expected [16-17].

Consequently, it is reasonably to conclude that crystalline $ZrC_{1-x}N_x$ phases are identified for samples with Zr content larger than 30 at. %, which represents a $ZrC_{1-x}N_x$ composition greater than 50% among all the phases in the films. The lower the $ZrC_{1-x}N_x$ phase content the more amorphous character is expected, mainly due to the reduction of the crystallites sizes and amount, and thus, the formation of a composite material is foreseen. However, in the case of large Ag current densities (0.75 mA cm^{-2}), the formation of such phase is limited to zero due to the formation of zirconium oxides that governs almost 60% of the total phases in the material.

4.2.3 Mechanical and Electrochemical Properties

The effect of the current density applied to the target and the gas fluxes during the sputtering process on the mechanical and electrochemical properties was evaluated. An initial statistical analysis was performed by fitting a quadratic model, allowing the determination of significant terms in the model for each property, illustrated in the Pareto charts of the standard effects in

Figure 4-6. The models were reduced taking into consideration only the significant terms of the model, obtaining significant models with R-squares equal to 0.74, 0.84 and 0.95 for the critical load (Lc_3), hardness and polarization resistance (R_p), respectively.

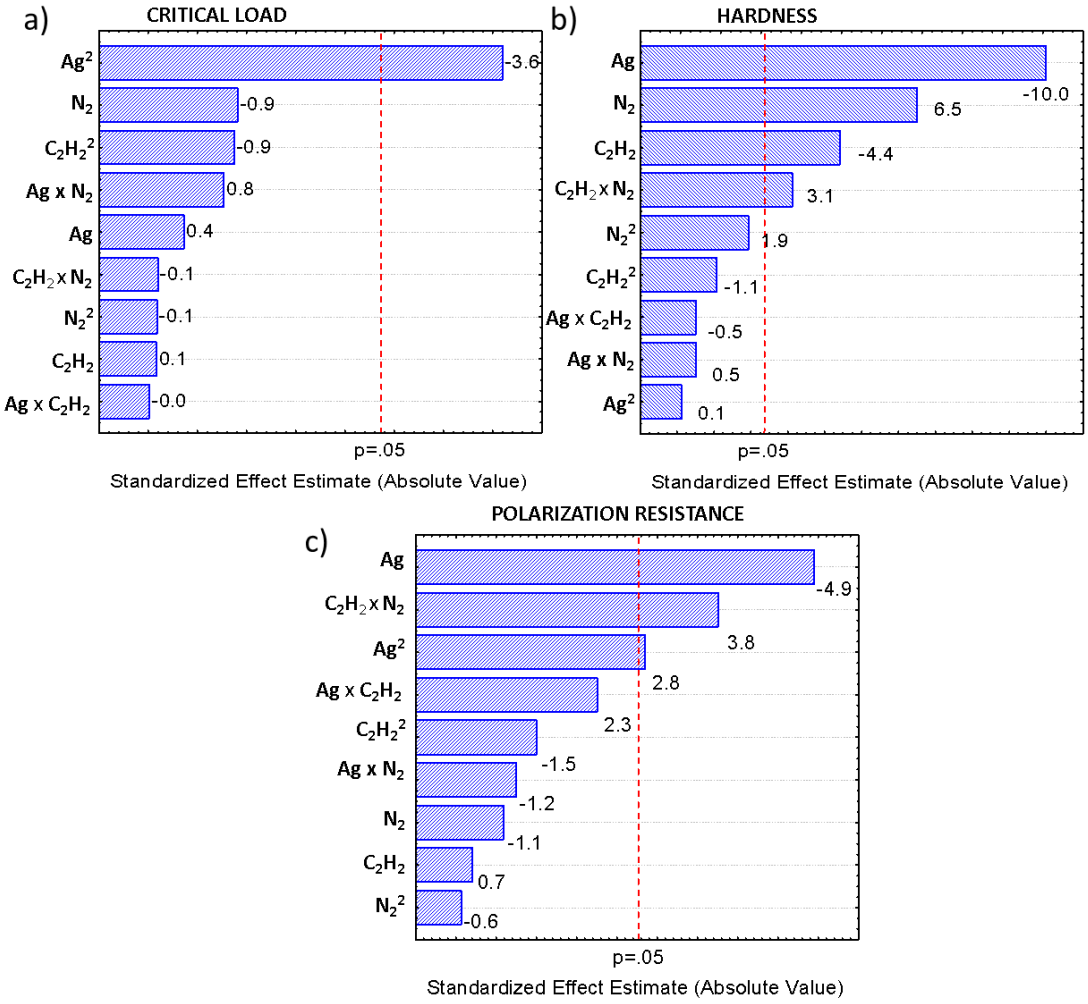

Figure 4-6 Pareto chart for the effects of silver current density (Ag), nitrogen flux (N_2), acetylene flux (C_2H_2) and their interaction on the functional properties of Zr-C-N-Ag films. a) Critical load (Lc_3), b) hardness and c) polarization resistance (Rp).

4.2.3.1 Scratch test

Three representative optical microscope images after scratch testing are shown in Figure 4-7. The coatings failures are highly dependent on their phase composition with a variety of cohesive failures identified in the scratch track as a combination of cracking, local spallation and longitudinal cracks. Samples deposited with the lowest current density applied to the silver target are the only ones with evident local spallation as shown in Figure 4-7a. As the Ag current density increases, the ratio between the soft and hard phases rises, and thus, hard pieces of the material are transported along the track in the softer phases, producing longitudinal cracks

into the scratch track, as observed for sample ZrCN16 and ZrCN3 in Figure 4-7b and c, respectively. All films reveal adhesive failure as either discontinuous or continuous perforation of the coatings, strongly dependent on the silver current density, without significant effect of the gas fluxes, as clearly depicted in the Pareto chart (Figure 4-6). This correlation is plotted in Figure 4-8, revealing a maximum coating adhesion at intermediate current densities applied to the silver target, reducing the adhesion either by increasing or decreasing that value. This behavior is explained by the enhanced toughness of the films, with increasing Ag content, due to the relaxation of the strain field around cracks through the silver ductile metallic phase [19].

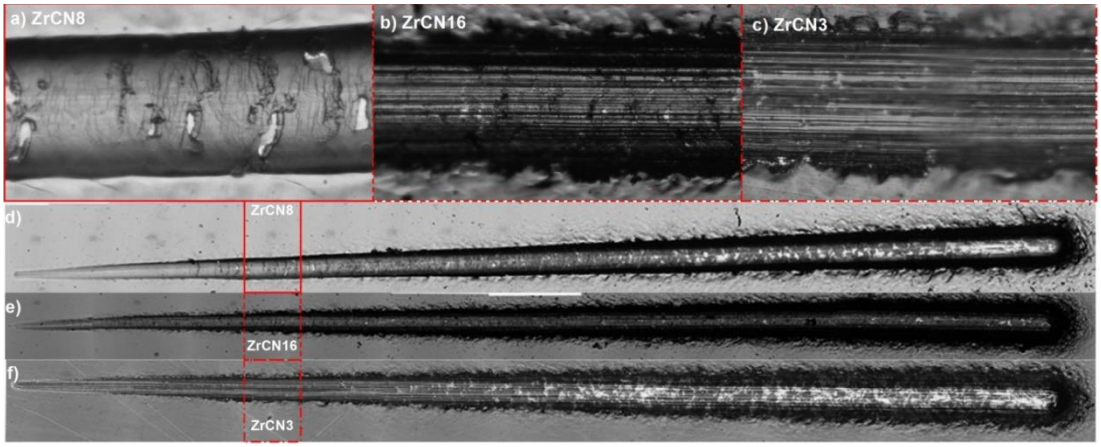

Figure 4-7 Scratch track optical images for three representative ZrCN-Ag coatings produced at different silver current densities applied to the silver target. ZrCN8 at 0.25 mA cm^{-2}, ZrCN 16 at 0.50 mA cm^{-2} ZrCN3 at 0.75 mA cm^{-2}.

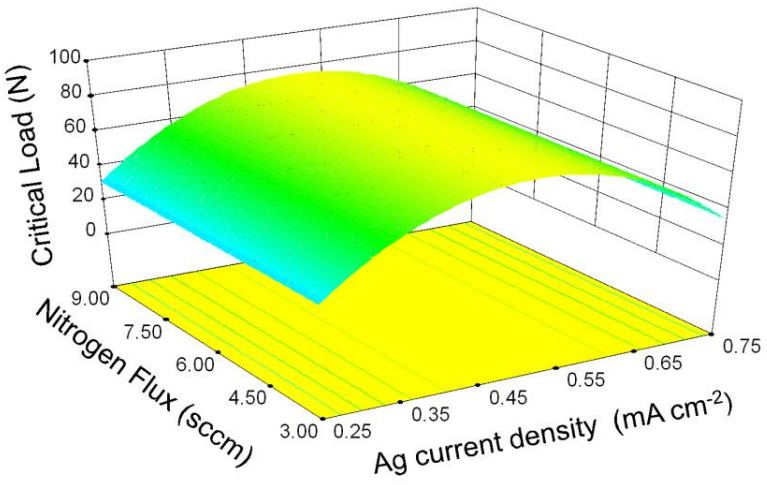

Figure 4-8 Response surface representing the critical load Lc_3 as a function of the nitrogen flux and the silver current density.

4.2.3.2 Nano-indentation

The hardness showed a linear decreasing dependency with increasing either the current density applied to the silver target, or the C_2H_2 flux or the N_2 flux. The interaction between the gas fluxes is also identified as a relevant parameter in the model and its influence can be observed in Figure 4-9. The deterioration of the mechanical properties due to the increase in the current density applied to the silver target is in agreement with previous results reported in the literature [10] and is explained by a combination of boundary amorphous carbon phases and a soft silver phase. . Increasing the silver current density induces a rise of the softer phases, such as Ag, a-(C, N) and zirconium oxides, at the expenses of the $ZrC_{1-x}N_x$ phase, degrading the hardness of the system. Moreover, these softs phases can relax the residual stress of the films, also contributing for reducing the hardness.

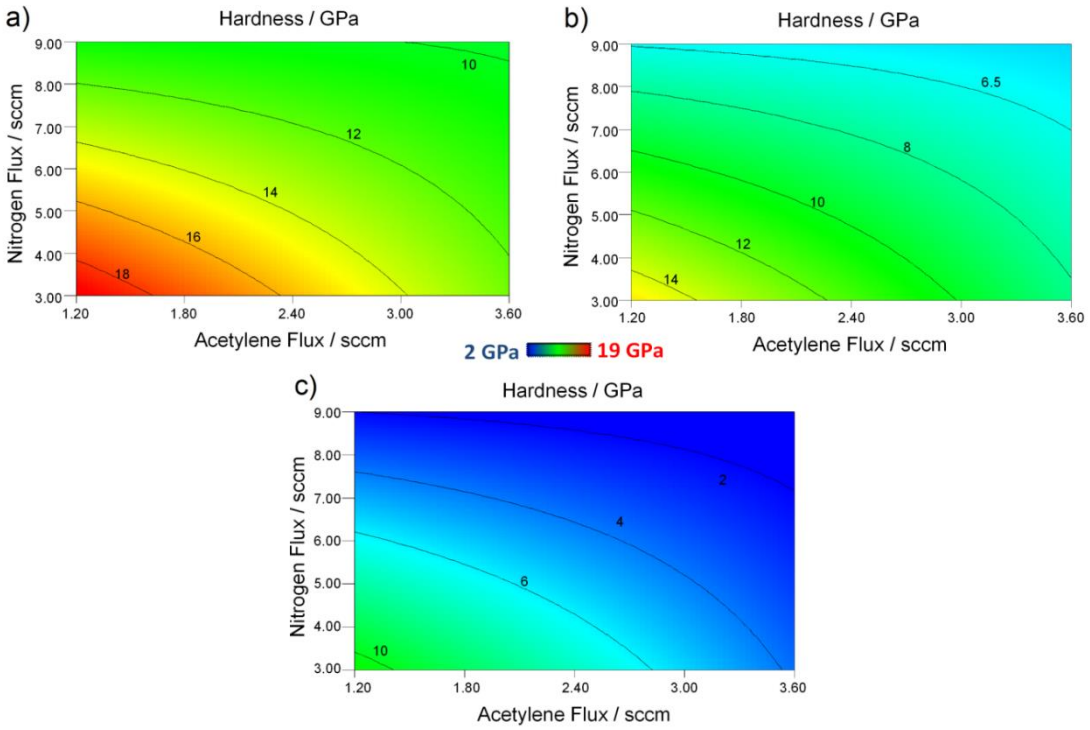

Figure 4-9 Contour line plots representing the effect of the gases interaction on the hardness for ZrCN-Ag films produced at different silver current densities a) 0.25 mA cm^{-2}, b) 0.50 mA cm^{-2} and c) 0.75 mA cm^{-2}.

In similar materials, low silver content may maintain or slightly improved the system hardness, forming nanocomposites materials by combining a nanocrystalline hard phase and a metallic phase, as reported by [20]. ZrCN8 is an example of such behavior in which the ratio (C+N)/Zr is 0.9 and the silver is around 6 at. %. However, most of the samples, possess a mixture of three or even four phases, combining amorphous carbon (a:C or CN_x), silver nanoparticles,

nanocrystalline $ZrC_{1-x}N_x$ and amorphous zirconium oxides, and thus, the hardness was generally reduced compared to the pure $ZrC_{1-x}N_x$ pure phase.

4.2.3.3 Electrochemical Impedance Spectroscopy

The corrosion resistance of the system was evaluated by determining the polarization resistance of the films, after modeling the electrochemical impedance spectroscopy results, as previously explained in the materials and methods section. The polarization resistance was also measured on the bare stainless steel, a value around 500 kΩ. The results evidence a clear corrosion deterioration tendency due to the increment of the Ag current density, reaching a point in which even the corrosion resistance of the stainless steel is greater than that for the coating, depending on the amount of Ag and zirconium oxides phases.

Comparing the polarization resistance with the structure of the films, for intermediate and high Ag current densities, it is evident that the $ZrC_{1-x}N_x$ phase crystallinity in the films plays an important role on their electrochemical behavior, since the best corrosion resistance is achieved in the films containing the highest amounts of the $ZrC_{1-x}N_x$ crystalline phase. The best corrosion resistance is reached for the lower Ag current density, improving up to 10 times the corrosion resistance of the bare stainless steel. The protective behavior of the film is attributed to the chemical stability of $ZrC_{1-x}N_x$. In addition, for higher Ag current density, the weakening of the electrochemical stability is due to the existence of a more electrochemical active phase (Ag metallic phase), compared to the mentioned ceramic phases, showing a clear tendency of reduction of the corrosion resistance as the ratio between the Ag metallic phase and the ceramic phases increases.

On the other hand, the ratio between the carbon and nitrogen content seems also to influence the corrosion resistance of the films, as shown in Figure 4-10. The plot suggests that when one of the gases is higher compared with the other, the corrosion resistance of the films is reduced. This may indicate that a C/N ration equal to the unit, in the $ZrC_{1-x}N_x$ solid solution, is expected to offer better corrosion resistance compared to other compositions. The highest Ag current density plot has been excluded from Figure 4-10 due to the low polarization resistance values ($\leq$ 0.05 MΩ).

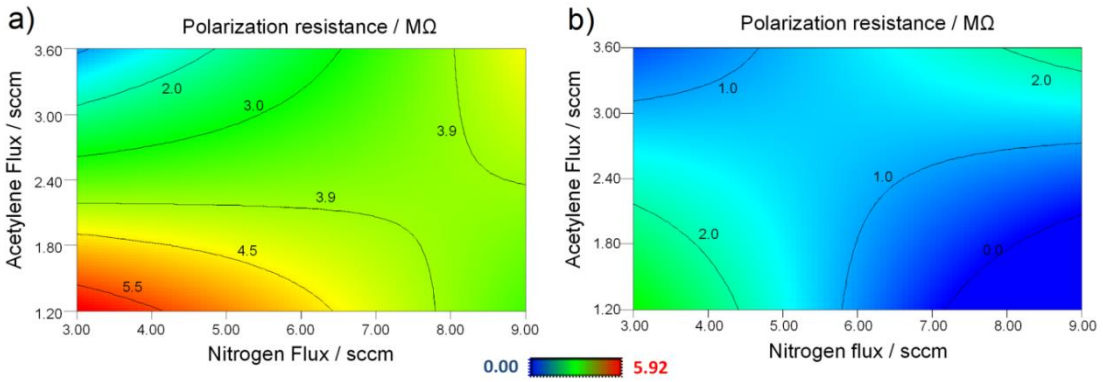

Figure 4-10 Contour line plots representing the effect of the gases interaction on the ZrCN-Ag films polarization resistance at different silver current densities. a) 0.25 mA cm^{-2} and b) 0.50 mA cm^{-2}.

4.2.4 Properties Optimization

Multiple responses optimization involves the determination of regions where the required criteria for a specific performance are simultaneously achieved, in order to find the best compromise between the studied properties. Figure 4-11 shows the overlaying response on a contour plot to visually find the best compromise between the three functional properties studied. The shaded area in the graphs represents the region in which feasible response values are achieved while the others areas do not fit the optimization criteria. In the current case, the hardness was selected to be higher than 17 GPa in order to guarantee that the mechanical properties are close to the previously reported by Sánchez-López et al. [10], which for TiCN/Ag films the best tribological performance was found for films with hardness around 18 GPa. Polarization resistance above 4.5 MΩ, signifying corrosion resistance 9-folds higher than the bare stainless steel and critical loads larger than 50 N to withstand mechanical solicitation.

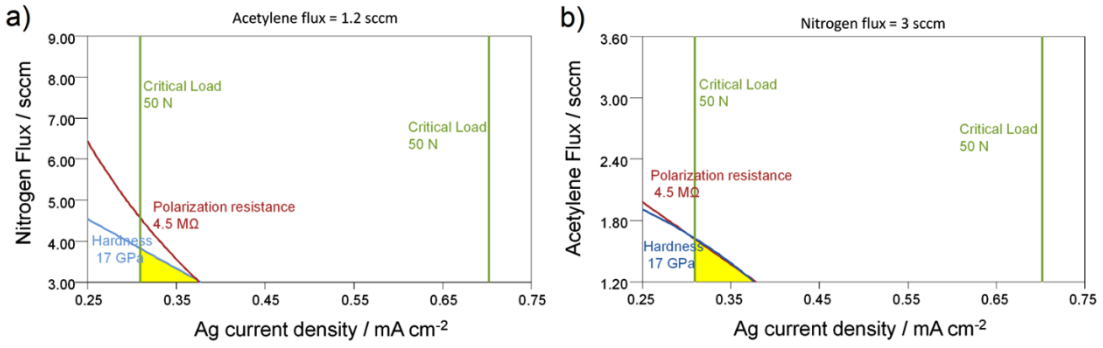

Figure 4-11 Optimum region by overlay plots of the three responses evaluated as a function of the a) nitrogen flux and silver current density and b) acetylene flux and silver current density.

By selecting a point within this shaded region, it is possible to ensure that the desired properties are satisfied. The optimal deposition conditions were identified as 0.33 mA cm^{-2} of Ag target

current density and 1.2 and 3.0 sccm of acetylene and nitrogen fluxes, respectively; the properties predicted for this optimal point are presented in Table 4-3.

Table 4-3 Chemical, mechanical and electrochemical properties predicted for the optimal point determined by RSM (Ag current density = 0.33 mA cm^{-2}, acetylene flux = 1.2 sccm and nitrogen flux = 3 sccm).

OPTIMAL POINT PROPERTIES PREDICTION		OPTIMAL POINT PREDICTED COMPOSITION (at. %)	
Response	Prediction	Element	Prediction
Hardness (GPa)	17.8 ± 1.4	Zr	43.9 ± 2.8
Polarization Resistance (MΩ)	5.04 ± 1.1	N	21.0 ± 4.8
Critical Load (N)	55.4 ± 14.2	C	19.2 ± 1.0
		Ag	7.7 ± 1.7
		O	8.2 ± 8.4

These optimal conditions were utilized to predict the chemical composition of the coating. The models were developed using similar statistical process making use of a central composite design and the chemical composition obtained by EPMA, as previously described in the materials and methods section. The R-Squared values for the Zr, C, N, Ag and O were 0.92, 0.99, 0.82, 0.96 and 0.62, respectively.

Accordingly, the predicted atomic concentration of the optimal film is shown in Table 4-3. The composition reveals a stoichiometric $ZrC_{0.5}N_{0.5}$ phase in which the ratio between the Zr and non-metallic elements (Zr/C+N) is close to the unit, and thus, the prediction is interpreted as a need for a stoichiometric zirconium carbonitride mixed with less than 8 at.% of silver and low residual oxygen, without the presence of amorphous carbon phases.

4.3 Conclusion

The optimization process revealed that the best mechanical and electrochemical performance was reached when stoichiometric $ZrC_{0.5}N_{0.5}$ phase is the main constituent of the materials, with low amounts of silver (<8 at. %) and residual oxygen, mainly explained by the electrochemical stability and mechanical performance of the Zr-C-N solid solution. The current density applied to the silver target was identified as the main parameter affecting the final properties of the films due to its direct relation to the incorporation of metallic silver in the system. However, the reactive gases, as well as the high amount of residual oxygen, were also found to be significant in the process

4.4References

1. Craciun, D.; Bourne, G.; Socol, G.; Stefan, N.; Dorcioman, G.; Lambers, E.; Craciun, V., Characteristics of Zrc/Zrn and Zrc/Tin Multilayers Grown by Pulsed Laser Deposition. *Applied Surface Science* **2011,** *257* (12), 5332-5336.

2. Zheng, J.; Hao, J.; Liu, X.; Gong, Q.; Liu, W., The Plasma Nitriding Treatment of Tin/Ticn Multilayer Films. *Applied Surface Science* **2013,** *268* (0), 195-203.

3. Wang, Q.; Zhou, F.; Wang, X.; Chen, K.; Wang, M.; Qian, T.; Li, Y., Comparison of Tribological Properties of Crn, Ticn and Tialn Coatings Sliding against Sic Balls in Water. *Applied Surface Science* **2011,** *257* (17), 7813-7820.

4. Balaceanu, M.; Braic, V.; Kiss, A.; Zoita, C. N.; Vladescu, A.; Braic, M.; Tudor, I.; Popescu, A.; Ripeanu, R.; Logofatu, C.; Negrila, C. C., Characteristics of Arc Plasma Deposited Tialzrcn Coatings. *Surface and Coatings Technology* **2008,** *202* (16), 3981-3987.

5. Vargas, M.; Castillo, H. A.; Restrepo-Parra, E.; De La Cruz, W., Stoichiometry Behavior of Tan, Tacn and Tac Thin Films Produced by Magnetron Sputtering. *Applied Surface Science* **2013,** *279* (0), 7-12.

6. Balaceanu, M.; Petreus, T.; Braic, V.; Zoita, C. N.; Vladescu, A.; Cotrutz, C. E.; Braic, M., Characterization of Zr-Based Hard Coatings for Medical Implant Applications. *Surface & Coatings Technology* **2010,** *204* (12–13), 2046-2050.

7. Braic, M.; Braic, V.; Balaceanu, M.; Zoita, C. N.; Kiss, A.; Vladescu, A.; Popescu, A.; Ripeanu, R., Structure and Properties of Zr/Zrcn Coatings Deposited by Cathodic Arc Method. *Materials Chemistry and Physics* **2011,** *126* (3), 818-825.

8. Hollstein, F.; Kitta, D.; Louda, P.; Pacal, F.; Meinhardt, J., Investigation of Low-Reflective Zrcn–Pvd-Arc Coatings for Application on Medical Tools for Minimally Invasive Surgery. *Surface and Coatings Technology* **2001,** *142–144* (0), 1063-1068.

9. Silva, E.; Rebelo de Figueiredo, M.; Franz, R.; Escobar Galindo, R.; Palacio, C.; Espinosa, A.; Calderon V, S.; Mitterer, C.; Carvalho, S., Structure-Property Relations in Zrcn Coatings for Tribological Applications. *Surface and Coatings Technology* **2010,** *205* (7), 2134-2141.

10. Sánchez-López, J. C.; Abad, M. D.; Carvalho, I.; Escobar Galindo, R.; Benito, N.; Ribeiro, S.; Henriques, M.; Cavaleiro, A.; Carvalho, S., Influence of Silver Content on the Tribomechanical Behavior on Ag-Ticn Bioactive Coatings. *Surface and Coatings Technology* **2012,** *206* (8–9), 2192-2198.

11. Alves, C. F. A.; Oliveira, F.; Carvalho, I.; Piedade, A. P.; Carvalho, S., Influence of Albumin on the Tribological Behavior of Ag–Ti (C, N) Thin Films for Orthopedic Implants. *Materials Science and Engineering: C* **2014,** *34* (0), 22-28.

12. Adamczyk, J.; Horny, N.; Tricoteaux, A.; Jouan, P. Y.; Zadam, M., On the Use of Response Surface Methodology to Predict and Interpret the Preferred C-Axis Orientation of Sputtered Aln Thin Films. *Applied Surface Science* **2008,** *254* (6), 1744-1750.

13. Tien, C.-L.; Lin, S.-W., Optimization of Process Parameters of Titanium Dioxide Films by Response Surfaces Methodology. *Optics Communications* **2006,** *266* (2), 574-581.

14. Chou, W.-J.; Sun, C.-H.; Yu, G.-P.; Huang, J.-H., Optimization of the Deposition Process of Zrn and Tin Thin Films on Si(1 0 0) Using Design of Experiment Method. *Materials Chemistry and Physics* **2003,** *82* (1), 228-236.

15. Calderon V, S.; Galindo, R. E.; Benito, N.; Palacio, C.; Cavaleiro, A.; Carvalho, S., Ag+ Release Inhibition from Zrcn–Ag Coatings by Surface Agglomeration Mechanism: Structural Characterization. *Journal of Physics D: Applied Physics* **2013,** *46* (32), 325303.

16. Severin, D.; Sarakinos, K.; Kappertz, O.; Pflug, A.; Wuttig, M., Tailoring of Structure Formation and Phase Composition in Reactively Sputtered Zirconium Oxide Films Using Nitrogen as an Additional Reactive Gas. *Journal of Applied Physics* **2008,** *103* (8), 083306-083306-5.

17. Ngaruiya, J.; Kappertz, O.; Liesch, C.; Müller, P.; Dronskowski, R.; Wuttig, M., Composition and Formation Mechanism of Zirconium Oxynitride Films Produced by Reactive Direct Current Magnetron Sputtering. *physica status solidi (a)* **2004,** *201* (5), 967-976.

18. Krzanowski, J. E., Phase Formation and Phase Separation in Multiphase Thin Film Hard Coatings. *Surface and Coatings Technology* **2004,** *188–189* (0), 376-383.

19. Zhang, S.; Sun, D.; Fu, Y.; Du, H., Toughening of Hard Nanostructural Thin Films: A Critical Review. *Surface and Coatings Technology* **2005,** *198* (1–3), 2-8.

20. Musil, J.; Vlček, J., Magnetron Sputtering of Hard Nanocomposite Coatings and Their Properties. *Surface and Coatings Technology* **2001,** *142–144* (0), 557-566.

CHAPTER V – Chemical and Structural Characterization of ZrCN-Ag Coatings

The following chapter is partially based on the results published in: S. Calderon V, A. Cavaleiro, S. Carvalho, Chemical and structural characterization of ZrCNAg coatings: XPS, XRD and Raman spectroscopy, Applied Surface Science, 346 (2015) 240-247.

5 Introduction

In chapter II, it was shown that by adding silver to a ceramic matrix, the mechanical, tribological, electrochemical and biological properties can be altered. In all cases, the chemical state, distribution and size of the silver nanoparticles play a decisive role on the mentioned properties, stressing the importance of understanding the structural characteristics of the material and phase distribution. Segregation of silver, the creation of an amorphous carbon-based phases, residual oxygen phase, and the coexistence of this diversity of phases are key factors for the functional characteristic of the films that will be discussed in subsequent chapters. As a result, in this chapter, a selected set of samples from the ZrCN-Ag coatings, described in previous chapter, were chosen for a complete chemical, structural and morphological characterization. The coatings, initially characterized by electron probe microanalysis (EPMA), were further studied by X-ray photoelectron spectroscopy (XPS), X-ray diffraction, scanning electron microscopy, transmission electron microscopy, and Raman spectroscopy, in order to understand how the functional characteristic of the ZrCN-Ag coatings are altered.

The samples were selected based on expected phases calculated by EPMA analysis. The ratio between C+N/Zr gives an estimative about the amount of the amorphous carbon nitride phases (a-(C,N)) present in the material. When the ratio is higher than the unit, the excess of C and N lead to the formation of amorphous carbon nitride phases, while for ratios equal or less than the unit these phases should not be expected. Three coatings without amorphous phases and three coatings with increasing amorphous carbon nitride phase content were selected, as shown in Table 5-1. The name of the samples have been altered accordingly to Table 5-1, using the coatings silver content, in order to facilitate the samples identification, which will be used throughout the thesis.

Table 5-1 List of sample selection and identification.

Sample		$\frac{C+N}{Zr}$
	Ag0	1.0
ZrCN8	**Ag6**	0.9
ZrCN14	**Ag7**	1.8
ZrCN10	**Ag9**	1.4
ZrCN16	**Ag13**	2.8
ZrCN20	**Ag20**	1.0

Hence, this set of samples will allow to determine:

- the effect of Ag addition in samples without a-(C, N) phase (Ag0, Ag6 and Ag20)
- the effect of the a-(C, N) phase for similar contents of silver (Ag6 and Ag7)
- the effect of increasing (C+N)/Zr ratio (Ag9, Ag7 and Ag13).

Consequently, this set of samples will be used in the next chapters as representative samples for the ZrCN-Ag coatings. In fact, additionally to the mentioned criteria, many of the other samples were discarded due to their large oxygen content, or very low functional properties, as described in previous chapter.

5.1 Samples characterization

Table 5-2 summarizes the deposition conditions and main chemical and structural characteristics of the selected samples.

The bulk chemical composition of the coatings was analyzed by electron probe microanalysis (EPMA). The surface composition and chemical binding energies was evaluated by X-ray photoelectron spectroscopy (XPS), before and after Ar^+ bombardment for different etching times. The crystalline phases and structure of the coatings was determine by X-ray diffraction (XRD) and electron diffraction. The morphology and distribution of the phases was determined by scanning electron microscopy (SEM), transmission electron microscopy (TEM) and high-resolution TEM. Raman spectroscopy was also utilized to identify the amorphous carbon nitride phases[3].

Table 5-2 Deposition parameters and coatings composition

Sample	Ag current density [mA cm^{-2}]	C_2H_2 [sccm]	N_2 [sccm]	Zr [%]	N [%]	C [%]	Ag [%]	O [%]	$\frac{C+N}{Zr}$
Ag0	0	1.2	3	49	33	15	0	3	1.0
Ag6	0.25	1.2	3	46	24	18	6	6	0.9
Ag7	0.25	1.2	9	32	39	18	7	4	1.8
Ag9	0.5	2.4	3	35	18	29	9	9	1.4
Ag13	0.5	2.4	9	21	30	27	13	9	2.8
Ag20	0.75	1.2	3	38	20	16	20	6	1.0
Standard deviations of the composition are between 0.5 and 1.2 at. %									

[3] For a more detailed description of the techniques and experimental procedures please see chapter III.

5.2 Results and discussion

In the following, it will be discussed more in detail specific issues about these coatings achieved through different characterization techniques.

5.2.1 Chemical characterization: chemical composition and chemical bonding

The surface of the films was analyzed by XPS before and after cleaning the surface by ion bombardment. In order to understand the chemical bonding state at the outmost surface, survey spectra taken before ion cleaning showed all expected elements such as C, Zr, O, N, and Ag (Figure 5-1).

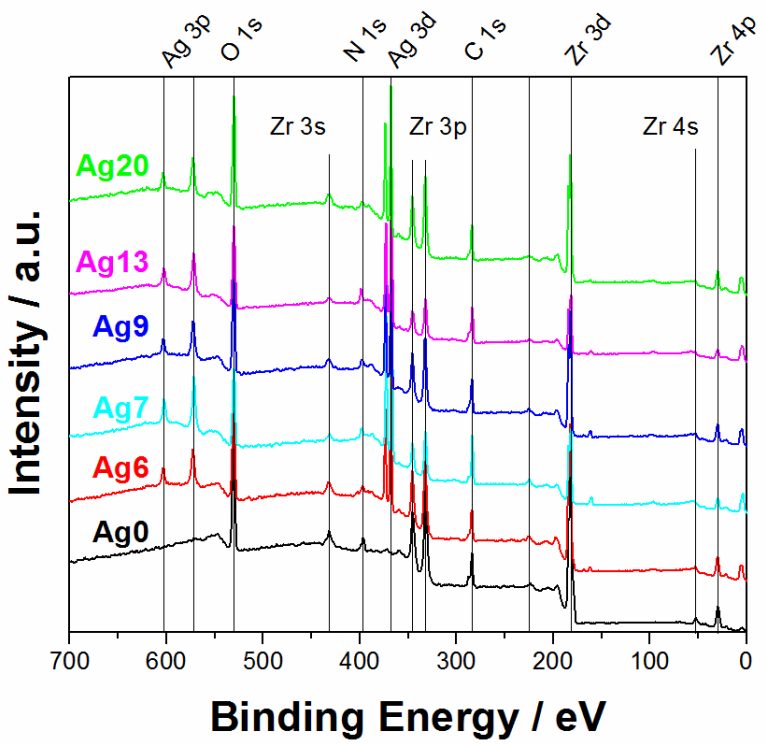

Figure 5-1 XPS survey spectra for ZrCN-Ag coatings shown from 0 to 700 eV.

The surface of the films showed carbon contamination, adjusted to 285 eV as calibration energy for the entire spectrum, to compensate any possible surface charge effect. Detailed spectra of C, Zr, O, N and Ag are displayed in Figure 5-2a, b, c, d and e, respectively. The spectra were organized from bottom to top as silver content increases in the coatings, previously calculated by EPMA. The peak assignment was performed mainly based on Refs [1-4]. The carbon spectrum, besides the defined peak at 285 eV attributed to C-C bond, shows C=O and C-N, all derived from the samples contamination. The Zr 3d spectra evidenced a highly oxidized zirconium at 182.3 eV, characteristic of Zr-O bond, associated to ZrO_2, with the corresponding O-Zr bond at

around 530.3 eV [5]. This surface oxidation is expected due to the high affinity of Zr to form oxides, particularly ZrO_2 with an enthalpy of formation around -1097.46 kJ/mol, compared to ZrN (-365.26 kJ/mol) or ZrC (-196.65 kJ/mol) [6]. In addition to zirconium oxide, some of the films evidenced ZrN or Zr-C-N (179.2 -180.0 eV) phases in low quantities. The respective bond state for N-Zr is observed at 397.3 eV, together with a small peak at C-Zr at 282 eV for Ag0, Ag6 and Ag20 [4].

The bonding state of the silver is characteristic of metallic silver with a peak located at binding energies around 368.4 eV [7]; however, two of the films showed an additional peak at 367.7 eV, associated to silver oxides (Ag_2O) [2]. This particular behavior is only observed in samples Ag7 and Ag13, which possess the highest C+N/Zr ratio and consequently higher a-(C, N) phase, as will be later demonstrated.

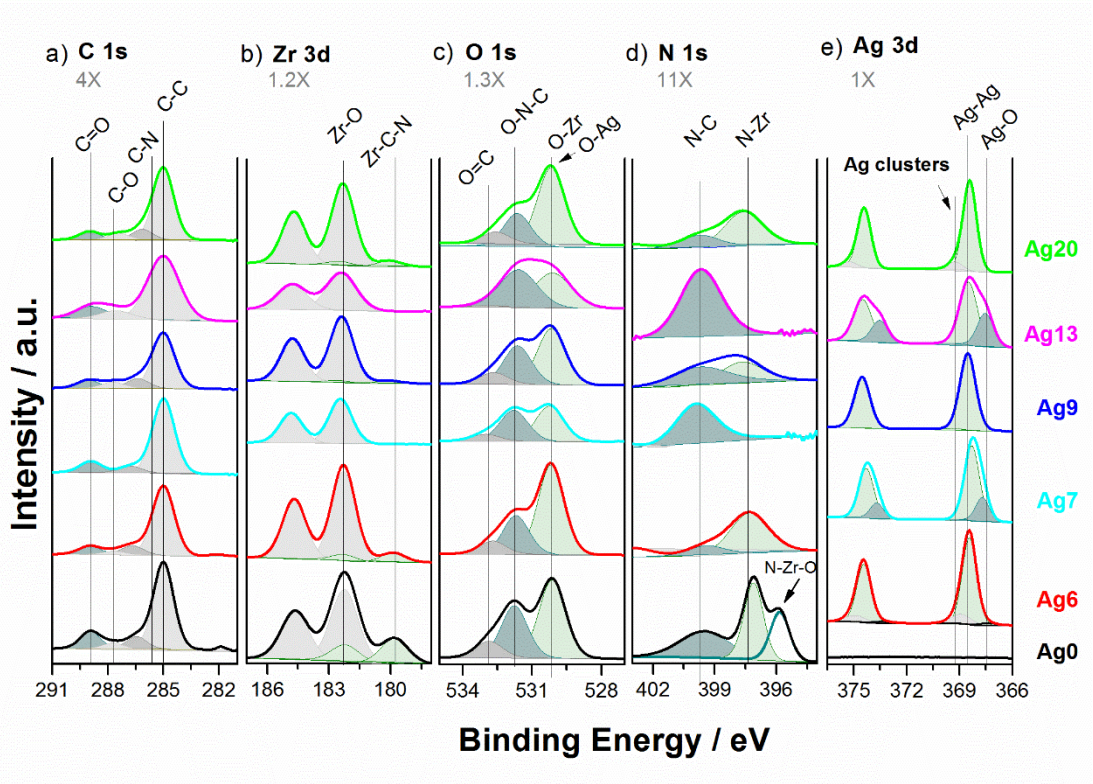

Figure 5-2 XPS spectra for ZrCN-Ag coatings before ion bombardment. Every element is displayed at different scales to clearly identify the peaks.

In order to better understand the bonding states of the films, the oxides and carbon impurities on the surface were removed by ion bombardment, during different times. Figure 5-3 shows the chemical bonding of two characteristic coatings (Ag6 and Ag7), which exhibit similar silver amount, but distinctive (C+N)/Zr ratios. It can be observed in Figure 5-3a that the carbon at

285 eV is substantially reduced after 2 min of bombardment, evidencing the emergence of a new peak at 282 eV, associated to C-Zr bonds that belongs to the ZrC_xN_{1-x} phase, and a peak for higher energies (283.5 eV), attributed by some authors to C-Zr-O [8]. Additionally, the intensities of C-C and C-N bonds are higher for Ag7 than Ag6, corroborating the existence of a-(C,N) phases in the Ag7. Similarly, the ZrO_2 oxide intensity on the surface decreases considerably, becoming almost unperceptive after 10 min of bombardment (Figure 5-3c). The ZrO_2 decreases more rapidly for the case of Ag6, indicating a thinner oxide layer when compared to Ag7. This behavior was also observed for sample Ag13 (not shown), which also showed a thicker ZrO_2 films formed on the surface compared to the other samples. After 2 min of ion bombardment, the reduction of the ZrO_2 (O-Zr) is accompanied with a temporarily intense occurrence of an O-N-Zr peak, which monotonically decreases as the ion bombardment continues. This oxidation behavior is associated to a graded oxidized layer, composed of ZrCN / ZrCN-(O) / ZrO_2, becoming a pure ZrO_2 phase after complete oxidation of the topmost surface. This behavior has been also reported for TiN surfaces [9].

The Zr signal also shows a clear evolution as a function of the ion bombardment, related to the disappearance of the ZrO_2 and the emergence of the ZrC_xN_{1-x} phase. It is also evident that not only Zr-N or Zr-C bonds are observed, but the presence of a third peak is required to completely fit the Zr spectra. This peak is associated to the presence of oxygen in the ZrC_xN_{1-x} phase and is located around 180.3 – 180.8 eV. However, due to the complexity of the Zr signal that contains 4 doublet peaks corresponding to Zr-N (179.9-180.0 eV), Zr-C (179.2 – 179.5eV), Zr-CN(O) (180.3-180.8 eV) [10] and Zr-O (182.3 eV), there is a high probability of reaching a relative minimum in the fitting process, obstructing the process. As a result, the presence of the previously mentioned chemical states were corroborated in the C, N and O spectra and all the analysis considering the deconvolution of the peaks is carried out based on the fitting analysis of the C, N and O.

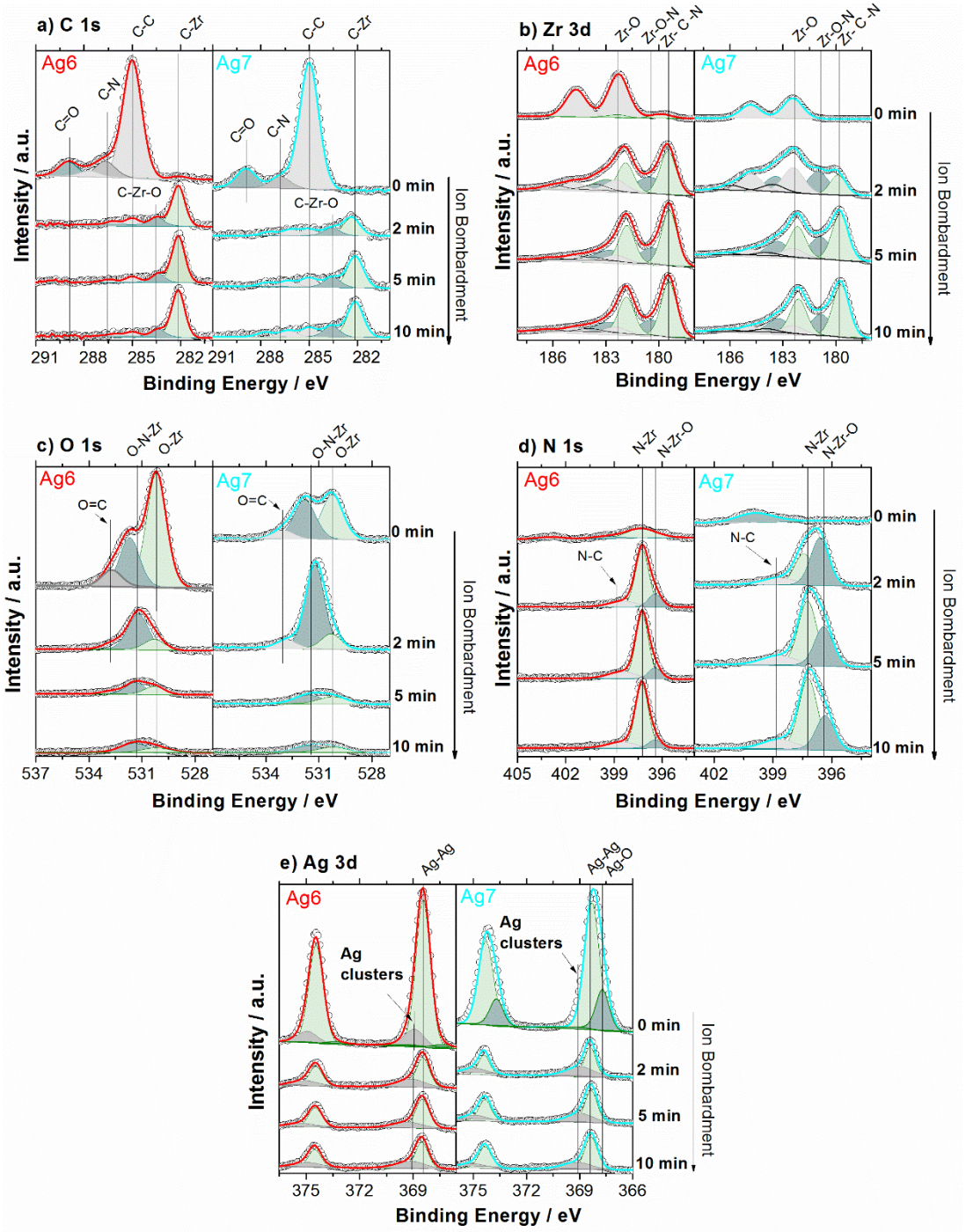

Figure 5-3 XPS spectra for Ag6 and Ag7 samples as a function of the ion bombardment time. Every element is displayed at different scales to clearly identify the peaks (Zr=1 X, Ag=3 X, O=3 X, C=12 X and N=4.8 X). Each element is equally scaled for Ag6 and Ag7.

The oxygen (Figure 5-3c) significantly decreases after 10 min of bombardment, showing mainly two peaks at ~ 530.2 eV and ~ 531.3 eV, attributed to O-Zr for ZrO_2 and O-N-Zr [10], respectively. The peak located at 531.3 eV is relatively larger than the ZrO_2 (530.2 eV) after 2 min of ion bombardment, and is subsequently reduced after further ion bombardment process. This behavior could be associated to a graded ZrCN(O) that forms during the oxidation process of

ZrC_xN_{1-x} phase, as previously reported by Saha et al. [9] in the oxidation of TiN. Correspondingly, nitrogen spectra (Figure 5-3d) supported the existence of Zr-O-N bonds with peaks located at 396.5 eV [10] and N-Zr at 397.3 eV respectively. The silver spectra (Figure 5-3), on the other hand, revealed a surface silver enrichment, reduced almost to ¼ of the initial intensity after 2 min of ion bombardment. A higher binding energy peak is also evidenced, related to silver clusters formed in the films and its width and position are associated with the cluster size and distribution [11].

The results of the previous analysis are summarized in the profile composition depicted in Figure 5-4. These data suggests the formation of an oxidized surface in the films, rich in silver and ZrO_2, with the presence of C as contaminant. After few nanometers (based on the energy and time used for the bombardment and corroborated by glow discharge optical emission spectroscopy) this layer disappears and the ZrCN(O) emerges, with the presence of metallic silver, silver clusters and C-C phases. The silver enrichment on the surface has been previously reported for similar systems (TiCN-Ag) [12] and is associated to redistribution and coalescence of silver particles on the first nm of the coatings.

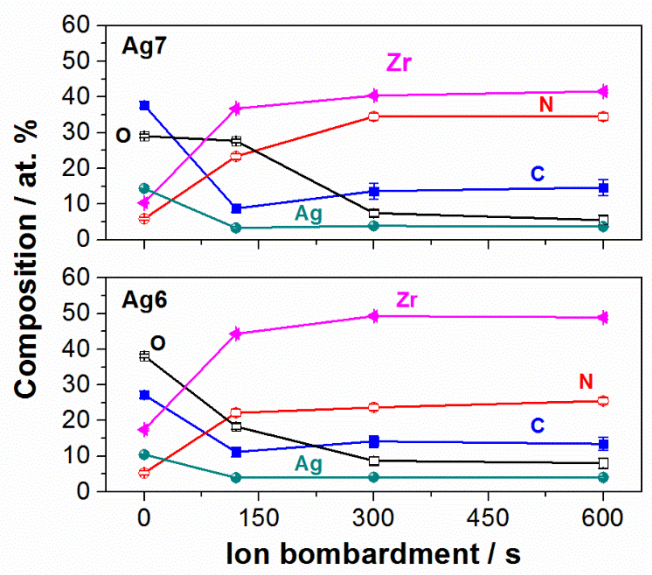

Figure 5-4 Profile composition for samples Ag6 and Ag7 calculated from the XPS spectra as a function of the ion bombardment time

To ensure that all the coatings reach a stable composition as observed in samples Ag6 and Ag7 (Figure 5-4), the films binding energies and composition were studied after 10 min of ion bombardment (Figure 5-5). The comparison shows that the differences in silver content are well correlated with the results observed in EPMA. The C-C bonds are clearly differentiated

(Figure 5-5a), demonstrating a reduction on the intensity directly correlated with the (C+N)/Zr ratio, calculated by EPMA, confirming the presence of amorphous carbon phases in the material, later verified by Raman spectroscopy. It is also shown that depending on the residual oxygen retained into the films, more oxygen is incorporated in the ZrC_xN_{1-x} and a low amount of ZrO_2 remains constant for all the coatings (Figure 5-5b and c). N and C spectra show the incorporation of oxygen into the ZrC_xN_{1-x} phase, at 396.5 eV and 283.5 eV, respectively, and the existence of O-Zr-N and O-Zr bonds at 531.3 and 530.2 eV, as previously discussed.

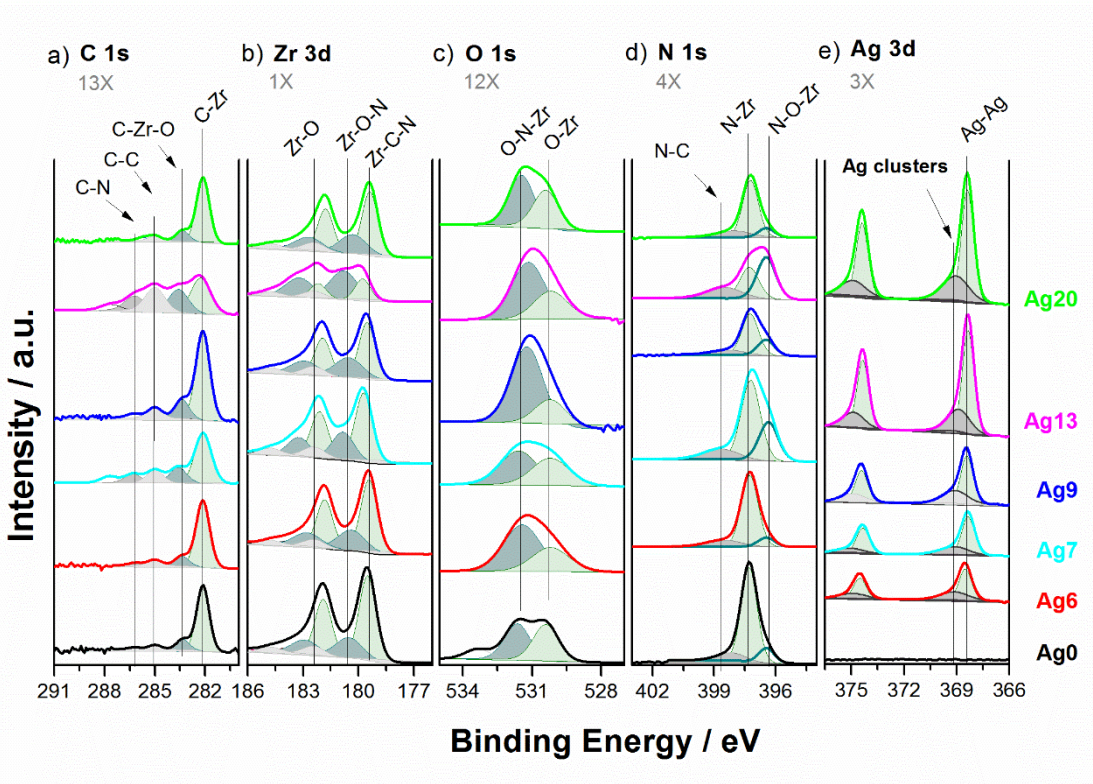

Figure 5-5 XPS spectra for ZrCN-Ag coatings after 10 minutes of ion bombardment.

After ion bombardment, a silver peak at higher energies (369.0 – 369.2 eV) than the Ag-Ag metallic peaks (368.4 eV) is observed, ascribed to silver in cluster forms. These clusters correspond to 35 ± 3 % of the total silver in the films, in every sample, indicating a constant ratio between the amount of silver in the films and the amount of clusters formed, even for different type of matrixes.

Consequently, after XPS analysis, it may be concluded that the bulk composition of the films is a complex mixture of phases: ZrCN(O), a-(C, N), metallic silver phases and residual ZrO_2. A general phase calculation was carried out taking into consideration all the previous analysis and the results are summarized in Figure 5-6. The residual ZrO_2 is, for every case, lower than 5 at.

% of the total composition of the films. For simplicity, the silver was considered as only one metallic phase, adding both metallic and clusters. Nevertheless, the concentration calculated by XPS must be treated carefully because the sputtering treatment, carried out to remove adventitious carbon and oxides, could lead to preferential the sputtering of some elements. For this reason, calculations about the stoichiometry of the ZrC_xN_{1-x} phase were not performed, but it is relevant to highlight that the amount of residual oxygen in the ZrC_xN_{1-x} phase was always lower than 5 at. %, as a result and in order to simplify the nomenclature the phase will be always addressed as ZrCN. In summary, two groups may be differentiated, films without and with amorphous carbon phases, as predicted in the previous chapter and in the introduction of the present chapter. Thus, when necessary, the first group will be named ZrCN/Ag (Ag0, Ag6 and Ag20), while the second one will be denominated ZrCN/Ag/a(C, N) (Ag7, Ag9 and Ag13).

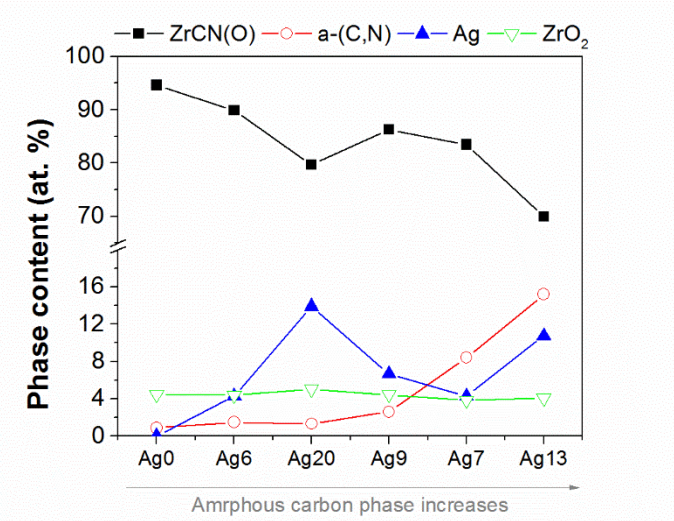

Figure 5-6 Phase composition calculated by XPS spectra after 10 min of ion bombardment as a function of the amorphous carbon content.

EDS analysis (shown in Figure 5-7) was carried out on both the surface and the cross section of the coatings performed in SEM and TEM observations, respectively, to verify that the preparation technique of the samples does not modified the chemistry of the coatings. Similar peaks and tendencies in their intensities are observed, although a slightly increase of oxygen could be detected in the films prepared for TEM analysis. This may be due to the exposure of the films to solvents such water, acetone and ethanol during the cross-section preparation. The intensities of silver peaks in the films with larger amount of amorphous carbon phases (Ag7 and Ag13) is more intense in the EDS-TEM analysis, when compared to EDS-SEM, which may be attributed to the preferential sputtering of carbon during the ion polishing process. In

addition, a very small signal closed to the Ag peak was observed for the 0 at% of silver sample, which was attributed to the incorporation of Ar ions during the ion polishing step of the samples preparation, which energy is located next to the silver line (Ar K_α 2.957 keV, Ag L_α 2.984 keV).

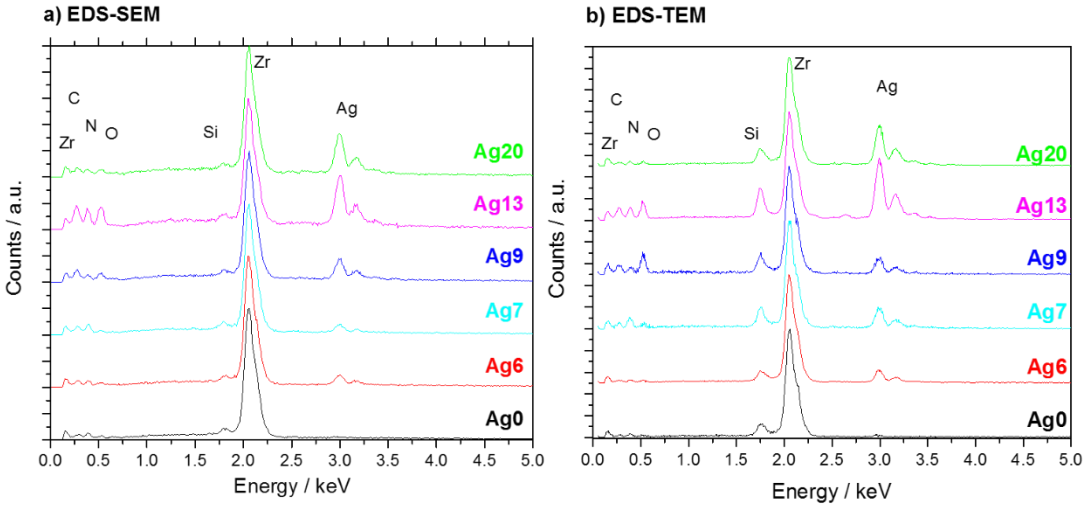

Figure 5-7 Energy dispersive spectroscopy performed by EDS coupled to a) SEM and b) TEM equipment.

5.2.2 Morphological characterization

Figure 5-8 depicts the SEM micrographs in cross-section and surface views of the coatings. The cross-section images of the coatings show mostly a columnar growth with less defined columns as silver and a-(C, N) phases increase. For ZrCN/Ag samples with high contents of silver, very small bright spots are observed which are believed to be silver nanoparticles. These white areas are also evident in the ZrCN/Ag/a-(C, N) coatings both in surface and cross-section analyses.

The surface morphology is much more compact as the amorphous phases content rises in the samples ZrCN/Ag/a-(C,N), revealing their predominant effect on controlling the morphology of the coatings as compared with silver. This effect can be explained by the ability of carbon phases to surround the ZrC_xN_{1-x} crystal in a composite-like configuration, in contrast to the silver phase, which tends to segregate and coalesce as isolated nanoparticles.

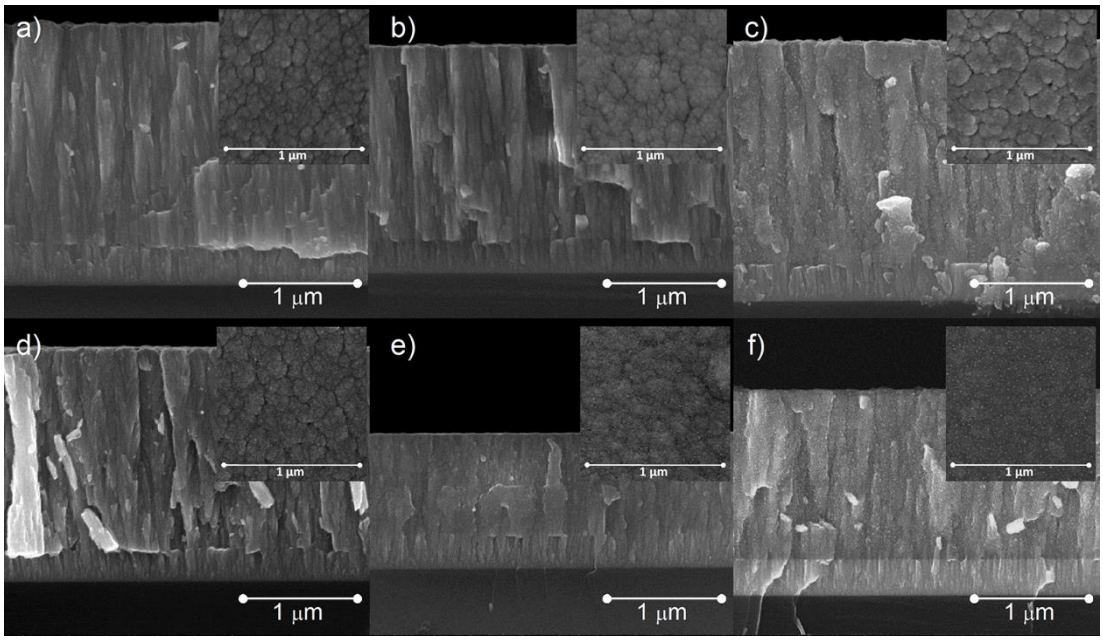

Figure 5-8 Surface and cross-section SEM images for ZrCN-Ag coatings a) Ag0, b) Ag6, c) Ag20, d) Ag9, e) Ag7 and f) Ag13

TEM images in Figure 5-9 show the more detailed morphologies of the cross section of the coatings. For the sample without silver, a few columns boundaries can be observed (Figure 5-9a), as bright lines perpendicular to the surface of the films. These boundary features are not visible for the other films, probably due to the densification of the films and/or silver incorporation along these zones. For the lowest content of silver, the coating showed small dark spots (<5 nm) homogeneously distributed that may correspond to silver nanoparticles; however, they could be also due to thickness or defect fringes. The increment of silver together with the amorphous phases produce changes in the morphology, as observed in the subsequent images (Figure 5-9 c-f). The presence of particles in the films is evident, growing in size as the silver content increases. For sample Ag13 and Ag20 the particles are well defined, taking elliptical or circular forms and varying from 5 nm to ~ 20 nm.

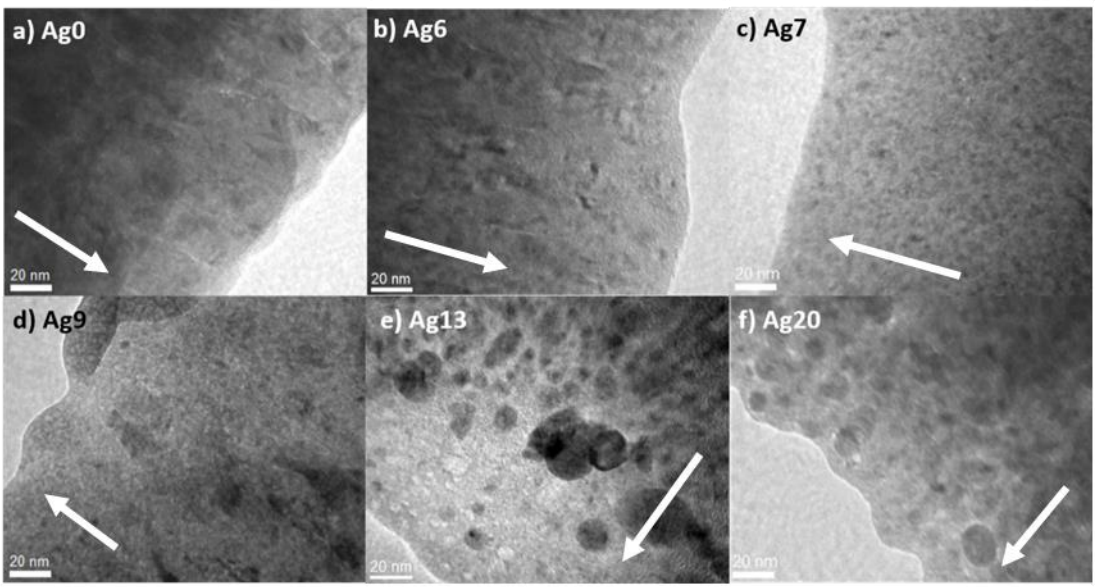

Figure 5-9 Transmission electron microscopy images of the ZrCN-Ag at 600 kX. The arrows in the figures indicate the coating growing direction.

Furthermore, the cross-section of the film close the outmost surface was also studied in the samples on the vicinity of the protective mounting epoxy. Silver segregation was observed, with particles encapsulated between the coatings surface and the epoxy used for the cross-section preparation, as shown in Figure 5-10. HR-TEM image of the particles were obtained in order to confirm the particle crystalline phase, as observed in Figure 5-10f, confirming that they are silver particles with (111) and (200) orientations. This segregation is believed to be due to diffusion and agglomeration of silver during the production of the films, as previously reported [13-14], and extensively discussed in the state of the art. The deposition of the coatings requires a constant flow of atoms sputtered from the target, which are deposited over the previous layer of material. This flow of material prevents the silver particles to agglomerate, by limiting the mobility. However, on the surface of the material, where no additional layer is deposited, the mobility of the species is less restricted, allowing the silver to agglomerate for reducing the surface energy.

The agglomeration was detected in different quantities, not only depending on the silver content, but also on the composition of the matrix. The highest silver agglomeration for Ag7, Ag13 and Ag20 indicates that the films with high amount of a-(C, N) phases may facilitate the silver mobility in the coatings. This is in agreement with a previous publication that states that silver has higher mobility in amorphous carbon phases when compared to transition metal nitrides [14]. Nonetheless, the case of Ag20, without (or with very low) content of a-(C, N) phases,

demonstrates that also the increase of silver in the matrix facilitates its mobility. Increasing the silver filling factor in the films makes the separation of the silver nanoparticles shorter, promoting the coalescence of the particles and the concentration of silver near to the surface. This agglomeration also corroborates the results obtained by XPS, before and after ion bombardment etching.

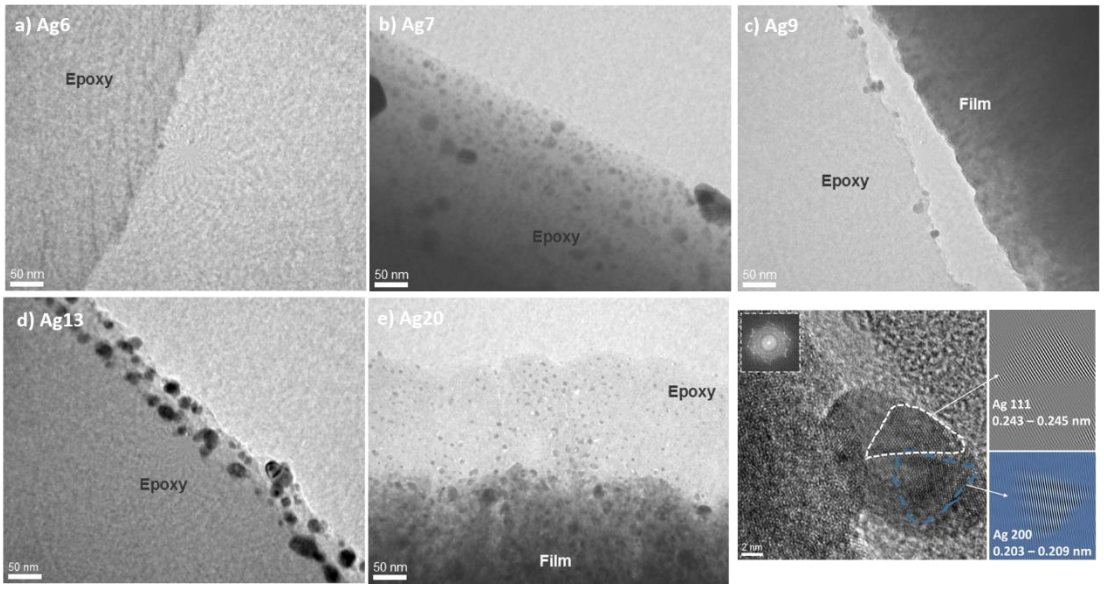

Figure 5-10 a) to e) Silver particles trapped in the epoxy from the surface of the ZrCN-Ag films and f) a HR-TEM for one of the silver particles

5.2.3 Structural characterization

Figure 5-11 shows the structural evolution as a function of the silver content in the films acquired by XRD. No clear tendencies are observed in the crystalline phases as silver is incorporated. ZrC_xN_{1-x} is characterized by a face-centered cubic lattice with diffraction peaks in the range [33.42 - 33.64 °] for the (111) plane and [38.78 - 39.04 °] for the (200) plane. (111) peak of FCC silver, at 38.30° in reference ICDD 01-087-0719, is expected to be overlapped with the (200) peak of the ZrC_xN_{1-x} phase, requiring a deconvolution for further analysis. The peaks were fitted using a Voigt function. Fixing the position of the FCC silver phase at 38.3°, supposing a constant cell size for the silver.

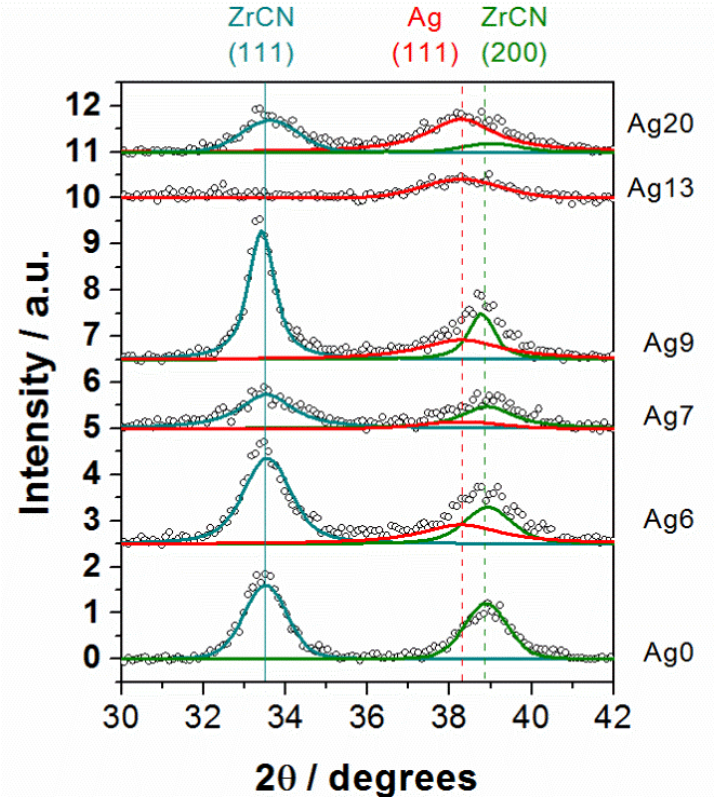

Figure 5-11 Coatings X-ray diffractograms, $ZrC_{0.5}N_{0.5}$ diffraction pattern (ICDD-03-065-8779) and Ag diffraction pattern (ICDD- 00-087-0719) are shown for comparison.

The silver grain size is very similar in all the films (~4 nm), while the ZrC_xN_{1-x} phase presents evident changes as shown in Table 5-3. The results may be analyzed by grouping the films in two sets considering the production parameters, as mentioned in the chapter introduction. In the first group, deposited at constant acetylene and nitrogen fluxes, a slight decrease of the ZrC_xN_{1-x} grain size is observed when the silver is increased. On the other hand, the second group, produced varying both silver current density and gases fluxes, showed a decrease on the grain size with the increase of a-(C,N) phase.

Table 5-3. Grain size and peak position for the crystalline ZrCN and Ag phases.

Sample	Ag current density [mA cm^{-2}]	C_2H_2 [sccm]	N_2 [sccm]	ZrCN Grain Size [nm]	ZrCN 111 peak position [degrees]	Ag Grain size [nm]
Ag0	0	1.2	3	7.2	33.52	-
Ag6	0.25	1.2	3	6.9	33.56	3.5
Ag7	0.25	1.2	9	3.8	33.55	3.7
Ag9	0.5	2.4	3	11.6	33.42	3.4
Ag13	0.5	2.4	9	-	-	3.7
Ag20	0.75	1.2	3	5.4	33.64	4.2

The position of (111) peak of ZrC_xN_{1-x} phase is also shown in Table 5-3 evidencing that the lowest peak position is reached for the Ag9 sample, which corresponds to the highest incorporation of C in the ZrC_xN_{1-x} lattice, as confirmed by XPS (Figure 5-5a). In fact, XPS intensity of the C-Zr peak for this coating is the highest among all the samples, since it was deposited with the highest C_2H_2/N_2 gas fluxes ratio.

In order to confirm the presence of the phases and obtain a more detailed structural characterization of the coatings, selected area diffraction patterns (SAD) and HR-TEM have been acquired for all the samples in different regions of the films.

Figure 5-12 shows the SAD patterns for all the samples. For clarity, a mathematical operation was applied to the patterns in order to reveal the weak diffraction lines (as explained in the methodology). Semicircles identifying the ZrCN FCC (red lines) and silver FCC (green lines) phases have been also added to the figures, in order to differentiate them. In general, the patterns consist of diffuse rings corresponding to a nano-polycristalline material with randomly distributed crystals. The diffraction lines are in agreement with the XRD results. Particularly, the lines for samples with larger amount of a-(C, N) showed more diffused lines (Ag7 and Ag13), while the other samples showed a combination of rings and spots corresponding to a larger distribution of crystals sizes of the phases. The silver diffraction lines corresponding to the plane (111) are not clearly distinguish for any of the samples, due to the overlapping between the ZrCN (200) and Ag (111) with theoretical interplanar distance of 0.231 nm and 0.233 nm, respectively. Thus, it is difficult to differentiate the contribution of silver and ZrCN. The direction (200) for the silver FCC, on the other hand, is not visibly for low Ag content in the films, while for the 13 and 20 at% (Ag13 and Ag20), this contribution is clearly present, compatible with the XRD results.

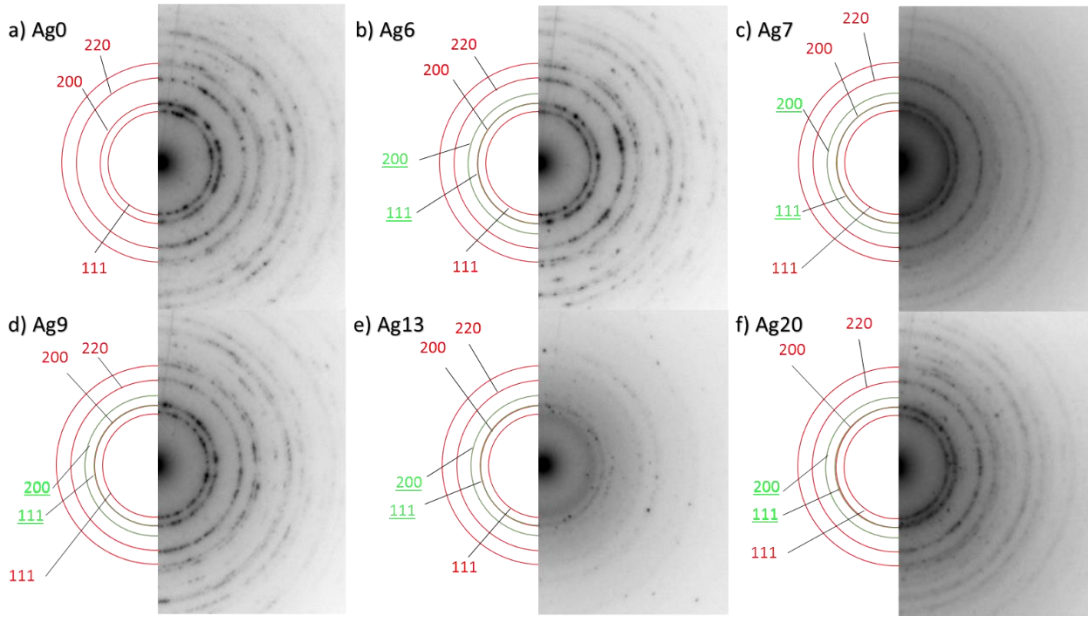

Figure 5-12 Selected area electron diffraction for the Zr-C-N-Ag coatings. The red lines correspond to the FCC $ZrC_{0.5}N_{0.5}$ standard pattern, while the green lines (underlined numbers) correspond to the FCC standard silver.

In order to confirm the existence of the silver nanoparticles, HR-TEM images were acquired in all the samples. Representative images for each sample are shown in Figure 5-13. In case of Ag0 large ZrCN crystallites are shown. Both (111) and (200) orientations were observed in different images with average interplanar distances (shown in Table 5-4) very similar to the ICDD-03-065-8779 corresponding to $ZrC_{0.5}N_{0.5}$ (0.267 nm for 111 and 0.231 nm for the plane 200). The silver nanoparticles existed in all the films with different sizes and distributions; some of them have been highlighted in the images with green dashed lines. As previously discussed, samples Ag6 and Ag20 possess very low amorphous carbon nitride content, and thus, the silver is surrounded by ZrCN crystallites, as observed in Figure 5-13 b and f. This makes the identification of the particles more difficult due to the low contrast between the crystalline regions. In addition, silver nanoparticles with (111) orientation presented similar interplanar distances with the ZrCN (200) plane, obscuring the process. However, some particles with grains oriented to (200) direction have been detected and these images are shown in Figure 5-13 to ensure that the selected regions corresponds to silver. The silver particles, in some cases, are polycrystalline showing both (111) and (200) grain orientations, as observed in Figure 5-13 f.

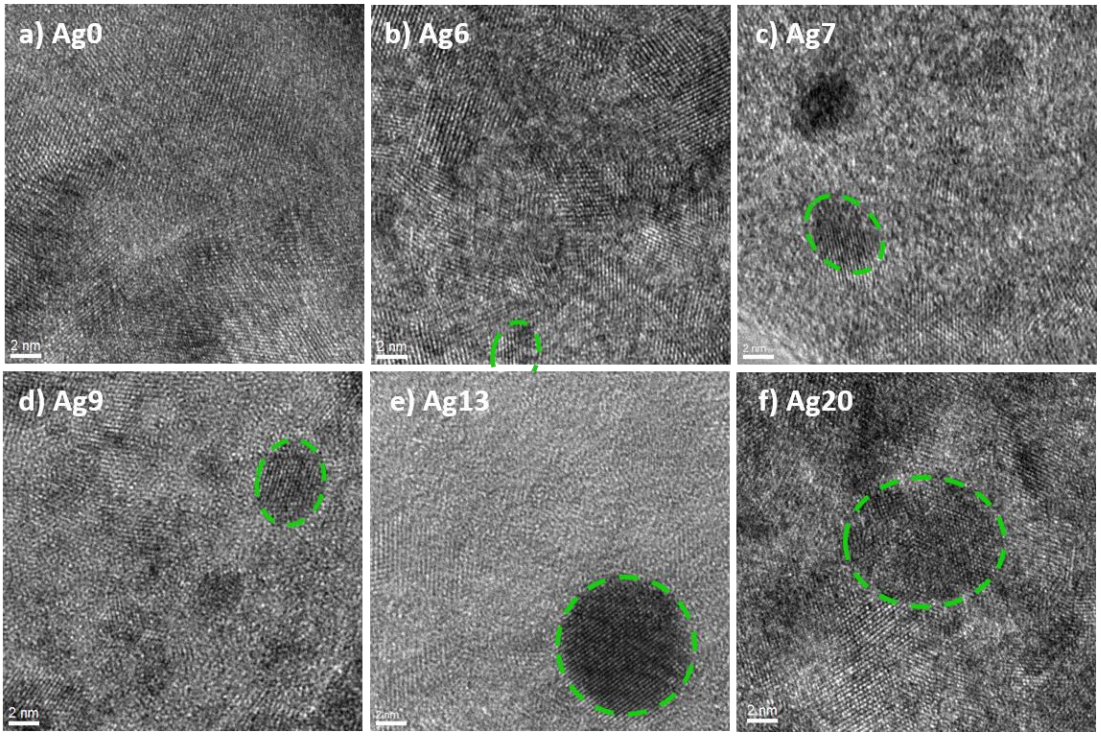

Figure 5-13 High resolution transmission electron microscopy images of the ZrCN-Ag coatings. The dashed lines identify a silver nanoparticle in the matrix.

Table 5-4 Interplanar distances for ZrCN and Ag phases calculated in HR-TEM images.

	ZrCN		Ag	
	(1 1 1)	(2 0 0)	(1 1 1)	(2 0 0)
Ag0	2.67	2.33	–	–
Ag6	2.71	2.37	2.30	2.10
Ag7	2.74	2.38	2.43	2.08
Ag9	2.69	2.35	2.43	2.09
Ag13	2.94	–	2.33	2.03
Ag20	2.61	2.31	2.37	2.09

The particles are usually surrounded by the amorphous phase, when existing in the matrix. For very large content of a-(C, N) (Ag13), for instance, the ZrCN is also expected to be encapsulated by this carbon amorphous phase. Bright field and dark field images of this sample were obtained in order to corroborate the presence of small grains of the ZrCN phase, and the results are shown in Figure 5-14. Dark-field micrographs were acquired in different position of the diffraction pattern (as shown in the inset of Figure 5-14a), revealing a large distribution of very small crystals that belong to both silver and ZrCN phases, with both silver and ZrCN crystals encapsulated by the amorphous phase. HR-TEM images also corroborate it (Figure 5-14d), differentiating the existence of both silver and ZrCN crystals in sample Ag13. The interplanar

distance of ZrCN showed larger values when compared to the others films, probably explained due to the existence of a cubic ZrON phase (0.292 nm for (222), ICDD-00-050-1170), validating the XPS analysis regarding the formation of Zr-O-N bonds. These grains were not observed in the other compositions, such as Ag7, but the occurrence of such phase should not be discarded, as the XPS revealed this bonding states.

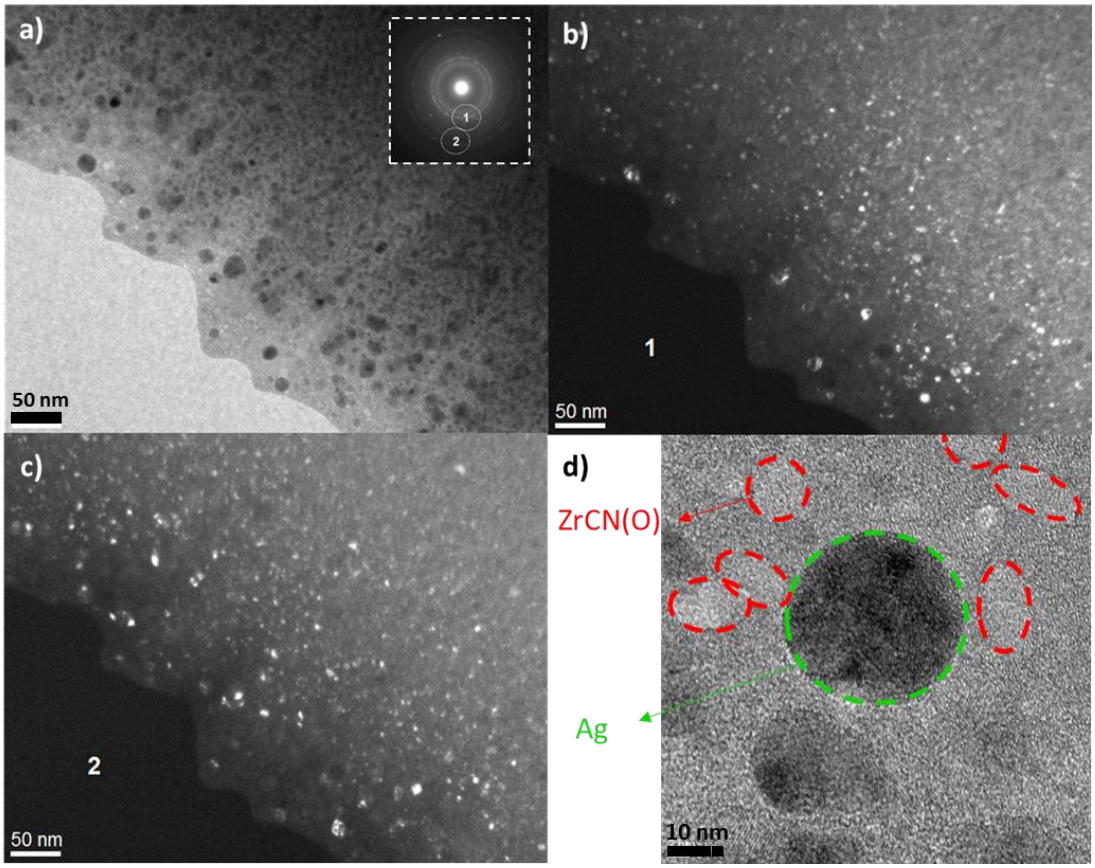

Figure 5-14 a) Bright field mode for sample Ag13, b) dark-filed mode of the samples Ag13 in the zone 1 highlighted in the diffraction pattern in the inset of figure a), c) dark-filed mode of the samples Ag13 in the zone 2 highlighted in the diffraction pattern in the inset of figure a) and d) HR-TEM images of the sample Ag13 with selecting both Ag and ZrCN(O) particles.

The crystalline and amorphous phases were additionally characterizaed by Raman spectroscopy. The ZrC_xN_{1-x} bands (the first order Raman scattering) are observed due to the disorder and imperfection of the structure caused by oxygen and carbon atoms in the lattice, as well as the high energy of the deposition process. These bands may be divided in low frequency modes (150–300 cm^{-1} region), corresponding to acoustic phonons, and high frequency optical phonons (400–650 cm^{-1}) [15], both transversal and longitudinal, as shown in Figure 5-15a. In addition to these bands, a small peak or shoulder is observed close to 700 to 750 cm^{-1}, attributed to the oxygen in the lattice. These peaks are detected in every film, with the

exception of Ag13 sample in which only the Zr-N-O peak is distinguished, which may be attributed to the low content of Zr and confirm the presence of such phase observed by XPS and HR-TEM.

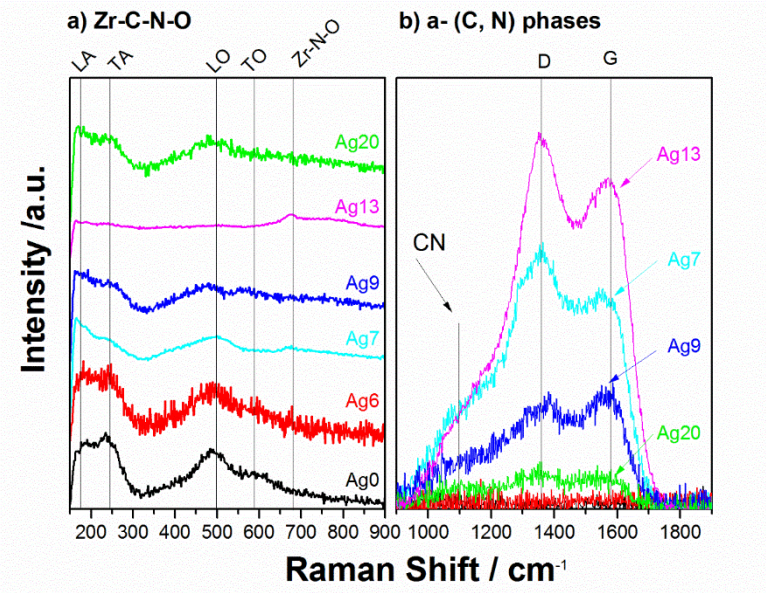

Figure 5-15 Coatings Raman spectroscopy for a) low Raman shift (150 and 900 cm^{-1}) associated to ZrNC(O) phase and b) high Raman shift (900 and 1900 cm^{-1}) attributed to amorphous carbon phases

The a-(C, N) phases were corroborated by C-C bonds identified by Raman spectroscopy (Figure 5-15b). The films exhibit two characteristic bands, around 1360 cm^{-1} and 1580 cm^{-1}, which correspond to the signal of disordered and graphitic carbon bonds [1, 16]. These two bands are more evident as the amount of carbon phases increases in the material, as observed in the phase composition graph (Figure 5-6). These results support the fact that the amorphous phases are incrementing in the same order as exposed by XPS. Ferrari et al. has extensively studied amorphous carbon phases by Raman spectroscopy and has found that the ratio between the D and G bands intensities may be related to the fraction of sp^3 bond in hydrogenated amorphous carbon phases [16]. In this report, the ratio between these two bands is virtually constant varying between 0.95 and 1.20, which implies a very similar structure for the a-(C, N) present in the films, with a low amount of sp^3 bonds, which may be explained by the presence of H in the films originated from the reactive C_2H_2 gas.

5.3 Conclusion

It was demonstrated the possibility of producing coatings with different silver content (0 to 16 at. %), in which zirconium carbonitrides (70 to 95 at. %), amorphous carbon nitride (0 to 16 at.

%) and residual zirconium oxide (~ 5 at. %) phases coexist with metallic silver. The profile analysis evidenced a highly oxidized surface due to the affinity of Zr to form ZrO_2, and silver segregation to the surface. The composition after Ar^+ bombardment revealed the contribution of silver clusters and metallic silver, together with the mentioned phases that vary in content depending on the deposition parameters. Finally, STEM images showed silver nanoparticles distributed in the Zr-C-N matrix with sizes around 2 to 20 nm, as well as silver surface agglomeration with sizes < 80 nm.

5.4 References

1. Braic, M.; Braic, V.; Balaceanu, M.; Vladescu, A.; Zoita, C.; Titorencu, I.; Jinga, V., (Zr, Ti) Cn Coatings as Potential Candidates for Biomedical Applications. *Surface and Coatings Technology* **2011,** *206* (4), 604-609.

2. Crist, B. V., *Handbooks of Monochromatic Xps Spectra*. XPS International: California 94040, USA, **1999**; p 548.

3. Calderon V, S.; Galindo, R. E.; Benito, N.; Palacio, C.; Cavaleiro, A.; Carvalho, S., Ag+ Release Inhibition from Zrcn–Ag Coatings by Surface Agglomeration Mechanism: Structural Characterization. *Journal of Physics D: Applied Physics* **2013,** *46* (32), 325-303.

4. Silva, E.; Rebelo de Figueiredo, M.; Franz, R.; Escobar Galindo, R.; Palacio, C.; Espinosa, A.; Calderon V, S.; Mitterer, C.; Carvalho, S., Structure-Property Relations in Zrcn Coatings for Tribological Applications. *Surface and Coatings Technology* **2010,** *205* (7), 2134-2141.

5. Arias, D.; Arango, Y.; Devia, A., Study of Tin and Zrn Thin Films Grown by Cathodic Arc Technique. *Applied Surface Science* **2006,** *253* (4), 1683-1690.

6. Chase, M. W., Jr., Nist-Janaf Themochemical Tables, Fourth Edition. *J. Phys. Chem. Ref. Data, Monograph 9* **1998**, 1-1951.

7. Manninen, N.; Galindo, R. E.; Benito, N.; Figueiredo, N.; Cavaleiro, A.; Palacio, C.; Carvalho, S., Ag–Ti (C, N)-Based Coatings for Biomedical Applications: Influence of Silver Content on the Structural Properties. *Journal of Physics D: Applied Physics* **2011,** *44* (37), 375501.

8. Chu, A.; Qin, M.; Rafi ud, d.; Zhang, L.; Lu, H.; Jia, B.; Qu, X., Carbothermal Synthesis of Zrc Powders Using a Combustion Synthesis Precursor. *International Journal of Refractory Metals and Hard Materials* **2013,** *36* (0), 204-210.

9. Saha, N. C.; Tompkins, H. G., Titanium Nitride Oxidation Chemistry: An X-Ray Photoelectron Spectroscopy Study. *Journal of Applied Physics* **1992,** *72* (7), 3072-3079.

10. Cubillos, G. I.; Bethencourt, M.; Olaya, J. J.; Alfonso, J. E.; Marco, J. F., The Influence of Deposition Temperature on Microstructure and Corrosion Resistance of Zroxny/Zro2 Coatings Deposited Using Rf Sputtering. *Applied Surface Science* **2014,** *309* (0), 181-187.

11. Siozios, A.; Zoubos, H.; Pliatsikas, N.; Koutsogeorgis, D. C.; Vourlias, G.; Pavlidou, E.; Cranton, W.; Patsalas, P., Growth and Annealing Strategies to Control the Microstructure of Aln:Ag Nanocomposite Films for Plasmonic Applications. *Surface and Coatings Technology* **2014,** *255* (0), 28-36.

12. Escobar Galindo, R.; Manninen, N. K.; Palacio, C.; Carvalho, S., Advanced Surface Characterization of Silver Nanocluster Segregation in Ag–Ticn Bioactive Coatings by Rbs, Gdoes, and Arxps. *Analytical and Bioanalytical Chemistry* **2013,** *405* (19), 6259-6269.

13. Chakravadhanula, V. S. K.; Mishra, Y. K.; Kotnur, V. G.; Avasthi, D. K.; Strunskus, T.; Zaporotchenko, V.; Fink, D.; Kienle, L.; Faupel, F., Microstructural and Plasmonic Modifications in Ag–Tio2 and Au–Tio2 Nanocomposites through Ion Beam Irradiation. *Beilstein Journal of Nanotechnology* **2014,** *5*, 1419-1431.

14. Manninen, N. K.; Galindo, R. E.; Carvalho, S.; Cavaleiro, A., Silver Surface Segregation in Ag-Dlc Nanocomposite Coatings. *Surface and Coatings Technology* **2015,** *267* (0), 90-97.

15. Moura, C.; Carvalho, P.; Vaz, F.; Cunha, L.; Alves, E., Raman Spectra and Structural Analysis in Zroxny Thin Films. *Thin Solid Films* **2006,** *515* (3), 1132-1137.

16. Ferrari, A.; Robertson, J., Interpretation of Raman Spectra of Disordered and Amorphous Carbon. *Physical review B* **2000,** *61* (20), 14095.

CHAPTER VI - Electrochemical Response of ZrCN-Ag-a(C,N) Coatings in Simulated Body Fluids

The following chapter is partially based on the results published in: S. Calderon V, A. Cavaleiro, S. Carvalho, Electrochemical response of ZrCN-Ag-a(C,N) coatings in simulated body fluids, Electrochimica Acta, (2015).

6 Introduction

Although ZrCN coatings have been recognized to improve the corrosion resistance of base material in different fluids [1-2], little is known about the ability of the films for protection in simulated body fluids. In addition, the complexity of the ZrCN-Ag system, which allows the co-existence of a large variety of phases such as ZrCN, amorphous carbon phases, metallic silver, and some residual oxides which may easily alter the electrochemical behavior of the system.

In chapter IV, a general electrochemical characterization was performed in order to be able to optimize the functional properties, evidencing that the corrosion resistance of the films may improve the corrosion resistance of the SS316L. Moreover, in previous reports, our group has described that the increase of silver metallic phase in ZrCN-Ag coatings, accompanied by a reduction of ZrCN grain size and the increase of amorphous phases in the material, could explain the more electrochemical active behavior of the samples in a simple electrolyte (NaCl 0.9%) [3].

In this chapter, the electrochemical behavior of ZrCN-Ag coatings with and without amorphous phases, deposited on 316L stainless steel, is completed; the evolution of the samples as a function of the immersion time in a more complex simulated body fluid, with composition that mimic the synovial fluid present in the human joints. The results are compared with the chemical and structural properties of the coatings, discussed in previous chapters.

6.1 Materials and methods

The coatings electrochemical behavior was evaluated by electrochemical impedance spectroscopy (EIS) at open circuit potential, after 1h of immersion for stabilization. The samples with best corrosion resistance properties were utilized for immersion tests in order to observe the evolution of the electrochemical parameters for 15 days. Potentiodynamic tests were performed in the two stages (as-deposited (after 1 h) and 336h after immersion in HBSS + A).

The surface composition before and after immersion tests was assessed by XPS, the surface free energy and the hydrophobicity parameters of surfaces were determined by the sessile drop contact angle technique[4].

[4] For a more detailed description of the techniques and experimental procedures please see chapter III.

6.2 Results and discussion

6.2.1 Electrochemical characterization

The electrochemical characterization is divided into two sections. The first section is focused on the phase composition effect on the electrochemical behavior, whereas, the second section discusses the electrochemical behavior of a selected set of samples as a function of immersion time in Hank's balanced salt solution with 10 g L^{-1} of albumin from bovine serum.

6.2.1.1 Electrochemical characterization vs. phase composition

The open circuit potential of all the samples shows a very stable behavior, varying between -70 to -150 mV for all the coatings with silver, while the films without silver (Ag0) clearly exhibited lower open circuit potential, around -220 mV, than all the other samples (Figure 6-1). This behavior can be understood on the basis of a mixture of electrical conductive phases and can be explained by the mixed potential theory which states that, for two conductive phases in electrical contact, the resulting OCP is located between the OCP of both phases [4]. Thus, the increase of the OCP for the coatings containing Ag and amorphous carbon phases is a consequence of the larger potential exhibited by these phases when compared to the pure ZrCN phase. When those phases are incorporated in the coatings, a nanocomposite material is created, where the formation of couples such as, ZrCN/Ag, ZrCN/a-(C,N), Ag/a-(C,N), promotes different electrochemical processes, which contribute to the open circuit potential values in the cell. In Figure 6-1, the OCP for a pure Ag [5] and a-C [6] films, produced in our group, were added for comparison.

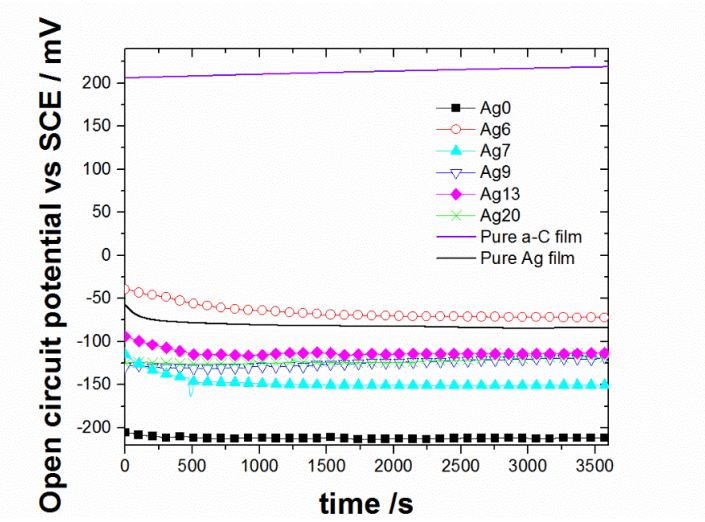

Figure 6-1 Open circuit potential evolution of ZrCN-Ag coatings as a function of immersion time.

The potentiodynamic curves for all the samples and the bared 316 L stainless steel are shown in Figure 6-2. Almost one order of magnitude reduction in density currents for the film with the lowest silver content (6 at. %) was observed, compared to SS316L, evidencing an improved corrosion resistance. For higher silver content (7 and 9 at. %) the reduction is also noticed, but only around the corrosion potential (Ecorr ± 100 mV); after this value, the density current is comparable to the stainless steel or even larger. Films with high silver content exhibit a more electrochemical active behavior as it is shown by the shift of the curves to higher density.

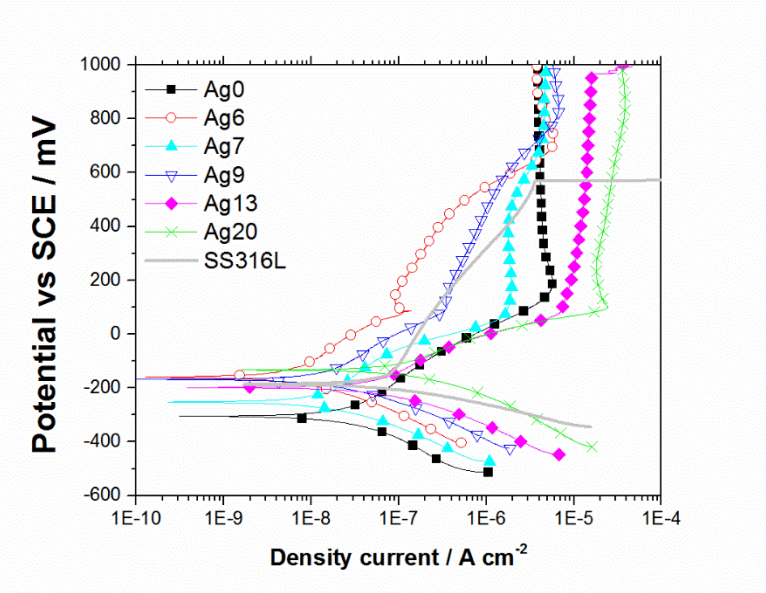

Figure 6-2 Potentiodynamic curves of ZrCN-Ag coatings in Hank's balanced salt solution with 10 g of albumin per liter.

The breakdown potential, usually associated to pitting for the stainless steel, is not clear in any of the films for the reported range of potential, revealing a larger resistance to pitting formation for the coated samples.

Figure 6-3 depicts the results of the EIS experiments, using both Nyquist plot and the phase vs frequency in Figure 6-3a and Figure 6-3b, respectively. Figure 6-3a shows a reduction of the impedance as the silver content is increased, with the exception of sample Ag0 that exhibits lower impedance values than Ag6 film. Figure 6-3b, on the other hand, shows that the coatings, with the exception of Ag13, evidenced one time constant, suggesting a dense structure of the coating. The behavior of Ag13 is typical of an electrochemical porous film. This film permits the penetration of the electrolyte creating a second time constant attributed to the pores in the film. In consequence, the data were fitted using two equivalent circuits, shown in Figure 6-3b inset. The equivalent circuit located in the top part of the inset was used for all the samples, including

the uncoated stainless steel, whereas sample Ag13 results were fitted using the second equivalent circuit. The capacitance elements are replaced by a constant phase element (CPE) in order to consider the surface roughness and heterogeneities [7-9]. Rp represents the polarization resistance element, which characterizes the charge transfer resistance of the material in both circuits. Moreover, two elements are added to the second circuit to take into consideration the higher porosity in the Ag13 film.

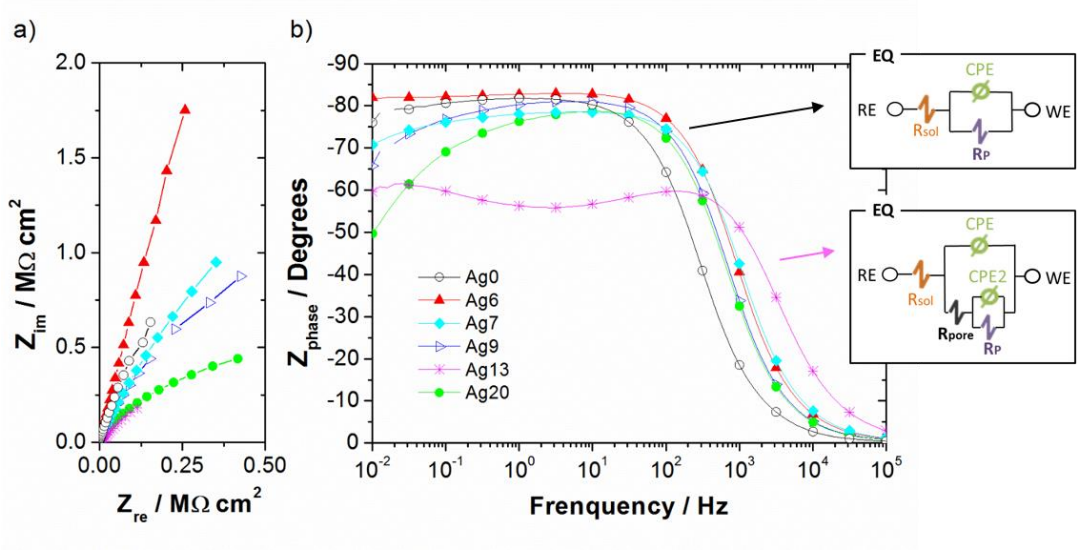

Figure 6-3 Nyquist plots of ZrCN-Ag coated SS316L steel, using Hank's balanced salt solution with 10 g L-1 of albumin at 37 °C. Inset: Equivalent circuit used to fit the EIS data, where the RE, Rsol, Rp, CPE and WE represents the reference electrode (SCE), solution resistance, polarization resistance, a constant phase element and the working electrode (sample), respectively.

The polarization resistance, displayed in Figure 6-4, showed a reduction as the silver content increases, associated to the more electrochemical active silver phase compared to the ceramic behavior of the ZrC_xN_{1-x} and amorphous carbon phases [3]. Although the silver content of the films is a decisive parameter affecting the electrochemical activity of the films, the morphology and phase structure changes promoted by compositional variations should not be disregarded. The carbon phases, for example, are also detrimental in this type of films, evidenced by the fact that for similar silver content (Ag6 with 6 at. % and Ag7 with 7 at. %) the polarization resistance and the potentiodynamic curves revealed a degenerated corrosion resistance for the Ag7 (sample with higher amount of amorphous carbon phases). Such behavior may be explained by the reduction of thickness (i.e. Ag7), as well as the increment of the number of diffusion paths for the electrolyte to contact a larger area in the films.

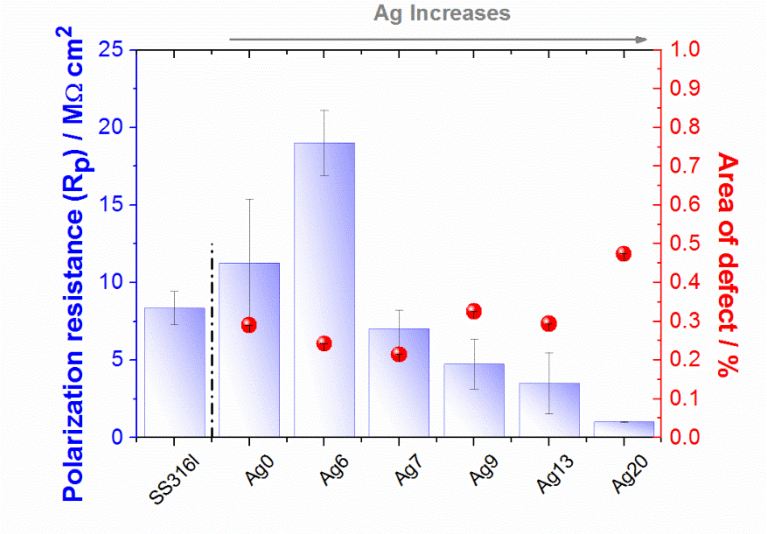

Figure 6-4 Bar plot of the polarization resistance of uncoated and ZrCN-Ag coated SS316L steel, in Hank's balanced salt solution with 10 g L-1 of albumin at 37 °C. Scatter plot of the area of defects on the material surface observed by optical microscopy.

As the coatings become less columnar-like, the number of boundaries between the columns or grains increases, as schematically shown in Figure 6-5. These boundaries can create zones with nanoporosity that permit the flux of ions, which alters the electrochemical behavior of the coatings. The boundaries regions can act as passivation zones, which improve the corrosion behavior of the material or behave as diffusion paths when the material is chemically inert, depending on the electrochemical activity of the phases. Both scenarios can be foreseen in the present materials due to the different phase compositions. Firstly, ZrC_xN_{1-x} phase can passivate at the boundaries regions, while in regions with pure carbon phases, the high inertness of the carbon may work purely as diffusion paths, explaining the additional deterioration of the films. Finally, the addition of silver also slightly promote the intensification of macro-defects (Figure 6-4), such as pin-holes and droplets on the surface of the films, which are known to produce larger contact areas between film and the electrolyte, producing higher electrochemical activity [7, 10-12].

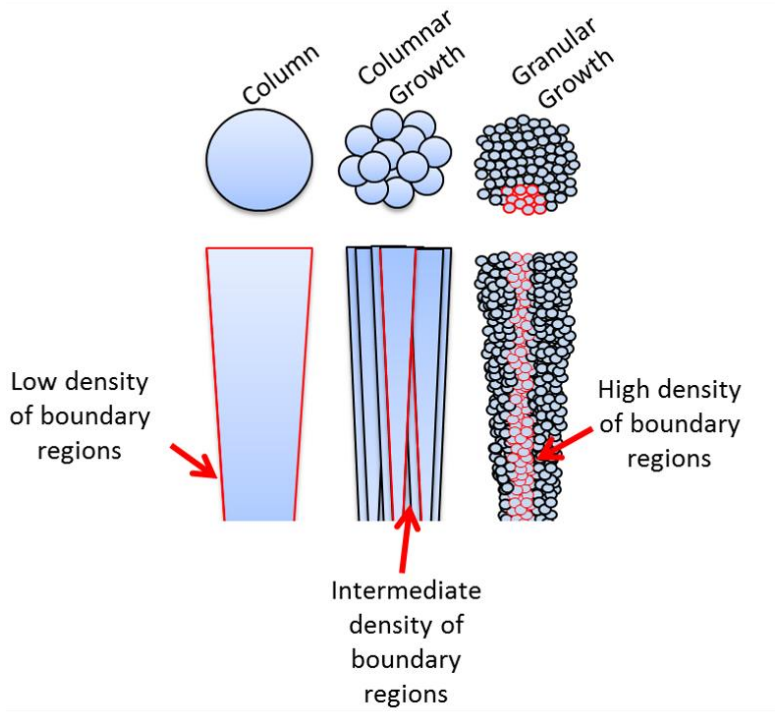

Figure 6-5 Scheme of the evolution of the film growth from columnar to granular and the impact on the boundary regions.

The enhanced corrosion behavior of the Ag6 sample, when compared to the Ag0, despite of the similarities in morphology, thickness, suggests that a material with a pure $ZrC_{0.5}N_{0.5}$ (Ag6) phase, with no amorphous phases, presents higher corrosion resistance than a compound with different stoichiometry ZrC_xN_{1-x} (Ag0) since, despite the fact that the ratio C+N/Zr is similar in both cases, the ratio between C/N for Ag0 is almost half of the Ag6, but additional research must be carried out to verify it.

The CPE parameter (Table 6-1), on the other hand, reflects the capacitive behavior of the interface between the fluid and the films, but both CPE and α parameters must be taken into consideration for its evaluation. α values are close to 1 for low content silver films, revealing a more capacitive behavior, but the admittance increases as the silver is introduced, probably due to higher contact areas between the films and the electrolyte induced by the more granular behavior, which also explains the higher CPE admittance in sample Ag13.

Table 6-1 EIS fitting parameters of ZrCN-Ag coatings in Hank's balanced salt solution with 10 g L-1 of albumin.

	Rsol [Ω cm²]	Rp [MΩ cm²]	Rpor [kΩ cm²]	CPE Yo [μS s$^{\alpha}$ cm²]	α-CPE	CPE2 Yo [μS s$^{\alpha}$ cm²]	α-CPE2
SS316L	44.3	8.3	-	25.9	0.92	-	-
Ag0	42.5	11.3	-	20.8	0.91	-	-
Ag6	64.1	18.6	-	7.7	0.94	-	-
Ag7	35.8	7.0	-	10.9	0.88	-	-
Ag9	38.9	4.5	-	12.9	0.91	-	-
Ag13	33.1	3.5	5.2	17.0	0.76	17.0	0.69
Ag20	41.9	1.0	-	15.5	0.87	-	-

6.2.1.2 Electrochemical Characterization vs immersion time in HBSS.

Three samples (Ag0, Ag6 and Ag9) were selected to evaluate the effect of the electrolyte as a function of the immersion time. The samples were selected taking into consideration that samples with low silver and amorphous carbon content coatings present better corrosion resistance, as shown in the previous section. Figure 6-6 shows the open circuit potential (OCP) as a function of the immersion time, evidencing similar tendencies for all the studied samples. A decrease of the OCP with increasing immersion time is observed, with a steeper trend for samples with silver. Similar behavior has been reported for albumin-containing electrolytes and metallic samples; the addition of protein to the electrolyte gives rise to an immediate drop of the OCP due to albumin adsorption [13]. Thus, the decrease of the OCP may be explained as a combination of three factors; the formation of a thicker zirconium oxide layer, the adsorption of albumin on the surface and the reduction of silver, due to its release from the material surface, which will be later corroborated by XPS. Additionally, the larger reduction on the films containing silver support the hypotheses, since lower albumin adsorption and none silver ion release are expected from Ag0 due to its hydrophilic character and due to 0 at.% of silver content on its composition, respectively, as later explained.

An overlap of the anodic polarization curves for the sample after 0h and 336 h of immersion is presented in Figure 6-7. After the immersion tests, and in agreement with the OCP results, the coatings tested showed a decrease in the corrosion potential when compared to the sample with 0h immersion time, as well as a more passive behavior, also explained by the formation of the zirconium oxide, the silver release and the protective albumin layer.

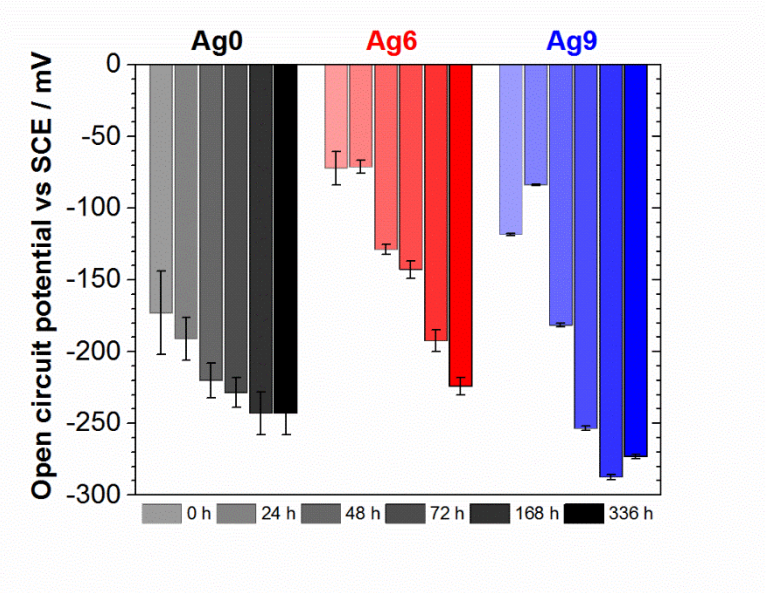

Figure 6-6 Open circuit potential as a function of the immersion time of ZrCN-Ag coatings in Hank's balanced salt solution with 10 g/L of albumin at 37 °C

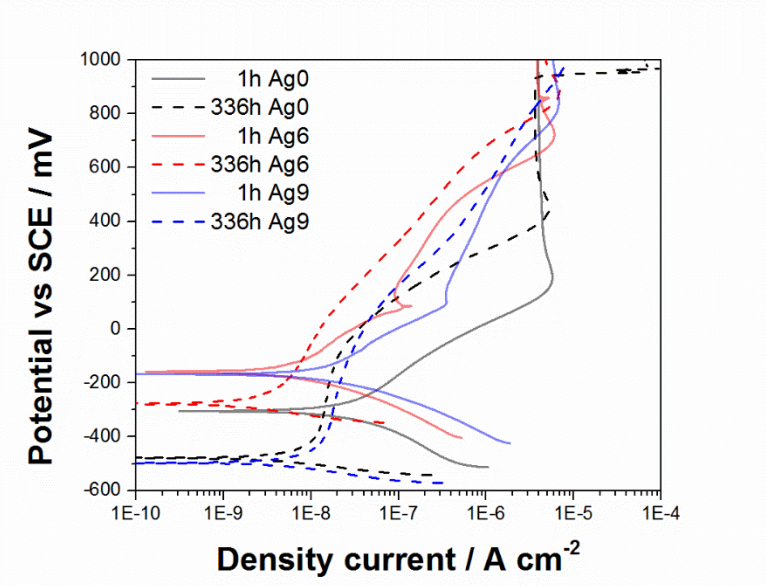

Figure 6-7 Potentiodynamic curves of Ag0, Ag6 and Ag9 in Hank's balanced salt solution with 10 g of albumin per liter after 1h and 336 h of immersion.

Electrochemical impedance spectroscopy experiments carried out with increasing immersion time, revealed an increment of the impedance as observed in the Nyquist plot in Figure 6-8. These results were also fitted using the equivalent circuit in the inset of Figure 6-3, as previously described. The polarization resistance increased as a function of time for all the samples (cf. Figure 6-9), during the first 72 hours of immersion, reaching then a plateau-like zone. This behavior is commonly associated to a passivation film that may be formed on the material

surface, inducing the blocking of the charge transfer and impeding the ionic exchange between the electrolyte and the material.

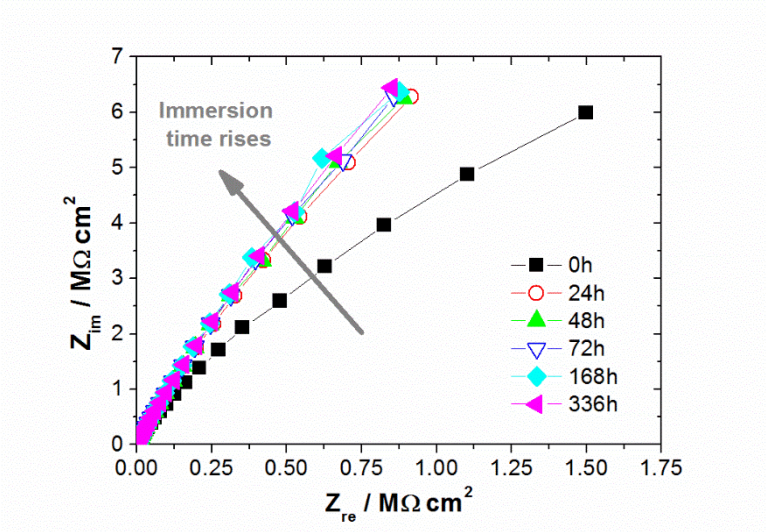

Figure 6-8 Nyquist plot for a representative coating (Ag6) as a function of the immersion time, using Hank's balanced salt solution with 10 g/L of albumin at 37 °C.

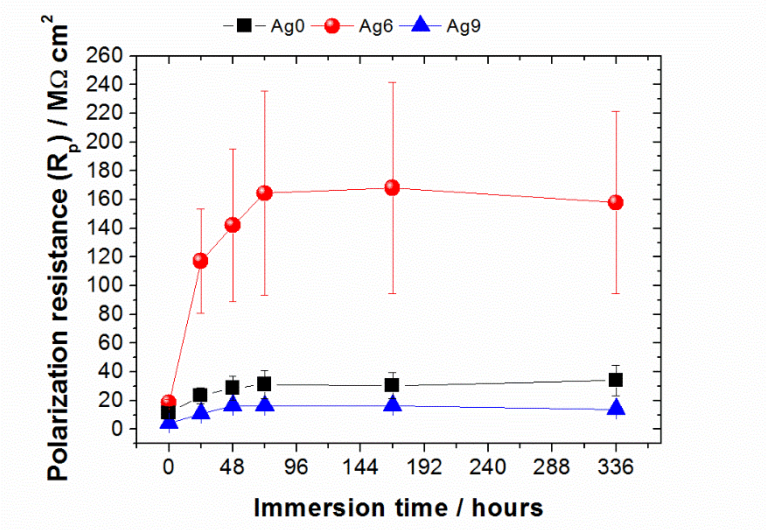

Figure 6-9 Polarization resistance (Rp) of ZrCN-Ag samples as a function of immersion time in Hank's balanced salt solution with 10 g/L of albumin at 37 °C.

The surface modified zone can be analyzed by X-ray photoelectron spectroscopy (XPS). Surface oxidation is expected due to the high affinity of Zr to form oxides, particularly ZrO_2 with an enthalpy of formation around -1097.46 kJ/mol compared to ZrN (-365.26 kJ/mol) or ZrC (-196.65 kJ/mol) [14]. Zr-O bonds were detected by XPS around 182.3 eV for Zr and 530.2 eV for O (Figure 6-10a and e). In addition, the formation of a layer rich in C-N, C-O and C-N-O, related to the adsorption of the albumin on the surface of the material is observed. This albumin layer

can be confirmed by the attenuation of the Zr-O, N-Zr, Zr-N and Ag-Ag bonds intensities, shown in Figure 6-10 before and after immersion. The formation of albumin can be roughly qualitatively characterized taking into consideration the N-C (399.8 ± 0.2 eV) peak intensity changes before and after immersion, associated to the amine or amide groups of the protein [15]. This peak evidenced that the films with silver (Ag6 and Ag9) showed 1.4 times more albumin adsorption than the sample without silver (Ag0). These differences of albumin adsorption are justified by the difference in the surface energy of the samples with and without silver (Table 6-1). The sample without Ag is the only hydrophilic, and hence, less albumin adsorption is predictable, since the albumin adsorbs more easily onto hydrophobic surfaces [16].

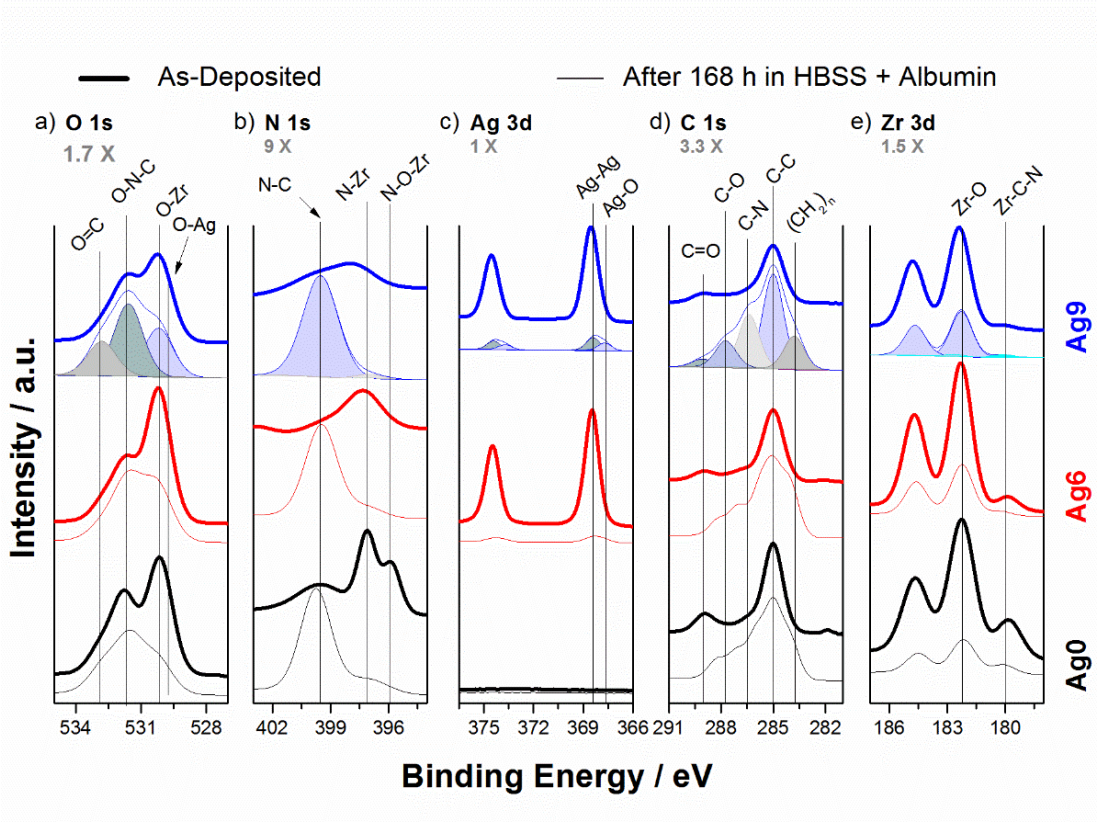

Figure 6-10 XPS spectra of Zr 3d, Ag 3d, O 1s, N 1s and C 1s core levels of ZrCN-Ag samples before and after 168h of immersion in Hank's balanced salt solution with 10 g L-1 of albumin at 37 °C. Every element is displayed at different scales to clearly identify the peaks. Each scale is shown below the element name.

Table 6-6-2 Water, formamide and bromonaphtalene contact angles, and surface interation (free Energy ΔG) between the water and the surface (ΔG LW = apolar Lifshitz–van der Waals component; ΔG AB = electron acceptor component).

	Interaction solid liquid (mJ m^{-2})			Contact angle (degrees)		
	ΔG	ΔG^{LW}	ΔG_{AB}	Water	Formamide	Bromonaphtalene
SS316L	-85.1	-75.4	-9.6	86 ± 5	68 ± 3	36 ± 3
Ag0	-105.1	-80.0	-25.1	64 ± 9	36 ± 5	23 ± 3
Ag6	-85.1	-76.9	-8.2	98 ± 2	62 ± 3	32 ± 6
Ag7	-74.3	-72.9	-1.3	101 ± 3	74 ± 6	41 ± 2
Ag9	-77.5	-72.1	-5.5	104 ± 1	70 ± 1	43 ± 1
Ag13	-86.6	-74.1	-12.5	96 ± 1	60 ± 2	39 ± 2
Ag20	-83.2	-76.8	-6.4	95 ± 3	64 ± 3	32 ± 5

Moreover, the relative intensity of silver is largely reduced after immersion, compared to the attenuation of Zr-O, N-Zr and Zr-N, as shown in Figure 6-10, attributed to a silver ion release to the electrolyte and/or the attenuation due to the adsorbed protein layer. The silver release has been previously demonstrated for similar materials, in very low quantities, in the first 7 to 15 nm of the material[17]. As a result, silver not only shows the characteristic binding energy of pure metallic state (Ag-Ag 368.4 eV) after immersion, but also an oxidized state at 367.7 eV.

The increase of the charge transfer resistance of the materials is a consequence of the three factors described above, providing protection to the coatings and enhancing the corrosion resistance of the material, which, in the case of Ag6, attains values almost one order of magnitude larger after 336h of immersion.

6.3 Conclusion

A large deterioration of the electrochemical stability of the films with high silver content increase was demonstrated, as well as the negative effect of the amorphous carbon phases on the polarization resistance of the coatings, ascribed to morphological changes. The immersion test revealed a progressive increment of the polarization resistance with time, attributed to surface and pores passivation, due to the formation of both ZrO_2 and albumin protective layers on the surface, as shown by X-ray photoelectron spectroscopy.

6.4 References

1. Gu, J.-D.; Chen, P.-L., Investigation of the Corrosion Resistance of Zrcn Hard Coatings Fabricated by Advanced Controlled Arc Plasma Deposition. *Surface and Coatings Technology* **2006,** *200* (10), 3341-3346.

2. Rie, K. T.; Gebauer, A.; Wöhle, J., Plasma Assisted Cvd for Low Temperature Coatings to Improve the Wear and Corrosion Resistance. *Surface and Coatings Technology* **1996,** *86–87, Part 2* (0), 498-506.

3. Calderon Velasco, S.; Lopez, V.; Almeida Alves, C. F.; Cavaleiro, A.; Carvalho, S., Structural and Electrochemical Characterization of Zr–C–N–Ag Coatings Deposited by Dc Dual Magnetron Sputtering. *Corrosion Science* **2014,** *80* (0), 229-236.

4. Pedrosa, P.; Lopes, C.; Martin, N.; Fonseca, C.; Vaz, F., Electrical Characterization of Ag:Tin Thin Films Produced by Glancing Angle Deposition. *Materials Letters* **2014,** *115* (0), 136-139.

5. Marques, S. M.; Manninen, N. K.; Ferdov, S.; Lanceros-Mendez, S.; Carvalho, S., Ti1−Xagx Electrodes Deposited on Polymer Based Sensors. *Applied Surface Science* **2014,** *317* (0), 490-495.

6. Manninen, N. K.; Calderón V, S.; Almeida Alves, C. F.; Carvalho, S.; Cavaleiro, A., Influence of Hydrogen Incorporation and Coating Thickness on the Corrosion Resistance of Carbon Based Coatings Deposited by Magnetron Sputtering. *Surface and Coatings Technology* **2015,** *275* (0), 127-132.

7. Liu, C.; Bi, Q.; Leyland, A.; Matthews, A., An Electrochemical Impedance Spectroscopy Study of the Corrosion Behaviour of Pvd Coated Steels in 0.5 N Nacl Aqueous Solution: Part Ii.: Eis Interpretation of Corrosion Behaviour. *Corrosion Science* **2003,** *45* (6), 1257-1273.

8. Ramírez, G.; Rodil, S.; Muhl, S.; Turcio-Ortega, D.; Olaya, J.; Rivera, M.; Camps, E.; Escobar-Alarcón, L., Amorphous Niobium Oxide Thin Films. *Journal of Non-Crystalline Solids* **2010,** *356* (50), 2714-2721.

9. Assis, S. L. d.; Wolynec, S.; Costa, I., Corrosion Characterization of Titanium Alloys by Electrochemical Techniques. *Electrochimica Acta* **2006,** *51* (8), 1815-1819.

10. Chou, W.-J.; Yu, G.-P.; Huang, J.-H., Corrosion Resistance of Zrn Films on Aisi 304 Stainless Steel Substrate. *Surface and Coatings Technology* **2003,** *167* (1), 59-67.

11. Liu, C.; Bi, Q.; Leyland, A.; Matthews, A., An Electrochemical Impedance Spectroscopy Study of the Corrosion Behaviour of Pvd Coated Steels in 0.5 N Nacl Aqueous Solution: Part I. Establishment of Equivalent Circuits for Eis Data Modelling. *Corrosion Science* **2003,** *45* (6), 1243-1256.

12. Lakatos-Varsanyi, M.; Hanzel, D., Cyclic Voltammetry Measurements of Different Single-, Bi- and Multilayer Tin and Single Layer Crn Coatings on Low-Carbon-Steel Substrates. *Corrosion Science* **1999,** *41* (8), 1585-1598.

13. Valero Vidal, C.; Igual Muñoz, A., Study of the Adsorption Process of Bovine Serum Albumin on Passivated Surfaces of Cocrmo Biomedical Alloy. *Electrochimica Acta* **2010,** *55* (28), 8445-8452.

14. Chase, M. W., Jr., Nist-Janaf Themochemical Tables, Fourth Edition. *J. Phys. Chem. Ref. Data, Monograph 9* **1998**, 1-1951.

15. Zanna, S.; Compère, C.; Marcus, P., Xps Characterisation of Bsa Adsorption on Stainless Steel. In *Passivation of Metals and Semiconductors, and Properties of Thin Oxide Layers*, Marcus, P.; Maurice, V., Eds. Elsevier Science: Amsterdam, **2006**, pp 365-370.

16. Serro, A. P.; Gispert, M. P.; Martins, M. C. L.; Brogueira, P.; Colaço, R.; Saramago, B., Adsorption of Albumin on Prosthetic Materials: Implication for Tribological Behavior. *Journal of Biomedical Materials Research Part A* **2006,** *78A* (3), 581-589.

17. Calderon V, S.; Galindo, R. E.; Benito, N.; Palacio, C.; Cavaleiro, A.; Carvalho, S., Ag+ Release Inhibition from Zrcn–Ag Coatings by Surface Agglomeration Mechanism: Structural Characterization. *Journal of Physics D: Applied Physics* **2013,** *46* (32), 325303.

CHAPTER VII- Biotribological Behavior of ZrCN-Ag Coatings against UHMWPE

The following chapter is partially based on the results published in: S. Calderon V, J.C. Sánchez-López, A. Cavaleiro, S. Carvalho, Biotribological behavior of Ag–ZrC_xN_{1-x} coatings against UHMWPE for joint prostheses devices, Journal of the Mechanical Behavior of Biomedical Materials, 41 (2015) 83-91.

7 Introduction

This chapter deals with mechanical and tribological properties of zirconium carbonitrides (ZrCN) coatings embedded with silver nanoparticles, and the correlation with the structural behavior of the samples reported in a previous chapter (chapter V). This analysis will help to assess the viability of this system to be used in the field of prosthetic devices. Nonetheless, taking into consideration that it has been evidenced that the wear of UHMWPE may be the limiting factor that compromises the long-term performance of joint prosthesis [1] by generating polymer debris particles, being highly susceptible to osteolysis, a leading cause of failure for such devices [2], specific attention is placed on UHMWPE.

Several authors have reported that the applied load [3-5] and the counterpart material properties, like hardness [2], roughness [1-2, 6-7] and ability to resist particle formation, are the main factors affecting UHMWPE wear. The environment in which the materials interact has also been identified to play a crucial role in the final tribological behavior. As a result, this chapter, will be focused on the analysis of the complete system coating/lubricant/counterpart, in order to comprehend the influence of the chemical, structural and morphological properties of ZrCN-Ag films on the tribological performance against UHMWPE, as counterpart, tested in Hank's balanced salt solution with albumin.

7.1 Samples tribological characterization

The hardness was evaluated by a MicroMaterials Nanotest system, using a nanoindentation technique. The tribological properties were evaluated by reciprocating friction tests using 10 mm ultrahigh molecular weight polyethylene (UHMWPE) balls in HBSS+BSA. The test parameters were set to 10 N of applied load; 20 mm/s of linear speed; 10 mm track length; 80000 cycles of duration at 1 Hz of acquisition rate, with initial Hertzian contact pressure was calculated in 40 MPa. Scanning electron microscopy images were obtained in order to characterize the surface of the samples after the mechanical solicitation. Raman spectroscopy was used to evaluate changes on the films and polymer before and after the tribological test. The contact angles of the samples were measured using ultra-pure water and an automated contact angle measurement apparatus (OCA 15 Plus; Dataphysics, Germany)[5].

[5] For a more detailed description of the techniques and experimental procedures please see chapter III.

7.2 Results and discussion

7.2.1 Hardness

The hardness results can be correlated with the structural and morphological characteristics of the films. This property has been reported to depend on the ratio between the soft and hard phases in the coatings [8]. As described in the structural characterization (chapter V), the films are mainly composed of three phases, metallic Ag, a-(C, N) and ZrCN. The plot of film hardness vs. ZrCN phase percentage gives a linear correlation (cf.

Figure 7-1). The hardness reduction with the diminution of the ZrCN phase percentage in the film, points out the ratio between hard and soft phases as the key-feature controlling the hardness properties, independently of the relative proportion between the silver and amorphous carbon phases. Previous works have already highlighted the negative influence of both silver and carbon amorphous phases on the hardness properties [8-11]. However, in order to discriminate the influence of silver and amorphous carbon on the hardness separately, a multiple linear regression was carried out using the Ag and a-(C,N) contents. These calculations found a linear regression with a confidence level greater than 95% ($p<0.05$) and R^2=0.994 (cf. Equation 7-1). This empiric mathematical correlation revealed that the effect of silver on hardness reduction is almost twice the carbon phase.

Equation 7-1 $$H = 20.35 - 0.385\,Ag\ phase - 0.204\,a-(C,N)\ phase\ [GPa]$$

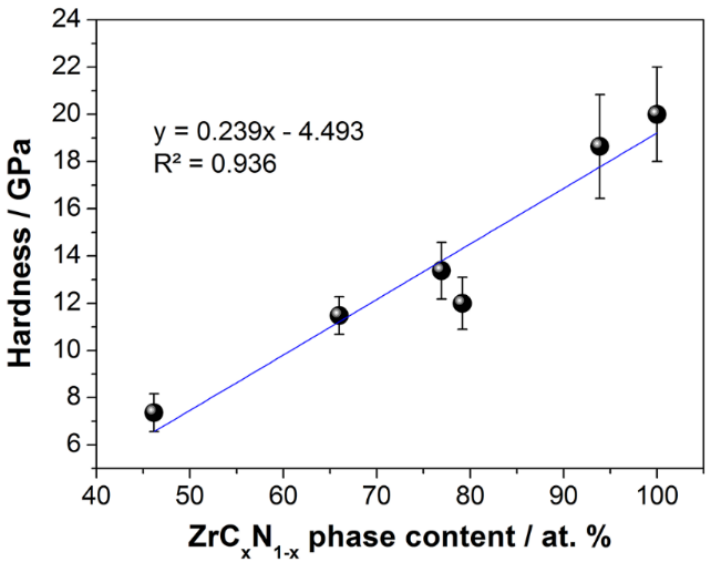

Figure 7-1 Films hardness evolution as a function of ZrCN phase content with its correspondent linear regression.

7.2.2Coefficient of friction

Figure 7-2 plots the dependence of the average COF measured for each sample versus the content of a-(C, N) phase, Rq roughness and hardness. In both cases, the lowest value is obtained with the uncoated substrates, pointing the importance of the surface properties in determining the mechanical strength of a material. Among the ZrCN-Ag samples, a significant reduction in the COF is observed when a-(C, N) is present. This diminution could be explained in a boundary lubrication regime (that can be expected in these lubricated tests), since the presence of this phase between surface asperities in close contact, where the liquid media could not get access or be hindered, would lead to a decrease in the friction. The low friction values achieved with C-based coatings in dry sliding are well known and were discussed in chapter II; however, a reduction of friction is also observed from 0.15 to 0.12 in the absence of the a-(C,N) phase, implicating that this should not be the only factor influencing the values of the COF. Figure 7-2b and c depicts the tendencies of COFs with the film roughness and hardness values, respectively. The observed increase of the measured COFs with these properties can be understood as a dominant ploughing component affecting the friction forces. Hard and rough surfaces create more interlocking points than soft smooth surfaces, and thus, when rubbing the films material against a softer polymer, as the UHMWPE used in the prostheses, a severe plastic deformation occurs and ploughs out a groove. This action creates a resistance to motion, and therefore, the higher the hardness and the roughness, the higher the measured friction value is.

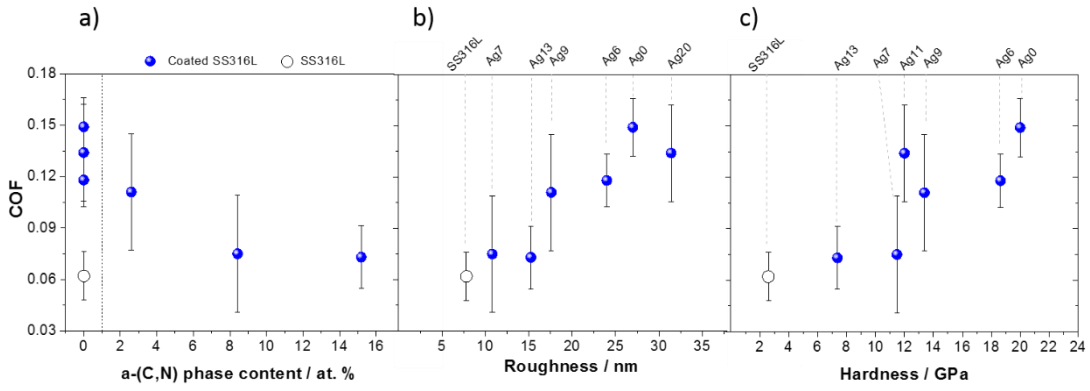

Figure 7-2 a) Films-UHMWPE coefficient of friction evolution as a function of a) carbon amorphous phases content , b) roughness and c) hardness of the coatings.

In addition to the material properties, the composition of the fluid is known to play an important role in the measurement of the COF of the tribological system, due to chemical and/or physical

interaction with the material surface. Albumin has demonstrated to protect the surface of the materials against wear; however, its role on the COF is not well understood. Fang et al. [12], for instance, have reported that the adsorption of albumin on both UHMWPE and CrCoMo surfaces may induce an increase of the COF due to the interaction between the molecules of albumin. Contrarily, Hall et al. [13] and others [14-15] have reported that the protection of albumin reduced both wear and COF. Despite of being a very complex process that depends on fluid pH, ionic strength and temperature [14], as well as on the hydrophobicity of the surface, several reports agree that the albumin adsorbs easier to hydrophobic surfaces than hydrophilic materials [14, 16]. In this case, the contact angle of each film, and the stainless steel, were evaluated in order to investigate the correlation between the adsorption of the albumin with the hydrophobic behavior of the coatings. The results showed that the only hydrophilic surface (Ag0) has the highest COF. However, among the other samples with similar hydrophobicity levels (see angle contact in Figure 7-3); the COFs did not show a clear correlation with the contact angle. This certainly means that the effect of ploughing in friction should be given more consideration than the decrease of adhesion forces by effect of chemical bonded layers (albumin) or solid lubricant (amorphous carbon-based phases).

7.2.3 Wear

The wear of the UHMWPE counterpart was evaluated by measuring the permanent scar left at the end of the tribological test.

The UHMWPE wear rate did not exhibit significant differences between the samples (1.4 to 2.0 $x10^{-6}$ mm^3 N^{-1} m^{-1}), hampering the analysis of the surface roughness, hardness and COF effects on the polymer wear, probably explained due to the formation of the protective albumin layer adsorbed on the material surfaces [13-15, 17]. Nonetheless, the UHMWPE wear rate shows a particular trend as a function of the silver content, indicating that the wear of the UHMWPE increases by increasing the silver content in the films, as seen in Figure 7-3. Recent investigations have found that silver nanoparticles on surfaces may delay the adsorption of the albumin [18], and therefore, the system may be less protected by the albumin as the amount of silver nanoparticles increases in the material. The hydrophobic character of the samples also influences the albumin adsorption [14, 16]. Thus, the high wear rate exhibited by sample Ag0 may also be due to low albumin adsorption, since it is the single sample showing a hydrophilic character. In summary, the wear of the soft UHMWPE material results from the balance between

(i) abrasive wear and plastic deformation, as determined by the film hardness, microasperities and debris particles, and (ii) boundary lubrication by albumin, controlled by the silver content and hydrophilic/hydrophobic character of the surface.

The wear rate of the films was not measurable in the present conditions, and therefore, the effect of phase composition (ZrCN, Ag and a-(C, N) phases) on the film wear could not be concluded.

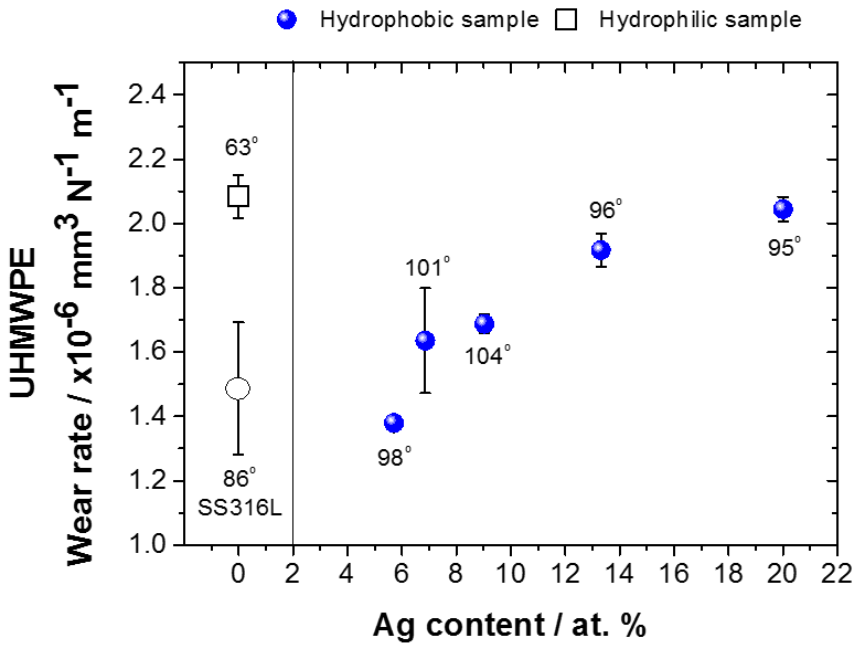

Figure 7-3 Films-UHMWPE wear factor evolution as a function of the silver content. The values in degrees represent the contact angle of each sample.

SEM examination of the film wear tracks and UHMWPE ball scars of two representative samples (Ag0 and Ag9), are shown in Figure 7-4. Although it is frequently reported the transfer of UHMWPE material to the counterpart, none of the samples showed the presence of transferred polymer material, as shown in Figure 7-4, fact explained by in the wiping effect of the lubricant [13].

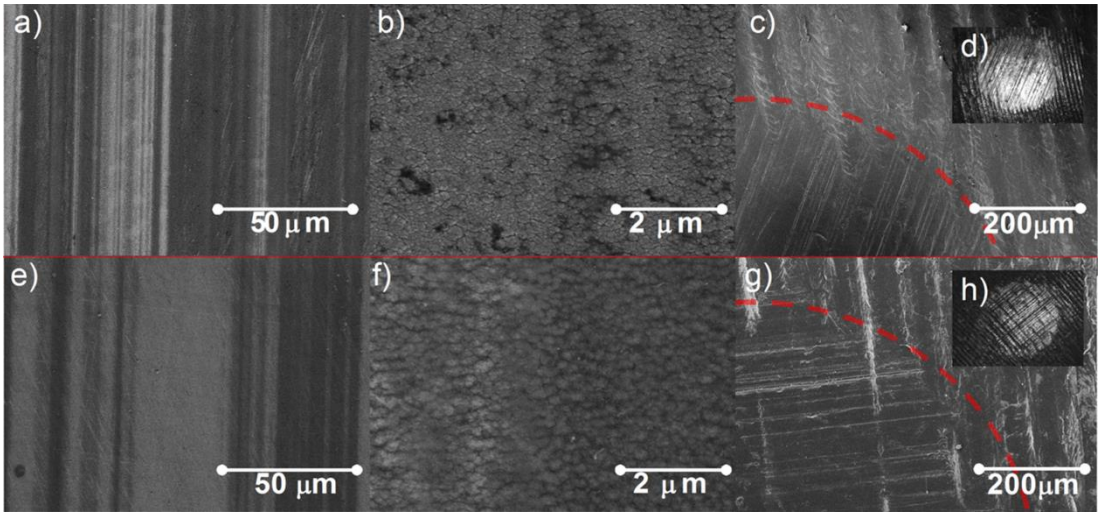

Figure 7-4 Scanning electron microscope images of the wear track on the films and wear mark on the UHMWPE of two representative samples a) and b) wear track of Ag0, c) wear mark on the UHMWPE used against sample Ag0, d) and e) wear track of Ag9, f) wear mark on the UHMWPE used against sample Ag9. Optical images of the UHMWPE scar rubbed against g) Ag0 and h) Ag9.

The wear debris are usually reported in the ranges of 0.1 to 100 μm [19], still being controversial the ability of the submicrometer particles to generate inflammatory response that results in osteolysis [20]. In this study, the wear debris from the polymer or films could not be detected either in the fluid or on the surface of the materials, analyzed by STEM and SEM, respectively. Thus, it is believed that the size of the particles is below 100 nm. In fact, roughness measurements of the films were below 100 nm, and hence, the abrasive crests of the films only trim nanometric parts of the polymer.

Raman spectroscopy performed in both the film wear track and the rubbed UHMWPE did not show any significant changes after the tribological test, as shown in Figure 7-5. However, the UHMWPE exhibits an increasing oxygen content trend as the wear rate increases as shown in Figure 7-6, which may be related to the polymer degradation, since the mechanical loading may promote the formation of radicals through bond scission, inducing the UHMWPE oxidation [21].

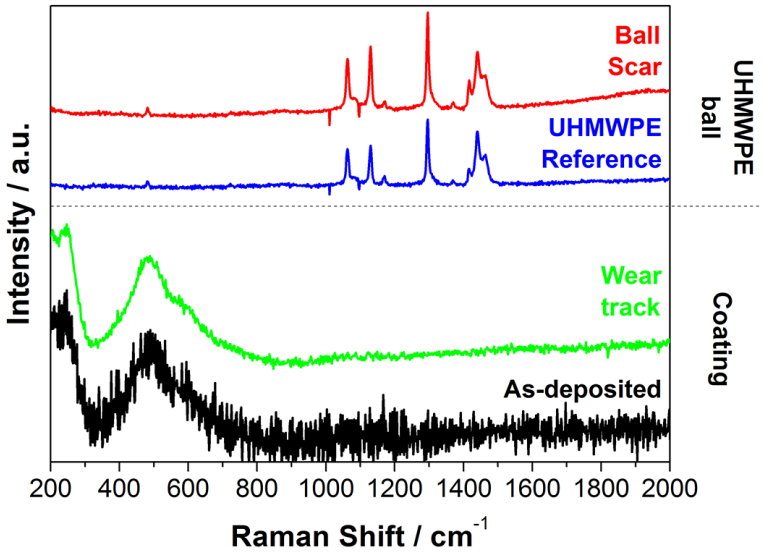

Figure 7-5 Raman spectroscopy before and after the tribological test for a representative sample (Ag6) and its corresponding UHMWPE counterpart.

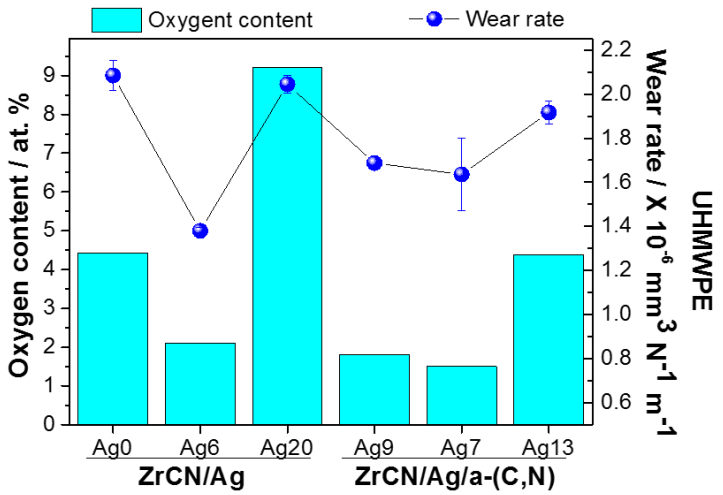

Figure 7-6 Energy dispersive X-ray analysis of oxygen on the polymer wear mark.

7.3 Conclusion

The result demonstrated that the hardness of the films is mainly controlled by the ratio between the hard (ZrCN) and the soft (Ag and amorphous carbon) phases of the films, fluctuating between 7.4 and 20.4 GPa. The coefficient of friction against ultra-high molecular weight polyethylene (UHMWPE) in Hank's balanced salt solution with 10 g L^{-1} albumin, is governed by both the surface roughness and the hardness. Whereas, the changes in the UHMWPE wear rate are in the same one order of magnitude (between 1.4 and 2.0 x10^{-6} mm^3 N^{-1} m^{-1}) for all samples, justified by the effect of the protective layer of albumin formed in the contact during the tests.

7.4 References

1. Goswami, T.; Alhassan, S., Wear Rate Model for Uhmwpe in Total Hip and Knee Arthroplasty. *Materials & design* **2008,** *29* (2), 289-296.

2. Buford, A.; Goswami, T., Review of Wear Mechanisms in Hip Implants: Paper I – General. *Materials & design* **2004,** *25* (5), 385-393.

3. Dong, G.-N.; Hua, M.; Li, J.; Chuah, K. B., Temperature Field and Wear Prediction for Uhmwpe Acetabular Cup with Assumed Rectangular Surface Texture. *Materials & design* **2007,** *28* (9), 2402-2416.

4. Rostoker, W.; Galante, J., Contact Pressure Dependence of Wear Rates of Ultra High Molecular Weight Polyethylene. *Journal of biomedical materials research* **1979,** *13* (6), 957-964.

5. Kim, D.-W.; Lee, K.-Y.; Jun, Y.; Lee, S.; Park, C., Friction and Wear Characteristics of Uhmwpe against Co-Cr Alloy under the Wide Range of Contact Pressures in Lumbar Total Disc Replacement. *International Journal of Precision Engineering and Manufacturing* **2011,** *12* (6), 1111-1118.

6. Cho, H. J.; Wei, W. J.; Kao, H. C.; Cheng, C. K., Wear Behavior of Uhmwpe Sliding on Artificial Hip Arthroplasty Materials. *Materials Chemistry and Physics* **2004,** *88* (1), 9-16.

7. Turell, M. E.; Friedlaender, G. E.; Wang, A.; Thornhill, T. S.; Bellare, A., The Effect of Counterface Roughness on the Wear of Uhmwpe for Rectangular Wear Paths. *Wear* **2005,** *259* (7–12), 984-991.

8. Yao, S. H.; Su, Y. L.; Kao, W. H.; Cheng, K. W., Evaluation on Wear Behavior of Cr–Ag–N and Cr–W–N Pvd Nanocomposite Coatings Using Two Different Types of Tribometer. *Surface and Coatings Technology* **2006,** *201* (6), 2520-2526.

9. Sánchez-López, J. C.; Abad, M. D.; Carvalho, I.; Escobar Galindo, R.; Benito, N.; Ribeiro, S.; Henriques, M.; Cavaleiro, A.; Carvalho, S., Influence of Silver Content on the Tribomechanical Behavior on Ag-Ticn Bioactive Coatings. *Surface and Coatings Technology* **2012,** *206* (8–9), 2192-2198.

10. Basnyat, P.; Luster, B.; Kertzman, Z.; Stadler, S.; Kohli, P.; Aouadi, S.; Xu, J.; Mishra, S. R.; Eryilmaz, O. L.; Erdemir, A., Mechanical and Tribological Properties of Craln-Ag Self-Lubricating Films. *Surface and Coatings Technology* **2007,** *202* (4–7), 1011-1016.

11. Han, J. G.; Myung, H. S.; Lee, H. M.; Shaginyan, L. R., Microstructure and Mechanical Properties of Ti–Ag–N and Ti–Cr–N Superhard Nanostructured Coatings. *Surface and Coatings Technology* **2003,** *174–175* (0), 738-743.

12. Fang, H.-W.; Hsieh, M.-C.; Huang, H.-T.; Tsai, C.-Y.; Chang, M.-H., Conformational and Adsorptive Characteristics of Albumin Affect Interfacial Protein Boundary Lubrication: From

Experimental to Molecular Dynamics Simulation Approaches. *Colloids and Surfaces B: Biointerfaces* **2009,** *68* (2), 171-177.

13. Hall, R. M.; Unsworth, A., Friction in Hip Prostheses. *Biomaterials* **1997,** *18* (15), 1017-1026.

14. Gispert, M. P.; Serro, A. P.; Colaço, R.; Saramago, B., Friction and Wear Mechanisms in Hip Prosthesis: Comparison of Joint Materials Behaviour in Several Lubricants. *Wear* **2006,** *260* (1–2), 149-158.

15. Gispert, M. P.; Serro, A. P.; Colaço, R.; do Rego, A. M. B.; Alves, E.; da Silva, R. C.; Brogueira, P.; Pires, E.; Saramago, B., Tribological Behaviour of Cl-Implanted Tin Coatings for Biomedical Applications. *Wear* **2007,** *262* (11–12), 1337-1345.

16. Wang, K.; Zhou, C.; Hong, Y.; Zhang, X., A Review of Protein Adsorption on Bioceramics. *Interface Focus* **2012,** *2* (3), 259-277.

17. Alves, C. F. A.; Oliveira, F.; Carvalho, I.; Piedade, A. P.; Carvalho, S., Influence of Albumin on the Tribological Behavior of Ag–Ti (C, N) Thin Films for Orthopedic Implants. *Materials Science and Engineering: C* **2014,** *34* (0), 22-28.

18. Kumari, P.; Majewski, P., Adsorption of Albumin on Silica Surfaces Modified by Silver and Copper Nanoparticles. *Journal of Nanomaterials* **2013,** *2013*, 839016-7.

19. Ge, S.; Wang, S.; Gitis, N.; Vinogradov, M.; Xiao, J., Wear Behavior and Wear Debris Distribution of Uhmwpe against Si3n4 Ball in Bi-Directional Sliding. *Wear* **2008,** *264* (7–8), 571-578.

20. Hamid Reza Seyyed Hosseinzadeh, A. E. a. A. S. S., The Bearing Surfaces in Total Hip Arthroplasty – Options, Material Characteristics and Selection. In *Recent Advances in Arthroplasty*, Fokter, D. S., Ed. INTECH: **2012**, p 614.

21. Kurtz, S. M., *The Uhmwpe Handbook: Ultra-High Molecular Weight Polyethylene in Total Joint Replacement*. Access Online via Elsevier: San Diego, **2004**; p 379.

CHAPTER VIII – Ag^{+} Release, Growth and Antibacterial Activity in ZrCN-Ag Coatings

The following chapter is partially based on the results published in: S. Calderon V; I. Ferreri; M. Henriques; J.T.M. De Hosson; A. Cavaleiro; S.Carvalho, Nano-Galvanic coupling for enhanced Ag+ release in ZrCN-Ag films: antibacterial application, Submitted July 2015.

8 Introduction

The main objective of this project is to characterize and optimize ZrCN-Ag coatings in order to determine the proper deposition parameters to maintain or improve functional properties of materials used in medical devices, such as corrosion and wear resistance. In previous chapters, these functional properties have been evaluated, establishing the effect of the structural and chemical features. Such analyses have pointed out silver as one of the most important parameters controlling the functional properties. However, up to this point the benefits of the silver have not been completely explored.

It was extensively explained, in the introduction of the thesis, that the incorporation silver into the ceramic matrix (Zr-C-N) plays the role of antibacterial agent of the materials, and hence, it is important to understand the stability of such phase (Ag) in the matrices, the silver ion release and the effectiveness as antibacterial agent.

Consequently, this chapter is focused on understanding the effect of the physical and chemical properties of the coatings (silver content and phase composition) on the evolution of silver as a function of the immersion time in an electrolyte isotonic with the human body. The samples were immersed in NaCl 0.9 %, a fluid isotonic to the human body, since a more complex electrolyte such as HBSS + BSA have demonstrate more interference on measuring the silver ion release. This property, together with the silver aggregation and the film physical and chemical properties are correlated with the antibacterial behavior.

8.1 Material and methods

GD-OES was used to determine the element distribution through the film thickness, before and after immersing the samples during 240 hours in 0.9 % NaCl. XPS was used to determine the silver oxidation state on the surface before immersion. TEM and HR-TEM images were utilized to elucidate the phase distribution of the material and the silver segregation. SEM images were obtained using a high resolution NanoSEM - FEI Nova 200 equipped in backscattered electron detector in TLD mode. Mainly two magnification are reported, 10.000X (10kX) for general view of the sample surfaces and 100.000X (100kX) for a more detail image. Both before and after immersion surface images are obtained to evaluate the evolution of silver after contacting the electrolyte. ICP was used to determine the Ag ion release in 0.9% NaCl, within a period of 30 days. The presence of Zr ions was also evaluated, but was not detected in the solution after 336 hours of immersion. The antibacterial properties of the coating were assessed by means

of the zone of inhibition (ZOI) test. All the characterization were performed on samples deposited on SS316L[6].

8.2 Results and discussion

As in previous chapter, the silver content will be here also used as the sample notation. The silver ion release and the silver evolution in the coating matrix as a function of the immersion time was assessed in order to determine their relation with the antibacterial properties of the ZrCN-Ag system. For that, the in-depth silver distribution in the as-deposited films was characterized.

8.2.1 As-deposited coatings

The depth profile composition of the samples obtained by GD-OES is shown in Figure 8-1. The first 100 nm of the films are shown in Figure 8-1 a - e, while the entire compositional profile of each sample is presented in the inset of the figures, respectively. Figure 8-1f, on the other hand, shows the surface binding states of silver for all the films obtained by XPS. The results reveal silver enrichment on the surface in the first 10 to 20 nm in depth, indicating a segregation process during the deposition, previously reported by other authors [1-4] and extensively on the state of art of this thesis. Such phenomenon is explained due to the large surface energy contained in smaller particles, which promotes their coalescence. During the deposition process, a constant flow of the sputtered species from the target are deposited over the previous layer of material, limiting the mobility of silver particles and preventing them to coalesce. However, on the surface of the material, when no new species are deposited, the mobility is less restricted, allowing the silver to diffuse laterally, coalescing and reducing the surface energy by crystal growth [5-6]. The whole process is enhanced due to the low reactivity of the silver with the matrix, which prevents the formation of strong bonds between the silver and the ZrCN and/or the carbon amorphous phases.

[6] For a more detailed description of the techniques and experimental procedures please see chapter III.

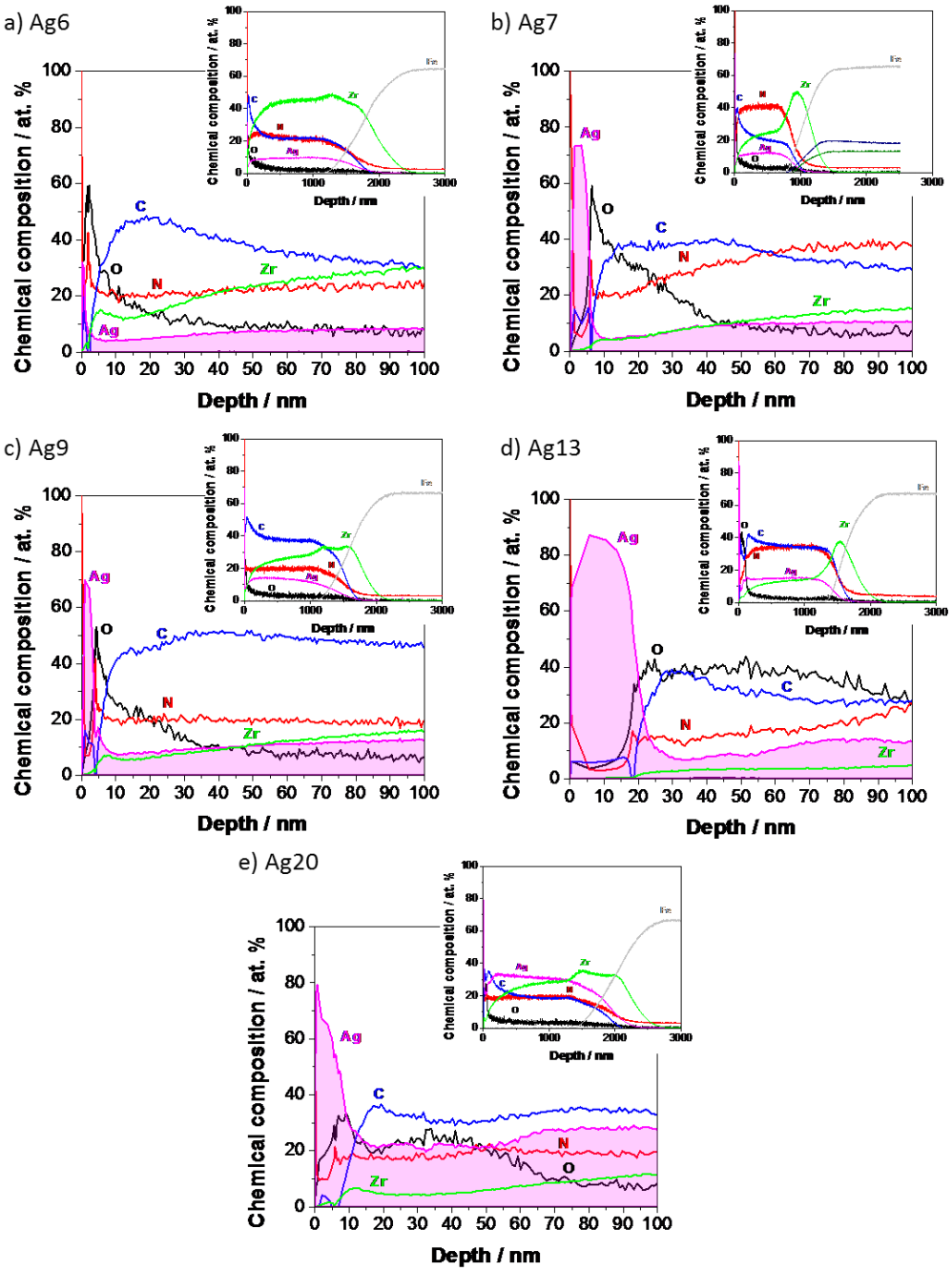

Figure 8-1 GD-OES depth profile near the surface (<100 nm) for samples a) Ag6, b) Ag7, c) Ag9, d) Ag13 and e) Ag20. The insets of each graph show the complete GD-OES depth profile.

The silver accumulation was previously demonstrated by XPS and TEM in chapter V. Small silver particles (< 20 nm) are observed by TEM for most of the films. High resolution TEM images, in Figure 8-2f, confirm the structure of the silver nanoparticles, reveling a FCC crystalline lattice and interplanar distance of 0.235 nm for the orientation (111) and 0.200 nm for the (200) plane in the face-centered cubic lattice. The polycrystalline nature of the nanoparticles, observed in Figure 8-2f, demonstrates the agglomeration and growing of the silver nanoparticles on the surface of the films.

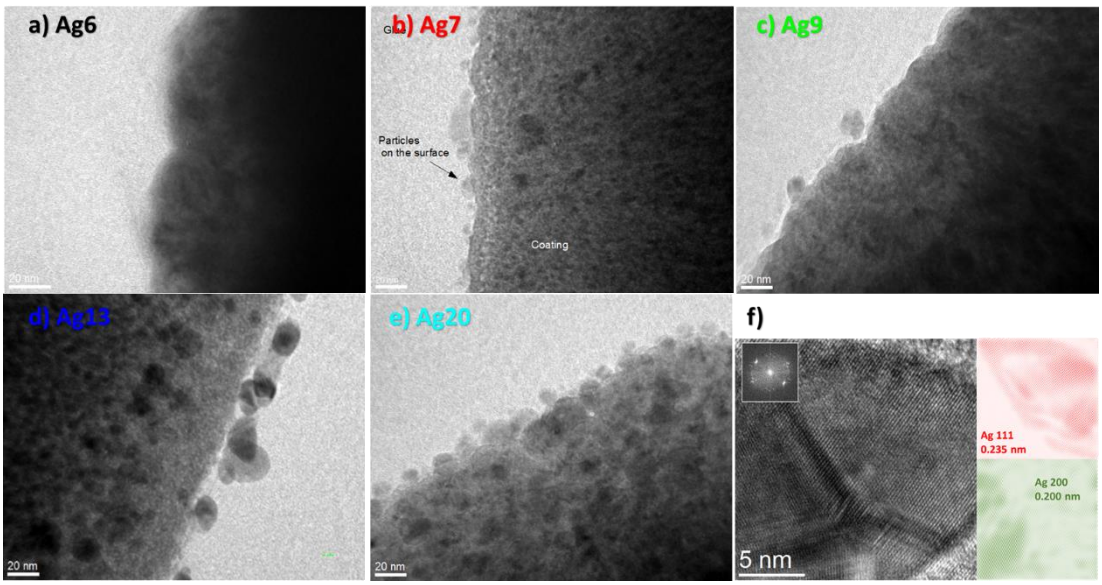

Figure 8-2 TEM images at the surface of as-deposited samples a) Ag6, b) Ag7, c) Ag9, d) Ag13, e) Ag20 and f) high resolution image of one particle observed on the surface demonstrating the polycrystalline nature

The images also evidenced variation on the amount of particles on the surface, depending on the composition of the films, which indicates dissimilar mobility of silver in different kind of matrices (ZrCN or ZrCN + amorphous carbon phases). Sample Ag7, for instance, showed a larger number of particles on the surface, as well as a deeper accumulation (GD-OES depth profile) when compared to Ag6 and Ag9, which possess comparable silver content. This seems to be related to a higher silver diffusivity when carbon amorphous phases exist, in good agreement with Manninen et al [6] results, showing that silver segregation to the surface can occur even at room temperature in DLC coatings (C-based material), contrarily to other materials where temperature is required for surface segregation [7-9]. Similar behavior occurs for sample Ag13, which possesses the highest amount of amorphous C phases (largest C+N/Zr), confirming that, in spite of its lower silver content, the segregation is similar when compared to sample Ag20.

8.2.2 Film immersion in NaCl 0.9 %

For a large number of medical application, the material should be tested in contact with simulated body fluids. Hence, the coatings were immerse into NaCl 0.9% electrolyte in order to evaluate the evolution of silver as a function of the immersion time. Subsequently, surface analysis using SEM images and silver ion concentration in the fluids were assessed. Figure 8-3 and Figure 8-4 show the top-view images obtained by SEM before and after 240h of immersion in the electrolyte. Two magnification are shown. The micrographs were obtained using a

backscattering electron detector in order to achieve a better contrast as a function of the surface composition. Before immersion, the particles were only clearly evidenced in sample Ag20, indicating that the particles on the other samples possess sizes lower than the SEM detection limit.

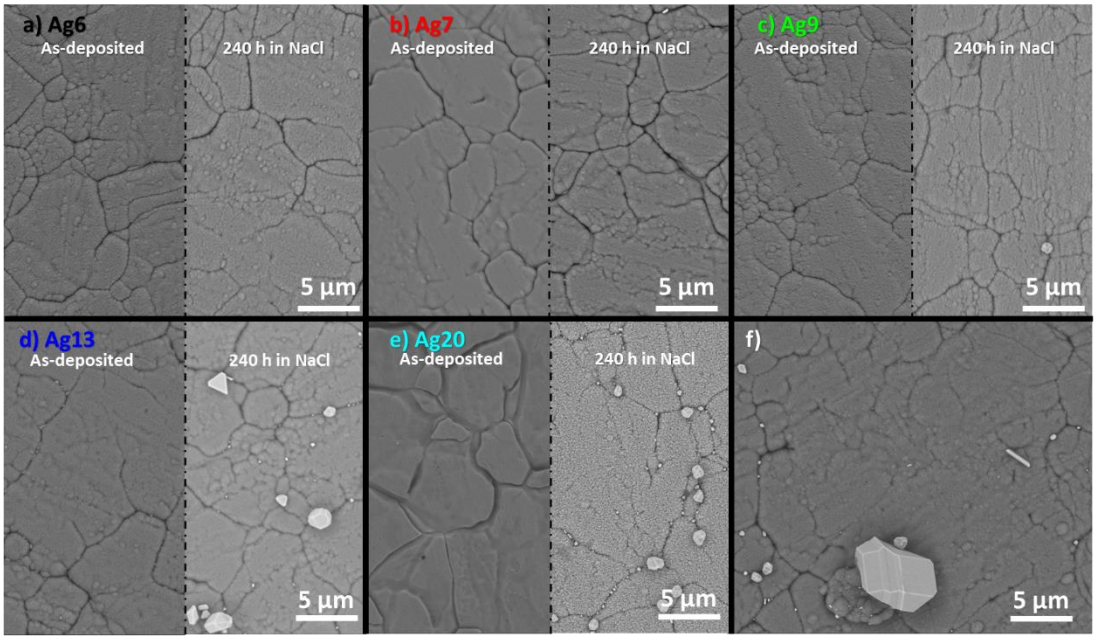

Figure 8-3 Coatings surface SEM images in backscattering mode at 10 kX before and after 240h immersion in NaCl 0.9% for a) Ag6, b) Ag7, c) Ag9, d) Ag13, e) Ag20 and f) example of a large crystal observed in samples with highest content of silver after immersion.

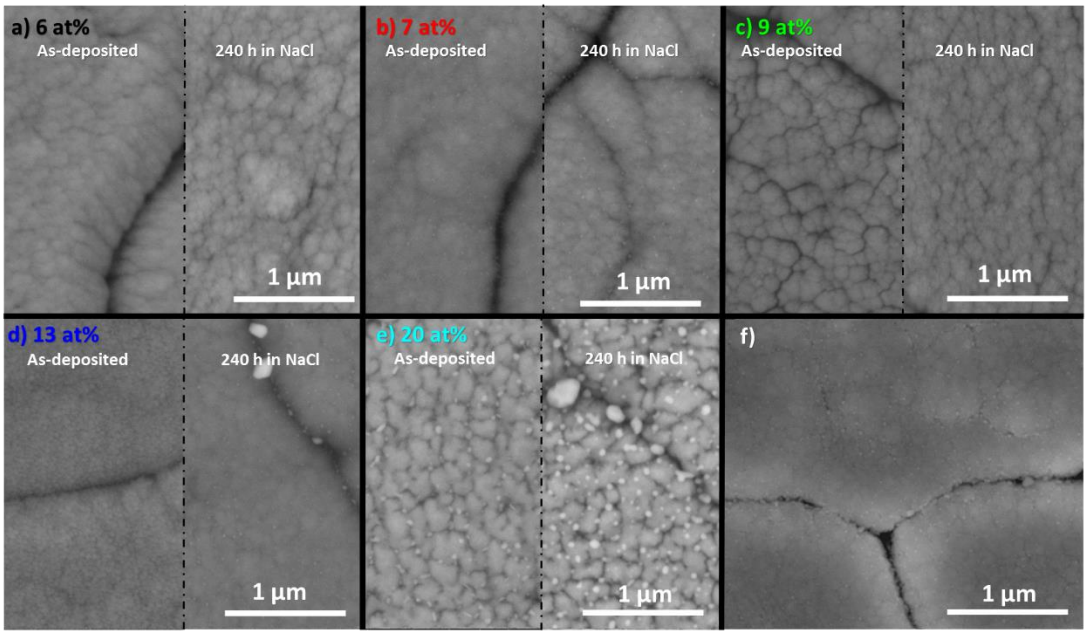

Figure 8-4 Coatings surface SEM images in backscattering mode at 100 kX before and after 240h immersion in NaCl 0.9% for a) Ag6, b) Ag7, c) Ag9, d) Ag13, e) Ag20 and f) example of the sample Ag13 using secondary electron detector at 100 kx after immersion

After 240 h of immersion in NaCl 0.9 %, the segregation of silver is evidenced as bright particles (heavier element) with large distribution of sizes, which depend on the silver content in the films. The analysis by EDS (Figure 8-5), using a spot acquisition, revealed that the particles are formed by silver; no chloride was detected.

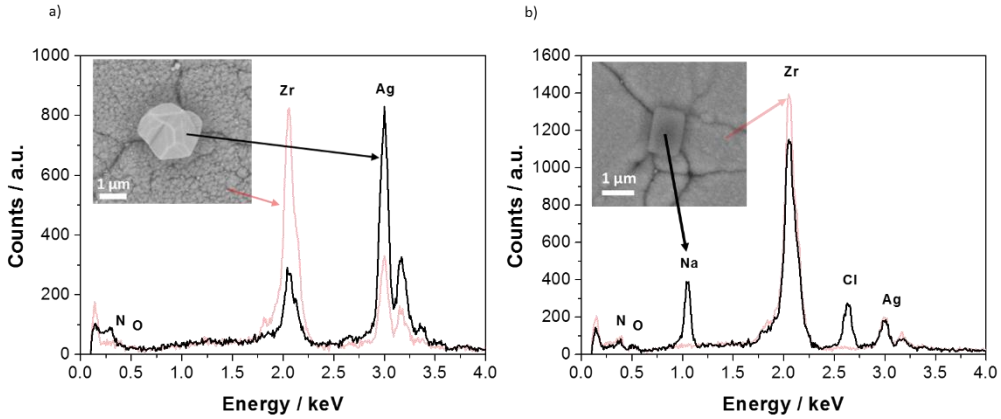

Figure 8-5 Energy dispersive X-ray spectroscopy inside and outside two different particles on the surface after sample immersion in NaCl 0.9 % a) silver crystal and b) NaCl crystal. The insets show the particle in which the analysis was carried out.

In order to quantify the segregation process after immersion, a statistical analysis of the samples surface was carried out to study the size distribution, the average size and the area covered by the particles in each sample, at two different magnifications (10 kX and 100 kX). The results are presented in Figure 8-6. At low magnification images, the results evidenced that the silver diffusion to the surface, quantified as the surface area covered by the silver, is in agreement with the amount of silver in the films, showing that as silver content increases, more silver can diffuse to the surface. However, for higher magnifications, only samples Ag7, Ag13 and Ag20 could be analyzed due to the lack of evidence of small particles in samples Ag6 and Ag9 (cf. Figure 8-6a). Figure 8-6b, displays the distribution of the nanoparticles (<100nm) at large magnification (100kX), indicating smaller nanoparticles size for sample Ag7 and Ag13, compared to sample Ag20 The latter, shows a very broad distribution of particle sizes.

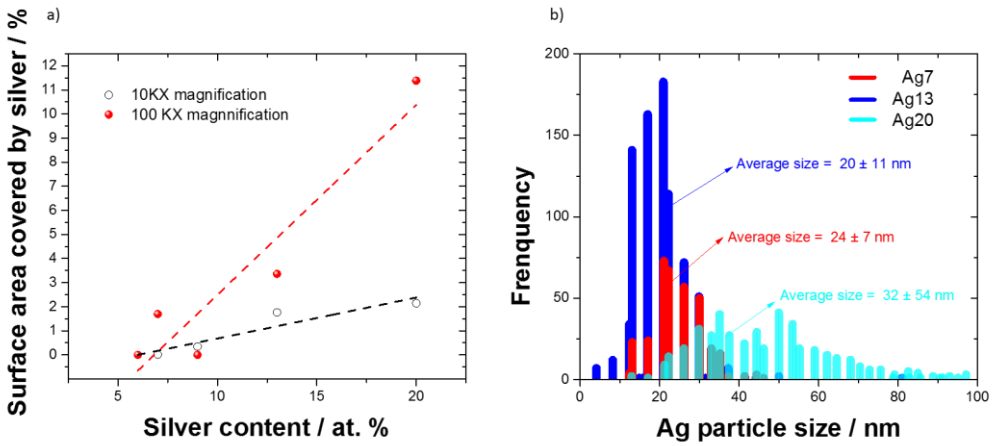

Figure 8-6 a) surface area covered by silver nanoparticles after immersion at two magnifications and b) histograms of silver nanoparticles size for samples Ag7, Ag13 and Ag20 after immersion from images obtained at 100 kX magnification.

This surface analysis suggests a bimodal distribution of the silver particles after immersion in NaCl 0.9 %, with particles sizes < 50 nm (100 kX) and > ~300 nm (observed at lower magnifications), which are expected to growth mimicking the Ostwald ripening process, where particles with lower sizes dissolve and those with larger sizes continue growing

The largest particles are located in the direction of the grain boundaries of the stainless steel, as shown in Figure 8-7, where the Ag growth for as-deposited samples is more evident (cf. Figure 8-2). This behavior is explained by the larger diffusion of silver and/or ions in the boundary regions, due to their less dense morphology, as previously discuss in systems such as CrN [10-11]. It is also important to notice that the particles are not composed by a group of small particles, which signify that silver is not agglomerating, but growing in these regions.

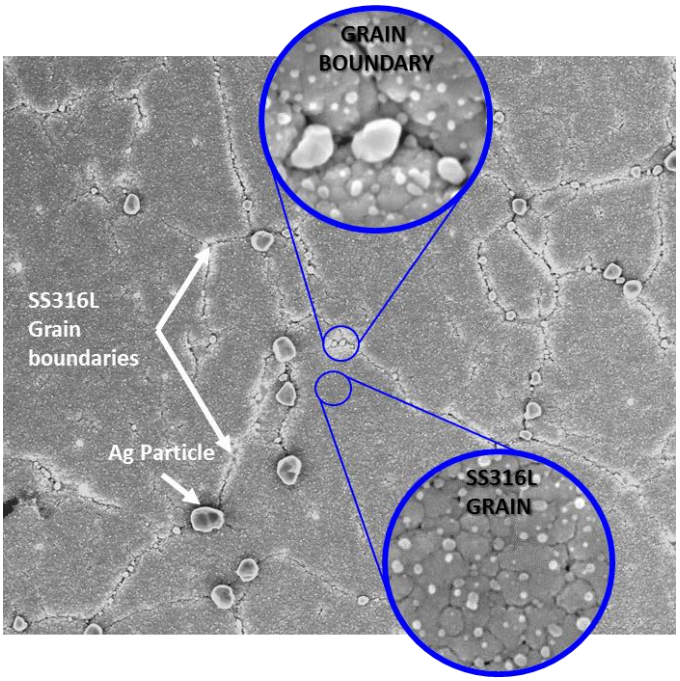

Figure 8-7 Surface SEM image of the silver agglomeration on the substrate grain boundaries (SS316L).

8.2.3 Silver ion release

Figure 8-8a displays the cumulative silver ion release obtained by ICP as a function of the immersion time of the samples in NaCl 0.9 %. The results revealed a fast release in the first 48 hours of immersion, reaching an almost constant ion concentration in the fluids, which indicates a very slow ion release from the samples after this period. This characteristic behavior was also found in similar samples [12-13] and in pure nanoparticles in natural waters [14].

The amount of silver ion release to the media does not follow the same trend as the silver accumulation on the surface, indicating that the low silver ion release is not due to the absence of silver on the surface, but due to growing of the silver nanoparticles. Similar tendencies of the silver release can be observed by GD-OES before and after immersion, as shown in Figure 8-8b. The silver in sample Ag20 is redistributed from the inside of the film to the surface, but with low silver release to the medium, while the silver in the other coatings partially release to the media, corroborating the ICP measurements.

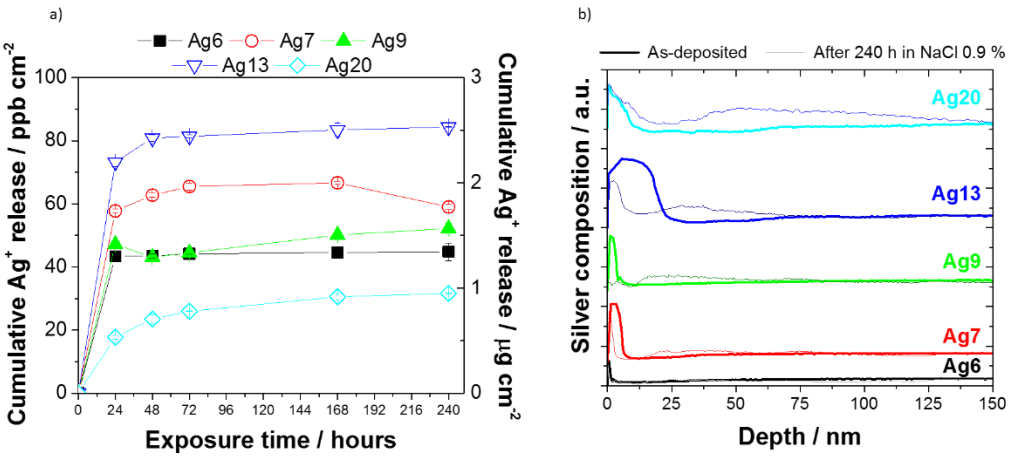

Figure 8-8 . a) silver ion release of the samples as a function of immersion time in NaCl 0.9 % and b) Ag GD-OES depth profile near surface (<150 nm) for the coatings before and after immersion in NaCl 0.9%.

This behavior evidences that the matrix surrounding the silver may contribute or even control silver ion release, when the samples are immersed in the electrolyte. It was observed that, when amorphous carbon phases are present in the films, the silver nanoparticles tend to be encapsulated by these phases, while for pure ZrCN-Ag films, Ag nanoparticles are surrounded by the crystalline ZrCN, as observed in high resolution TEM images shown in Figure 8-9a. Each of these phases (Ag, ZrCN and a-(C,N)) possesses different open circuit potentials when immersed in NaCl, and therefore, will act as anode or cathode in a reaction, when electrically in contact, depending on their distribution.

In order to confirm the hypothesis the OCP of pure silver [15], amorphous carbon films [16] and ZrCN films was measure in NaCl and the average after one hour of immersion is reported Figure 8-9b, together with a scheme of the phases. It may be observed that silver can act as the cathode, since its open circuit potential measured in NaCl (-0.02 V) is higher than that of a pure ZrCN film (-0.22 V) as for Ag6 and Ag20 samples. However, if silver is surrounded by an amorphous carbon phase (with OCP ~0.14 V), as for Ag7, Ag9 and Ag13, silver behaves as the anode of the reaction, promoting a higher silver ion release, explaining the increase of silver ion release as the amorphous phase content increases in the coatings.

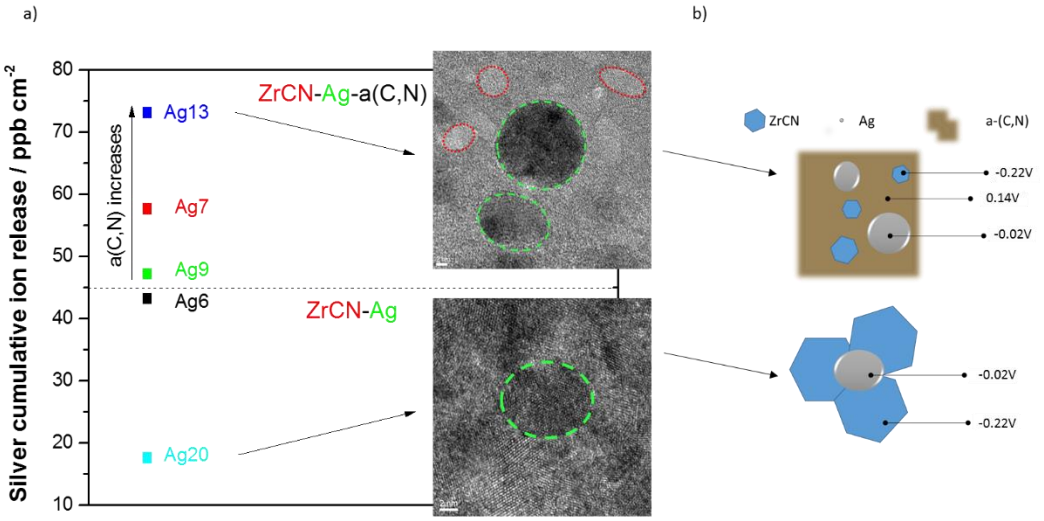

Figure 8-9 a) comparison between the silver ion release after 24 h obtained by ICP phase distribution images obtained by HR-TEM. b) scheme of the phase distribution for both ZrCN-Ag-a(C,N) and ZrCN-Ag systems and the corresponding open circuit potential when immersed in NaCl 0.9 at%.

On the other hand, the higher silver ion release observed on the coatings with amorphous phases also suggest that the lower size of the silver particles and the oxidized state of this silver may produce a rapid release of the oxidized silver following the Equation 8-1 [17].

Equation 8-1 $Ag_2O(s) + H_2O = 2Ag^{+} + 2OH^{-}$

8.2.4 Bacterial Zone of inhibition test

The ZOI test was used to evaluate the ability of the films to prevent the growth of *S. epidermidis,* as shown in Figure 8-10. Figure 8-10a displays the samples after the bacteria incubation period (24 hours). Around the edges of the samples, a small clearer area (darker zone) can be observed in most of the samples, which corresponds to the zone where bacteria growth does not occur. A pure ZrCN sample has been used as control in order to observe the absence of the ZOI (labeled Ag0). A more intense bright zone is observed in the edge of this sample, corresponding to the growth of bacteria. Similarly, sample Ag6 did not show a visible ZOI and despite of possessing a less intense edge of bacteria growing, no ZOI could be quantified. Sample Ag7 to Ag20 showed a more defined inhibition zones, quantified using a normalized area of inhibition, Equation 8-2, in order to take into consideration size variation of the samples in the repetitions.

Equation 8-2 $Normalized\ ZOI = \frac{Area_{ZOI} - Area_{Sample}}{Area_{Sample}}$

where the $Area_{ZOI}$ and $Area_{sample}$ correspond to the external and internal rectangles drawn in Figure 8-10b, respectively, for each sample.

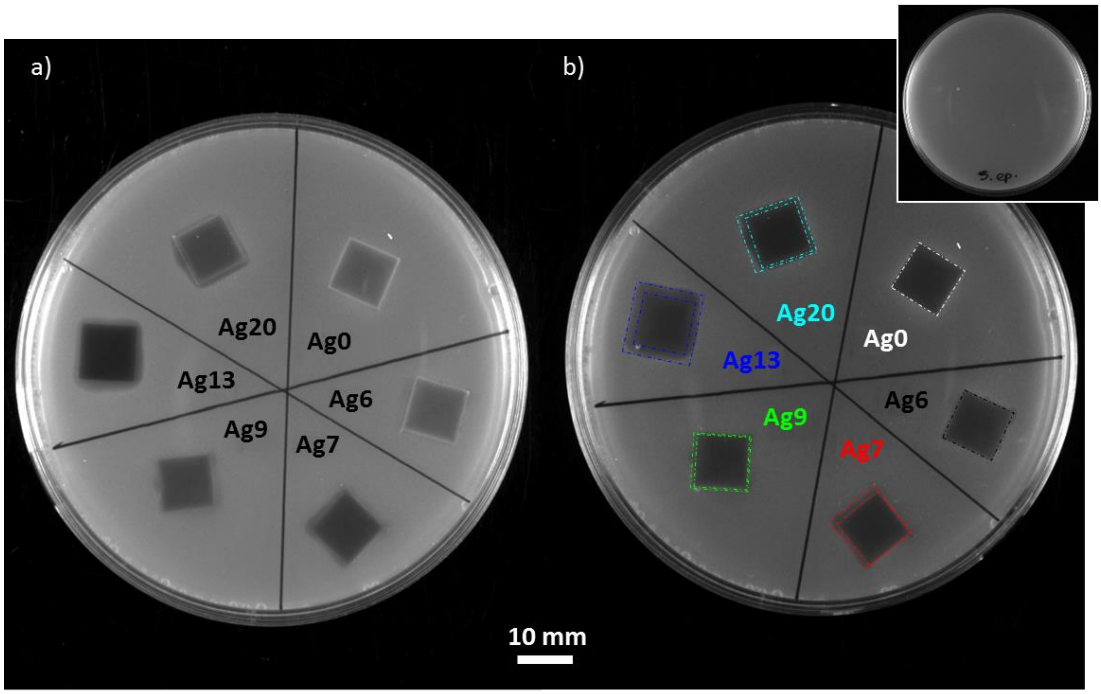

Figure 8-10 Zone of inhibition assays for ZrCN-Ag coatings a) raw image after 24h of the test, b) highlighting the ZOI area. The inset shows a growth control Petri dish for the *S. epidermidis*.

The result of the normalized ZOI can be observed in Figure 8-11 as a function of the silver content in films and the silver ion release. The results reveal that the size of the bacterial zone of inhibition is not evidently related to the silver content in the coatings, in some extend expected due to the lack of correlation between the silver content and the silver ion release, demonstrated in the previous section. On the other hand, although the silver ion release seems to be directly correlated with the ZOI area for most of the samples (Figure 8-11b), unexpectedly the sample with the lowest silver ion release exhibits a comparable ZOI to the intermediate silver ion release sample. This suggests that the size of the ZOI may be also related with the availability and form of silver on the surface in order for the bacteria to react with it. However, it must be stressed that silver ionization in NaCl may differ from the Ag^+ release in the bacteria agar, as shown in [18]; however, the tendencies are expected to be similar.

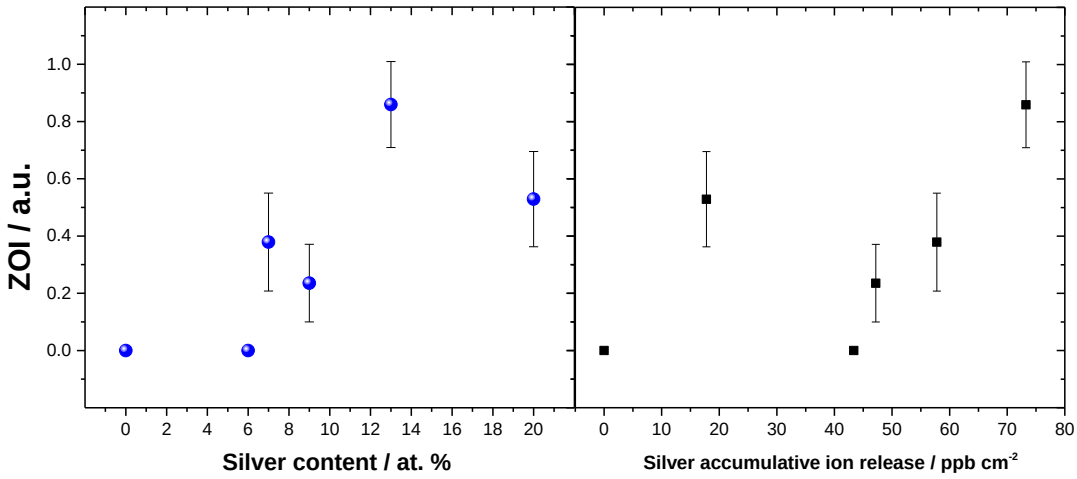

Figure 8-11 Normalized zone of inhibition area for ZrCN-Ag coatings as a function of a) silver content and b) silver ion release.

Taking into consideration both the silver ion release and the amount of silver nanoparticles on the surface of the samples, the antibacterial behavior of the coatings should be a compromise between different factors, as follows: i) the ability of the material to form silver particles on the surface, ii) the size of the silver particles and iii) the amount of silver ions released. In the first case, for example, sample Ag20 showed the lowest silver ion release and the largest particles on the surface; however, it shows a ZOI area size located between the ZOI sizes of Ag7 and Ag13. On the other hand, samples Ag6 and Ag9 with higher silver release compared to Ag20 sample, exhibit lower or none ZOI. This behavior may be associated to the amount of silver present on the surface.

In the second and third scenarios, although samples Ag7 and Ag13 present less silver segregation on the surface, when compared to sample Ag20, they show a comparable (Ag7) or larger (Ag13) ZOI area, indicating that an additional factor should be taken into consideration. Lower size nanoparticles have been demonstrated to increase the antibacterial activity of the silver, due to either their ability to penetrate the bacteria wall [19] or the increase of the silver ion release [20]. Therefore, this may be the key factor acting as antibacterial agent in these two samples; however, the higher silver ion release must not be disregarded.

It should be also taken into consideration that the method used for antibacterial evaluation is highly depending on the sample surface, which is placed directly in contact with the bacteria broth; this is different from the procedure where species need to be dissolved in the agar. Thus, the silver segregation may play an important role on the antibacterial activity of the coatings,

since the silver segregation on the coatings surface will provide the system with enough antibacterial agent to act against the bacteria. In addition, this mechanism may be exploited as a self-controlling material to provide antimicrobial activity, due to the fact that despite of being an antibacterial surface, the silver ion release is kept below the toxicity levels and may prevent the contamination of the environment in which the material is located.

8.3 Conclusion

The results demonstrate that silver segregates on the surface of the coatings, highly dependent on the matrix composition. The silver ionization is found to be <100 ppb cm^{-2} also influenced by the matrix and phase distribution. The inhibition of bacterial growth depends on the ability of the material to form silver particles on the surface, the size of the silver particles and the amount of silver ions released to the medium.

8.4 References

1. Barshilia, H. C.; Kumar, P.; Rajam, K. S.; Biswas, A., Structure and Optical Properties of Ag–Al2o3 Nanocermet Solar Selective Coatings Prepared Using Unbalanced Magnetron Sputtering. *Solar Energy Materials and Solar Cells* **2011,** *95* (7), 1707-1715.

2. Papi, P. A.; Mulligan, C. P.; Gall, D., Crn–Ag Nanocomposite Coatings: Control of Lubricant Transport by Diffusion Barriers. *Thin Solid Films* **2012,** *524* (0), 211-217.

3. Wickens, D. J.; West, G.; Kelly, P. J.; Verran, J.; Lynch, S.; Whitehead, K. A., Antimicrobial Activity of Nanocomposite Zirconium Nitride/Silver Coatings to Combat External Bone Fixation Pin Infections. *International Journal of Artificial Organs* **2012,** *35* (10), 817-825.

4. Escobar Galindo, R.; Manninen, N. K.; Palacio, C.; Carvalho, S., Advanced Surface Characterization of Silver Nanocluster Segregation in Ag–Ticn Bioactive Coatings by Rbs, Gdoes, and Arxps. *Analytical and Bioanalytical Chemistry* **2013,** *405* (19), 6259-6269.

5. Chakravadhanula, V. S. K.; Mishra, Y. K.; Kotnur, V. G.; Avasthi, D. K.; Strunskus, T.; Zaporotchenko, V.; Fink, D.; Kienle, L.; Faupel, F., Microstructural and Plasmonic Modifications in Ag–Tio2 and Au–Tio2 Nanocomposites through Ion Beam Irradiation. *Beilstein Journal of Nanotechnology* **2014,** *5*, 1419-1431.

6. Manninen, N. K.; Galindo, R. E.; Carvalho, S.; Cavaleiro, A., Silver Surface Segregation in Ag-Dlc Nanocomposite Coatings. *Surface and Coatings Technology* **2015,** *267* (0), 90-97.

7. Muratore, C.; Voevodin, A. A.; Hu, J. J.; Jones, J. G.; Zabinski, J. S., Growth and Characterization of Nanocomposite Yttria-Stabilized Zirconia with Ag and Mo. *Surface and Coatings Technology* **2005,** *200* (5–6), 1549-1554.

8. Mulligan, C. P.; Blanchet, T. A.; Gall, D., Crn–Ag Nanocomposite Coatings: Effect of Growth Temperature on the Microstructure. *Surface and Coatings Technology* **2008,** *203* (5–7), 584-587.

9. Mulligan, C. P.; Blanchet, T. A.; Gall, D., Crn–Ag Nanocomposite Coatings: High-Temperature Tribological Response. *Wear* **2010,** *269* (1–2), 125-131.

10. Siozios, A.; Zoubos, H.; Pliatsikas, N.; Koutsogeorgis, D. C.; Vourlias, G.; Pavlidou, E.; Cranton, W.; Patsalas, P., Growth and Annealing Strategies to Control the Microstructure of Aln:Ag Nanocomposite Films for Plasmonic Applications. *Surface and Coatings Technology* **2014,** *255* (0), 28-36.

11. Mulligan, C. P.; Gall, D., Crn–Ag Self-Lubricating Hard Coatings. *Surface and Coatings Technology* **2005,** *200* (5–6), 1495-1500.

12. Akhavan, O.; Ghaderi, E., Capping Antibacterial Ag Nanorods Aligned on Ti Interlayer by Mesoporous Tio2 Layer. *Surface and Coatings Technology* **2009,** *203* (20-21), 3123-3128.

13. Calderon V, S.; Galindo, R. E.; Oliveira, J. C.; Cavaleiro, A.; Carvalho, S., Ag+ Release and Corrosion Behavior of Zirconium Carbonitride Coatings with Silver Nanoparticles for Biomedical Devices. *Surface and Coatings Technology* **2013,** *222* (0), 104-111.

14. Dobias, J.; Bernier-Latmani, R., Silver Release from Silver Nanoparticles in Natural Waters. *Environmental Science & Technology* **2013,** *47* (9), 4140-4146.

15. Marques, S. M.; Manninen, N. K.; Ferdov, S.; Lanceros-Mendez, S.; Carvalho, S., Ti1−Xagx Electrodes Deposited on Polymer Based Sensors. *Applied Surface Science* **2014,** *317* (0), 490-495.

16. Manninen, N. K.; Calderón V, S.; Almeida Alves, C. F.; Carvalho, S.; Cavaleiro, A., Influence of Hydrogen Incorporation and Coating Thickness on the Corrosion Resistance of Carbon Based Coatings Deposited by Magnetron Sputtering. *Surface and Coatings Technology* **2015,** *275* (0), 127-132.

17. Li, X.; Lenhart, J. J.; Walker, H. W., Dissolution-Accompanied Aggregation Kinetics of Silver Nanoparticles. *Langmuir* **2010,** *26* (22), 16690-16698.

18. Calderon V, S.; Ferreri, I.; Galindo, R. E.; Henriques, M.; Cavaleiro, A.; Carvalho, S., Electrochemical Vs Antibacterial Characterization of Zrcn-Ag Coatings. *Surface and Coatings Technology* **2015,** *275* (0), 357-362.

19. Sondi, I.; Salopek-Sondi, B., Silver Nanoparticles as Antimicrobial Agent: A Case Study on E. Coli as A model for Gram-Negative Bacteria. *Journal of Colloid and Interface Science* **2004,** *275* (1), 177-182.

20. Jung, W. K.; Koo, H. C.; Kim, K. W.; Shin, S.; Kim, S. H.; Park, Y. H., Antibacterial Activity and Mechanism of Action of the Silver Ion in Staphylococcus Aureus and Escherichia Coli. *Applied and environmental microbiology* **2008,** *74* (7), 2171-2178.

PRODUCTION AND CHARACTERIZATION OF ZrCN-Ag COATINGS DEPOSITED BY MAGNETRON SPUTTERING

CHAPTER IX – Conclusions and Further Studies

9 Conclusion and further studies

ZrCN-Ag coatings were successfully deposited by dual magnetron sputtering, in order to evaluate its ability as a bio-materials to be applied in prosthetic devices. The chemical, structural, morphological, mechanical, tribological and electrochemical properties of the coatings were assessed and their correlation have been performed.

An optimization process was used in order to determine the best deposition conditions to achieve an enhanced adhesion, corrosion resistance and mechanical performance varying gas fluxes and silver target current density. The amount of silver showed to be the main parameter controlling all these functional properties. It was demonstrated that silver nanoparticles must be combined with a well-defined $ZrC_{1-x}N_x$ crystalline phase in order to reach a protective ZrCN + Ag film, schematically summarized in Figure 9-1. However, very high silver content is even detrimental for a well-defined $ZrC_{1-x}N_x$ crystalline phase

Both mechanical and electrochemical properties are altered by the addition of acetylene and nitrogen gases to the deposition process. In fact, the effect of each gas is not statistically significant, but the ratio between them seems to affect these properties. Therefore, it is proved that the ratio between the reactive gases must be properly established to achieve a stoichiometric $ZrC_{0.5}N_{0.5}$ crystalline phase in order to enhance the mechanical and corrosion resistances of the coatings.

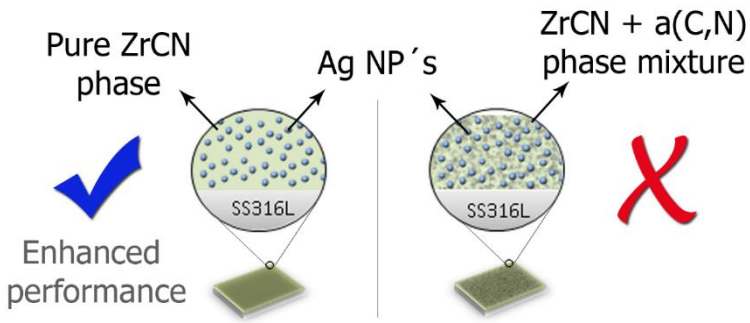

Figure 9-1 optimization process for Zr-C-N-Ag films

Different phases were found, analyzed and interpreted using XPS, XRD, TEM, and Raman techniques. Mainly two groups or regimes can be highlighted. In the first group, a pure ZrCN FCC crystalline phase with FCC metallic silver nanoparticles with very low or none a-(C, N) phases, with low variations of the ZrCN grain size and constant silver grain size. These films

showed the presence of ZrCN(O) and ZrO_2, without any evidence of silver oxidation on the surface and very low content of oxygen in the ZrCN(O) phase in the bulk composition. Silver is surrounded by the ZrCN phase. The second group is composed of samples with an increasing content of a-(C, N) phases, responsible for the reduction of the ZrCN grain size, silver oxidation and the formation of a thicker ZrO_2 on the surface of the films. The a-(C,N) encapsulates both ZrCN and silver particles, as schematically presented in Figure 9-2.

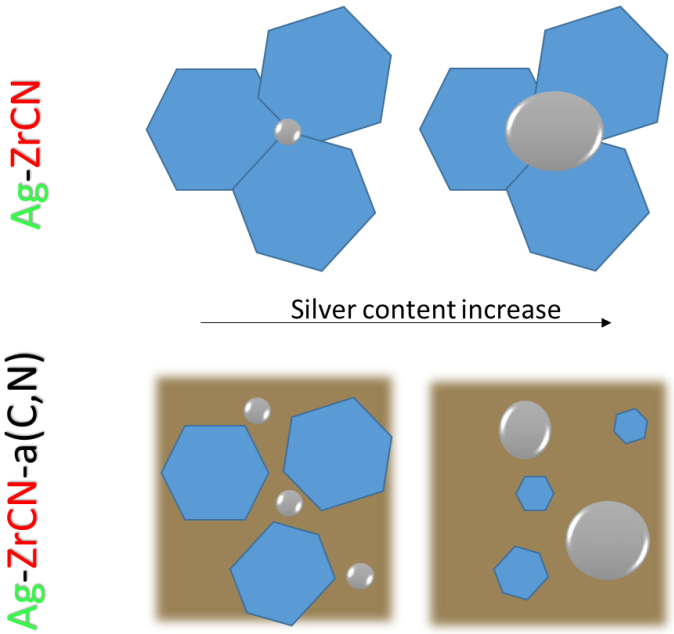

Figure 9-2 Phase distribution scheme

The hardness of the system is highly dependent on the content of the ZrCN crystalline phase, being reduced with increasing silver and amorphous carbon phases. The COFs revealed a dominant ploughing mechanism on the friction forces dependent on the roughness and hardness of the films. No wear rate was measurable on the coatings and the UHMWPE wear rate did not exhibit significant differences between the samples, attributed to the formation of a protective layer of albumin on the material surface. The small variance of the UHMWPE wear rate was correlated to this protective layer, which is dependent on the hydrophobic/hydrophilic surface character, as well as on the silver content.

The electrochemical characterization revealed an enhanced corrosion resistance, in Hank's balanced salt solution with 10 g L^{-1} of BSA, of stainless steel when coated with ZrCN-Ag-a(C,N) coatings with low contents of silver and amorphous carbon phases. When increasing the silver and amorphous carbon contents, electrochemical porous material is produced, inducing a reduction of the charge transfer resistance. Immersion test, on the other hand, showed a

constant increase of the polarization resistance of the material for the first 72 h of immersion, attaining a constant value thereafter. This behavior is attributed to a passivation layer created by the surface oxidation of both Zr and Ag, as well as the adsorption of albumin onto the surface. In addition, a low silver release is detected, which also decreased the electrochemical activity of the surfaces.

These three functional properties, hardness, wear and corrosion resistance, are schematically summarized in Figure 9-3. Considering these results, potentially interesting coatings for the industry are foreseen. The development of coatings with low silver and amorphous carbon phase contents should be performed, testing the tribo-corrosion mechanisms of the coatings in larger number of cycles than the ones produced in this work, as well as using prosthesis simulators.

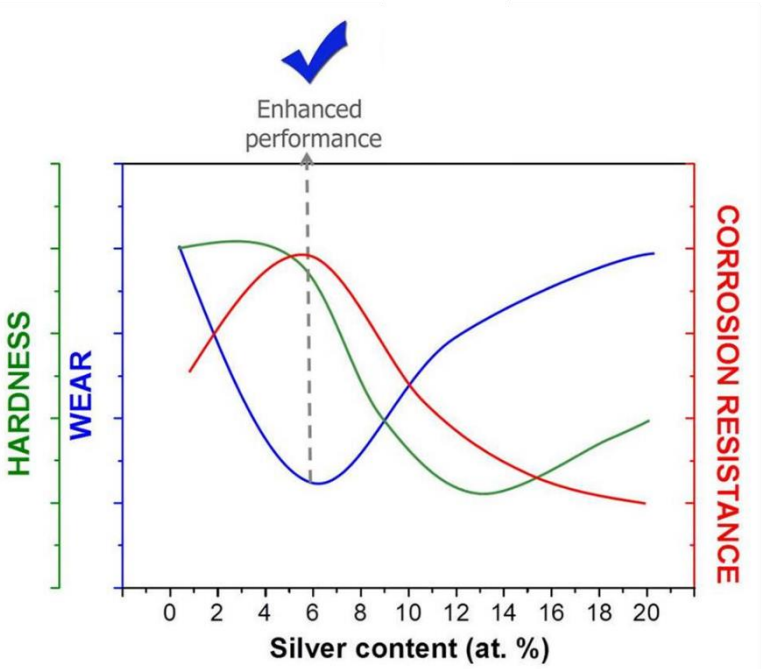

Figure 9-3 Hardness, corrosion resistance and wear behavior of ZrCN-Ag coatings summary

The immersion tests of the samples in NaCl 0.9% w/v also revealed silver ion release lower than 100 ppb cm^{-2} in all the samples and silver segregation and growth after 240 h of immersion, via an Oswald ripening process. The highest silver release was found for coatings containing smaller particles and silver in oxidized state, which correspond to amorphous carbon phases containing films. This fact is explained due to a electrochemical activation of the silver due to the surrounding phase (ZrCN or a-(C,N)), which activate or reduce the silver release, as schematized in Figure 9-4.

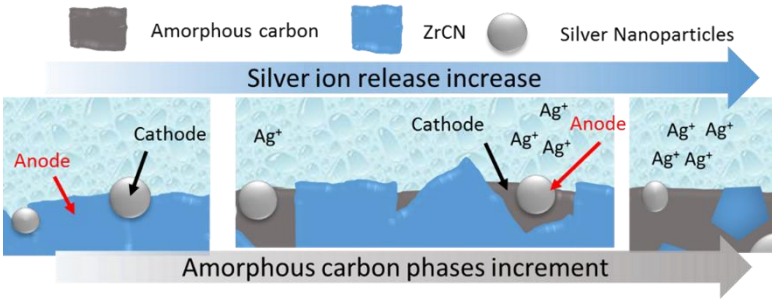

Figure 9-4 Scheme of phase distribution and determination of anode and cathode in the electrochemical reaction that triggers the silver release.

The bacterial zone of inhibition *against S. epidermidis* found in the tested coatings, was explained by a combination of three factor i) the ability of the material to form silver particles on the surface, ii) the size of the silver particles and iii) the amount of silver ions produced by those particles.

The results support the idea of utilizing ZrCN-Ag coatings as a surface modification option for multifunctional purposes, adding functionalities, such as corrosion resistance, maintaining or even improving their mechanical and tribological performance. However, the preliminary antimicrobial test revealed only small zones of inhibition of bacteria growth. Therefore, a detailed study with a complete biological focus is proposed, in order to better understand the influence of different matrices on the silver antibacterial action and its enhancement, without provoking undesired response in the human body, such as cytotoxicity.

After a more detailed biological response study of the coatings, the optimized coating must be tested in conditions that mimic the prosthetic devices, by coating real devices, using medical devices simulators. Both tribological and corrosion resistance behavior should be tested simultaneously in order to be able to take into consideration the synergy of these effects.

Additionally, the results of these thesis showed no measured wear in the coatings, but small difference in the wear resistance of the counter part by changing the chemical and physical properties of the coatings, and therefore, it would be of great interest to study the behavior of the coatings against several counter parts, or even between two coated surfaces in order to elucidate a possible enhancement in the tribological performance.

Finally, if positive results are observed in terms of biological performance and specialized tribo-corrosion test, an *in vivo* approach should be pursued.